

Bangor University

DOCTOR OF PHILOSOPHY

Suspended sediment dynamics in the upper Gulf of California

Alvarez Sánchez, Luis Gustavo

Award date:
2003

Awarding institution:
University of Wales, Bangor

[Link to publication](#)

General rights

Copyright and moral rights for the publications made accessible in the public portal are retained by the authors and/or other copyright owners and it is a condition of accessing publications that users recognise and abide by the legal requirements associated with these rights.

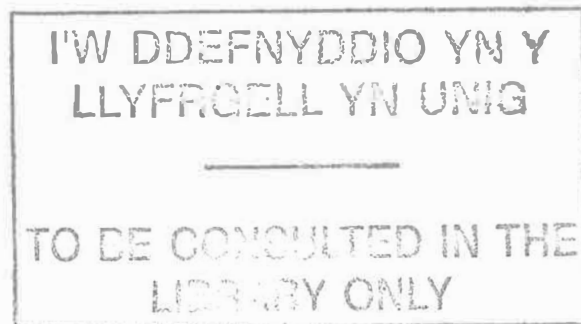
- Users may download and print one copy of any publication from the public portal for the purpose of private study or research.
- You may not further distribute the material or use it for any profit-making activity or commercial gain
- You may freely distribute the URL identifying the publication in the public portal ?

Take down policy

If you believe that this document breaches copyright please contact us providing details, and we will remove access to the work immediately and investigate your claim.

Download date: 10. Apr. 2024

Suspended Sediment Dynamics
in the
Upper Gulf of California



A thesis submitted in accordance with the requirements of the University of Wales
for the degree of Doctor of Philosophy.

by

Luis Gustavo Alvarez Sánchez

University of Wales, Bangor
School of Ocean Sciences
Menai Bridge
Anglesey LL59 5EY
United Kingdom

September, 2003



Abstract.

Until 1930 the Upper Gulf of California was an estuarine system into which $20 \times 10^9 \text{ m}^3 \cdot \text{yr}^{-1}$ of fresh water, and $180 \times 10^6 \text{ tons} \cdot \text{yr}^{-1}$ of sediment were supplied by the Colorado River. Damming of the river and the high evaporation turned the Upper Gulf into an inverse estuary with high turbidity, attributed to tidal erosion and resuspension of bed deposits in the river delta. The origin and distribution of suspended particulate matter has been scarcely studied, mostly through indirect estimates of turbidity levels. The tide has been assumed to control the amount of sediment in suspension, but detailed observations of suspended matter concentration and tidal forcing were unavailable prior to this study.

In August 1997 an intense survey was made across the Upper Gulf in which current meters, transmissometers, optical backscatter sensors and an acoustic Doppler current profiler were deployed during one fortnightly cycle. Water column data using a profiling CTD and optical sensors were obtained during spring and neap tides at fixed stations, as well as in a gulf-wide survey. During a preliminary two-day survey in June 1996 two current meters were deployed off the western coast of the Upper Gulf. Observations using CTD and an optical sensor were made during spring and neap tides. The surveys have supplied the first detailed profiles of SPM concentration, current velocity and hydrography, under contrasting tidal conditions, and continuous records of near-bed and mid-water SPM concentration during a fortnightly cycle.

A tidal logarithmic bottom boundary layer was observed in a nearly homogeneous water column over most of the fortnightly cycle, except during short periods near slack water, and during neap tides. Observed SPM concentration varied from $10^{-2} \text{ kg} \cdot \text{m}^{-3}$ to $10^{-1} \text{ kg} \cdot \text{m}^{-3}$ near the sea bed, and decreased upwards to $\sim 0.005 \text{ kg} \cdot \text{m}^{-3}$ near the sea surface. The main control of SPM concentration was tidal resuspension, as shown by the quarter-diurnal, fortnightly-modulated peaks in the SPM time series. In contrast, during neap tides the interaction between slow tidal currents and near-bed gravity current events induced weak resuspension peaks at the semidiurnal frequency. Critical bed stress for erosion was in general $0.6 \text{ Pa} - 0.7 \text{ Pa}$ during spring tides and one order of magnitude smaller during neap tides. A sediment deposition threshold was not evident in the data. The bed stress–SPM concentration time series follows a continuous deposition model better than a mutually exclusive erosion–deposition model for cohesive sediments. A simple erosion–deposition point model overestimated the observed SPM concentration due to an excess of erosion over deposition, a discrepancy ascribed to an underestimation of the prescribed single-class particle settling velocity. Based on observed current velocity and calibrated acoustic backscatter signal levels from the ADP, the maximum horizontal SPM fluxes were $\pm 30 \text{ g} \cdot \text{m}^{-2} \cdot \text{s}^{-1}$ during spring tides and $-6 \text{ g} \cdot \text{m}^{-2} \cdot \text{s}^{-1}$ during neaps. A residual SPM flux of $-2.5 \text{ g} \cdot \text{m}^{-2} \cdot \text{s}^{-1}$ out of the Upper Gulf was obtained in neap tides due to the near-bed flow of denser, warm and saline water during gravity current events. This result shows that the inverse estuarine nature of the Upper Gulf is a key factor influencing the transport of suspended sediment at least during summer.

Acknowledgements.

I would like to express my gratitude to my supervisor Dr. Sarah E. Jones for her guidance throughout this study, which demanded many hours of work at sea, and for the productive discussions during the data analysis and writing of this thesis. Thanks to Prof. John H. Simpson for his critical review of basic chapters of this dissertation. I would like to thank Dr. José Luis Ochoa for his helpful comments during the thesis progress. My gratitude to Dr. Mario Martínez García, former director of CICESE, for his support during the initial stages of this study, and also to Dr. F. Javier Mendieta, director of CICESE, for providing financial assistance to conclude my PhD program. Thanks also to my colleague Miguel Lavín for his words of encouragement and his assistance during the work at sea.

Technical support was most valuable during sea operations and in data reduction and display. Special recognition is due to Rafael Ramírez M., the project technician, for his assistance and hard work. Also my gratitude for the technical support provided by Víctor Godínez, Salvador Sánchez (Chava), Carlos Cabrera, Juan Francisco Moreno, from CICESE and to Neil R. Fisher and David M. Probert from the School of Ocean Sciences (UWB), all participants in the intensive sea operations. My appreciation to the students who helped with the field work at sea, especially to Ana María Ramírez. Thanks are due to Capt. Gerardo Sánchez and crew of CICESE's research vessel *B/O Francisco de Ulloa*, and to the technical staff of the oceanographic equipment support group at CICESE.

I want to express my appreciation to Drs. Des Barton from (SOS) and Teri, for their hospitality and long-lasting friendship.

I would like to thank my wife Rosa and children Luis and Mónica for their constant love and support.

The financial support by ANUIES (México) through a one-year part-time SUPERA studentship is acknowledged. This study was funded by CONACyT (research grant 3007P-T) and CICESE (research grant 5430).

Contents.

1. Oceanography of the Upper Gulf of California. An overview.	1
1.1. Geographical setting.	1
1.2. Bottom configuration and sediments.	2
1.3. Thermohaline structure.	3
1.4. Tides and tidal currents.	5
1.5. Circulation and mixing.	6
1.6. Sediment transport.	8
1.7. Summary.	10
2. Aims and motivation for the present study.	22
3. The observational program.	26
3.1. Instrument moorings.	26
3.2. Current measurements.	27
3.2.1. Acoustic Doppler current profiler.	27
3.2.2. Current meters.	28
3.3. Optical instruments.	30
3.3.1. Optical backscatter sensors (OBS).	30
3.3.2. Transmissometers.	31
3.4. CTD Spatial survey and tidal cycle stations.	33
4. Results.	41
4.1. Bathymetry.	41
4.2. Spatial survey.	41
4.2.1. Hydrography.	
4.2.2. Suspended particulate matter (SPM).	42
4.3. Fortnightly time series.	42
4.3.1. Currents.	42
4.3.1.1. Basic current statistics. West side.	43
4.3.1.2. Basic current statistics. East side.	44

4.3.2. SPM concentration time series.	45
4.3.2.1. Near bed SPM time series.	45
4.3.2.2. Mid-water SPM time series.	46
4.3.3. Tide and wind conditions.	47
4.4. Tidal cycle stations.	47
4.4.1. Hydrography.	47
4.4.2. Suspended particulate matter (SPM).	49
4.4.2.1. Spring tides.	49
4.4.2.2. Neap tides.	50
5. Velocity profiles and boundary layer parameters.	71
5.1. Introduction.	71
5.2. Analysis of velocity profiles.	73
5.3. Results.	76
5.3.1. Bed roughness scale z_0 .	77
5.3.2. Friction velocity u_* and bed shear stress τ_0 .	77
5.3.3. Bottom drag coefficient C_D .	78
5.3.4. Summary.	79
6. The sediment resuspension process.	89
6.1. Introduction.	89
6.2. Erosion-deposition process.	90
6.3. Erosion parameters extraction method.	92
6.3.1. Erosion parameters from vertically integrated SPM concentration.	93
6.3.1.1. Critical bed stress for erosion τ_{0e} .	93
6.3.1.2. Erodibility α .	95
6.3.2. Erosion parameters from single level SPM concentration.	96
6.3.2.1. Critical bed stress for erosion τ_{0e} .	97
6.3.2.2. Determination of the rate of change of concentration α_{sl} .	99
6.4. Deposition parameters.	100
6.5. A simple point model.	100

6.5.1. Vertically integrated SPM concentration.	102
6.5.2. Single level near-bed SPM concentration.	103
7. Horizontal SPM fluxes.	114
7.1. Introduction.	114
7.2. Observations.	116
7.3. Data analysis.	117
7.3.1. Acoustic signal strength and SPM concentration.	117
7.3.2. Horizontal SPM fluxes.	118
7.3.3. Near-bed velocity profiles.	119
7.3.4. Near-bed horizontal SPM fluxes.	119
7.4. Results.	120
7.4.1. Hydrographic setting. Along-gulf transects.	120
7.4.2. SPM fluxes. Fortnightly cycle.	120
7.4.3. SPM fluxes. Near-bed series.	121
8. Discussion.	130
8.1. Currents and boundary layer parameters.	130
8.2. SPM concentration and tidal effects.	137
8.3. Suspended sediment dynamics.	138
8.3.1. Point models of SPM dynamics.	141
8.3.2.1. Vertically integrated SPM concentration.	141
8.3.1.2. Single level SPM concentration.	144
8.4. SPM fluxes.	145
8.4.1. SPM and acoustical backscatter signal.	145
8.4.2. Horizontal SPM flux.	147
8.4.2.1. Gravity current effects.	147
8.4.2.2. Topographic effects.	148
8.5. Concluding remarks.	150
8.6. Ways forward	151
References.	162
Appendix	174

List of Figures.

Figure 1.1. Bathymetry and regions of the Gulf of California.

Figure 1.2. Geographic and bathymetric features of the Upper Gulf of California.

Figure 1.3. Bathymetry of the Upper Gulf of California. Dashed lines are estimated depth contours (after Thompson, 1968).

Figure 1.4. Distribution of mean grain size (ϕ units) in the Upper Gulf and delta tidal channels (Carriquiry and Sánchez, 1999).

Figure 1.5. Distribution of surface temperature, salinity and density (σ_t) in December (left) and August (right) in the Upper Gulf of California (after Lavín et al., 1998).

Figure 1.6. Tidal residual currents (left) and 30-day residual trajectories (right) in the northern Gulf of California. The boundary of the Upper Gulf is indicated.

Figure 1.7. Tidal and wind induced residual currents in the northern Gulf of California, with a south wind (left) and with a north wind at $5 \text{ m}\cdot\text{s}^{-1}$ (right). The Upper Gulf is located as in Figure 1.7 (after Marinone and Lavín, 1997).

Figure 1.8. The modelled stratification parameter Φ in the northern Gulf of California for September and December (after Argote et al., 1994).

Figure 1.9. Recent dispersal patterns (arrows) of suspended load and bed load in the Upper Gulf of California (after Thompson, 1969).

Figure 1.10. Model of bed sediment transport patterns and deposition in the Upper Gulf of California (Carriquiry and Sánchez, 1999).

Figure 1.11. Qualitative distribution of turbidity based on Secchi disk readings. Darker areas indicate more turbid waters (after Hendrickson, 1973).

Figure 2.1. Conceptual model of contrasting flow, salinity and suspended matter (SPM) distribution along: a) the classic estuary, and b) the inverse estuary (after Postma, 1967).

Figure 3.1. Instrument mooring sites in the Upper Gulf of California. Moorings were deployed at sites W1, W2, W3, E1, E2 in August 1997 and at site J in June 1996.

Figure 3.2. Schematic view of the ADP mooring at site W (left), and the current meter and SPM sensors at sites W1 and E1 (right). No current meters were deployed at sites W2 and E2.

Figure 3.3. Calibration of the OBS sensor against SPM concentration from filtered water samples obtained in August 1997 across the Upper Gulf.

Figure 3.4. Calibration of the SeaTech transmissometer beam attenuation against SPM concentration from filtered water samples obtained in August 1997 across the Upper Gulf. a) calibration line for beam attenuation $> 8 \text{ m}^{-1}$; b) calibration line for beam attenuation $< 8 \text{ m}^{-1}$.

Figure 3.5. Along-gulf CTD station lines made in August 1997.

Figure 3.6. Across-gulf CTD station lines made on the western side, in August 1997.

Figure 4.1. Bathymetry of the Upper Gulf of California from surveys made in 1994-1997. Depth contours relative to Mean Sea Level.

Figure 4.2. Temperature and salinity in the Upper Gulf of California at the sea surface and at 4 m above the bed. CTD stations (dots) were made in August 13–15 and 23–24, 1997.

Figure 4.3. Density and SPM concentration in the Upper Gulf of California at the sea surface and at 4 m above the bed. CTD and OBS casts (dots) were made in August 13–15 and 23–24, 1997. The SPM distribution is based on casts made under low velocity conditions ($<0.15 \text{ m}\cdot\text{s}^{-1}$).

Figure 4.4. Currents measured at site W1 on the western side of the Upper Gulf at 1.2 m and at 4.2 m above sea bed (speed only). Positive along-gulf velocity corresponds to flood current.

Figure 4.5. Currents measured at site E1 on the eastern side of the Upper Gulf at 4.2 m and at 12.5 m above the sea bed. Positive along-gulf velocity corresponds to flood current.

Figure 4.6. SPM concentration time series from OBS sensors on the western side of the Upper Gulf. Site W2, 1 m and 3.7 m above the bed; site W3, 1 m and 6 m above the bed.

Figure 4.7. SPM concentration time series from OBS sensors on the eastern side of the Upper Gulf at site E2, at 1 m and 3.7 m above the sea bed.

Figure 4.8. SPM concentration time series from transmissometers on the western side of the Upper Gulf at site W1, at 1 m and 3.7 m above the sea bed.

Figure 4.9. SPM concentration time series from transmissometers on the eastern side of the Upper Gulf at site E1, at 1 m and 12 m above the sea bed.

Figure 4.10. Tide and winds during the August 1997 survey in the Upper Gulf. (a) Tide measured by the ADP pressure sensor at site W3. (b) Winds from observations made by the *R/V D. Starr Jordan* while under-way across the Northern Gulf.

Figure 4.11. Spring-tide time series of temperature, salinity and density (σ_t) observed at site J in June, 1996.

Figure 4.12. Neap-tide time series of temperature, salinity and density (σ_t) observed at site J in June, 1996.

Figure 4.13. Time series of SPM concentration and current velocity 1 m above sea bed observed at site J in June, 1996 under: a) spring tides and b) neap tides. The solid line is along-gulf velocity (positive for flood) and the dashed line is across-gulf velocity.

Figure 4.14. Spring-tide time series of temperature, salinity and density (σ_t) observed at site W3 in August, 1997.

Figure 4.15. Neap-tide time series of temperature, salinity and density (σ_t) observed at site W3 in August, 1997.

Figure 4.16. Time series of SPM concentration and current velocity 1.2 m above sea bed observed at site w3 in August, 1997 under: a) spring tides and b) neap tides. The solid line is along-gulf velocity (positive for flood) and the dashed line is across-gulf velocity.

Figure 4.17. Spring-tide time series of temperature, salinity and density (σ_t) observed at site E1 in August, 1997.

Figure 4.18. Neap-tide time series of temperature, salinity and density (σ_t) observed at site E1 in August, 1997.

Figure 4.19. Time series of SPM concentration and current velocity 4.2 m above sea bed observed at site E1 in August 1997, under: a) spring tides and b) neap tides. The solid line is along-gulf velocity (positive for flood) and the dashed line is across-gulf velocity.

Figure 5.1. Comparison between velocity components 1.2 m above the bed from the current meter at site W1 and the ADP at site W3 (left frames). Cross-correlation of velocity components from both sites (right frames).

Figure 5.2. Velocity components u, v at site W3 at 5 m and 15 m above the sea bed (upper frames). Progressive vector plots at the same levels during the fortnightly cycle (lower frames). Neap tides are at the start and at the end of the distance plots.

Figure 5.3. Logarithmic layer thickness above 1.2 m (a), and correlation coefficient R (b) of the log-layer fits during the fortnightly cycle. $R < 0.9$ is not shown.

Figure 5.4. Selected along-gulf velocity profiles measured by the ADP at site W3 over one semidiurnal cycle (circles). The fitted log-layer profiles are indicated by the solid lines. (a) spring tides; (b) neap tides.

Figure 5.5. Bed roughness length z_0 obtained by log-layer analysis, plotted as the 95% confidence interval during the fortnightly cycle.

Figure 5.6. Friction velocity u_* obtained by log-layer analysis, plotted as the 95 % confidence interval during the fortnightly cycle.

Figure 5.7. Bed shear stress τ_0 obtained by log-layer analysis, plotted as the 95% confidence interval during the fortnightly cycle.

Figure 5.8. Distribution of the bed roughness z_0 during the fortnightly cycle (top) and histogram of z_0 (bottom). Values larger than 0.5 m were not included in the histogram.

Figure 5.9. Drag coefficient C_D based on the reference velocity $U_{1.2}$ observed at site W3, at 1.2 m above the sea bed. The 95% confidence interval is indicated. The friction velocity u_* was obtained from the log-layer analysis.

Figure 5.10. Drag coefficient C_D under ebb and flood based on the reference velocity $U_{1.2}$ observed at site W3, at 1.2 m above the sea bed. The 95% confidence interval is indicated. The friction velocity u_* was obtained from the log-layer analysis.

Figure 5.11. Drag coefficient C_D under spring tides based on the reference velocity $U_{1.2}$ observed at site W3 at 1.2 m above the sea bed. The 95% confidence interval is indicated. The friction velocity u^* was obtained from the log-layer analysis.

Figure 5.12. Drag coefficient C_D under neap tides based on the reference velocity $U_{1.2}$ observed at site W3 at 1.2 m above the sea bed. The 95% confidence interval is indicated. The friction velocity u^* was obtained from the log-layer analysis.

Figure 6.1. Conceptual diagram of the critical bed stress for erosion (τ_{0e}) and for deposition (τ_{0d}) in the sediment resuspension-settling cycle. M is the SPM content in the water column and τ_0 is the bed stress (after Clarke and Elliott, 1998).

Figure 6.2. Conceptual diagram of the centroid method showing the critical bed shear stress for erosion τ_{0e} , the centroid, and the slope angle of the line through the points.

Figure 6.3. Time series current speed 1.2 m above the bed (S), SPM concentration at 1 m above the sea bed (C) and SPM concentration vertically integrated (M) during the tidal cycle stations at site W3 under spring (a) and neap tides (b).

Figure 6.4. Critical bed stress for erosion at sites W1 and W3 during the fortnightly cycle, estimated by least squares fits. The black circles are the values obtained from the vertically integrated SPM concentration during tidal cycle stations under spring and neap tides. Open circles are values extracted from single-level SPM concentration time series. The solid line is the Msf tidal frequency fit to these points and the dashed line is the tidal amplitude (m). Site W1 is 3.4 km northwest of site W3, on the west side of the Upper Gulf.

Figure 6.5. Critical bed stress for erosion at sites E1 and J (black circles). The values were obtained by least squares fits from the vertically integrated SPM concentration during the tidal cycle stations under spring and neap tides. Open circles are the values extracted from single-level SPM concentration time series. The solid line is the Msf tidal

frequency fit to these points and the dashed line is the tidal amplitude (m). Site E1 is on the east side and site J is on the west side of the Upper Gulf.

Figure 6.6. Asymmetric two-harmonic least squares fits of the critical bed shear stress for erosion extracted from single level observations at sites W1 and W3 on the western side of the Upper Gulf.

Figure 6.7. Calculated erosion rate (E), deposition rate (D) and vertically integrated SPM concentration M (dotted line) at site J using parameters derived by (a) least squares, and (b) centroid method. The observed vertically integrated SPM concentration is shown by the solid line in the lower panels of (a) and (b).

Figure 6.8. Calculated erosion rate (E), deposition rate (D) and vertically integrated SPM concentration M (dotted line) at site W3 using parameters derived by (a) least squares, and (b) centroid method. The observed vertically integrated SPM concentration is shown by the solid line in the lower panels of (a) and (b).

Figure 6.9. Calculated erosion rate (E), deposition rate (D) and vertically integrated SPM concentration M (dotted line) at site E1 using parameters derived by (a) least squares, and (b) centroid method. The observed vertically integrated SPM concentration is shown by the solid line in the lower panels of (a) and (b).

Figure 6.10. Simulated SPM concentration at site W3, 1.2 m above the sea bed (black trace). The erosion threshold was prescribed as: constant (a), variable symmetric, given by equation 6.4 (b), and variable asymmetric, given by equation 6.7 (c). The concentration rate of change ($0.000011 \text{ kg}\cdot\text{m}^{-3}\cdot\text{s}^{-1}$) and a background concentration ($0.011 \text{ kg}\cdot\text{m}^{-3}$) were kept constant. The observed SPM concentration is also shown (gray trace).

Figure 7.1. Instrument mooring sites J, W3 and E1, and three along-gulf transects (A, B, C) of hydrographic stations made in the Upper Gulf in August 1997.

Figure 7.2. Observed SPM concentration vs ADP acoustic signal strength (circles). The regression line (solid line) is shown with the 68% confidence interval (dashed lines).

Figure 7.3. Along-gulf velocity profiles during one semidiurnal cycle, under spring and neap tides at sites J (June, 1996), W3 and E1 (August 1997). Circles represent the observations and the solid lines represent the logarithmic fits for which the roughness length was less than 0.2 m.

Figure 7.4. Vertical distributions of salinity, sigma-t and SPM concentration observed on 14 August 1997. (a) transect A and (b) transect B shown in Figure 7.1. Station numbers are shown above each transect. The ADP was moored near station 71 in transect A.

Figure 7.5. Vertical distributions of salinity, sigma-t and SPM concentration observed on 23 August 1997, along transect C shown in Figure 7.1. Station numbers are shown above each transect. The mooring site E1 was located near station 325.

Figure 7.6. Horizontal SPM fluxes derived from ADP data at the level of the gravity current core (5.2 m above the bed), at site W3. Fluxes along- (thin line) and across-gulf (heavy line) are 5-minute averages.

Figure 7.7. Comparison between horizontal SPM fluxes at 5.2 m above the bed at site W3, obtained from OBS (circles) and ADP backscatter (solid line), under spring and neap tides. The flux scale in the lower right frame is a factor four larger.

Figure 7.8. Profiles of time-averaged along-gulf SPM fluxes at site W3 in August 1997: (a) averaged over six semidiurnal cycles in neap tides, (b) averaged over 14.7 days, and (c) averaged over six semidiurnal cycles in spring tides. Negative fluxes are outward the Upper Gulf. The dotted lines indicate the 68% confidence interval for each profile.

Figure 8.1. Relationship between $C_{D1.2}$ from the quadratic law (y-axis) and that from the logarithmic profile law (x-axis), as an internal consistency test following Collins *et al.* (1998). The dashed line has slope 1 as reference.

Figure 8.2. Fortnightly variation of the bed roughness z_0 averaged over consecutive semidiurnal cycles. Conventional average (Z_{0ca}) and exponent average (Z_{0ea}), after Cheng, *et al.* (1999).

Figure 8.3. Along-gulf velocity 1.2 m above the sea bed at site W3 (thin line). The superimposed heavy line corresponds to time intervals during which the logarithmic profiles were valid ($R \geq 0.95$).

Figure 8.4. Hypothetical behaviour of SPM concentration and bed shear stress as described by two conceptual models: the continuous deposition model (non-cohesive sediments), and the mutually exclusive erosion and deposition model (cohesive sediments), after Sanford and Halka (1993).

Figure 8.5. Segment of a core showing the upper 5 cm of the sea bed sediments in the central Upper Gulf. The core was obtained during spring tides when current speed was $\sim 0.7 \text{ m}\cdot\text{s}^{-1}$. The top 2 cm show coarser texture overlying muddy sediments. The thin surface film was a fluff layer that settled from the water column trapped inside the core.

Figure 8.6. Spring tide temperature, salinity, sigma-t and SPM concentration from casts made every half-hour at site W3, in August 1997. Along-gulf velocity vectors drawn in the lower frame are at 1.2 m and 15.0 m above the sea bed. Arrows pointing to the left indicate outflow from the Upper Gulf.

Figure 8.7. Neap tide temperature, salinity, sigma-t and SPM concentration from casts made every half-hour at site W3, in August 1997. Along-gulf velocity vectors drawn in the lower frame are at 1.2 m and 15.0 m above the sea bed. Arrows pointing to the left indicate outflow from the Upper Gulf.

Figure 8.8. Neap tide SPM concentration from casts made every half-hour at site J, in June 1996. Along-gulf velocity vectors are drawn at 1 m and 5 m above the sea bed. Arrows pointing to the left indicate outflow from the Upper Gulf.

Figure 8.9. Progressive vectors plot using simultaneous velocity data from opposite sides of the Upper Gulf during neap tides, at 1.2 m from the bed: W1 (west side) and E1 (east side). The plot represents 1.3 days.

List of Tables.

Table 1.1. Amplitudes and phases for the seven major diurnal and semi-diurnal constituents in the Upper Gulf of California (after Morales-Pérez y Gutiérrez de Velasco, 1989).

Table 3.1. ADP sensor specifications.

Table 3.2. Deployment parameters of the acoustic Doppler profiler at site W3. Bottom depth: 25 m below MSL.

Table 3.3. Sensors of the Aanderaa current meters.

Table 3.4. Sensors of the General Oceanics current meters.

Table 3.5. Current meter deployment at site W1. Water depth: 21 m below MSL.

Table 3.6. Current meter deployment at site E1. Water depth: 30 m below MSL.

Table 3.7. Specifications of the profiling CTD unit on board the *Francisco de Ulloa*.

Table 4.1. Basic current statistics from current meter Aanderaa 651, 1.2 m above the sea bed, at site W1. The azimuth angle of the principal axes is indicated.

Table 4.2. Basic current statistics from current meter Aanderaa 652, 4.2 m above the sea bed, at station W1. The time span corresponds to that of current meter at 1.2 m.

Table 4.3. Basic current statistics from current meter GO606, 4.2 m above the sea bed, at site E1. The azimuth angle of the principal axes is indicated.

Table 4.4. Basic current statistics from current meter GO405, 12.5 m above the sea bed, at site E1. The azimuth angle of the principal axes is indicated.

Table 5.1. Drag coefficient C_D with the 95% confidence interval obtained by least squares fit.

Table 6.1. Critical erosion bed stress τ_{0e} based on depth integrated SPM time series from sites J, W3 and E1 using the least squares method with 2 hours of data . n is the number of averaged values.

Table 6.2. Mean critical erosion bed stress τ_{0e} based on depth integrated SPM time series from sites J, W3 and E1. τ_{0e} was read directly from the dM/dt vs τ_0 plot. n is the number of averaged values.

Table 6.3. Mean erodibility α based on vertically integrated SPM time series from sites J (June, 1996), W3 and E1 (August 1997) using the least squares method with 2 hours of data. n is the number of averaged values.

Table 6.4. Mean erodibility α based on vertically integrated SPM time series from sites J (June, 1996), W3 and E1 (August 1997) using the centroid method with 2 hours of data. n is the number of averaged values.

Table 6.5. Critical erosion bed stress τ_{0e} based on single level SPM time series from sites W1, W3 and E1 (August 1997) using the centroid method with 2 hours of data. n is the number of averaged values.

Table 6.6. Concentration rate of change α_{sl} ($\text{kg m}^{-3} \text{s}^{-1}$) based on single level time series from sites W1, W3 and E1 (August, 1997) using the centroid method with 2 hours of

data. Spring tides (SP), neap tides (NP). n is the number of averaged values and s.d. is the standard deviation.

Table 6.7. Erosion and deposition parameters used in the point modelling of vertically integrated SPM concentration at sites J, W3 and E1 under spring tide conditions. The settling velocity w_s was measured with settling tubes, and the near bed concentration C_b was measured 1 m above the sea bed.

Table 7.1. Horizontal along-gulf SPM fluxes during spring (Sp) and neap (Np) tides. Fluxes at sites J and W3 were integrated over the indicated depths. Fluxes at site E1 were estimated at 4.2 m above the bed. The numbers in parenthesis indicate the full semidiurnal cycles used in the calculations.

Table 8.1. Statistics of settling velocity obtained at site W3 from observed SPM at 2 m and 3 m above the bed and the Rouse profile assumption. N is the number of samples.

Table A.1.. Sample calculation of the critical bed shear stresss for erosion and erodibility.

1. Oceanography of the Upper Gulf of California: An overview.

1.1 Geographical setting.

The northwest end of the Gulf of California, north of 31° N, is known as the Upper Gulf of California, henceforth called the Upper Gulf (Fig. 1.1). It is a semi-enclosed basin surrounded by arid alluvial plains and piedmont deposits. It forms a triangle of about 75 km per side with the old Colorado River mouth at its northern corner (Fig. 1.2). Until 1935 the Colorado River was the main source of terrigenous sediments that formed the extensive delta on the Gulf's northwest end. Since then, the river has been diverted and dammed so its annual average discharge has reduced from $21 \times 10^9 \text{ m}^3$ to less than $1 \times 10^9 \text{ m}^3$ (a minimum of $0.1 \times 10^9 \text{ m}^3$ was reported in 1962). It can be assumed that water and sediment discharge is negligible at present (Thompson, 1969; Schreiber, 1969; Baba, *et al.*, 1991). In the last 40 years only the water discharge of 1993 reached levels comparable to those before 1935.

Large-scale winds blow mostly in the along-gulf direction, a mode accounting for 63 % of the variance, according to Merrifield and Winant (1989). These are monsoonal in nature, with northwest winds in winter and southeast winds in summer. More variable winds occur in the transitional months of spring and fall. A breeze system is superimposed on the synoptic wind reaching speeds of 5 to $7 \text{ m} \cdot \text{s}^{-1}$ in the afternoon. Observations made on the western side of the Upper Gulf show that in late spring the sea breeze regime dominates but later in the summer the breeze system is modified by synoptic scale events lasting about 4 days and averaging 5 to $6 \text{ m} \cdot \text{s}^{-1}$ in intensity (Delgado-Gonzalez *et al.*, 1994). Intense northwest-northeast wind events ($>5 \text{ m} \cdot \text{s}^{-1}$) lasting 1 to 10 days can occur from October to March. These events account for most of the latent heat loss and the low humidity conditions in the northern Gulf of California (Reyes and Lavín, 1997).

1.2. Bottom configuration and sediments.

1.2.1. Bathymetry.

About 10 km before reaching the Gulf, the old river channel splits into two tidal channels forming Isla Montague. A third minor channel forms Pelicano Island on the eastern side (Fig. 1.3). These islands are tidal flats barely rising above the extreme spring tide levels. On the western side, off Baja California, a smooth plain extends from mean sea level down to a depth of about 15 m, sloping to the east-southeast at an average angle of 0.05° or roughly 1/1200. This plain can be found as far south as San Felipe, near 31° N. In contrast, on the opposite side, off Sonora the depths drop to 20-30 m near the coast. The bottom is irregular, consisting of 8 to 10 m ridges intervening with flat-bottomed troughs that are best developed near the mouth of the river. Some ridges can be traced to the southeast for 20 to 30 km, trend approximately parallel to the Gulf's axis and seem to reach the edge of the 200m-deep Wagner Basin. These ridges are thought to represent tidal current ridges similar to those found in other areas of strong tidal currents. At least one of the channels may represent the former entrenched course of the Colorado River. However, the configuration of these bottom features is only an approximation, since it is based on interpretative contours (Thompson, 1969).

1.2.2. Sea bed sediments.

Mineral and grain-size distribution indicate that the bottom sediments of this region were supplied by the Colorado River before dams were built. An estimated annual load was 180×10^9 kg with 70 to 80% of silt and clay and the remainder made of fine to very fine sand. Textural classification of bed surface sediments yielded three groups: silt clay, sand-silt-clay and sand. Minor occurrences of muddy sand and clayed silt are reported. Silt clay (size 5ϕ – 7ϕ) predominates off Baja California, north of latitude 31° , over the gentle sloping plain to depths of about 12 m and inside the wide channels formed by along-gulf ridges. (Fig.1.4). Coarser sandy sediments (size

2ϕ – 4ϕ) are found over a narrow belt around the whole Upper Gulf from the intertidal zone to the shallow subtidal zone. This belt of apparently relict sands widens on the south-eastern part off Sonora, and reaches depths of 50 m. Near the ancient river mouth a complex pattern of the three textural classes are found: fine sand occurs over the crest of the tidal current ridges, and silty clay is found in the intervening troughs (Thompson, 1968; Thompson, 1969; Carriquiry and Sánchez, 1999).

1.3. Thermohaline structure.

The inverse estuarine character of the Upper Gulf was revealed by its thermohaline regime. Whereas the along-gulf temperature gradient reverses from summer to winter, the sign of the salinity and density gradients remains the same throughout the year with both properties generally increasing toward the head. The seasonal changes in the hydrography are controlled mainly by the meteorology because the Upper Gulf is shallow, less than 15 m deep over ~50% of the area. Hydrographic observations have shown a slight vertical stratification apparently restricted to neap tide conditions. Thus, a vertically mixed regime prevails mainly sustained by strong tidal currents. The persistent high density water around the head of the Upper Gulf creates a pressure gradient force which induces sporadic gravity currents near the bed toward deeper water when vertical tidal mixing diminishes in neap tides. These currents contribute to the flushing of saline water and to the formation of the high salinity water mass found in the deeper waters of Wagner Basin (Lavín *et al.*, 1995; López, 1997; Lavín *et al.*, 1998). Contrasting thermohaline winter and summer conditions are shown in Figure 1.5 and described next.

1.3.1. Temperature.

Surface temperatures are highly variable and follow the diurnal and seasonal trends of air temperature. The mean annual range in water temperature is 16 °C with maximum of 29 °C in August and minimum of 12.1 °C in December. Inside the delta tidal channels winter temperatures may be as low as 8.2°C due to low overnight air

temperatures. Isothermal conditions in the vertical were observed in August and February in water depths less than 25 m. Surface minus bottom temperature differences were maximum in June (3.3°C) and in October (-1.3°C). In general, in the shallower areas of Upper Gulf water temperatures at 10 m depth were about 1°C warmer than at the surface from October to February and colder after March (Hendrickson, 1973). Diurnal heating can generate transient thermal stratification of sea surface waters. Temperature increases toward the estuary head in summer, to a maximum of ~ 32 °C. In winter the horizontal gradient reverses and temperature decreases to ~15 °C at the head. The observed head to mouth surface temperature difference is roughly 1-2 °C (Fig. 1.5).

1.3.2 Salinity and density.

The scarce rainfall averaging 68 mm·yr⁻¹ and the high mean evaporation rate of 0.9 m·yr⁻¹ contribute to the high salinity of the Upper Gulf of California (Miranda-Reyes *et al.*, 1990; Lavín and Organista, 1988). North of 31° N, the mean surface salinity ranges from 36.0 in January to 37.6 in June, decreasing slightly towards the bottom with an average difference of less than 0.5. This high salinity water has been identified as Colorado Delta Water by Bray and Robles (1991). Large horizontal gradients near the surface develop in January along the western side where the hyper-saline waters from the delta channels meet the less saline waters of the Upper Gulf (Martinez-Rojas-Reynoso, 1990; Hernandez-Ayón *et al.*, 1993). The horizontal gradients of salinity and density have revealed that inverse estuarine conditions prevail in the Upper Gulf (Fig.1.5): salinity and density (σ_t) increase toward the shallow northwest end of the estuary where they reach 38.8 and 23.4 in summer, and 36.7 and 27.2 in winter, respectively. Inside the delta channels summer salinity increases to 40, (Alvarez-Borrego *et al.* 1975; Hernández-Ayón *et al.* 1993; Lavín *et al.* 1998). Low salinities are rarely found. Rainfall has a significant effect on salinity only along the coastline. Compared with the salinity of central waters, a reduction of 0.3 to 0.4 has been found along the coasts of Sonora and Baja California (Hendrickson, 1973). About 30 km inside the delta tidal channels low salinity values

of 33 have been reported during winter due to fresh groundwater input. Carbajal *et al.* (1997) modelled the former estuarine conditions using the Colorado River discharge before the dams were built. In a year of unusually high precipitation the Colorado River input to the Upper Gulf developed classic estuarine conditions (Lavín and Sánchez, 1999). Low salinities extended over the shallow western Upper Gulf with a minimum of 32 observed near the head.

1.4. Tides and tidal currents.

1.4.1 Tides.

Tides in the Gulf of California are co-oscillating with the Pacific Ocean tides. Numerical modelling and early observations indicate that near resonant conditions in the semidiurnal band yield amplification of the M_2 tide over the shallower northwest region. It is the dominant constituent with amplitudes of 2 m and it accounts for most of the turbulent dissipation (Hendershott and Speranza, 1971; Filloux, 1973). The spring tidal range of the total tide exceeds 6 m over most of the Upper Gulf and may reach 10 m in the extreme northern part (Mathews, 1969). Predominance of the semi-diurnal tide is shown by the ratio $(K_1+O_1)/(M_2+S_2)$ which decreases from 3.0 near the middle of the Gulf to 0.28 or less at the northern end (Mathews, 1969; Morales-Pérez y Gutiérrez de Velasco, 1989). Table 1 shows the 7 most important diurnal and semidiurnal constituents over the Upper Gulf region.

Table 1.1. Amplitudes and phases for seven major diurnal and semi-diurnal constituents in the Upper Gulf of California (after Morales-Pérez y Gutiérrez de Velasco, 1989).

Constituent.	Amplitude (m)	Phase lag (105° W)
M_2	1.80	60
S_2	1.00	60
N_2	0.42	60
K_2	0.28	60
K_1	0.41	80
O_1	0.28	76
P_1	0.13	80

1.4.2 Tidal currents.

The first account of the impressive tidal ranges and currents is due to the Spanish explorers of the Upper Gulf in the mid 16th century. Sparse observations by Thompson (1969) indicate that the tidal currents near the delta are nearly rectilinear and parallel to the Gulf's axis. Velocity exceeding $1 \text{ m}\cdot\text{s}^{-1}$ was reported near the river mouth. A spring tide maximum flood current of $1.35 \text{ m}\cdot\text{s}^{-1}$ was observed 15 km south of the mouth whereas inside the delta channels currents up to $2.9 \text{ m}\cdot\text{s}^{-1}$ have been measured (Zamora-Casas, 1993). Carbajal (1993) used a fine grid (3') three-dimensional barotropic and baroclinic model forced by the seven most important tidal constituents. Extreme amplitudes of the M_2 tidal elevation (2 m) and velocity ($1.40\text{-}1.60 \text{ m}\cdot\text{s}^{-1}$) were computed in the vicinity of the Colorado River mouth. These results are similar to the observations reported by Thompson (1969).

1.5. Circulation and mixing.

1.5.1 Transient and residual circulation.

The sub-tidal circulation in the Upper Gulf is not well known. Based on a few observations Thompson (1969) suggested that slight rotary tidal currents result in clockwise motion over the deeper parts and counter-clockwise motion near the coast. The latter is in agreement with the sedimentologic studies by Gorsline (1967) who suggested that flood currents move up along the eastern shore and ebb currents flow down the western shore. No direct evidence of this pattern has yet been reported but it is consistent with the patterns of turbid water revealed by ERTS satellite imagery. The westward distribution of nutrient-rich water advected from the delta channels also supports the idea of a counter-clockwise motion in the near-shore region (Hernandez-Ayón *et al.*, 1993). A thermally driven convection system has been proposed to

dominate the circulation just south of the Upper Gulf (Hendrickson, 1973). It assumes that in winter the surface circulation is clockwise becoming counter-clockwise in summer with bottom circulation opposite to that at the surface. The proposed circulation in the Upper Gulf is toward the delta in summer and away from it in winter.

The wind and tidal residual circulation has been extensively studied in the Gulf of California by means of numerical modelling since 1989 (Quirós *et al.*, 1992; Carbajal, 1993; Marinone, 1997; Argote *et al.*, 1998). Two- and three-dimensional models in barotropic and baroclinic versions have provided different patterns of the tidal and wind induced residual circulation in the northern Gulf. However, the coarse spatial grids (6–14 km) were inadequate for the small extent of the Upper Gulf and its complex bathymetry. A 6.6-km grid size barotropic model forced by wind and tides computed tidal residual currents $0.01\text{--}0.02\text{ m}\cdot\text{s}^{-1}$ in the Upper Gulf (Fig. 1.6). A westward transverse residual current in the middle and a southward current along the west coast are the two main discernible circulation patterns. A $5\text{ m}\cdot\text{s}^{-1}$ south wind induced a northward current of up to $0.05\text{ m}\cdot\text{s}^{-1}$ on the eastern side of the mouth (Fig. 1.7). A north wind reversed the pattern and induced an enhanced southward current along the western coast (Marinone y Lavín, 1997).

Hydrographic data analysis by Lavín *et al.* (1995) and 3D baroclinic model simulations forced by winds, evaporation and heat fluxes (López, 1997) suggested that winter winds cause denser, high salinity and low temperature water to form over the shallow coastal regions of the northern Gulf, just southwest of the Upper Gulf. After sinking on the eastern side, this water flows counter-clockwise around the slopes of the Wagner Basin at depths of 75 m or more. The coarse vertical resolution of the model and the lack of tidal mixing did not allow for a proper representation of the processes in the shallow Upper Gulf.

1.5.2 Vertical mixing.

The vertically mixed regime of the shallow Upper Gulf has been attributed to fast tidal currents. The general lack of stratification has been shown by the vertical distribution of water properties described in several studies (Hendrickson, 1973; Lavín *et al.*, 1998). In a modelling study of the M_2 tidal mixing Durazo-Arvizu (1989) concluded that water is vertically mixed in depths less than 40 m, and that in summer a thermal front separates mixed waters from the stratified waters further south. The modelling work by Argote *et al.* (1995) has shown that the Upper Gulf is one of two sites in the Gulf of California in which the M_2 tide dissipation exceeded $0.5 \text{ W}\cdot\text{m}^{-2}$. A curved frontal band roughly joining San Felipe and Puerto Peñasco separated vertically mixed from stratified waters (Figure 1.8). Interestingly, it was estimated that the wind influence on the front position was minor.

1.6. Sediment transport.

1.6.1 Bed load and suspended load.

In a broad study Thompson (1968, 1969) described the sedimentation environment of the Colorado River delta region in which the Upper Gulf was included. Based on textural patterns of the seabed deposits he concluded that the suspended and bed components of the river load followed divergent paths when entering the Gulf (Fig 1.9). Modern dispersal of bed load sand seems to occur only over the elongated tidal current ridges on the eastern half of the Upper Gulf. Clay and silt transport shifted towards the western half as a suspended load; part settled to form extensive coastal mud flats off Baja California and the rest perhaps reached deeper waters. It was suggested that tidal currents are the main conveyor of sediments in this region and that the slight rotary motion of these currents caused a westward drift of the suspended sediments, transverse to both the Gulf's axis and the bed load transport trend. Since the observed sediment concentration decreased to the southeast, away from the river mouth, it was assumed that flood currents displaced less turbid water towards the mouth with a slight shift to the east, and ebb currents transported more turbid water away from the mouth region, with a shift to the west. The result was a westward net

transport of fine suspended sediments. Seston concentration measured by García de Ballesteros and Larroque (1974) revealed a gradient to the southeast in May and October. They also reported that concentrations near the bed were lower than at the surface by ~50%. More recent studies based on spatial trends of textural parameters of bed sediment have shown littoral transport to the south along the western coast opposing that along the eastern coast (Carriquiry and Sánchez, 1999). However, the mouth of the tidal inlets on both sides of the Upper Gulf are displaced north, due to the northward growth of the south sandspit. This growth may indicate that littoral drift is dominated by southeast waves rather than by northwest waves, which are generated along a shorter fetch. Over the shallow Upper Gulf the transport trend was cross-basinal, from Sonora to Baja California, in support of the notion that the west coast is a sediment depocenter slowly prograding toward the east (Fig. 1.10). Fine sediment dispersal studies based on bed samples throughout the northern Gulf have shown that clay is derived mainly from the eroding Colorado River delta and transported southward along the Baja California coast. This fine material making up to 50% of the sediments was found as far south as Tiburon Basin. The origin of this clay was traced back to the delta and Upper Gulf deposits which once in suspension can be transported by the currents of the northern Gulf (Daeslé *et al.*, 2002).

1.6.2. Turbidity and resuspension.

High altitude and satellite remote sensing studies of the northern Gulf of California began in 1969. Since then, water turbidity has assumed an increased importance relative to other properties. The most impressive aspect of turbidity in this region is the remarkable spatial variation across and along the Gulf's axis. According to Gayman (1969) strong northerly winds seem to increase the turbidity levels along the Baja California coast while along the opposite coast littoral currents transport less turbid waters toward the river mouth. This pattern was also revealed by monthly Secchi disk observations across the Upper Gulf north of latitude 31° (Hendrickson, 1973). The disk readings ranged from 0.1 m to 21.9 m in the Upper Gulf, and sediment concentration was as high as ~10,800 g·m⁻³ near Montague Island. Very

clear water with deep blue colour was associated with depths greater than 40 m. (Fig. 1.11). No seasonal trend in turbidity was evident. Turbidity stratification has been found by Austin (1972), in the form of alternating layers of clear and turbid water along latitude 31° N and 31.3° N.

Since there is no significant input of terrigenous sediments to the Upper Gulf, intense tidal resuspension of fine bottom sediments seems to be the main cause of high turbidity. It has been proposed that the resuspension processes in the Upper Gulf may affect areas 250 km to the south. Based on mineralogic composition of bottom sediments, Baba, et al (1991) have proposed that Colorado river fine sediments reach the area just north of Angel de la Guarda Island, near 30°N (Fig. 1), a consequence of active resuspension by tidal and wind wave mixing in the delta region. Seston concentrations inside the delta channels (up to 5,000 g·m⁻³) were well correlated with semidiurnal and fortnightly tidal cycles (Zamora Casas, 1993; Cupul Magaña, 1994). The last author proposed that the delta has reached a destructive stage, since the net sediment transport is toward the deeper waters of the Upper Gulf.

1.7. Summary.

The Upper Gulf of California is a shallow sea surrounded by arid lands. It is less than 40m deep with a complex bathymetry consisting of ridges and troughs in the along-gulf direction. Well-mixed conditions prevail throughout the year according to hydrographic data and vertical mixing numerical models. High evaporation rate and negligible river discharge transformed the Upper Gulf into an inverse estuary in which salinity and density increase toward the head.

Intense dynamic processes are dominated mainly by semidiurnal tides having up to 10 m range and 1-3 m·s⁻¹ extreme tidal currents near the head of the Gulf. A counter-clockwise circulation has been proposed based on water properties and turbidity patterns. Modelled tidal residual currents are 0.01 to 0.02 m·s⁻¹ over most of the Gulf. Wind-induced residual currents are ~0.05 m·s⁻¹ showing a complex circulation pattern.

The circulation is not yet well known due to the lack of long term observations and the poor resolution of the numerical model grids.

The high turbidity of the Upper Gulf is thought to be due to advection of sediment-laden water from channels inside the river delta, now in a destructive stage. Resuspension of bed sediments is also believed to cause high seston concentrations of up to $100 \text{ g}\cdot\text{m}^{-3}$. Recent sediment dispersal studies have found that fine particulate matter resuspended in the Upper Gulf is distributed over most of the northern Gulf. However, besides one local quantitative study on suspended sediment concentration in the delta channels, no studies have been done on the resuspension process and sediment fluxes in the Upper Gulf. This dynamic environment seems to bypass sediments from the delta to deeper waters at rates, and along pathways, so far unknown.

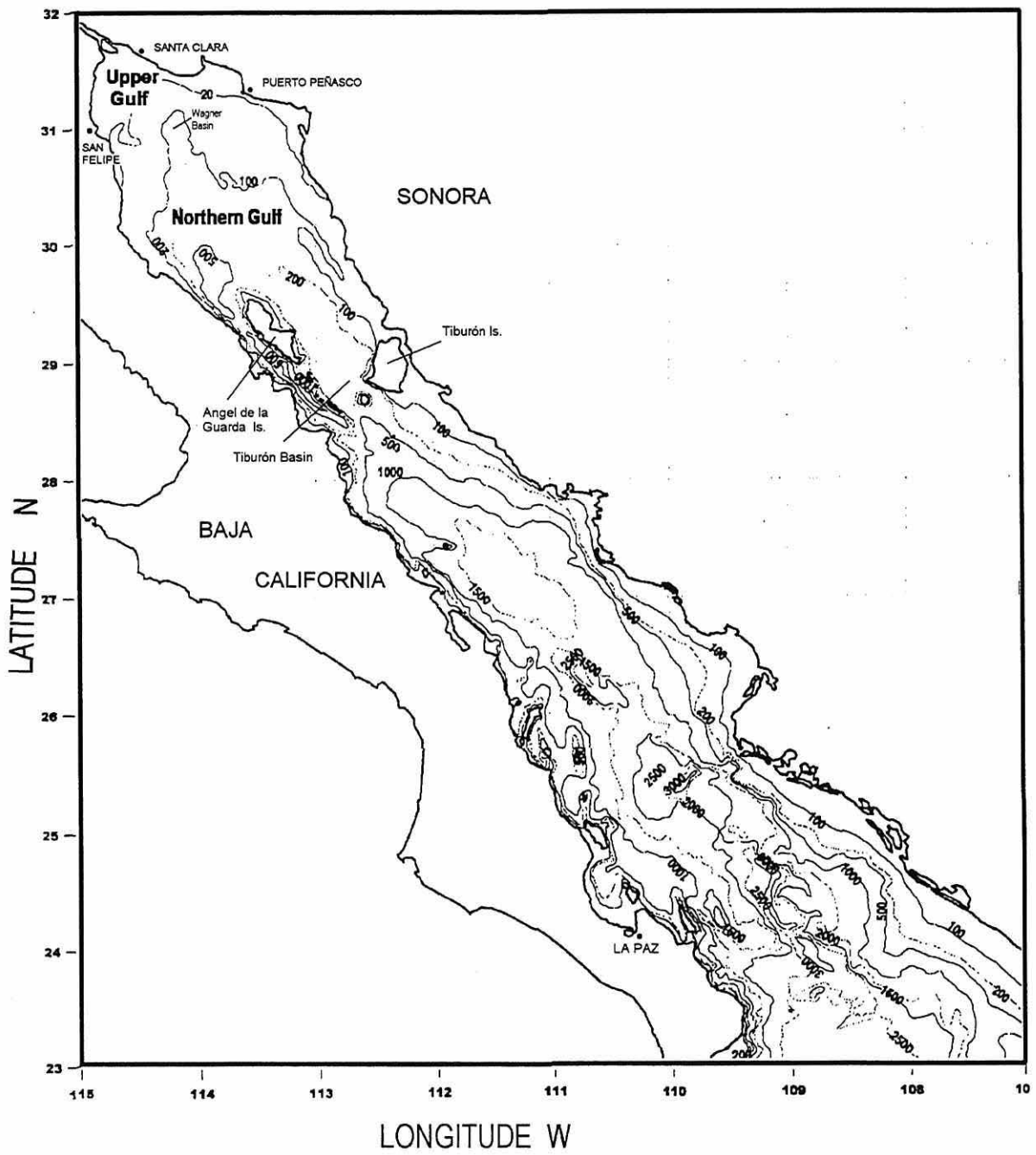


Figure 1.1. Bathymetry and regions of the Gulf of California. Depth contours in metres.

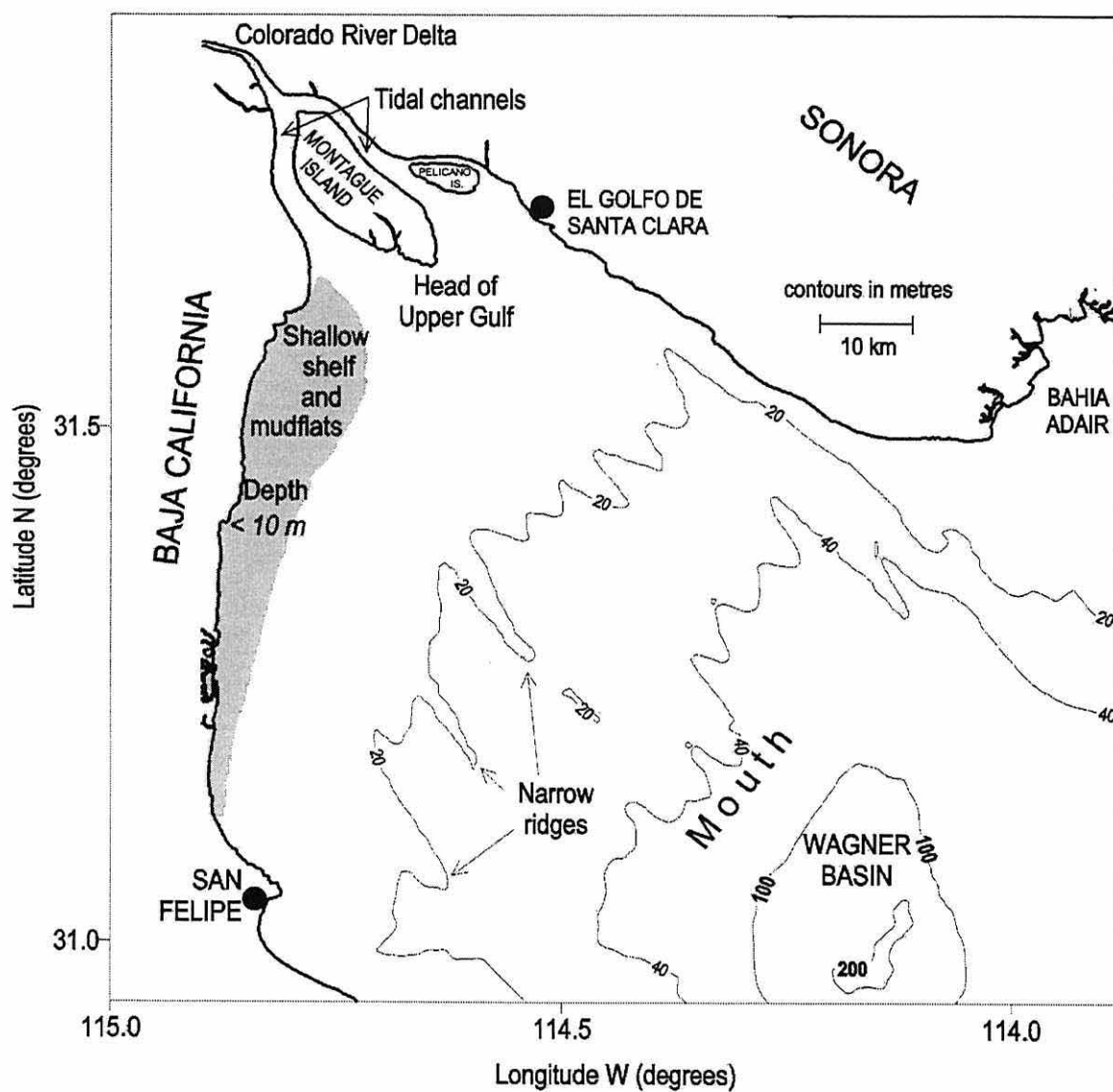


Figure 1.2. Geographic and bathymetric features of the Upper Gulf of California.

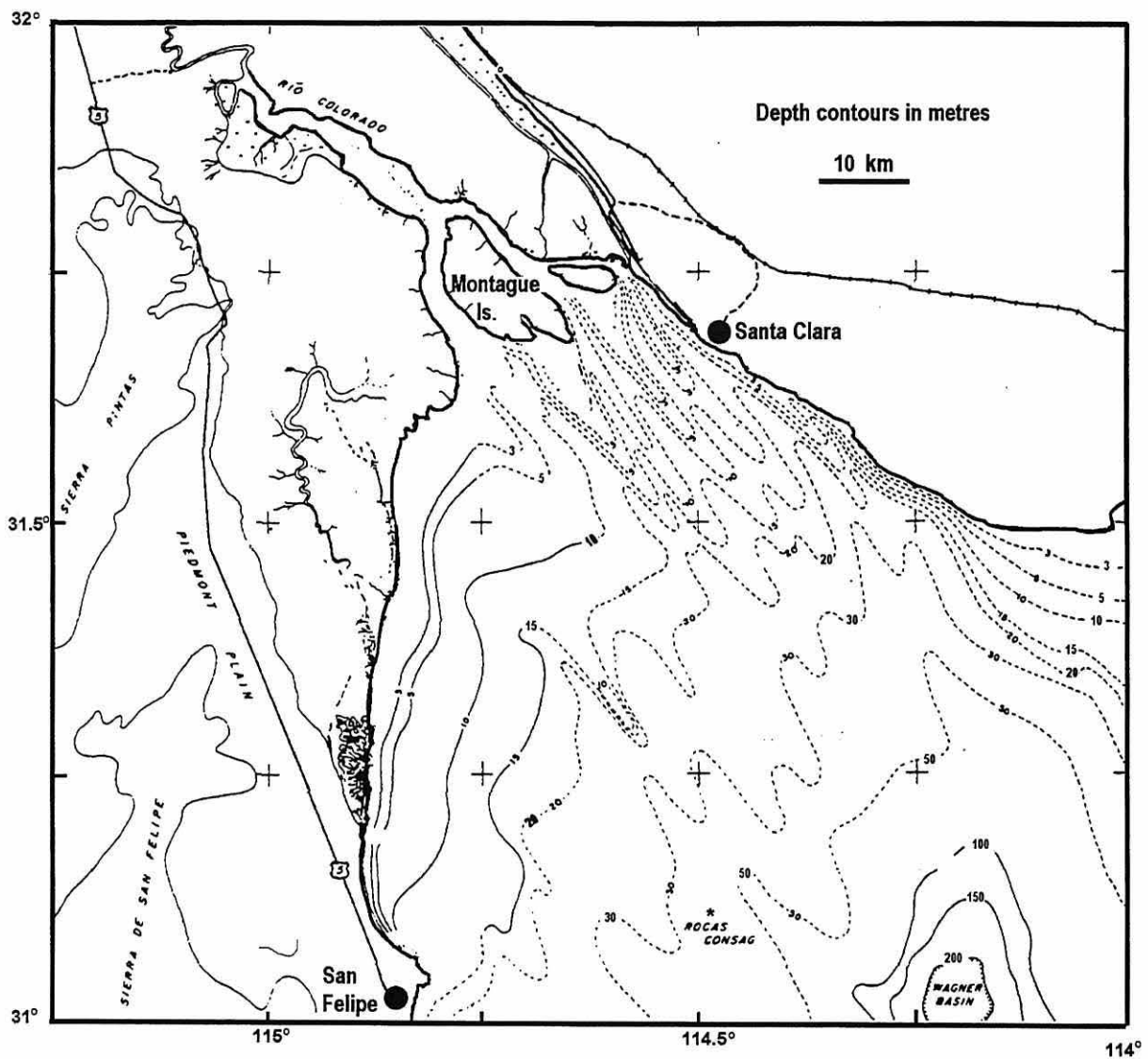


Figure. 1.3. Bathymetry of the Upper Gulf of California. Dashed lines are estimated depth contours (after Thompson, 1968).

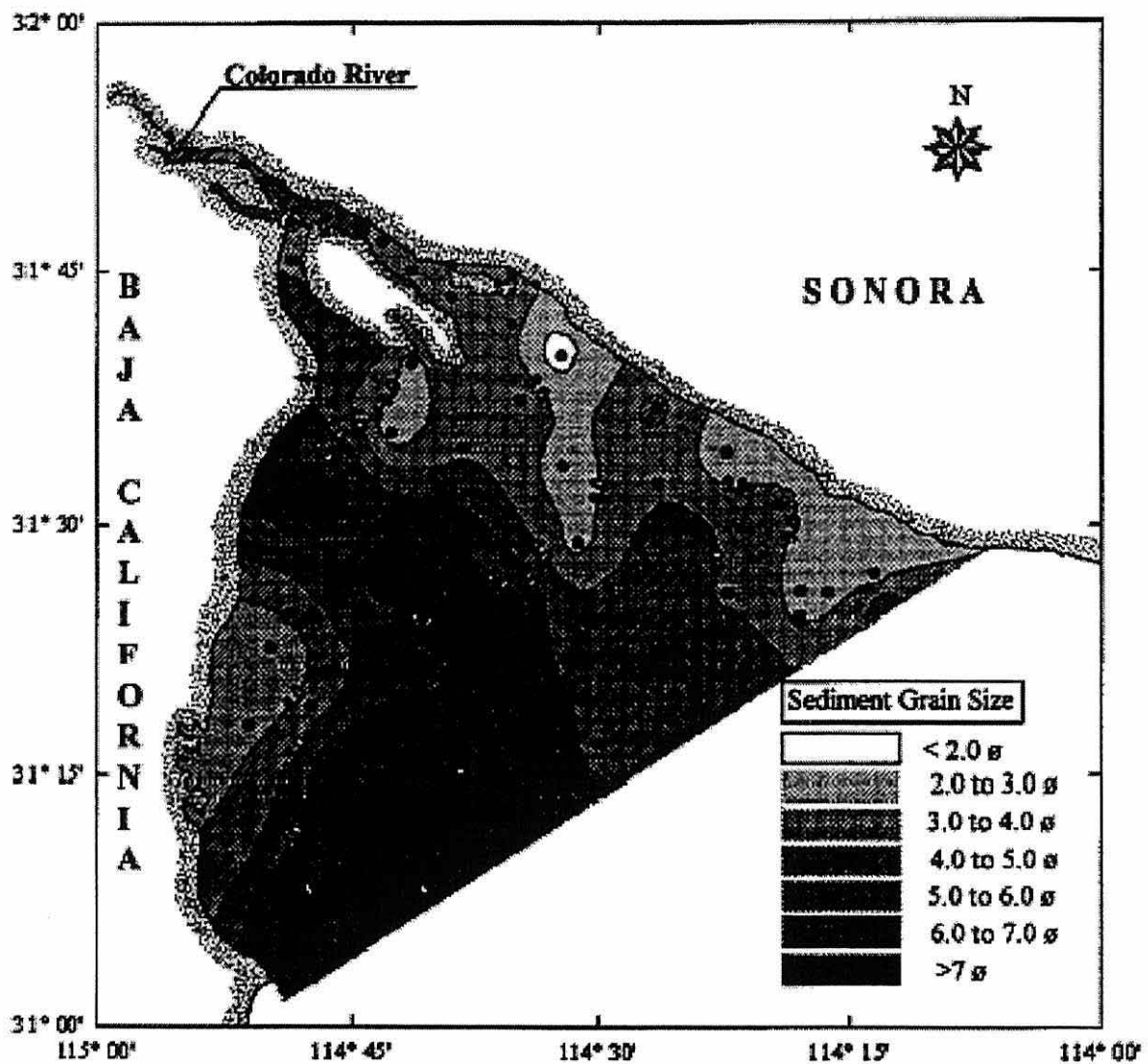


Fig. 2. Spatial variation of sediment mean grain size (in phi units) in the Colorado River delta and Upper Gulf of California.

Figure 1.4. Distribution of mean grain size (ϕ units) in the Upper Gulf and delta tidal channels (Carriquiry and Sánchez, 1999).

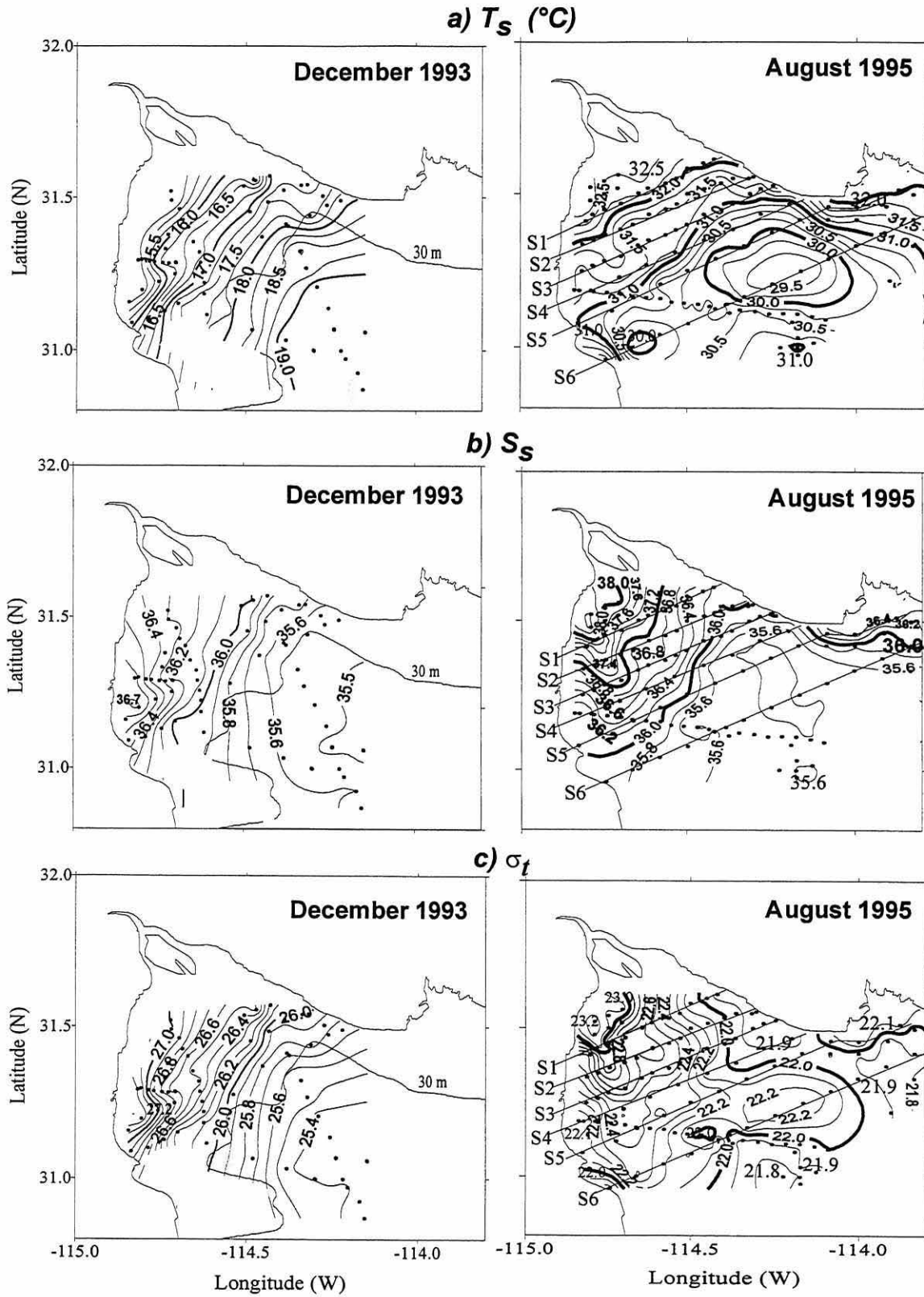


Figure 1.5. Distribution of surface temperature, salinity and density (σ_t) in December (left) and August (right) in the Upper Gulf of California (after Lavín et al., 1998).

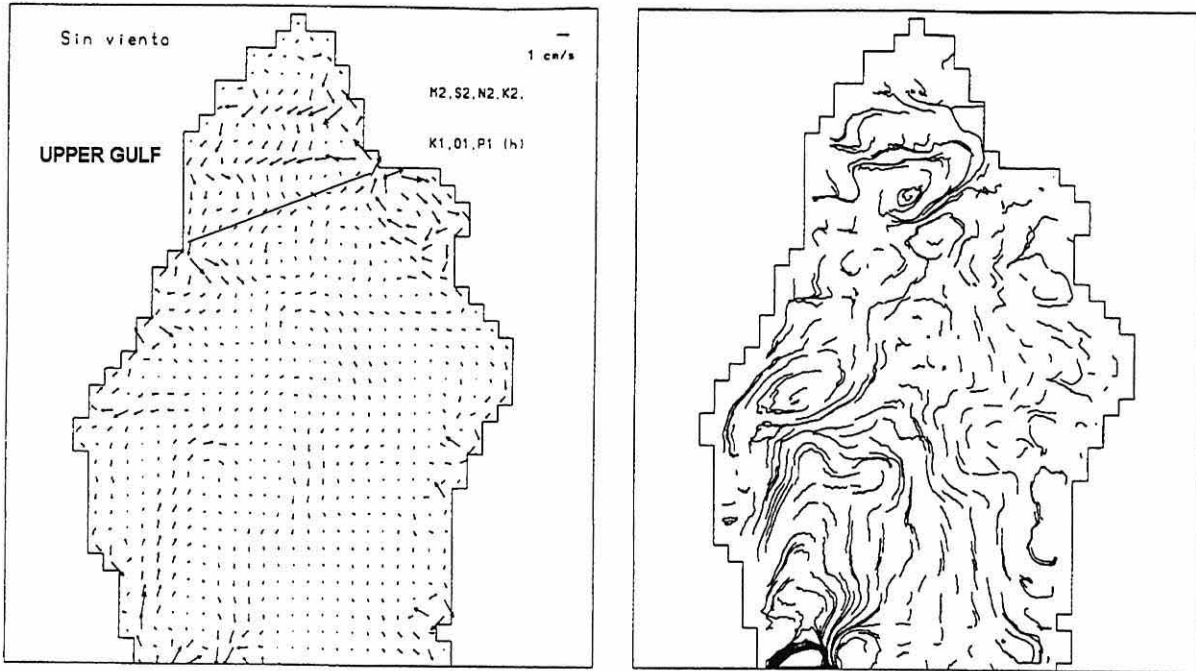


Figure 1.6. Tidal residual currents (left) and 30-day residual trajectories (right) in the northern Gulf of California. The boundary of the Upper Gulf is indicated.

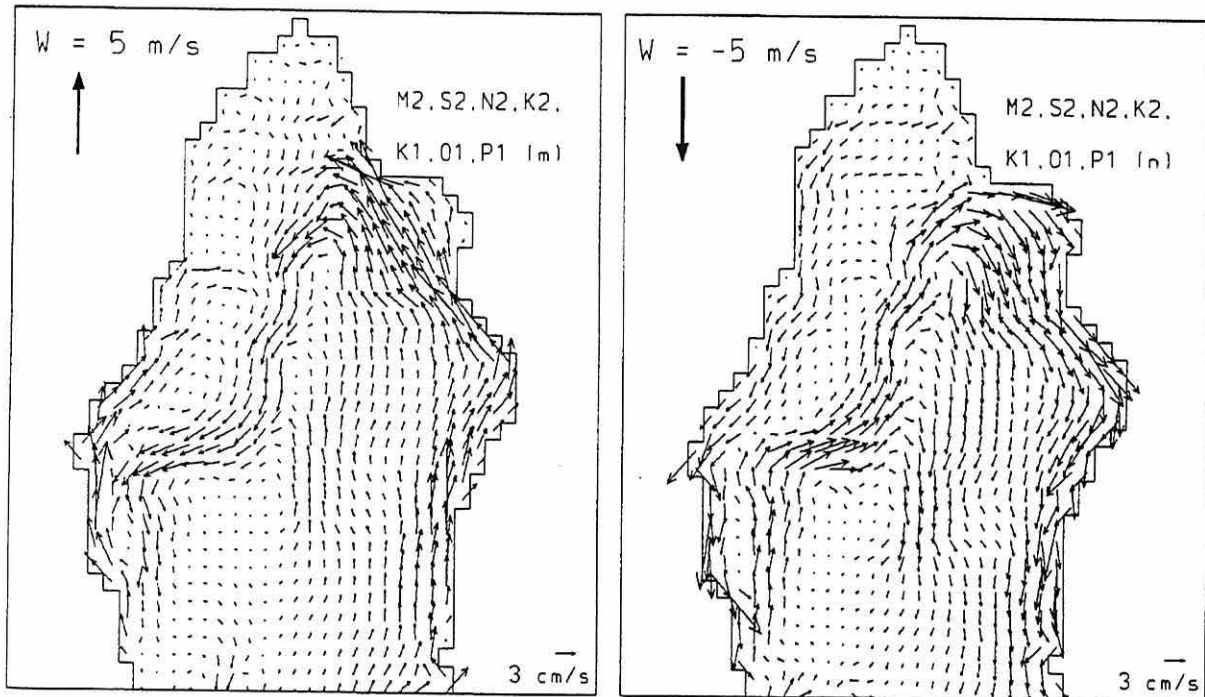


Figure 1.7. Tidal and wind induced residual currents in the northern Gulf of California, with a south wind (left) and with a north wind at $5 \text{ m}\cdot\text{s}^{-1}$ (right). The Upper Gulf is located as shown in Figure 1.7 (after Marinone and Lavín, 1997).

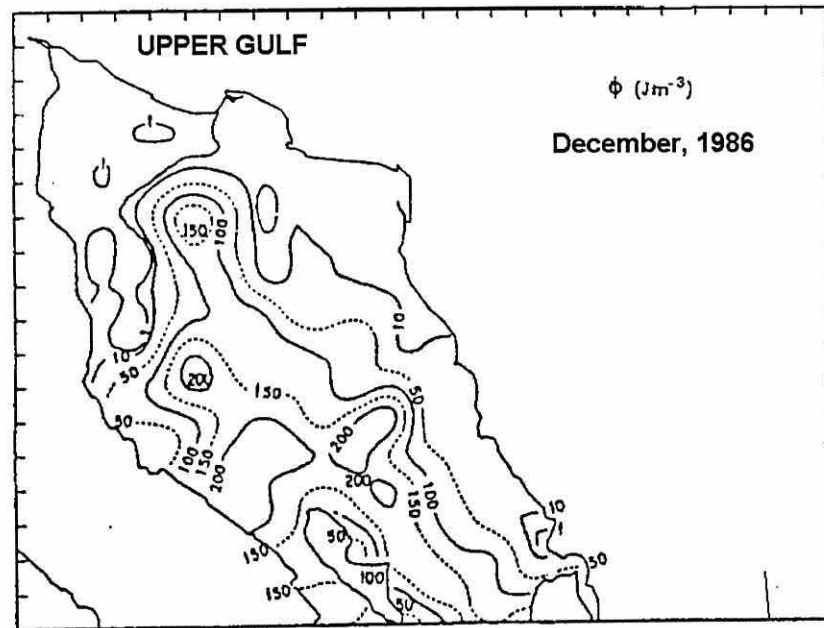
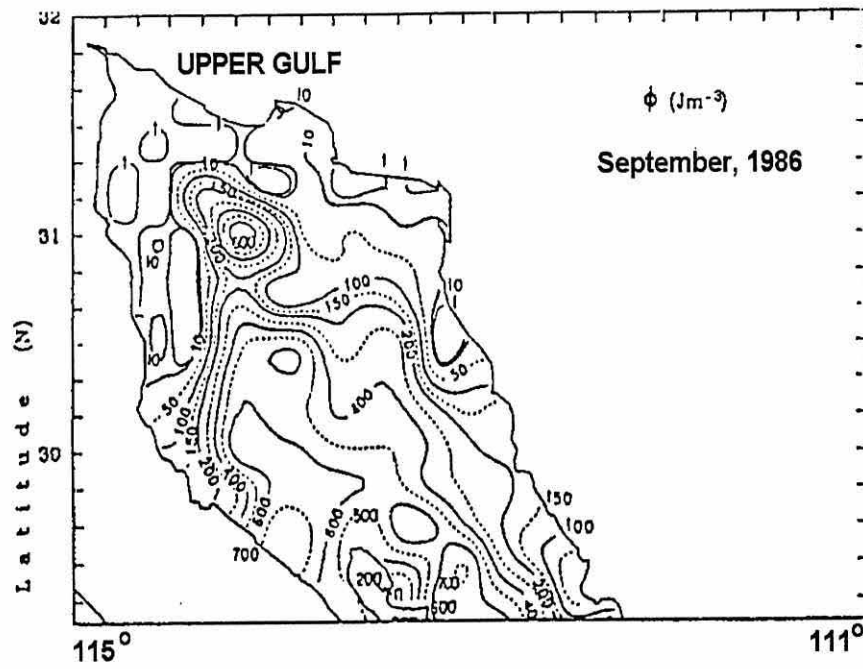


Figure 1.8. The modelled stratification parameter Φ in the northern Gulf of California for September and December (after Argote et al., 1994).

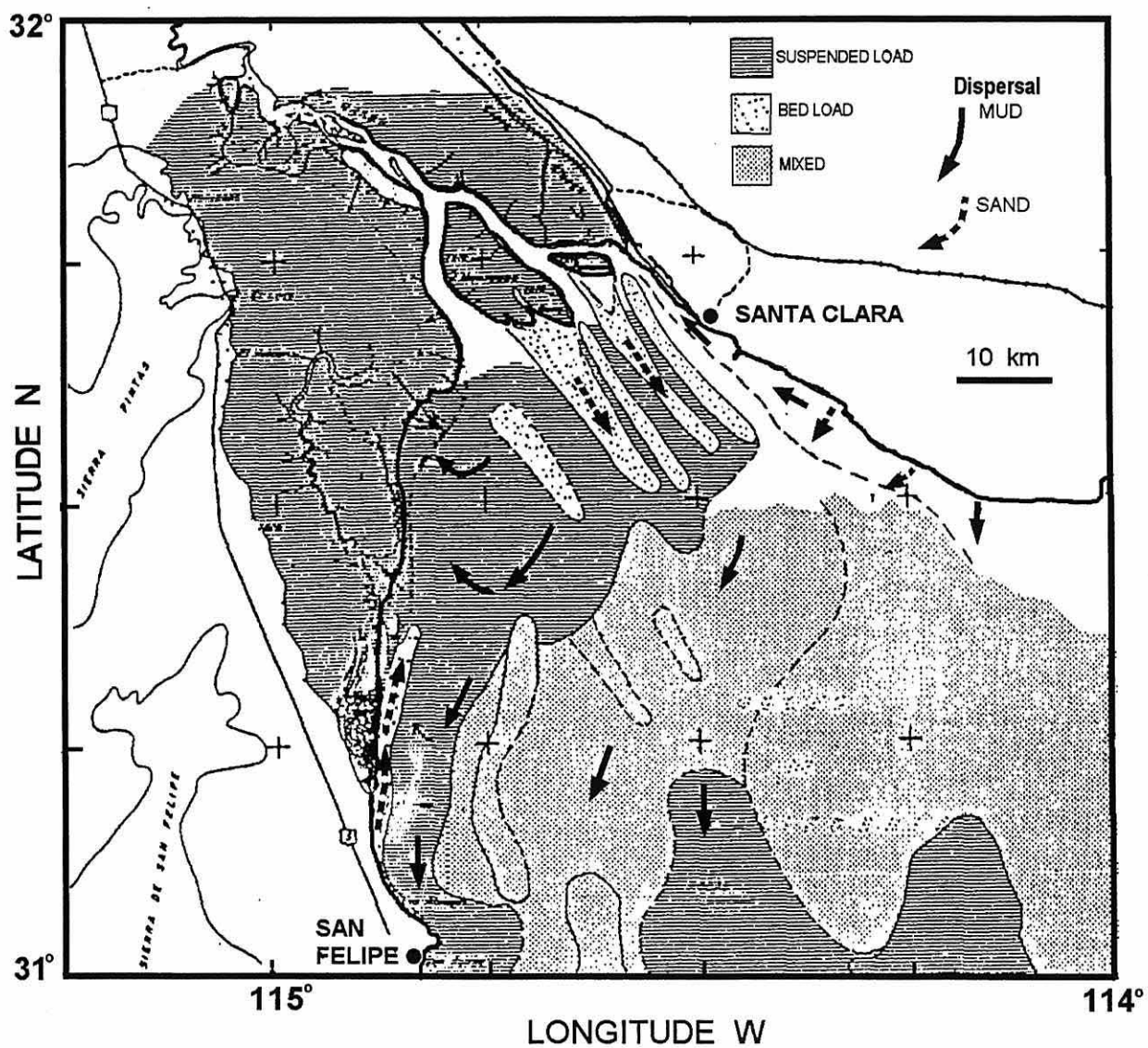


Figure 1.9. Recent dispersal patterns (arrows) of suspended load and bed load in the Upper Gulf of California (after Thompson, 1969).

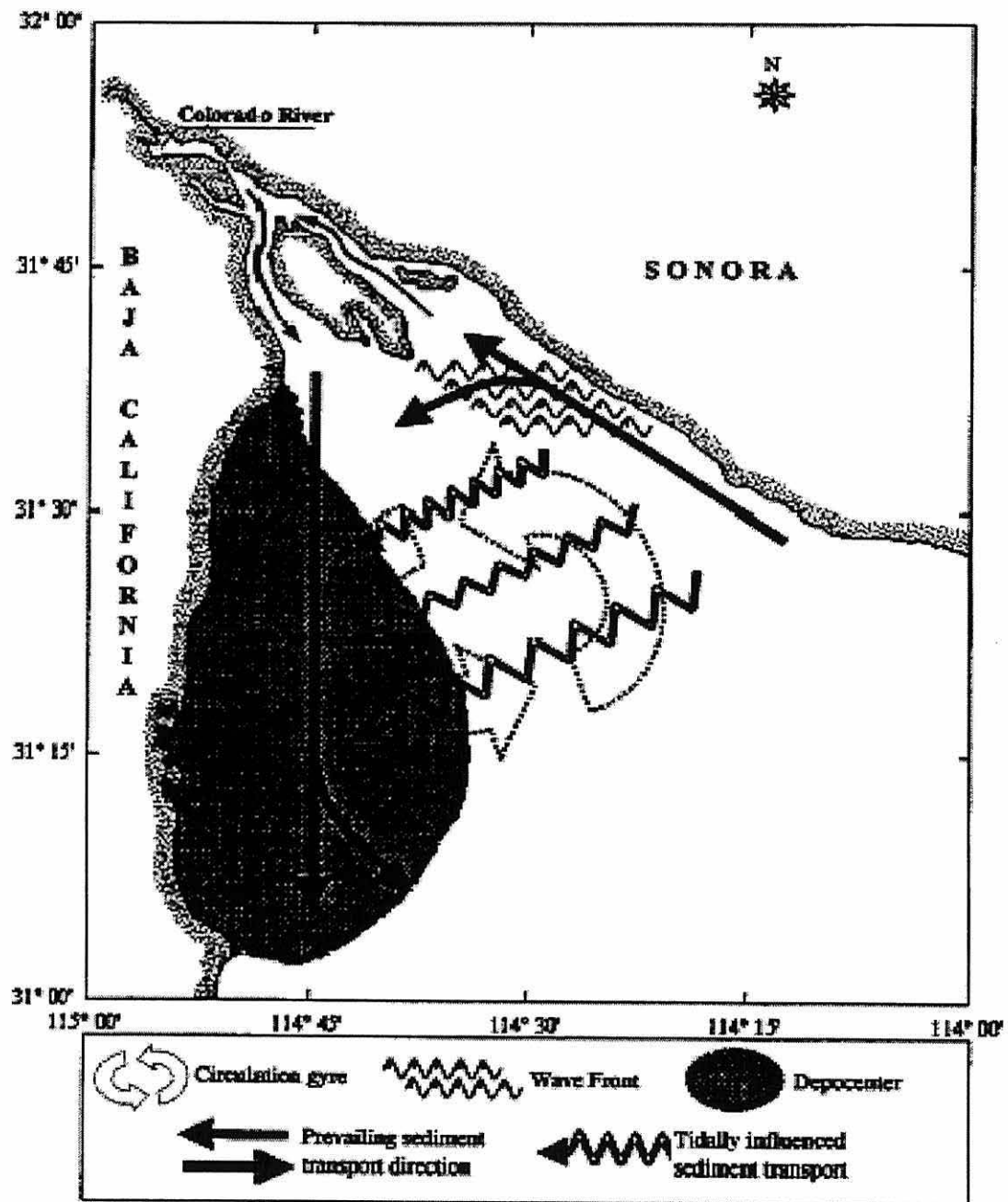


Figure 1.10. Model of bed sediment transport patterns and deposition in the Upper Gulf of California (Carriquiry and Sánchez, 1999).

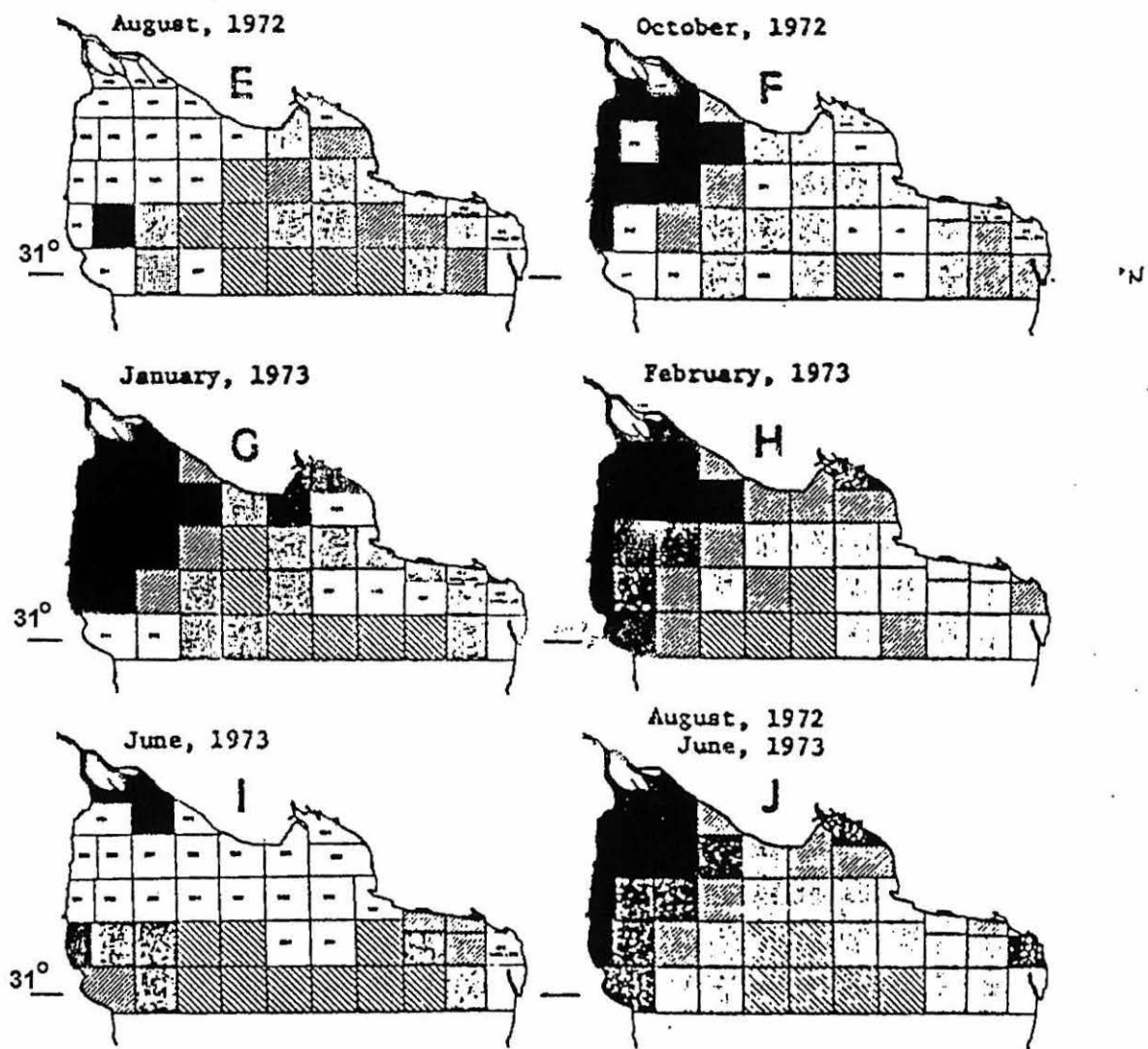


Figure 1.11. Qualitative distribution of turbidity based on Secchi disk readings. Darker areas indicate more turbid waters (after Hendrickson, 1973).

2. Aims and motivation of the present study.

The Upper Gulf of California was once a wide and rich estuarine system into which the Colorado River supplied $20 \times 10^9 \text{ m}^3 \cdot \text{yr}^{-1}$ of fresh water, and $180 \times 10^9 \text{ kg} \cdot \text{yr}^{-1}$ of sediment. The high amount of solids in suspension is believed to have given the river its geographical name (the “red river”). The damming of the river has drastically reduced both the fresh water and the sediment supply to the Upper Gulf since about 1930. However, the Upper Gulf still maintains high turbidity levels due to its macro-tidal regime and the nature of the bed deposits. The strong tidal currents and mixing have continued to rework the tidal flats and shallow deposits of the delta that became the source of fine sediments. About 30 years ago, an early investigator wrote: “..turbidity of these waters has assumed an increased importance relative to other properties..”, and pointed out that “the most impressive single aspect of the turbidity of the northern Gulf is the extreme (spatial) variation...”. Reported Secchi disk readings from a single cruise ranged over three orders of magnitude within a distance of a few tens of kilometres (Hendrickson, 1973).

Surrounded by arid lands of Baja California and Sonora, and having freshwater input below the amount lost by evaporation this semi-enclosed sea has turned into an inverse estuary in which high salinity prevails throughout the year. The term “inverse estuary” (Pritchard, 1967) emphasises the pattern of longitudinal circulation which is opposite to that of classic estuaries. In contrast with the abundant literature on classic estuaries very few studies exist on inverse estuaries, probably because of their relative scarcity. The Red Sea, the Arabian Sea, the Persian Gulf and the Gulf of California belong to the category of inverse estuaries (Bowers, 1989). Fundamental differences between classic and inverse estuaries were summarised by Postma (1967), as shown in Figure 2.1. It shows that in an inverse estuary:

1. salinity increases from open ocean values near the mouth, to higher values at the head of the estuary,
2. a near-bed gravitational circulation of denser and saltier water is directed toward the mouth,

3. concentration of suspended particulate matter (SPM) decreases monotonically from head to mouth.

The first feature has been described widely in the Upper Gulf through hydrographic surveys since the early 1900s. The second feature, which had not been observed until recently, is under active research at present. In contrast, estimation of the amount of sediments in suspension has been mostly qualitative based on the horizontal distribution of turbidity from satellite imagery and Secchi disk readings. Furthermore, turbidity depends mainly on SPM sources and fluxes which have been scarcely studied in inverse estuaries. According to Groen (1967) and Postma (1967) the near-bed circulation of inverse estuaries has an important role in suspended sediment export to the open sea.

The present environmental significance of the Upper Gulf originated from its high productivity, its capacity to sustain a declining but still important shrimp fishery and a developing shrimp-farming industry. The turbid waters shelter larvae and juveniles of valuable living resources that include at least two endangered species. Therefore, the area was declared a biosphere reserve in 1993 (the second largest in Mexico) and its boundaries and sub-divisions fixed according to the distribution of bottom depth and turbidity. An accurate description of these two factors has not however been accomplished.

Pollutants such as pesticides can be transported adsorbed onto suspended particles. Once particles settle, pollutants can remain within the bed deposit until resuspension brings them back to the water column. Since agricultural runoff water enters the Colorado River delta channels, waterborne toxic chemicals have been detected in biota and sediments, in particular at sites where bed sediments have been disturbed (García-Hernández *et al.*, 2001). Therefore, resuspension may play a significant role in releasing pollutants from bed deposits where net erosion rates exceed deposition rates.

The aim of this study was to investigate for the first time the physical processes that may control the concentration and fluxes of suspended particulate matter in the Upper Gulf of California. The time scales of interest were *a priori* set within a fortnightly cycle, since the semi-diurnal tide and its neap-spring modulation are likely to account for large

changes in mixing intensity. The approach is an observational one, taking advantage of new self-recording optical instruments, current meters and particle analysers which were unavailable a quarter of a century ago. The data set combined point measurements at fixed levels in the water column, short-term profiling surveys of the water column at opposite sides of the Upper Gulf, and a Gulf-wide spatial survey. A hindcasting procedure then attempts to reproduce the observed time series by single-point modelling. The aim was to identify the main physical controls and evaluation of the parameters that better reproduce the observations.

Thesis plan.

In Chapter 1 the background to this study is presented. A summary of the oceanographic conditions of the Upper Gulf is given and the macro tidal and inverse estuarine character of this shallow region is emphasised. Chapter 2 outlines the aims and motivations of the present study. Chapter 3 is a description of the observational program: instrument mooring sites, tidal station observations and spatial surveys across the study area. Instrument specifications, calibration procedures and data recovery are described. Chapter 4 contains a description of the measured variables and their main statistics: bottom relief, hydrography, SPM and currents. Three observational procedures are presented: spatial surveys, tidal cycle stations spanning 1-4 semidiurnal cycles and single level time series during a full fortnightly cycle. In Chapter 5 the log-layer model for the bottom boundary layer is used for the analysis of observed velocity profiles. The bed shear stress, bed roughness scale and drag coefficient derived from this analysis are described. Contrasting conditions between spring and neap tides are emphasised. Chapter 6 is focused on the erosion-deposition process and forcing. The effects of the semidiurnal tide and gravity current events during neap tides are described. Erosion and deposition rates are estimated using parameters extracted from field data. The resulting balances are described in terms of a simple erosion-deposition point model. Chapter 7 deals with horizontal fluxes of particulate matter, estimated from velocity profiles and acoustically measured SPM concentration. Contrasting net fluxes during spring and neap tides are described and the influence of gravity current events is assessed. Finally, a discussion of the main findings is presented and the concluding remarks are given in Chapter 8.

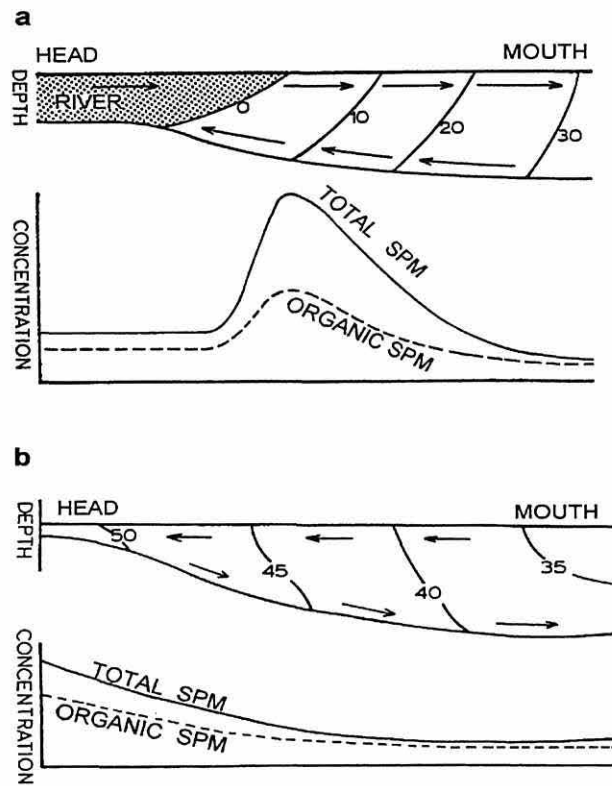


Figure 2.1. Conceptual model of contrasting flow, salinity and suspended matter (SPM) distribution along a) the classic estuary, and b) the inverse estuary (after Postma, 1967).

3. The observational program.

Preliminary observations were made from 1994 to 1996 on board the *B/O Francisco de Ulloa* of CICESE, when bathymetric data and the first tidal cycle time series were obtained. The bathymetric survey was made using an on-board continuous depth recorder and GPS positioning. Sounding lines across the Upper Gulf were set perpendicular to the bottom relief features partially described in earlier studies. Depths relative to mean sea level were obtained by removing the tidal elevation using predictions at San Felipe, Puerto Peñasco and Santa Clara. In June 1996 CTD and optical backscatter (OBS) profiles were made at site J on the western side of the Upper Gulf, in 18 m water depth (Fig. 3.1). The casts were made every 0.5 hours during four semidiurnal cycles under spring and neap tides. Two General Oceanic current meters were moored at this site at 1m and 5 m above the bed and operated during the same period. The instrument specifications, moorings and data recovery are described in Section 3.1.

The main cruise was made on board the *B/O Francisco de Ulloa* on August 11 to 28, 1997. The intensive observational program spanned a spring-neap tidal cycle and included three kinds of sampling methods:

- a) instrument moorings on the East and West sides of the Upper Gulf,
- b) CTD casts and water sampling over tidal cycles at fixed sites on both sides of the Upper Gulf,
- c) spatial CTD and water sampling survey across the Upper Gulf.

3.1. Instrument moorings.

Three U-type moorings were deployed at sites W1, W2, W3 on the western side of the Upper Gulf and two moorings at sites E1, E2 on the eastern side. The water depth at these five sites varied from 20 to 30 m, as shown in Figure 3.1. Current meters and

transmissometers were deployed at W1 and E1. Optical backscatter sensors (OBS) were installed at W2 and E2. At site W3 an upward-looking acoustic Doppler current profiler (ADP) was mounted at the sea bed, next to a pair of OBS sensors fixed to the mooring line. The typical configurations are shown schematically in Figure 3.2.

3.2. Current measurements.

3.2.1. The acoustic Doppler current profiler.

An acoustic Doppler profiler (ADP) measures the current velocity using the Doppler shift effect: if an acoustic energy source is moving relative to the receiver, the frequency of the sound reaching the receiver is shifted from the transmit frequency. A monostatic transducer (transmitter and receiver) generates short sound pulses of a known frequency. These propagate through the water along a narrow beam a few degrees wide. The sound is back-scattered by particulate matter in suspension which may consist of sediment, plankton, bubbles, etc. Part of this energy travels back along the beam axis and is received by the transducer. An internal processing module measures the change in frequency due to the motion of suspended particles carried as passive tracers by the currents. This Doppler shift is proportional to the water velocity along the beam axis. The system used in this work was a SonTek™ ADP current profiler operating at a frequency of 1.5 MHz with three transducers emitting beams oriented 25° off the vertical. Specifications of the ADP sensors are given in Table 3.1

Table 3.1. ADP sensor specifications

Variable	Sensor	Range	Accuracy	Resolution
Velocity	Acoustic	$\pm 10 \text{ m s}^{-1}$	$\pm 1\%$ of measured velocity	0.001 m s^{-1}
Direction	Compass		$\pm 0.5^\circ$	0.1°
Tilt		$0 - 50^\circ$	$\pm 0.2^\circ$	0.1°
Pressure	Strain gage	$0 - 60 \text{ dbar}$	0.1%	
Temperature	Thermistor	$0 - 40 \text{ }^\circ\text{C}$	$0.1 \text{ }^\circ\text{C}$	

The ADP was deployed at site W3, looking upwards, on a bottom-mounted flat plate. This site is 25 m deep, relative to mean sea level, 15 nautical miles NE of San Felipe, on the western side of the Upper Gulf. The current profiles consist of consecutive 5-minute averages over 0.5 m vertical depth bins. Valid velocity bins started at 1.2 m above the sea bed and extended up to 14-16 m. The deployment settings are shown in Table 3.2.

Table 3.2. Deployment parameters of the acoustic Doppler profiler at site W3. Bottom depth: 25 m below MSL.

Bottom-mounted, upward- looking ADP.	
Acoustic frequency	1500 kHz
Sampling interval	300 s
Averaging time	300 s
Blanking distance	0.4 m
Centre of first bin	1.2 m above seabed
Vertical bin size	0.5 m
Start date; time (105° W)	11-08-1997; 18:35
Length of the series	15.7 days

3.2.2. Current meters

Two current meter types were used: Aanderaa and General Oceanics. Their specifications are given in Tables 3.3 and 3.4

Table. 3.3. Sensors of the Aanderaa current meters.

Variable	Sensor	Range	Accuracy	Resolution
Speed	Rotor	0.02 – 2.95 m s ⁻¹	± 0.01 m s ⁻¹	± 0.02 m s ⁻¹
Direction	Compass	0 – 360°	± 7.5°	± 5°
Temperature	Thermistor	-0.3 – 32.1 °C	±0.05 °C	± 0.1% of range

Table.3.4. Sensors of the General Oceanics current meters.

Variable	Sensor	Range	Accuracy	Resolution
Speed	Tilt sensor	0 – 3.60 m s ⁻¹	0.01 m s ⁻¹	0.01 m s ⁻¹
Direction	Compass	0 – 360°	2°	1°
Temperature	Thermistor	-5 – 45 °C	0.25 °C	1/64 °C

The current meters were moored at two sites on opposite sides of the Upper Gulf: site W1, 3.9 km northwest of site W3, on the western side, and site E1 on the eastern side (Fig. 3.1). At each site three current meters were deployed at 1.2, 4.2, and 12.2 m above the sea-bed, in water depth of 21 m and 30 m, respectively. The current meter at 12.2 m at site W1 did not operate so Table 3.5 summarizes the deployment details for instruments at 1.2 m and 4.2 m only.

Table 3.5. Current meter and transmissometer deployment at site W1 in 1997. Water depth: 21 m below MSL.

Instrument	Aanderaa 651	Aanderaa 652	TR-21	TR-22	TR-20
Height above bed	1.2 m	4.2 m	1 m	3.7 m	12.5 m
Start – end dates	13/08 – 23/08	13/08 – 28/08	13/08 – 28/08	13/08 – 28/08	
Length of the series	10.2 days	14.8 days	14.8 days	14.8 days	
Sampling interval	5 min	5 min	1 min	1 min	
Data recovery	speed, direction, temperature	speed, temperature	light atten.	light atten.	no data

The velocity data recovery was limited by instrument failures. At site E1 the current meter at 1.2 m above the bed had only 3 days of valid records after which the rotor and fin became obstructed by drifting algae. This did not occur in the more turbid

waters on the western side where little or no drifting debris was observed. Table 3.6 shows a summary of the deployment details at E1.

Table 3.6. Current meter and transmissometer deployment at site E1 in 1997. Water depth: 30 m below MSL.

Instrument	Aanderaa 653	GO 606	GO 405	TR-23	TR-4
Height above bed	1.2 m	4.2 m	12 m	1 m	12 m
Start to end dates	13/08–17/08	13/08–28/08	13/08–28/08	14/08–28/08	14/08–28/08
Length of the series	~3 days	14.6 days	14.6 days	14.7 days	14.7 days
Sampling interval	5 min	5 min	5 min	1 min	1 min
Data recovery	speed, direction, temperature	speed, temperature	speed, temperature	light atten.	light atten.

3.3. Optical instruments

3.3.1 Optical backscatter sensors (OBS):

The optical backscatter sensors operate by emission of light at a wavelength of 880 nm. The light back-scattered by suspended particles within 5 cm of the instrument is detected by a light sensor which outputs 0 to 5 volts with a 10 Hz frequency response. A 14-bit data logger was programmed to store one voltage reading every 5 minutes. This reading represents the 5-minute average stored at the end of the interval. The response of the OBS is linear for the expected range of particle concentration in the Upper Gulf. The sensitivity of the sensors is adjusted to within 1% so that for most purposes they are interchangeable, according to the manufacturer (Seapoint Turbidity Meter, User Manual). The OBS deployment data is given in Table 3.7.

Table 3.7. OBS sensors deployment at sites W2, W3 and E2 in August 1997.

Site	W2		W3		E2	
Sampling interval	5 min		5 min		5 min	
Water depth	16 m		25 m		21 m	
Height above bed	1 m	3.7 m	1 m	6 m	1 m	3.7 m
Start to end date	11-27	11-17; 23-27	11-27	11-16 23-27	11-17 25-27	11-18
Length of the series	15.8 days	~10 days*	15.7 days	~9 days*	14.6 days	7 days*

* gaps in the series due to instrument saturation

The OBS mounted on the CTD frame was calibrated against filtered water samples obtained throughout the Upper Gulf survey. They were drawn from GO water bottles that sampled near the bed, at mid water and near the surface over the spring-neap tidal cycle. Figure 3.3 shows the calibration line and data points. Calibration of the moored OBS sensors by the same method was not possible as the water samples were not obtained at the same depth as the moored sensors. Therefore, the calibration of the CTD mounted OBS was considered valid for the moored backscatter sensors by assuming that the sensors are interchangeable with the sensitivity varying within 1%.

3.3.2 Transmissometers.

Two types of transmissometers were used. A Sea-Tech instrument was attached to the CTD frame for profiling at the CTD stations. Five transmissometers designed and built by the University of Wales, Bangor (UWB) were moored at sites W1 and E1 shown in Figure 3.1. One instrument at W1, 12m above the sea bed, failed to record any data. The transmissometers operate by emitting a collimated 660 nm light beam which is attenuated as it is transmitted along a fixed path-length x , depending on the amount of suspended particles in the water. A receiving light sensor yields 0 to 5 volts or a count output (depending on the specific data logger design) from which the attenuation coefficient a can be obtained. The attenuation coefficient varies linearly with the amount of suspended matter in the water provided that the size and other

optical characteristics remain constant. The Sea-Tech transmissometer mounted on the CTD frame was calibrated against filtered water samples. In this case, $x = 0.1$ m, and the attenuation coefficient

$$\alpha = -(1/x) \ln (V_m / 5.0) \quad 3.1$$

was obtained from the measured voltage V_m and converted into SPM concentration by a linear regression procedure. The calibration line and data points are shown in Figure 3.4. It was found that two regression lines, corresponding to different ranges in beam attenuation, were needed in order to fit the observed beam attenuations to gravimetrically obtained concentrations. This was also found to be the case in a previous study involving a wide concentration range in the Mersey estuary, UK (Jones, pers. comm.) and probably reflects the fact that particle sizes are generally larger at high concentrations as these high concentrations are due to resuspension of coarser particles at high current velocities. Transmissometers are less sensitive to large particles (Baker and Lavelle, 1984), resulting in a lower slope for the relationship between beam attenuation and concentration. The calibrated Sea-Tech transmissometer was used to cross-calibrate the moored UBW transmissometers for which the attenuation coefficient is given by:

$$\alpha = -\frac{1}{x} \ln \frac{(V_m - V_d)}{(V_{100} - V_d)}, \quad 3.2$$

where x is the transmissometer path-length in meters, V_m is the instrument count measured under field conditions, V_d is the count with a blocked light path, and V_{100} is the count that would be measured in clean water, at $x = 0$. The path-length of the transmissometers TR21-TR23 was 0.1 m, and of TR4 was 0.25 m. Since a V_{100} reading was not available before the deployment, it was determined for TR4 and TR22 by assuming that the same attenuation coefficient α was measured by the CTD transmissometer and by the moored transmissometer at the same depth and time.

Then:

$$-\frac{1}{x} \ln(V_{tr100} - V_d) = -\frac{1}{x} \ln(V_{tr} - V_d) - a_{trCTD} \quad 3.3$$

where V_{tr100} and V_{tr} are the count readings for the moored transmissometers and a_{trCTD} is the attenuation coefficient as measured by the CTD transmissometer. A linear regression of the first right-hand term versus a_{trCTD} yields a slope ~ 1 and V_{tr100} can be obtained from the ordinate intercept for each moored transmissometer. The CTD casts were not generally deep enough to reach the transmissometers moored 1 m above the sea bed so there were no a_{trCTD} values available at these levels. In this case the transmissometer readings were compared with the calibrated upper instrument while the two instruments were either in the air or immersed in the same tank of clean water. V_{tr100} was then obtained by assuming that the expression

$$-\frac{1}{x} \ln \frac{(V - V_d)}{(V_{100} - V_d)} = -\frac{1}{x'} \ln \frac{(V' - V_d)}{(V'_{100} - V_d)} \quad 3.4$$

holds for two instruments (one of which is indicated by prime) under the same conditions at the same time. The attenuation coefficient was then calculated using equation 3.2.

3.4. CTD spatial survey and tidal cycle stations.

A Sea-Bird Electronics CTD model SBE-9 was used for measuring the temperature-salinity-depth profiles by sensors calibrated at the factory. A rosette unit fitted with Niskin water bottles allowed the retrieval of water samples at specific depths. The sensor type and specifications are shown in Table 3.8. The OBS sensor and the SeaTech transmissometer were connected to the auxiliary CTD channels.

Table 3.8. Specifications of the profiling CTD unit on board the *Francisco de Ulloa*.

Sensor (Type)	Range	Precision	Resolution
Conductivity (Resistor cell SBE4)	0 to 70 mmho cm ⁻¹	0.003 mmho cm ⁻¹	0.0004 mmho cm ⁻¹
Temperature (Thermistor SBE3)	-5 to 35 °C	0.002 °C	0.0002 °C
Pressure (Paroscientific Digiquartz)	0 to 15000 psia	0.015% of the full scale	0.001% of the full scale

Post- processing of the CTD raw data was performed with the software supplied by Sea-Bird Electronics.

A gulf-wide spatial survey of CTD-OBS-transmissometer casts was made at 67 stations in seven along-gulf transects, as shown in Figure 3.5. Transects were made in August 13-15 and 23-27 under mid-range tides, halfway between spring and neaps. In addition, 34 closely spaced stations were made in four transects oriented across-gulf on the western side of the Upper Gulf, under similar tidal conditions, as shown in Figure 3.6. Four tidal cycle stations were made in August 1997 from the anchored vessel at sites W3 and E1 under spring and neap tide conditions. CTD-OBS-Transmissometer casts were made every 0.5 hours. A total of six tidal cycle stations were made (included those of June 1996, at site J) lasting from 1 to 4 semidiurnal cycles. The sites are shown in Figure 3.1.

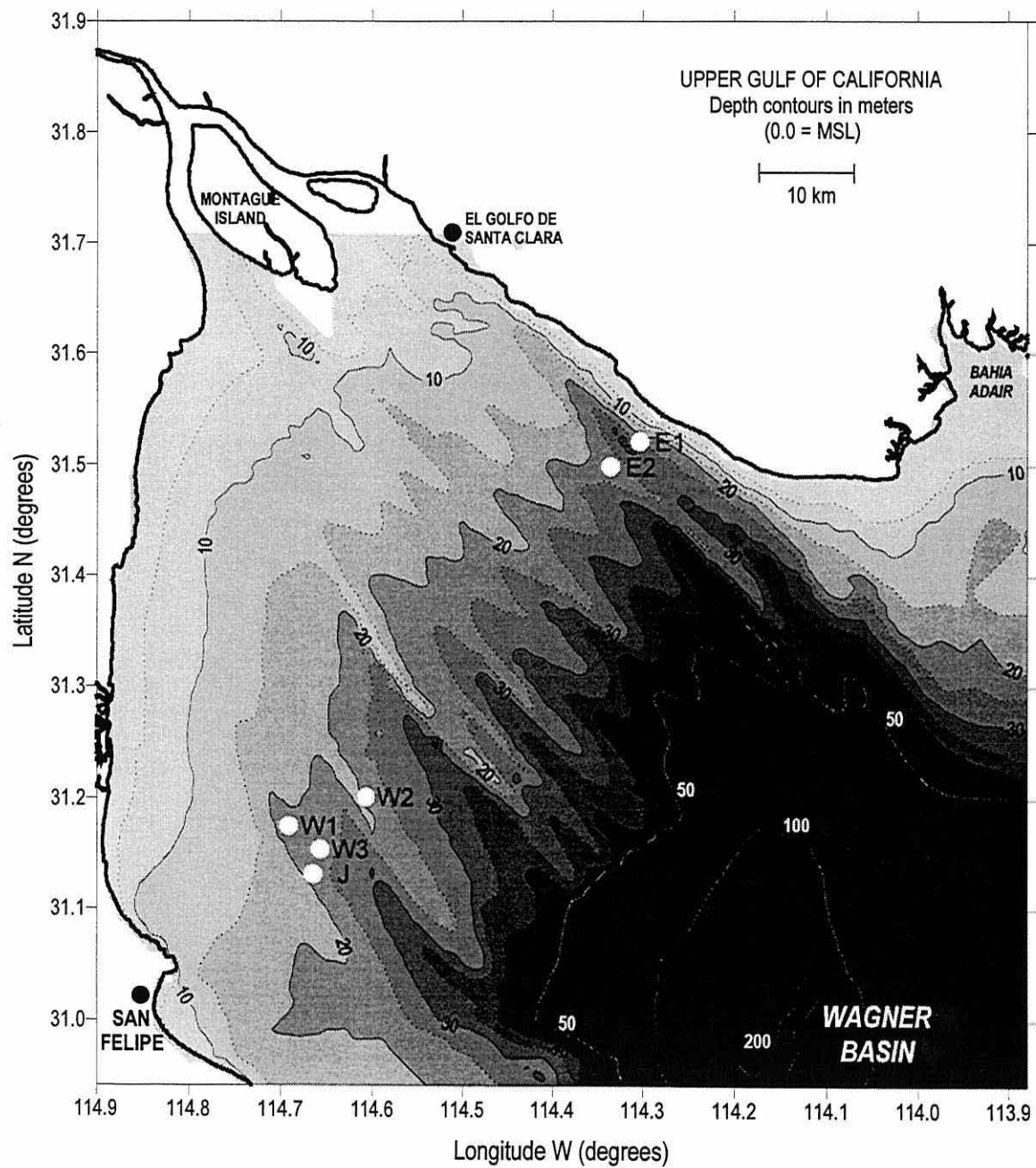


Figure 3.1. Instrument mooring sites in the Upper Gulf of California, in August 1997. The mooring at site J was made in June 1996.

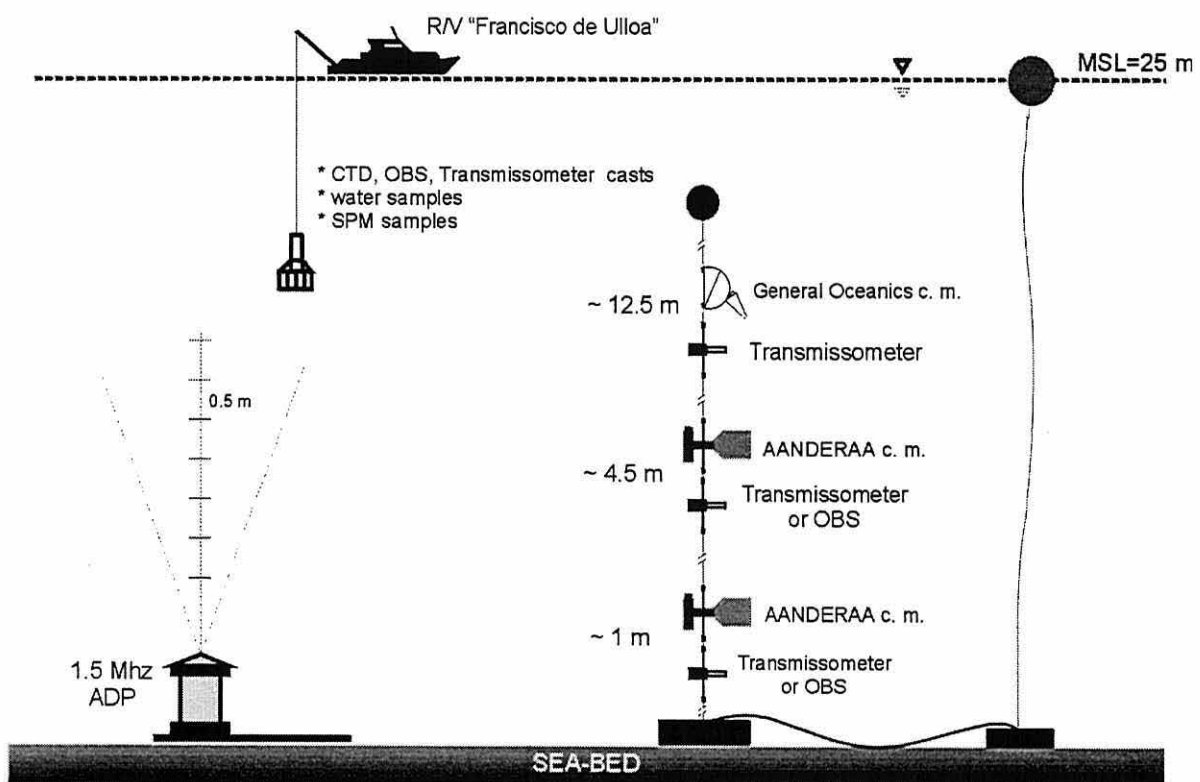


Figure 3.2. Schematic view of the ADP mooring at site W3 (left), and the current meter and SPM sensors at sites W1 and E1 (right). No current meters were deployed at sites W2 and E2.

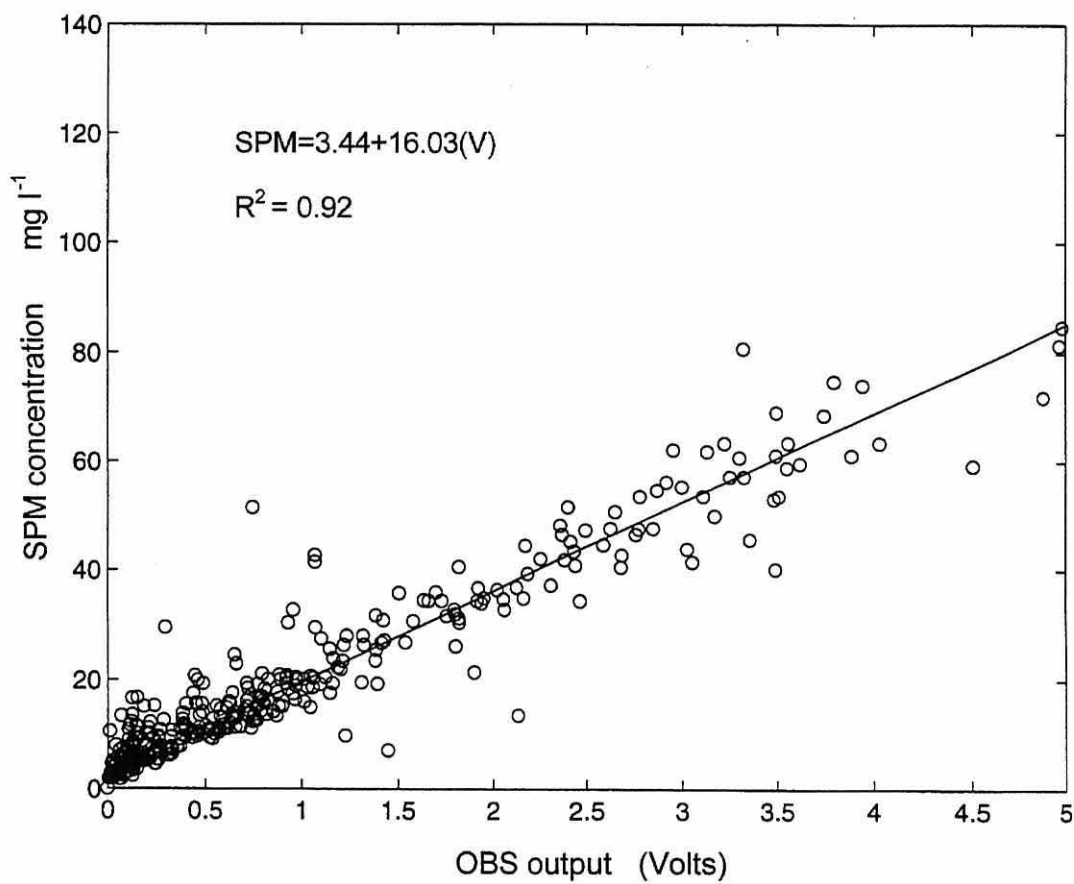


Figure 3.3. Calibration of the OBS sensor against SPM concentration from filtered water samples obtained in August 1997 across the Upper Gulf.

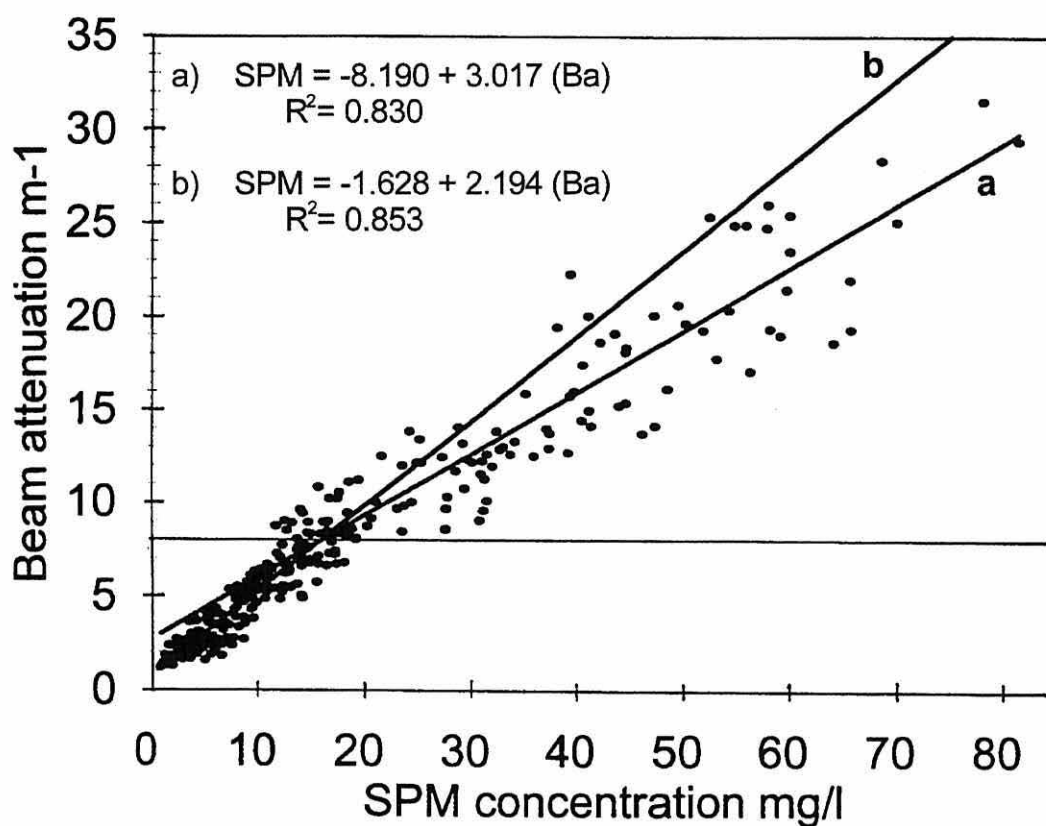


Figure 3.4. Calibration of the SeaTech transmissometer beam attenuation against SPM concentration from filtered water samples obtained in August 1997 across the Upper Gulf. a) calibration curve for beam attenuation $> 8 \text{ m}^{-1}$; b) calibration curve for beam attenuation $\leq 8 \text{ m}^{-1}$

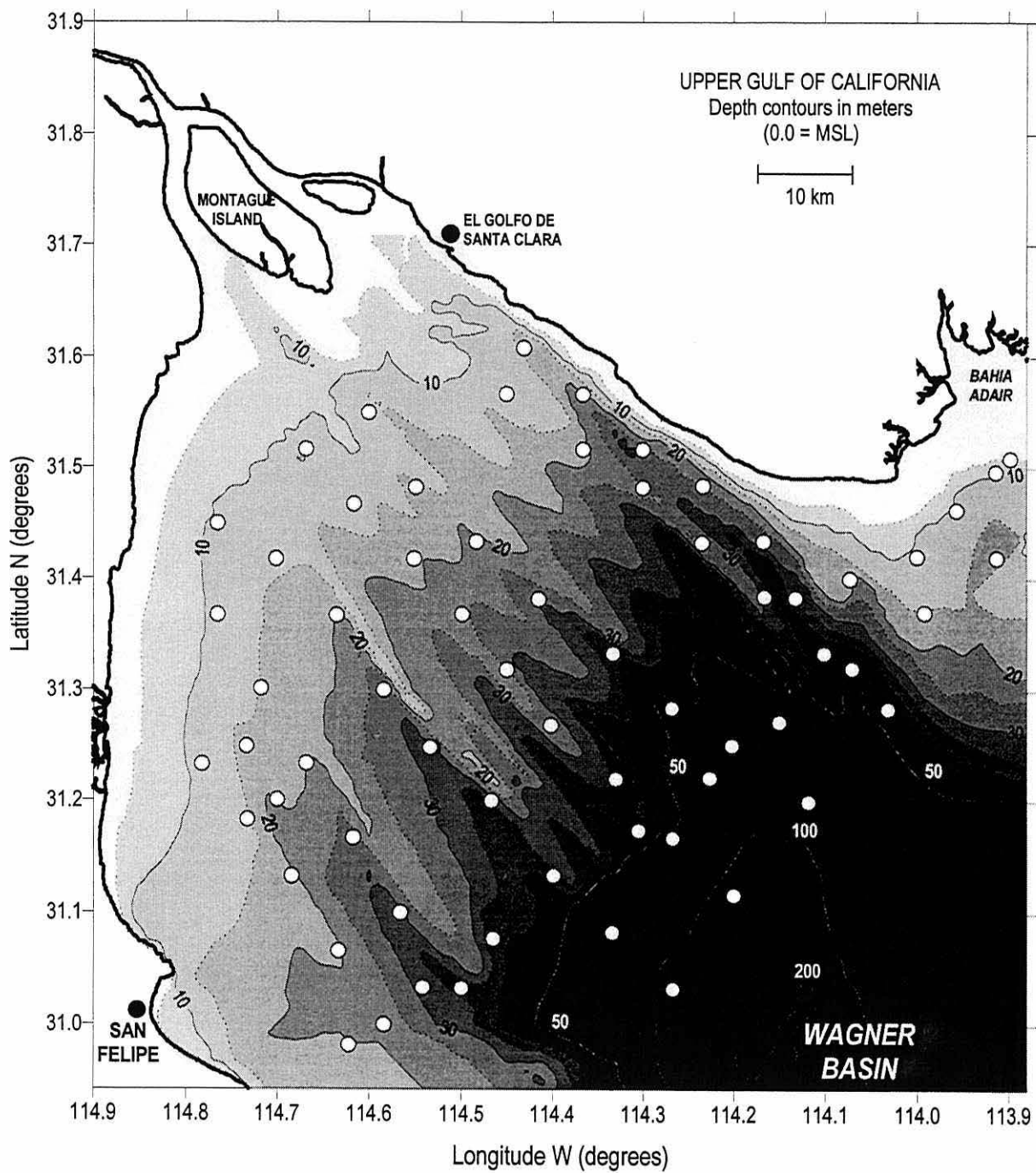


Figure 3.5. Along-gulf CTD station lines made in August 1997.

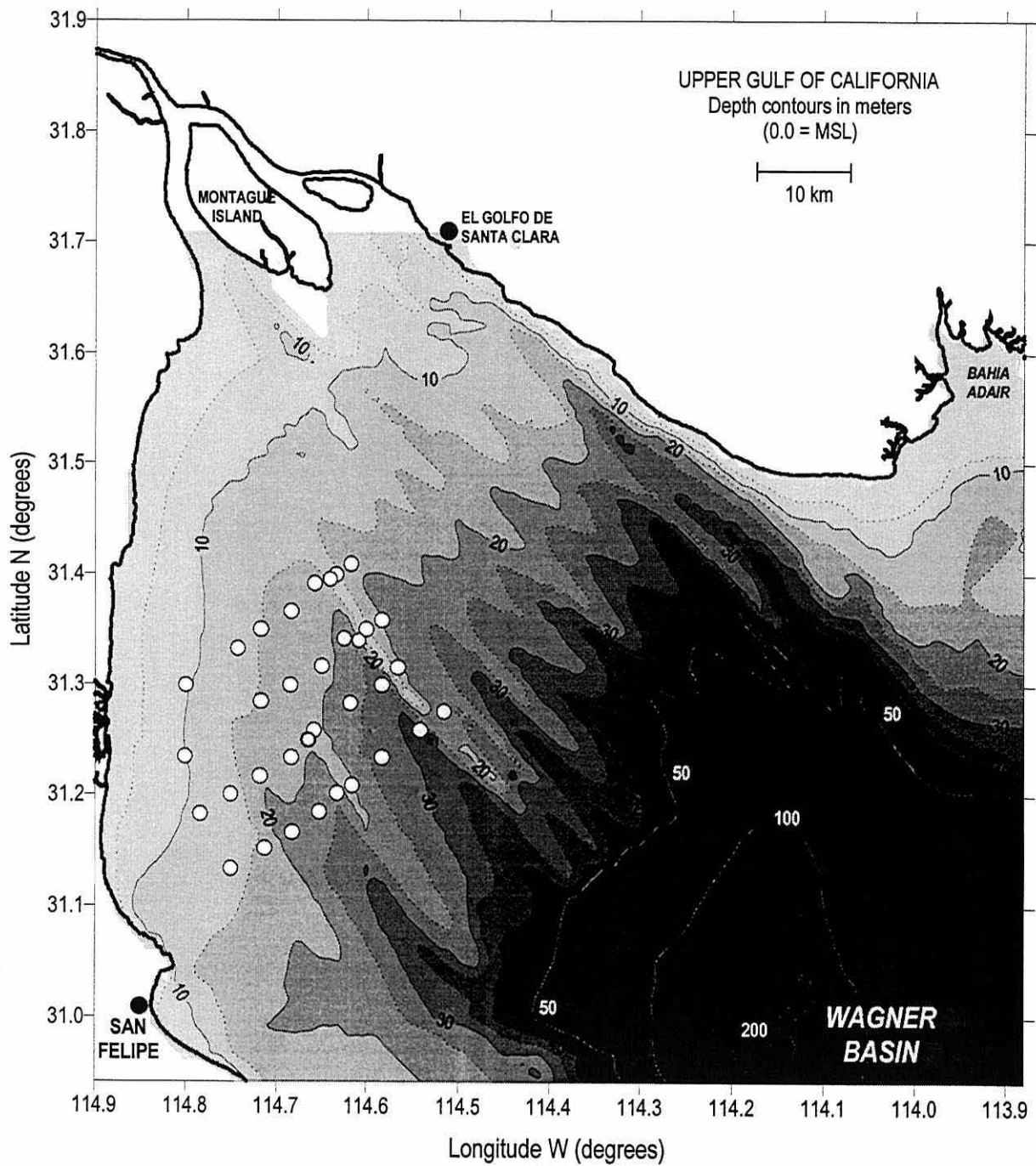


Figure 3.6. Across-gulf CTD station lines made on the western side, in August 1997.

4. Results.

4.1. Bathymetry.

The bathymetric map is shown in Figure 4.1. On the western side off Baja California a shallow platform 20-30 km wide has a gentle east-southeast sloping bottom (slope 0.5×10^{-3} to 0.7×10^{-3}) to depths of about 20 m. There is no shallow platform on the eastern side, off Sonora. Instead, a narrow, 20-40 m deep channel borders most of the coastline and runs along ~60 km until it reaches the north edge of Wagner Basin. A shallow platform exists south of Bahía Adair on the east end of the Upper Gulf. Eight along-gulf ridges and channels can be traced from the shallow head of the Upper Gulf to the edge of the 200m deep Wagner Basin. The intervening channels have a gentle slope of 6×10^{-4} and can be traced to the edge of Wagner Basin at depths near 50 m where the bottom slope increases by one order of magnitude. The wider channels of the western side show an asymmetric cross section due to different slopes of the ridge flanks. Looking southeast along a ridge the slope of the right flank is $O(10^{-2})$ and that of the left flank is $O(10^{-3})$. The crest-to-crest separation of the ridges is ~6 km on the eastern half of the Upper Gulf and ~12 km on the western half. Two outstanding ridges keep their identity along more than 50 km on the central and eastern areas.

4.2. Spatial survey.

4.2.1 Hydrography

Horizontal distributions of temperature, salinity and density at the surface and 4 m above the bed are shown in Figures 4.2 and 4.3. This was the deepest level common to all casts. The maximum values of these variables were observed at the shallow head of the Upper Gulf and along the Baja California coast, and lower values occurred on the eastern side of the mouth, toward Sonora. Warmer water was observed over the coastal areas and lower temperatures prevailed toward the middle and southern Upper Gulf. Horizontal gradients of salinity and σ_t were oriented NW-SE near the head and off Sonora, while off Baja California the trend was E-W. A near-bottom tongue of warmer, saltier and denser water appeared as an eastward intrusion north of San Felipe, apparently associated with the higher values near the west coast.

Surface minimum (maximum) values were 30.2°C (31.4°C) for temperature, 35.0 (37.0) for salinity, and 21.5 (22.7) for σ_t . At the head of the Upper Gulf near-bottom water was saltier and denser. Salinity and σ_t were ~ 0.3 units higher close to the bed than at the surface. No temperature inversions between the two depths were observed.

4.2.2. Suspended particulate matter (SPM).

Horizontal distributions of SPM are shown in Figure 4.3 for the sea surface and 4 m above the bed. Fewer stations were plotted in order to reduce the spatial effects of phase differences in the tidal resuspension cycle. The stations nearer to the head of the Upper Gulf were also excluded. The distributions are based on casts made around slack water time, when currents at 1.2 m above the bed were less than $0.15 \text{ m}\cdot\text{s}^{-1}$. Surface concentration was $\sim 5 \text{ g}\cdot\text{m}^{-3}$ in most of the Upper Gulf except in a small area north of San Felipe off the west coast, where SPM concentrations were $10\text{--}15 \text{ g}\cdot\text{m}^{-3}$. Here the largest horizontal gradient of $10^{-3} (\text{g}\cdot\text{m}^{-3})\cdot\text{m}^{-1}$ trended mainly E-W. At 4 m above the bed concentration was two to three times as high as at the surface. SPM concentration up to $35 \text{ g}\cdot\text{m}^{-3}$ formed cores detached from the coast over the western half of the Upper Gulf. A more uniform decrease from head to mouth occurred off the eastern side. Here the gradient was about $0.5\times 10^{-3} (\text{g}\cdot\text{m}^{-3})\cdot\text{m}^{-1}$ while around the high concentration cores the horizontal gradient was 10^{-3} to $5\times 10^{-3} (\text{g}\cdot\text{m}^{-3})\cdot\text{m}^{-1}$.

4.3. Fortnightly time series.

4.3.1. Currents.

The observed currents were oscillatory, nearly rectilinear, and revealed the dominant forcing of the semidiurnal tide that prevails in the Upper Gulf. A marked fortnightly modulation is evident in the series spanning the full spring-neap tidal cycle. The records from two levels show slower currents closer to the bed, as is commonly observed near the solid boundary. Maximum current speeds were in the range $0.5 - 0.9 \text{ m}\cdot\text{s}^{-1}$ during spring tides. Neap-tide maximum speeds were below $0.3 \text{ m}\cdot\text{s}^{-1}$. A summary of the measurements made on opposite sides of the Upper Gulf are given below in terms of the current velocity projected on the principal axes, along-gulf and

its perpendicular, across-gulf, as defined in Chapter 3. The flood and ebb stages correspond with the along-gulf inflow (+) and outflow (–) respectively.

4.3.1.1. Basic current statistics. West side.

Figure 4.4 shows the time series of along-gulf and across-gulf components of near bed current velocity measured 1.2 m above the bed at site W1. The predominant along-gulf component is evident in the series, as is the asymmetry of the ebb and flood cycles at the beginning of the series, in neap tides, when ebbing currents dominated. The neap tide at the end of the measurement period was not sampled due to instrument failure. The basic current statistics are given in Table 4.1.

Table 4.1. Basic current statistics from current meter Aanderaa 651, 1.2 m above the sea bed, at site W1. The azimuth angle of the principal axes is indicated.

Site W1 bottom depth: 21 m	Along-gulf: 323.8° (m s ⁻¹)	Across-gulf: 53.8° (m s ⁻¹)	Current speed (m s ⁻¹)
maximum flood	0.52	0.08	0.53
mean flood	0.22	0.01	0.22
std. dev. flood	0.13	0.03	0.13
maximum ebb	-0.55	-0.08	0.55
mean ebb	-0.24	0	0.25
std. dev. ebb	0.13	0.03	0.13

The current meter at 4.2 m above the sea bed measured current speed only due to compass malfunction. However, this instrument operated the full fortnightly cycle and measured neap tide currents at both end of the series as shown in Figure 4.4. Asymmetry between ebb and flood currents can be inferred from consecutive neap tide current peaks. Table 4.2 contains the current statistics.

Table 4.2. Basic current statistics from current meter Aanderaa 652, 4.2 m above the sea bed, at station W1. The time span corresponds to that of current meter at 1.2 m.

Site W1 Bottom depth: 21 m	Current speed (m s ⁻¹)
maximum flood	0.61
mean flood	0.26
std. dev. Flood	0.16
maximum ebb	0.63
mean ebb	0.29
std. dev. Ebb	0.16

4.3.1.2. Basic current statistics. East side.

The velocity data at the eastern side of the Upper Gulf were available from 4.2 m and 12.5 m above the sea bed at site E1, as shown in Figure 4.5. Both instruments operated over the full fortnightly cycle. Asymmetry in the ebb-flood cycles is evident during spring tides, when maximum ebb currents were ~10-15% faster than maximum flood currents. In contrast with the western side ebb flow dominance during neap tides was not observed. Tables 4.3 and 4.4 contain the basic statistics of the observed currents.

Table 4.3. Basic current statistics from current meter GO606, 4.2 m above the sea bed, at site E1. The azimuth angle of the principal axes is indicated.

Site E1 bottom depth: 25 m	Along-gulf: 303.5° (m s ⁻¹)	Across-gulf: 33.5° (m s ⁻¹)	Current speed (m s ⁻¹)
maximum flood	0.655	-0.327	0.657
mean flood	0.247	0.01	0.256
std. dev. flood	0.158	0.055	0.154
maximum ebb	-0.78	0.327	0.78
mean ebb	-0.29	0.006	0.298
std. dev. ebb	0.193	-0.30	0.188

Table 4.4. Basic current statistics from current meter GO405, 12.5 m above the sea bed, at site E1. The azimuth angle of the principal axes is indicated.

Site E1 bottom depth: 25 m	Along-gulf: 306.8° (m s ⁻¹)	Across-gulf: 36.8° (m s ⁻¹)	Current speed (m s ⁻¹)
maximum flood	0.764	-0.21	0.765
mean flood	0.262	-0.004	0.272
std. dev. flood	0.189	0.058	0.184
maximum ebb	-0.895	0.214	0.895
mean ebb	-0.302	0.002	0.312
std. dev. ebb	0.242	0.055	0.236

4.3.2. SPM concentration time series.

4.3.2.1. Near-bed SPM time series:

Four outstanding features were revealed by the SPM measurements made ~1 m above the bed by the transmissometers and OBS sensors, moored at sites W1, W2, W3, on the west side and E1, E2 on the east side of the Upper Gulf (Figs. 4.6-4.9):

1. strong quarter diurnal signal with concentrations between 10 and 100 g·m⁻³,
2. fortnightly modulation of the concentration signal which clearly shows the neap-spring tidal cycle,
3. slowly varying “background” SPM concentrations of 10 to 20 g·m⁻³ with higher values during spring tides, also associated with the fortnightly cycle,
4. “twin-peak” structure with maxima at maximum flow and high water minima < low water minima during spring tides, and weak or absent during neaps.

In contrast with the local quarter diurnal resuspension signal in SPM concentration, the “twin-peak” structure results when a horizontal gradient in background SPM concentration is displaced past the moorings by the oscillatory tidal current. The observed uneven minima in concentration are due to superposition of the quarter diurnal and the semi diurnal advection signals. For SPM concentration decreasing to

the Southeast, the lower minima in SPM concentration occur near the end of the flood tide current, as shown in the time series of near-bed concentration (Figs. 4.6-4.9). Besides these periodic signals six to eight high SPM concentration events were measured by the OBS sensors during neap tides. These were measured by instruments 1m above the bed at sites W2 and W3 during neap tides and reached concentrations similar to or larger than the maximum spring tide values. These transient events occurred during the two neap tide periods (Fig. 4.6), and appear superimposed on the periodic concentration signal. Some of these events, with lower concentrations, can be traced in the series measured at the same sites 3.7 m and 6.0 m above the bed. Similar events were not detected by the transmissometers moored at sites W1 and E1, as shown in Figures 4.8 and 4.9.

At site E2 SPM concentration from OBS sensors at 1 and 3.7 m above the bed was in general 5 to 10 $\text{g}\cdot\text{m}^{-3}$ during neap tides at the beginning of the series (Fig. 4.7). After five days the instrument 1 m above the bed was saturated with concentration of about 95 $\text{g}\cdot\text{m}^{-3}$ and that at 3.7 m above the bed was saturated with about 20 $\text{g}\cdot\text{m}^{-3}$ due to its higher gain. Just before saturation the SPM signal varied between ~ 10 and 95 $\text{g}\cdot\text{m}^{-3}$ and remained saturated afterwards during six days corresponding to spring tides. At 3.7 m above the bed a clear quarter diurnal signal and “twin-peak” structure is discernible with concentration between ~ 10 and 20 $\text{g}\cdot\text{m}^{-3}$. After August 20 the instrument remained saturated for the rest of the deployment.

4.3.2.2. Mid-water SPM time series.

SPM concentration at 12.0 m above the bed was measured by one transmissometer at site E1 in water 30 m deep. Neap-tide concentrations were 5 to 10 $\text{g}\cdot\text{m}^{-3}$ and increased to values near 20 $\text{g}\cdot\text{m}^{-3}$ during springs with a maximum of 25 $\text{g}\cdot\text{m}^{-3}$. The periodic quarter-diurnal signal present in near-bed SPM concentration was also observed in the mid-water series, but it was weak and occurred only from neap to maximum spring tides. The periodic behaviour was masked afterwards by higher frequency fluctuations.

4.3.3. Tide and wind conditions.

Figure 4.10a shows the tidal elevation derived from the pressure measured in decibars (1 decibar=1 m water column). The tide was semidiurnal with maximum spring tide range of 7.4 m on August 19 and the minimum range of ~1 m during neap tides. The observed tides were in agreement with the predictions at San Felipe within 1%. The wind observations by the *R/V David Starr Jordan* during August 15-31 are shown in Figure 4.10b. The most frequent winds were from the sector ESE-SSW accounting for 73% of the time, or up to 87% if the sector WSW is included. Wind speed ranged from 2 to 6 m·s⁻¹ for 77% of the time and exceeded 10 m·s⁻¹ for only 5% of the time. One event of persistent moderate winds occurred during August 15-17 with southerly winds at about 10 m·s⁻¹. The general trend during the fortnightly cycle shows faster winds at the end of neap tides and lighter winds in springs. During the moderate wind event of August 15-17 the visually estimated wave height was 1-1.5 m with period 4-5 seconds.

4.4. Tidal cycle stations.

4.4.1. Hydrography.

Time series of temperature, salinity, σ_t and SPM observed on the western side in spring and neap tides are shown in Figures 4.11 to 4.13 for site J (June, 1996), and in Figures 4.14 to 4.16 for site W3 (August, 1997). Figures 4.17 to 4.19 correspond to site E1 (August, 1997) on the eastern side of the Upper Gulf.

The spring tide series of June, 1996, at site J show that temperature, salinity and sigma-t remained nearly homogeneous during the four semidiurnal cycles of the series (Fig. 4.11). The nearly vertical isolines indicate that well mixed conditions prevailed from near the bottom to near the surface. Most of the water column had temperature 28.0 to 28.2 °C, salinity 36.1 to 36.3, and sigma-t 23.2 to 23.4. Events of warmer and less dense water were observed in the upper 3-5 m apparently due to solar heating. The neap tide series revealed the development of a near-bed stratification event (Fig. 4.12). The nearly homogeneous conditions observed during the first semidiurnal cycle

evolved into a two-layer structure having an interface 5-8 m above the bed. The difference in upper-lower layer values was -1°C for temperature, -1 for salinity and -0.3 sigma-t units for density.

In August, 1997, spring tide observations at W3 show nearly homogeneous conditions during the two-day series (Fig. 4.14). The temperature, salinity and density variation was small ($30.2\text{--}30.8^{\circ}\text{C}$, $36.2\text{--}36.4$, and $22.3\text{--}22.7$ sigma-t units, respectively). Slight stratification involving a vertical temperature rise of 0.5°C was observed close to the surface during most of the daylight hours, possibly the effect of solar heating. This increase in temperature reflects a transient buoyant layer near the surface, as revealed by the density structure. Salinity values were similar to those of June 1996 but temperature was about 2°C warmer and sigma-t was about 0.7 units lower. The neap-tide series are shown in Figure 4.15. Despite being limited to 1.2 semidiurnal cycles, the results show a denser near-bottom layer 5–8 m thick overlaid by almost homogeneous less dense water. The near-bed water was up to 0.5°C warmer and 0.6 more saline than the upper layer. The density changed by 0.2–0.3 sigma-t units across a 2-m thick interface that displayed a wave-like pattern. At the end of the series the interface spread upward over most of the water column. The weakening of the vertical density gradient at the end coincided with the onset of strong southerly winds and rough seas that prevented longer observations.

At site E1 off the east coast the water was deeper (32 m) and vertically mixed conditions during spring tides were also evident except in the surface layers that became stratified by warmer less dense water. In general the water away from the surface had temperature 0.5°C higher, salinity 0.5 lower and sigma-t 0.5 lower compared with that on the west coast the day before. This is consistent with the spatial distribution 4 m above the bed, shown in Figures 4.2 and 4.3. During neap tides (Fig. 4.18) there was vertical stratification but the two-layered structure observed previously on the west side was observed only in salinity on the east side. The bottom layer that formed the lower half of the water column at the beginning of the series became thinner (6-8 m) toward the end of the three semidiurnal periods. Temperature was $1.0\text{--}1.5^{\circ}\text{C}$ higher than at site W3 on the west side 13 days earlier. Salinity and sigma-t were both lower by ~ 0.6 and ~ 0.8 units respectively

4.4.2. Suspended particulate matter (SPM).

Characteristics common to all the series are an increase of SPM with depth at all times. No measurements were made within 1 m from the bed. The main differences correspond to contrasting tidal conditions; therefore the series from sites J, W3 and E1 are described next under the headings –springs or –neaps.

4.4.2.1. Spring tides.

Site J was the shallower (20 m) of the two western sites. SPM concentrations were $\sim 30 \text{ g}\cdot\text{m}^{-3}$ about 1 m above the bed and less than $20 \text{ g}\cdot\text{m}^{-3}$ over most of the water column (Fig. 4.13). The series revealed high concentration pulses extending over the entire water column at the quarter-diurnal (M_4) frequency. The concentration peaks are well correlated with the maximum tidal current throughout most of the water column. Close to the sea bed the maximum SPM concentration was nearly simultaneous with the maximum current velocity but near the surface SPM maximum values lagged 1–2 hours behind the near-bed peak currents. The quarter-diurnal peaks in SPM concentration occurred in pairs separated by a minimum higher than the previous minimum concentration. This “twin-peak” structure is shown by the $10 \text{ g}\cdot\text{m}^{-3}$ concentration contour.

At site W3 (25 m) maximum SPM concentration exceeded $60 \text{ g}\cdot\text{m}^{-3}$ at 1 m above the bed (with instantaneous peaks up to $80 \text{ g}\cdot\text{m}^{-3}$). As shown in Figure 4.16 concentration in the water column was in general 10 to $40 \text{ g}\cdot\text{m}^{-3}$ with surface values up to $20 \text{ g}\cdot\text{m}^{-3}$. The quarter diurnal and twin peak signals were also evident at W3, as well as the good correlation between high concentration and high velocity near the bed. Near surface concentration maxima lagged 2-3 hours behind near bed maxima.

Site E1 on the eastern side of the Upper Gulf was the deepest (30 m). The time series shown in Figure 4.19 span three semidiurnal cycles and show near bed concentrations similar to those at W3 but lower concentrations above mid-water. The quarter diurnal

and twin-peak features are evident in the near bed contours but nearly vanish in upper levels so that the $10 \text{ g}\cdot\text{m}^{-3}$ contour displays semidiurnal peaks instead of quarter-diurnal. This seems to be associated with a marked asymmetry in the quarter diurnal peaks i.e. one of the twin peaks has lower concentrations and tends to fade out further up the water column. The currents measured 4.2 m above the bed revealed maximum ebb currents $\sim 5\text{-}10\%$ faster than maximum flood currents. The peaks showing higher concentrations coincided with the ebb current stage.

During spring tides the “twin-peak” structure was observed through most of the water column at the three sites. However, in upper levels away from the bed, the lower minima in SPM concentration did not coincide with the end of the flood tide. This was caused by a lag in the upward diffusion of SPM relative to the near-bed levels. The vertical mixing time t for fine particles to reach a height h in open channel flow, assuming no settling is (Julien, 1995):

$$t = h (0.1 u_*)^{-1}$$

by taking an average $u_* = 0.025 \text{ m}\cdot\text{s}^{-1}$, and $h = 15 \text{ m}$ for J and 30 m for E1, the mixing times are 1.7 hours and 3.3 hours, respectively. These are similar to the observed time lags in Figures 4.13a and 4.19a. At W3 the mixing time is between that at J and E1.

4.4.2.2. Neap tides.

Neap tide SPM concentrations were lower by a factor of 2–3 compared with those observed in springs. The higher concentrations were constrained to a layer 4–8 m thick above the bed with maximum near-bed values of $20\text{-}30 \text{ g}\cdot\text{m}^{-3}$. Concentrations did not decrease below $10 \text{ g}\cdot\text{m}^{-3}$ within this layer. At site J (Fig. 4.13) the $10 \text{ g}\cdot\text{m}^{-3}$ contour revealed a semidiurnal signal but did not show evidence of the quarter diurnal frequency observed during spring tides. There was a marked asymmetry in the ebb-flood velocity cycles in which ebb currents predominated with little or no current reversals. This behaviour is also discernible in the series from site W3 (Fig. 4.16)

despite the length of the series being restricted to 15 hours. At site E1 on the eastern side of the Upper Gulf (Fig. 4.19b) the concentrations were similar but in contrast with the two western sites, the series show that a weak quarter diurnal signal was present near the bed, as shown by the $20 \text{ g}\cdot\text{m}^{-3}$ concentration contour.

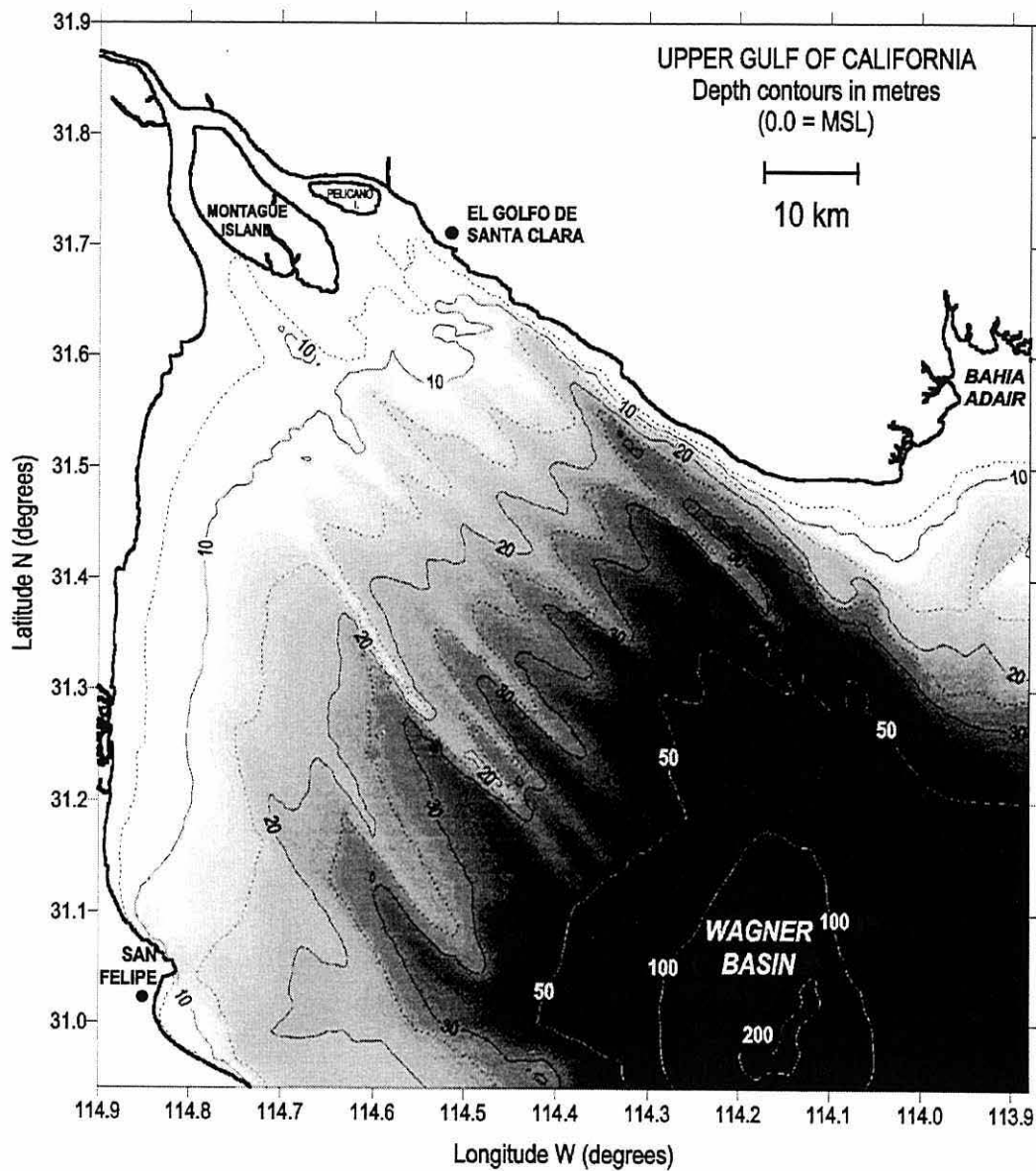


Figure 4.1. Bathymetry of the Upper Gulf of California from surveys made in 1994–1997. Depth contours in metres relative to mean sea level.

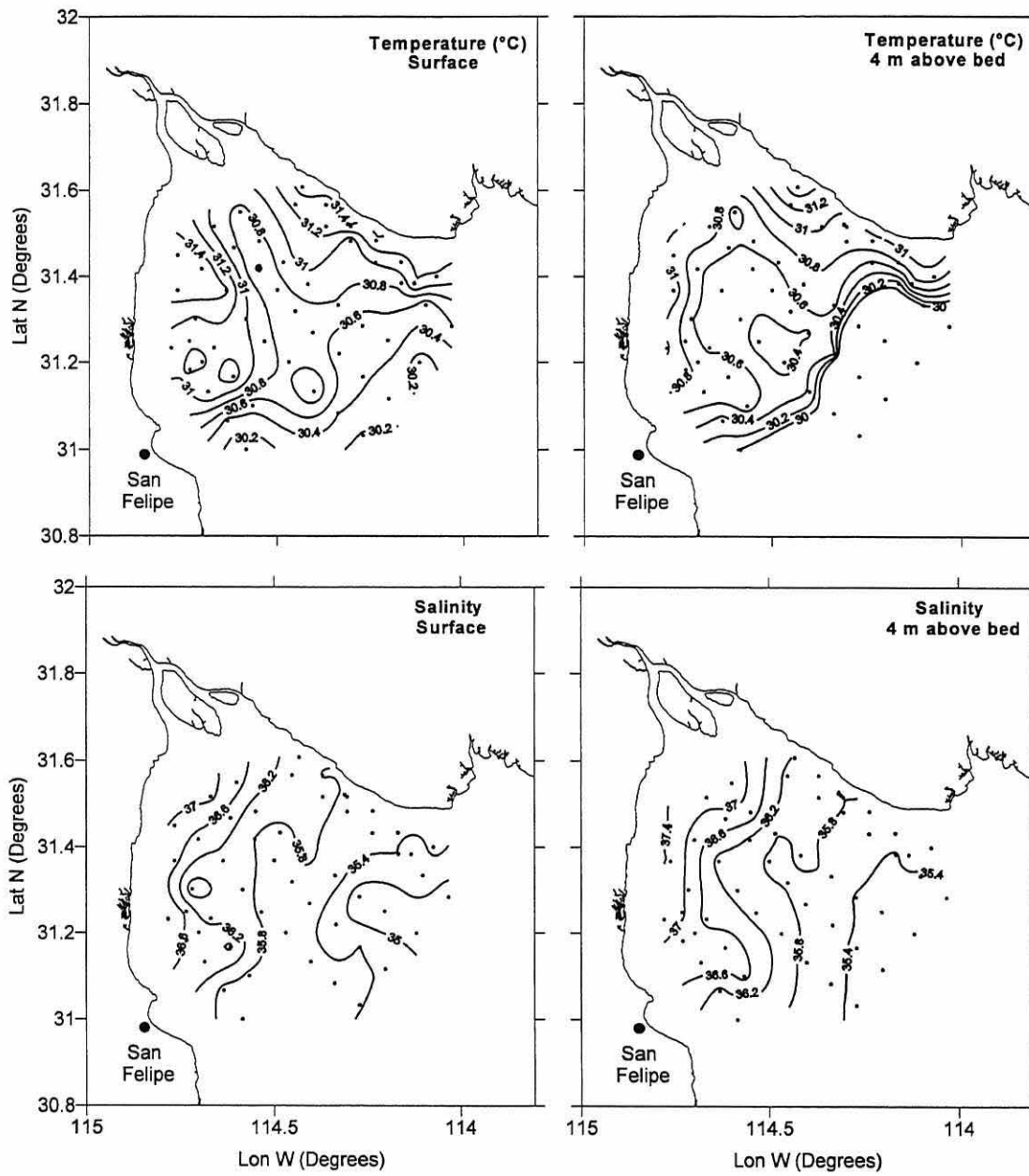


Figure 4.2. Temperature and salinity in the Upper Gulf of California at the sea surface and at 4 m above the bed. CTD stations (dots) were sampled in August 13–15 and 23–24, 1997.

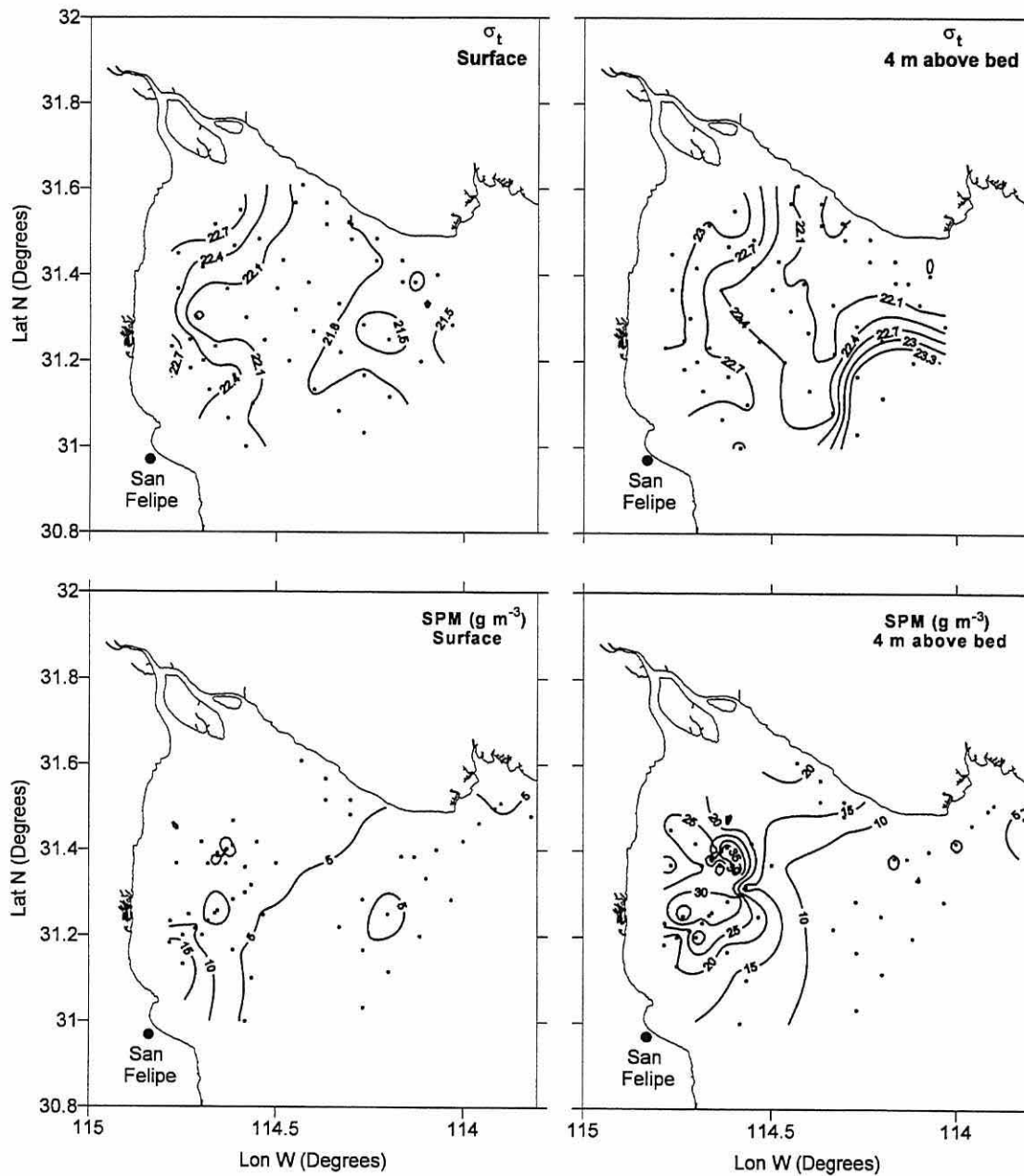


Figure 4.3. Density and SPM concentration in the Upper Gulf of California at the sea surface and at 4 m above the bed. CTD and OBS casts (dots) were made in August 13–15 and 23–24, 1997. The SPM concentration distribution is based on casts made under slow currents ($<0.15 \text{ m}\cdot\text{s}^{-1}$).

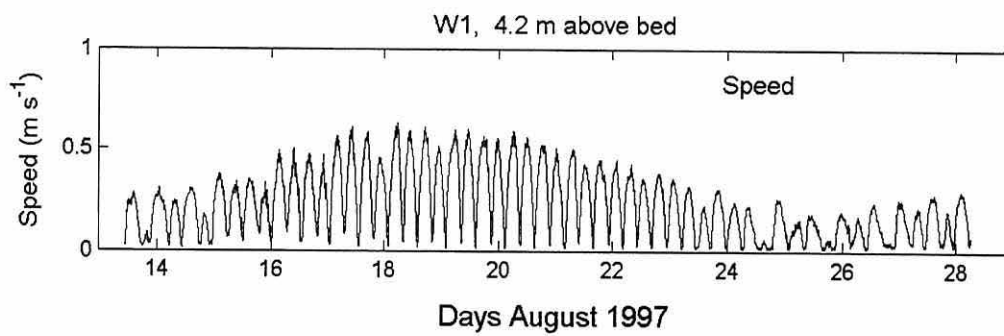
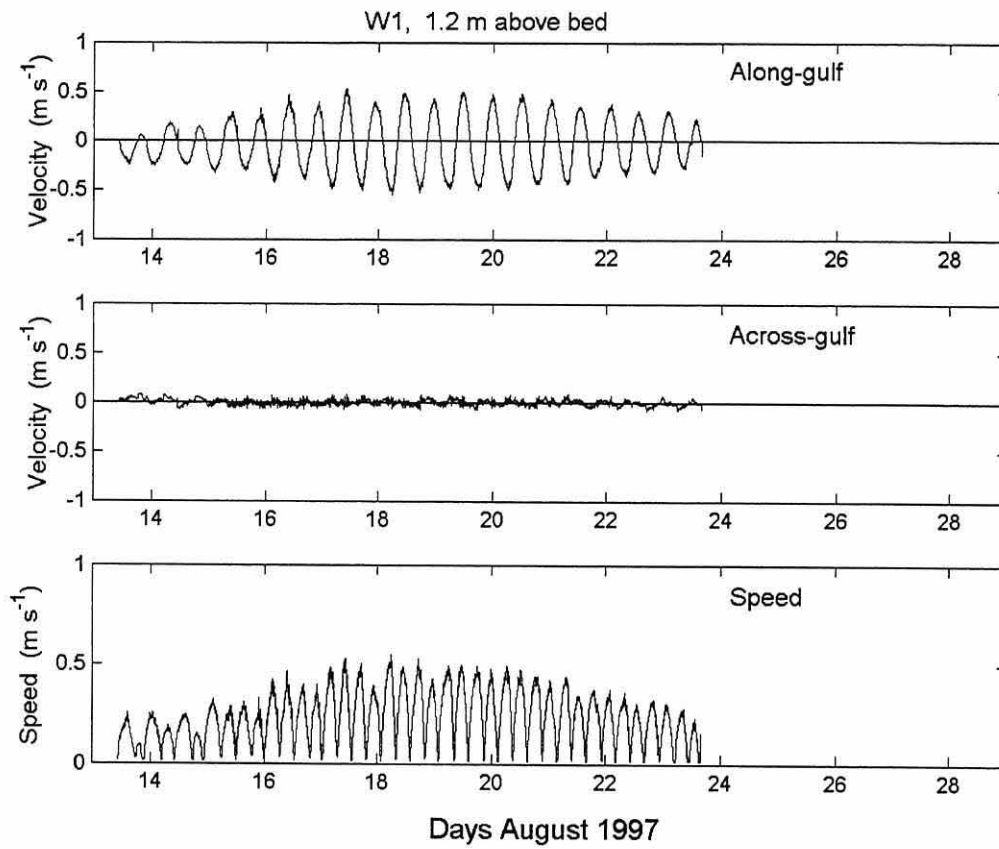


Figure 4.4. Currents measured at site W1 on the western side of the Upper Gulf at 1.2 m and at 4.2 m above sea bed (speed only). Positive along-gulf velocity corresponds to flood current.

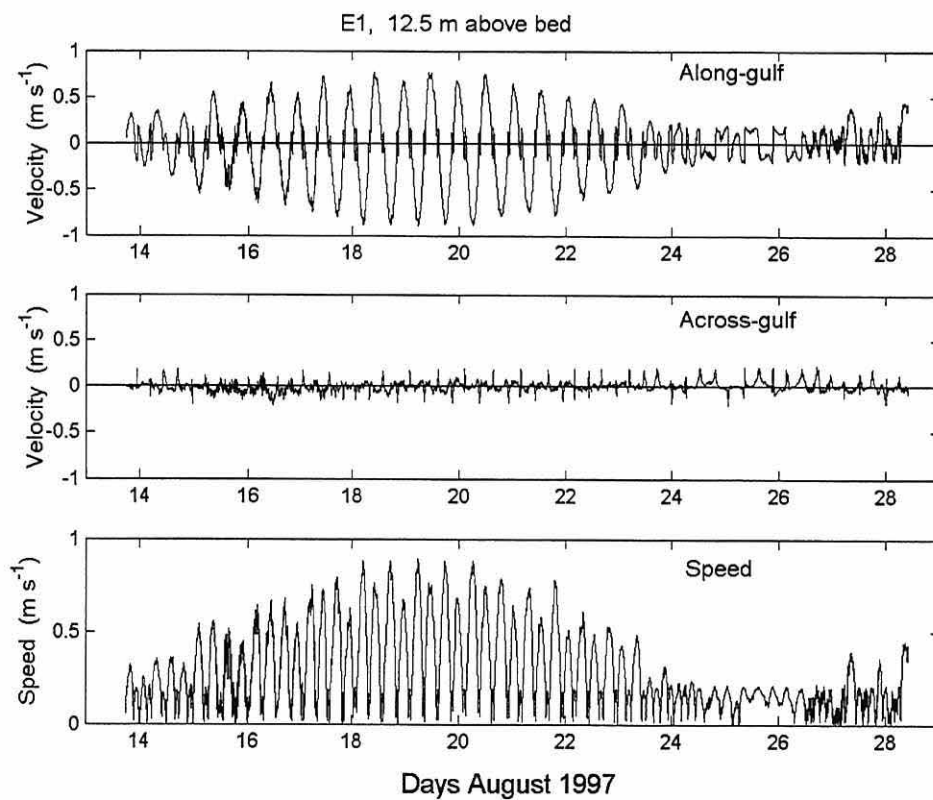
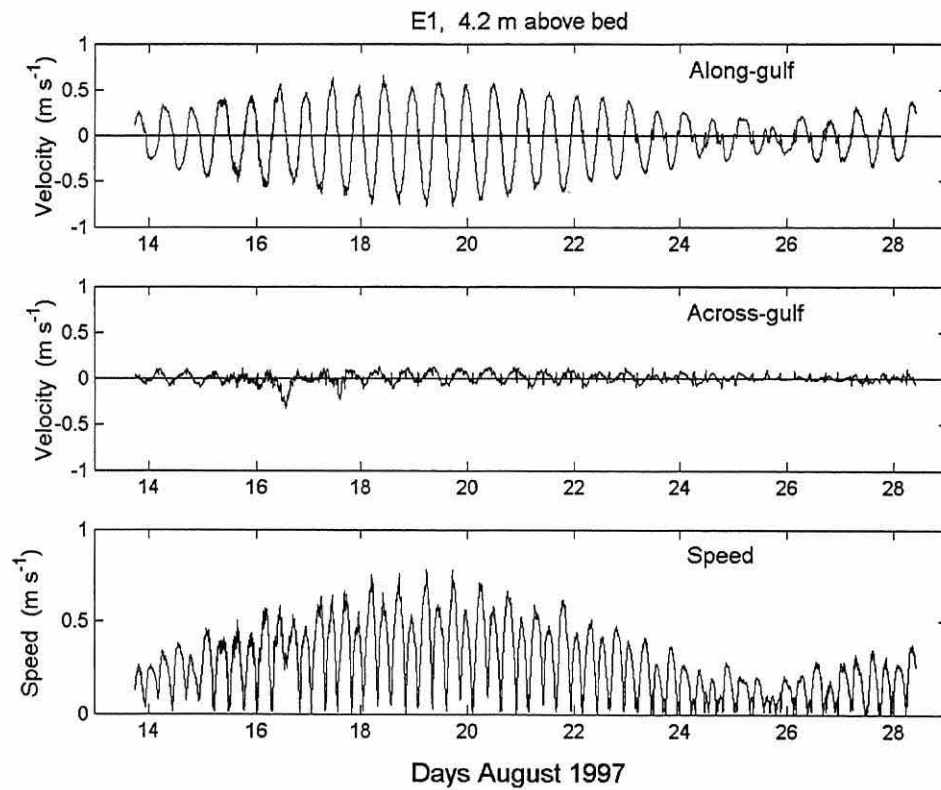


Figure 4.5. Currents measured at site E1 on the eastern side of the Upper Gulf at 4.2 m and at 12.5 m above the sea bed. Positive along-gulf velocity corresponds to flood current.

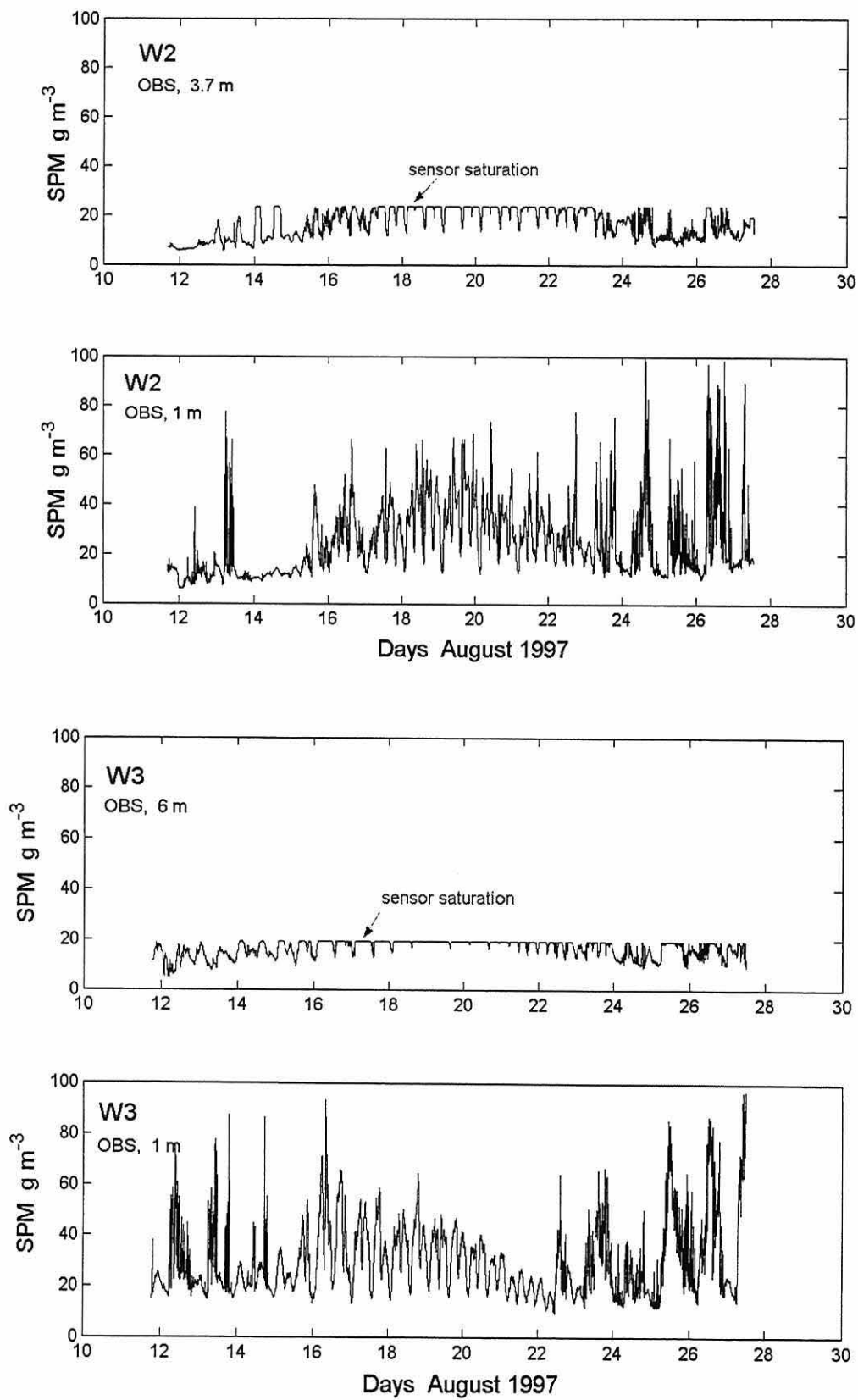


Figure 4.6. SPM concentration time series from OBS sensors on the western side of the Upper Gulf. Site W2, 1 m and 3.7 m above the bed; site W3, 1 m and 6 m above the bed.

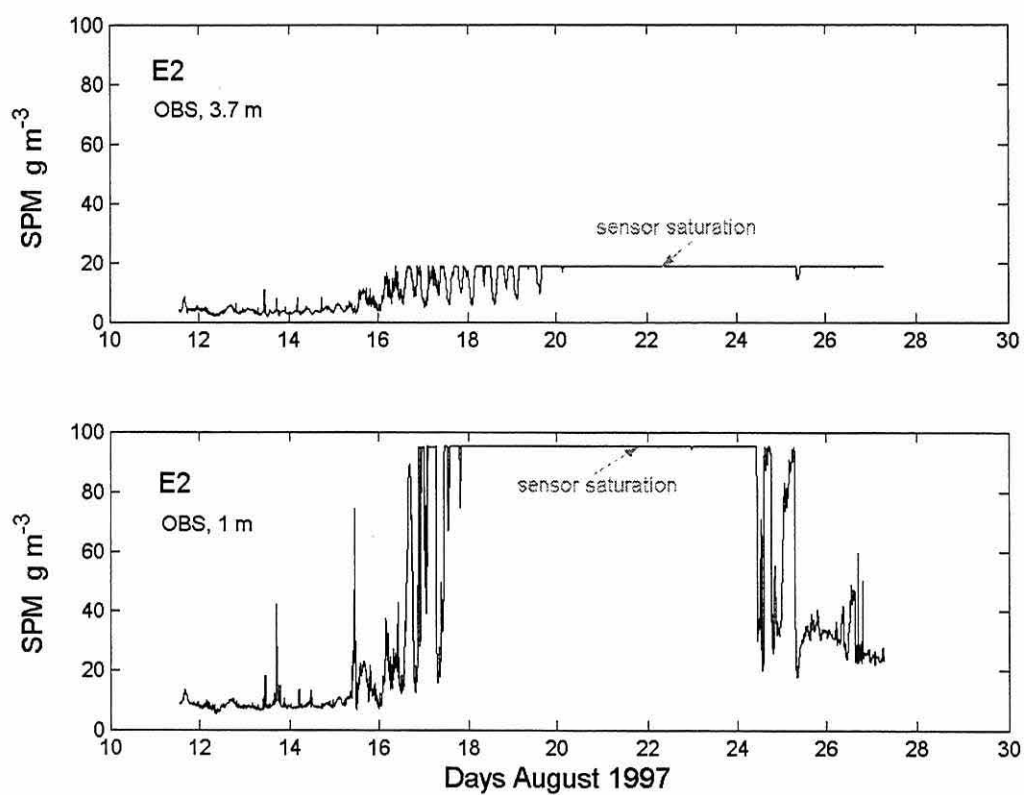


Figure 4.7. SPM concentration time series from OBS sensors on the eastern side of the Upper Gulf at site E2, at 1 m and 3.7 m above the sea bed.

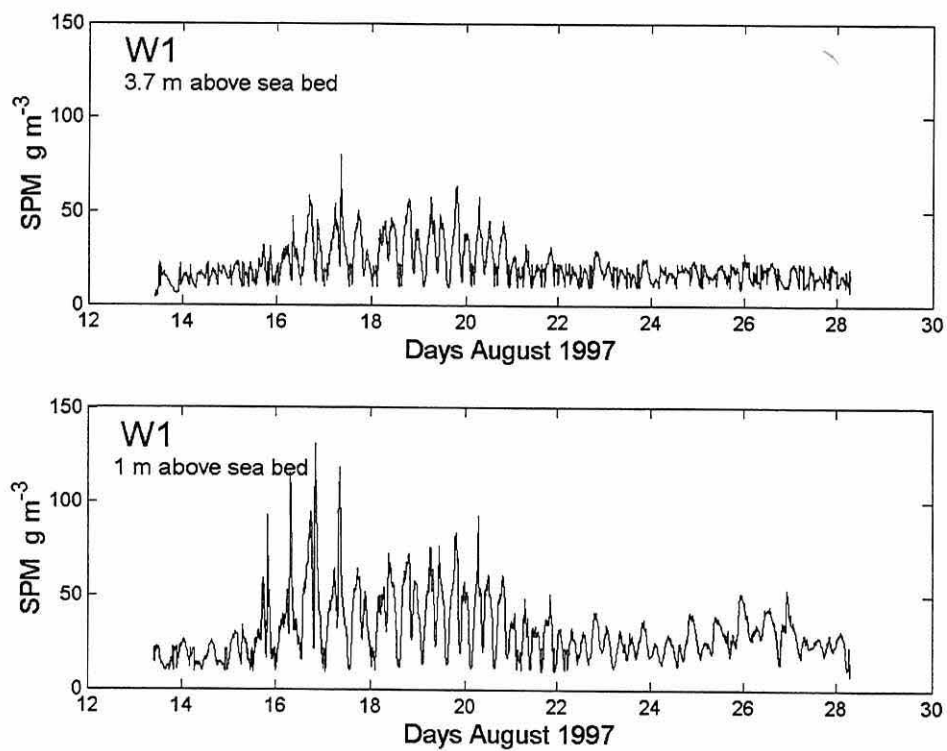


Figure 4.8. SPM concentration time series from transmissometers on the western side of the Upper Gulf at site W1, at 1 m and 3.7 m above the sea bed.

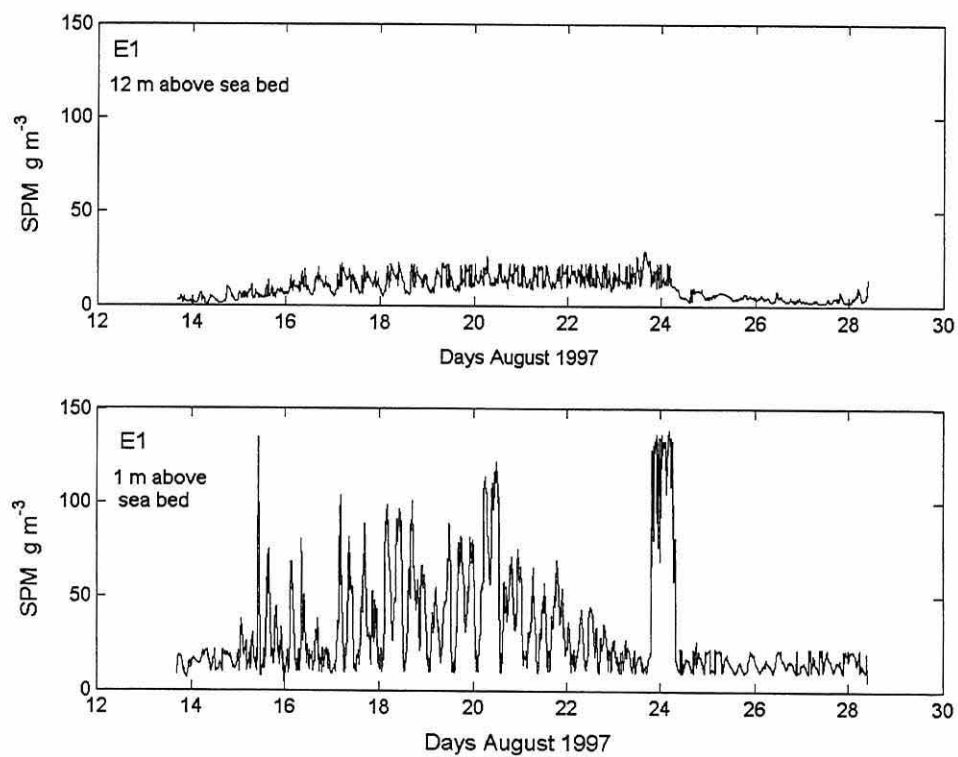
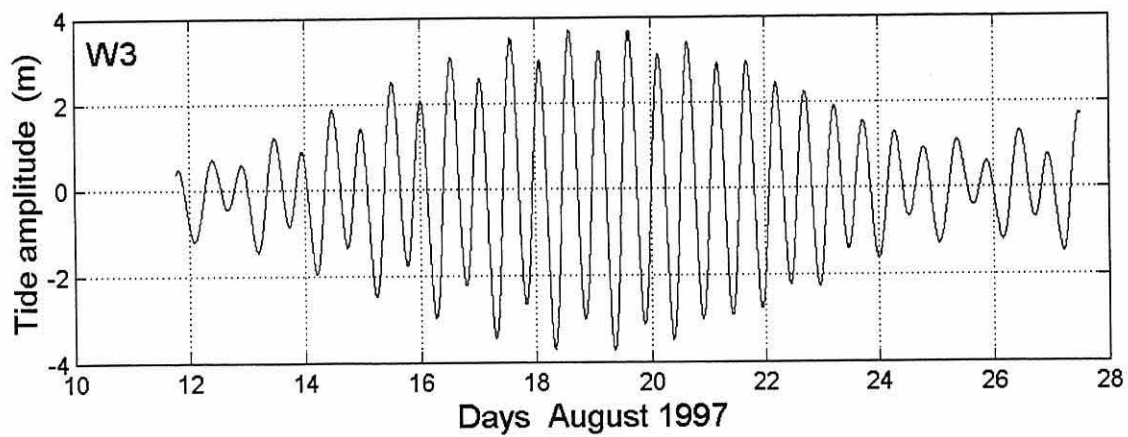


Figure 4.9. SPM concentration time series from transmissometers on the eastern side of the Upper Gulf at site E1, at 1 m and 12 m above the sea bed.



b

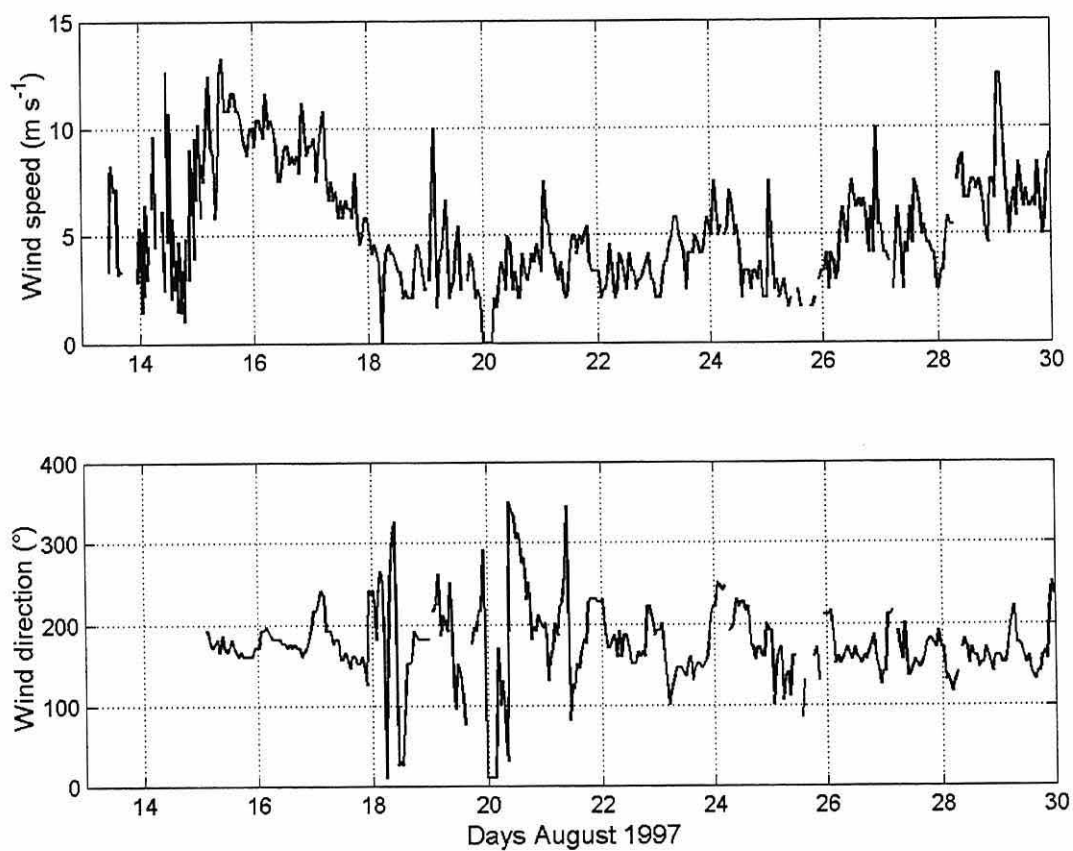


Figure 4.10. Tide and winds during the August 1997 survey in the Upper Gulf. (a) Tide measured by the ADP pressure sensor at site W3. (b) Winds from observations made by the *R/V D. Starr Jordan* while under-way across the Northern Gulf.

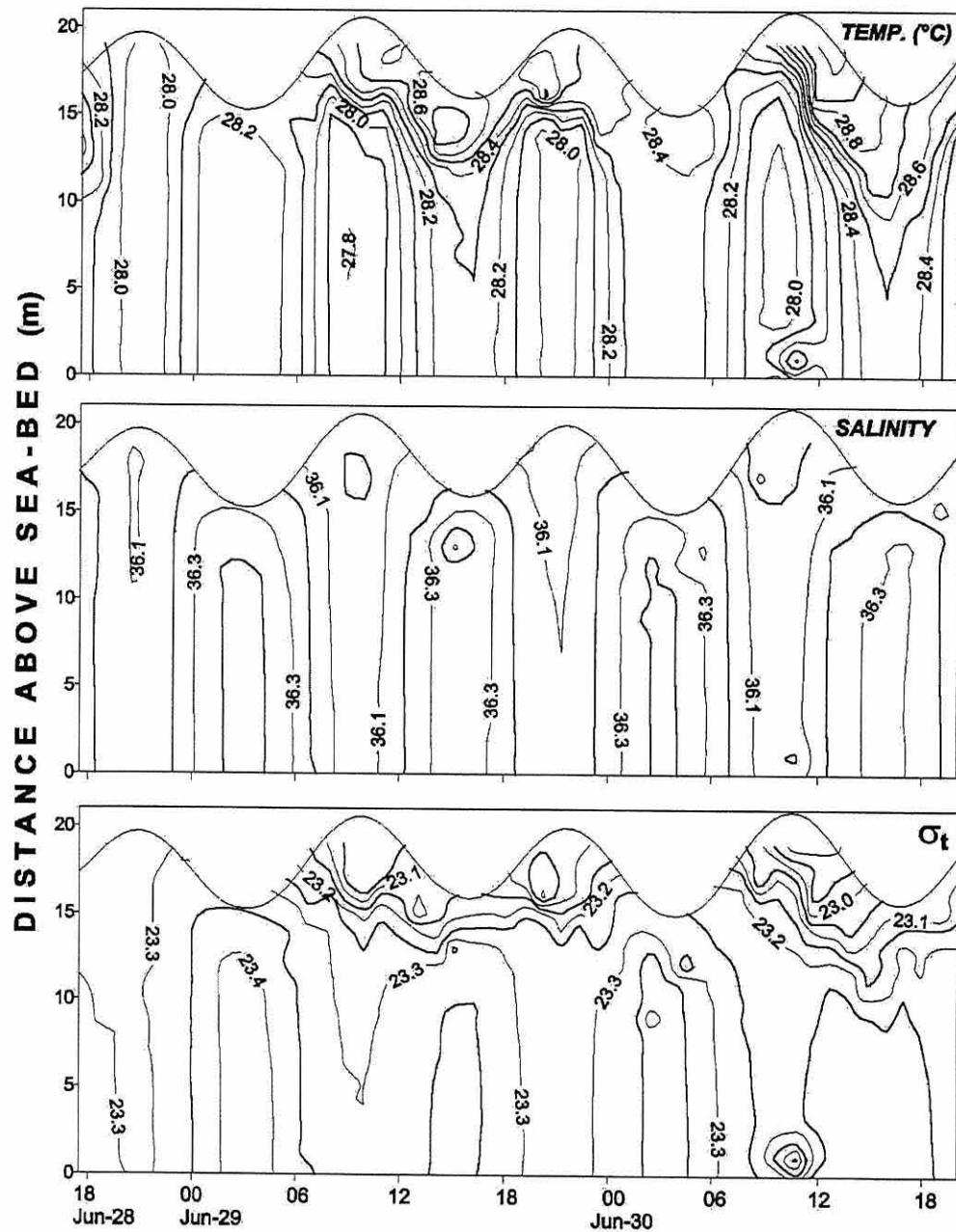


Figure 4.11. Spring-tide time series of temperature, salinity and density (σ_t) observed at site J in June, 1996 when vertically mixed conditions prevailed over most of the water column.

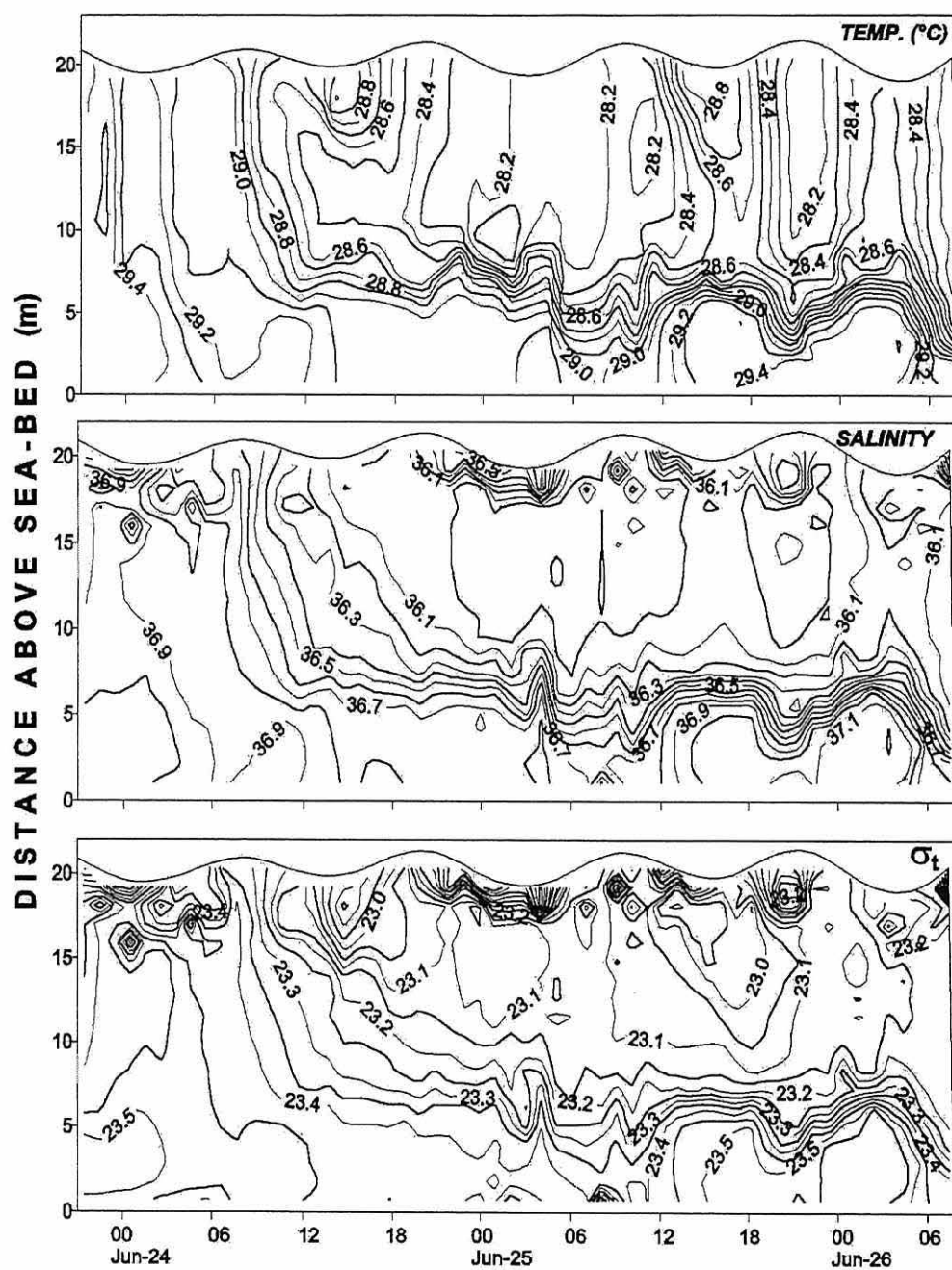


Figure 4.12. Neap-tide time series of temperature, salinity and density (σ_t) observed at site J in June, 1996 when vertical stratification developed.

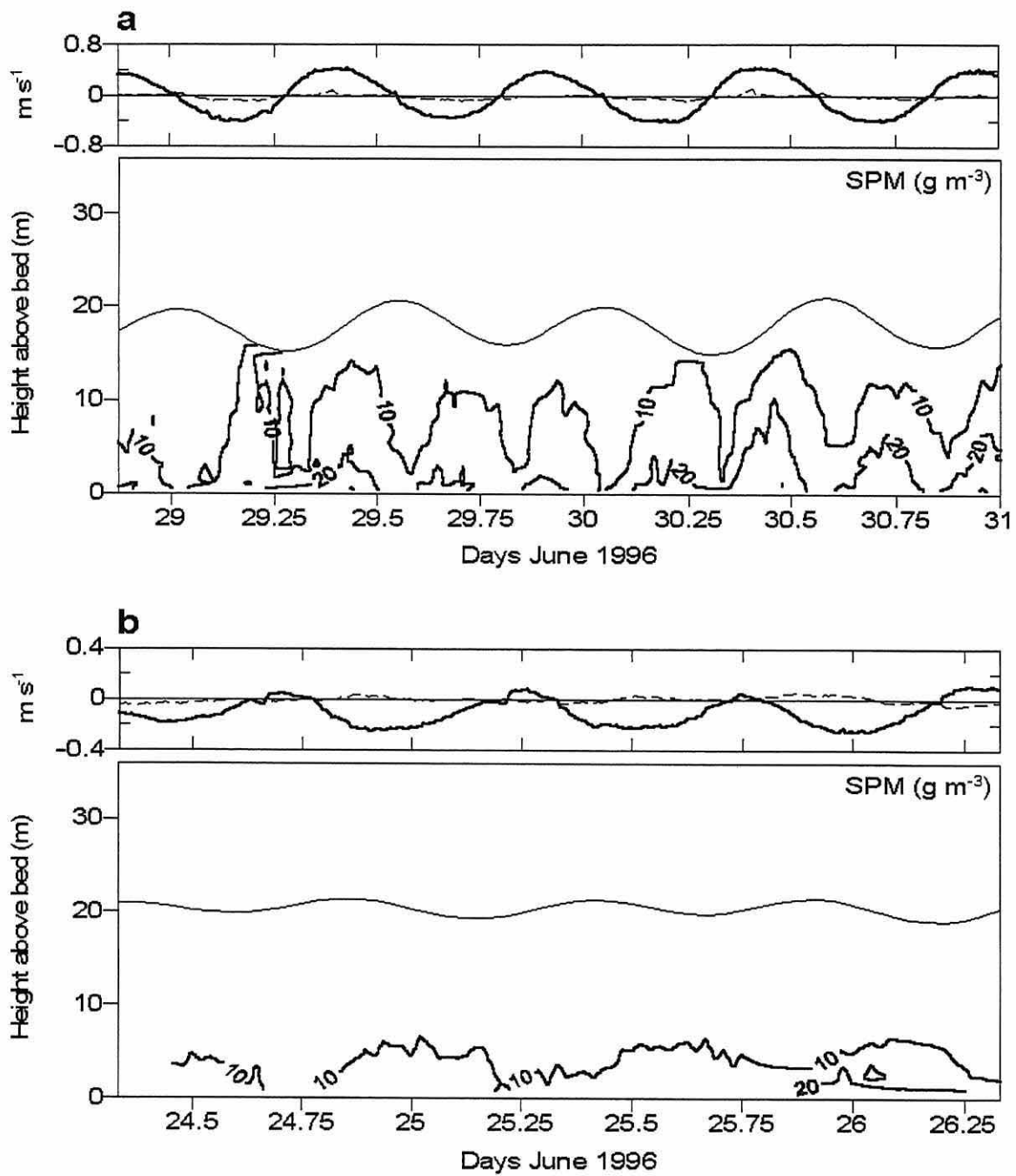


Figure 4.13. Time series of SPM concentration and current velocity 1 m above sea bed observed at site J in June, 1996 under: a) spring tides and b) neap tides. The solid line is along-gulf velocity (positive for flood) and the dashed line is across-gulf velocity.

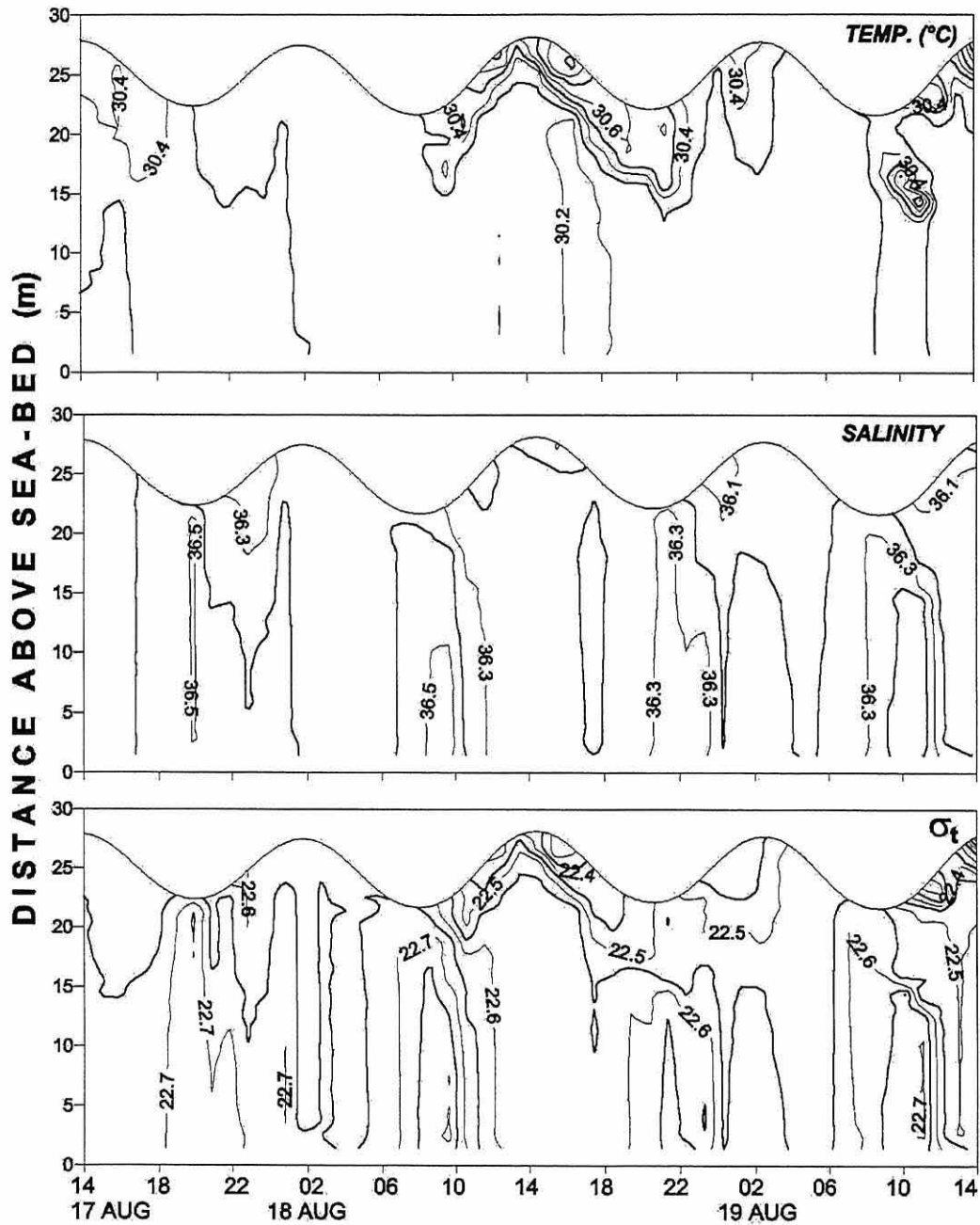


Figure 4.14. Spring-tide time series of temperature, salinity and density (σ_t) observed at site W3 in August, 1997 when vertically mixed conditions prevailed over most of the water column.

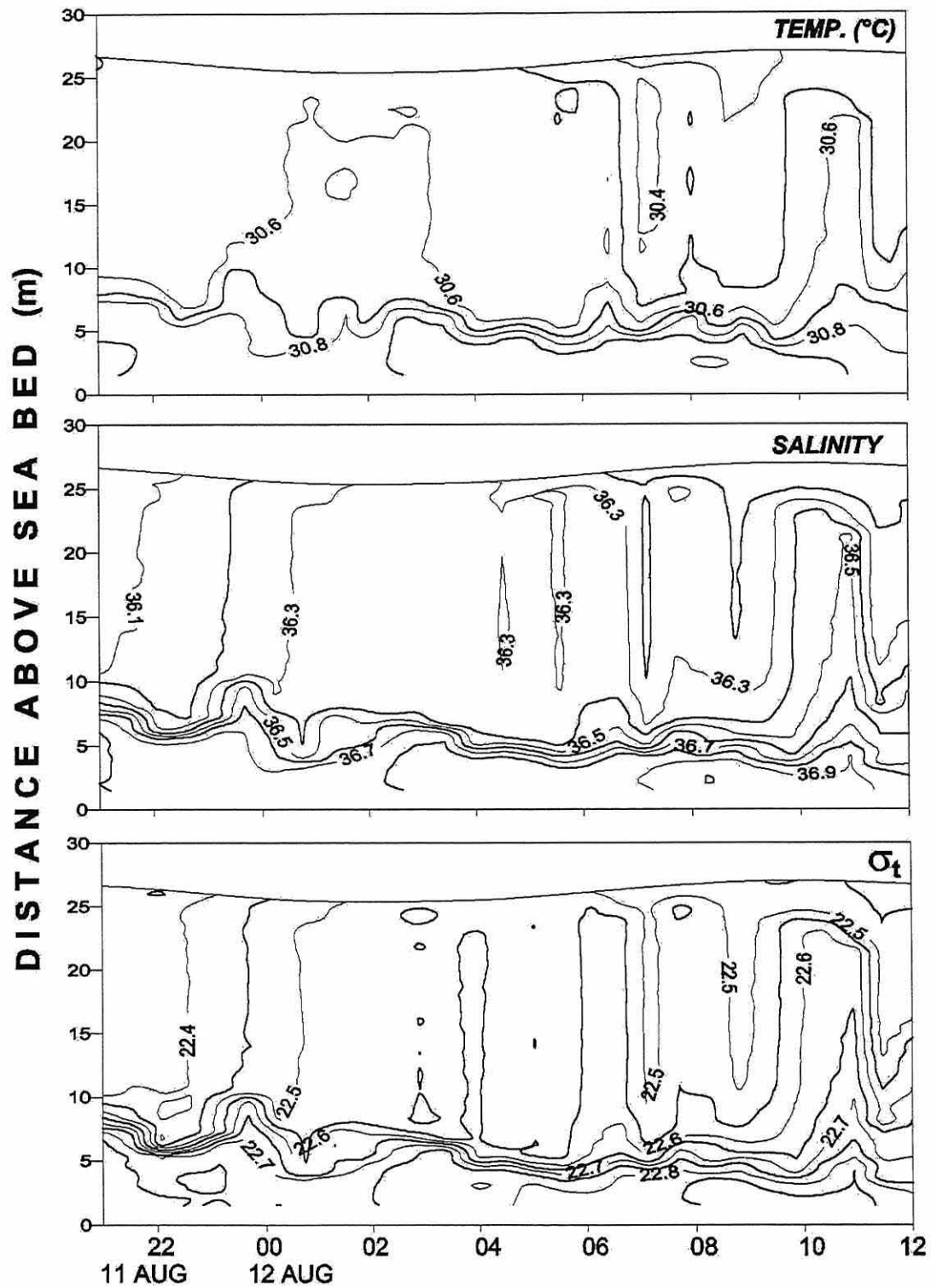


Figure 4.15. Neap-tide time series of temperature, salinity and density (σ_t) observed at site W3 in August, 1997 when vertical stratification developed.

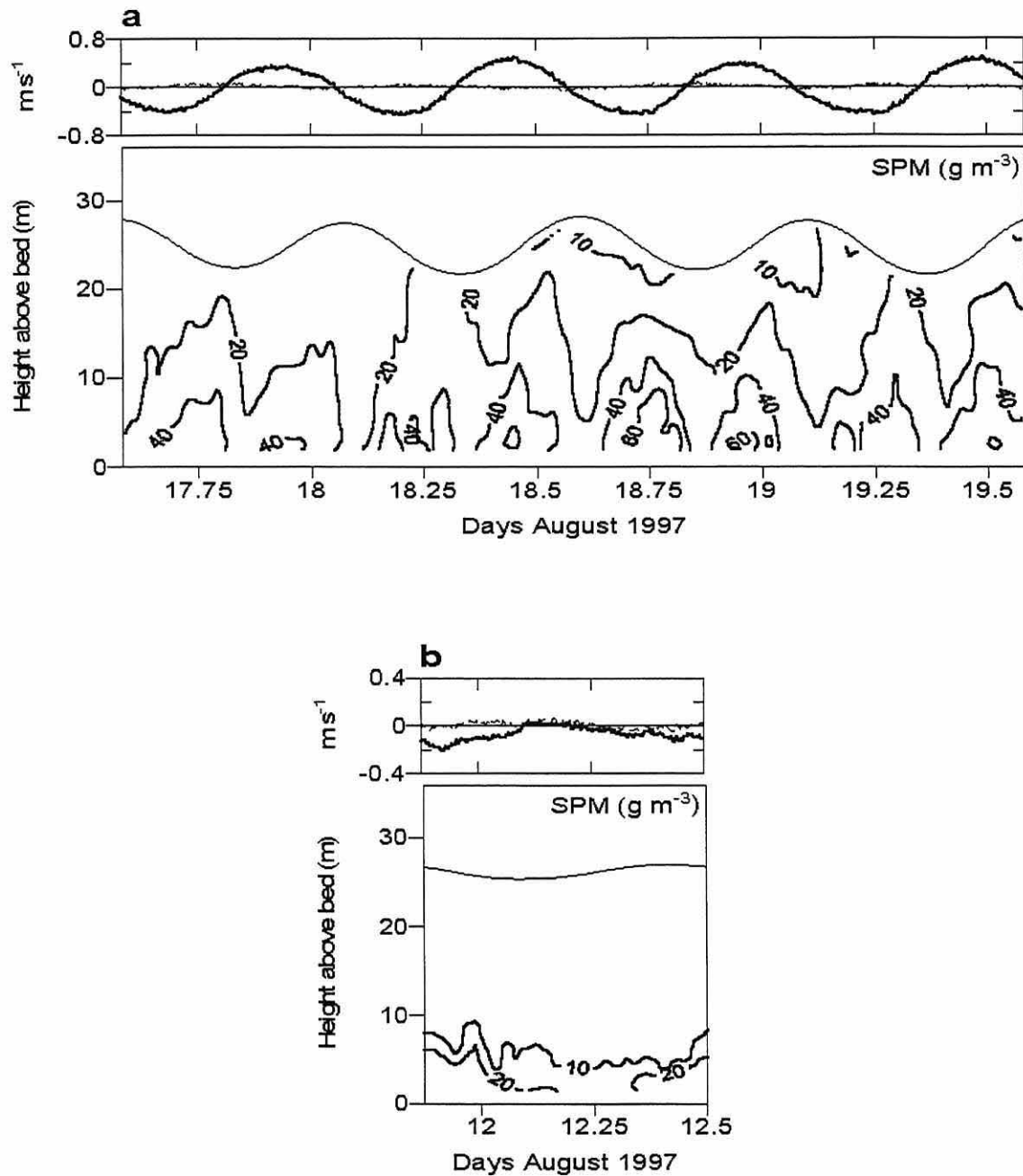


Figure 4.16. Time series of SPM concentration and current velocity 1.2 m above sea bed observed at site w3 in August, 1997 under: a) spring tides and b) neap tides. The solid line is along-gulf velocity (positive for flood) and the dashed line is across-gulf velocity.

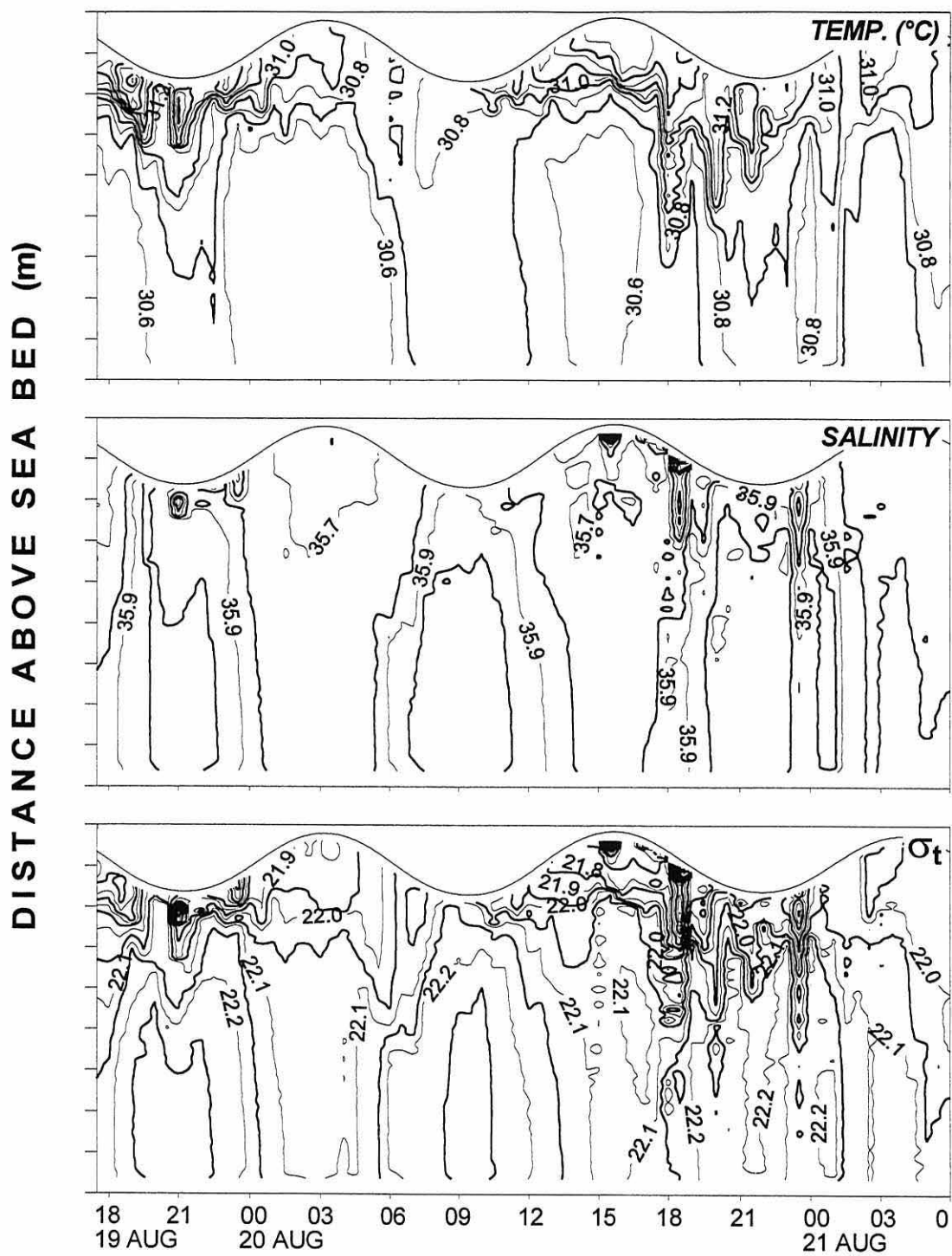


Figure 4.17. Spring-tide time series of temperature, salinity and density (σ_t) observed at site E1 in August 1997, when vertically mixed conditions prevailed over most of the water column.

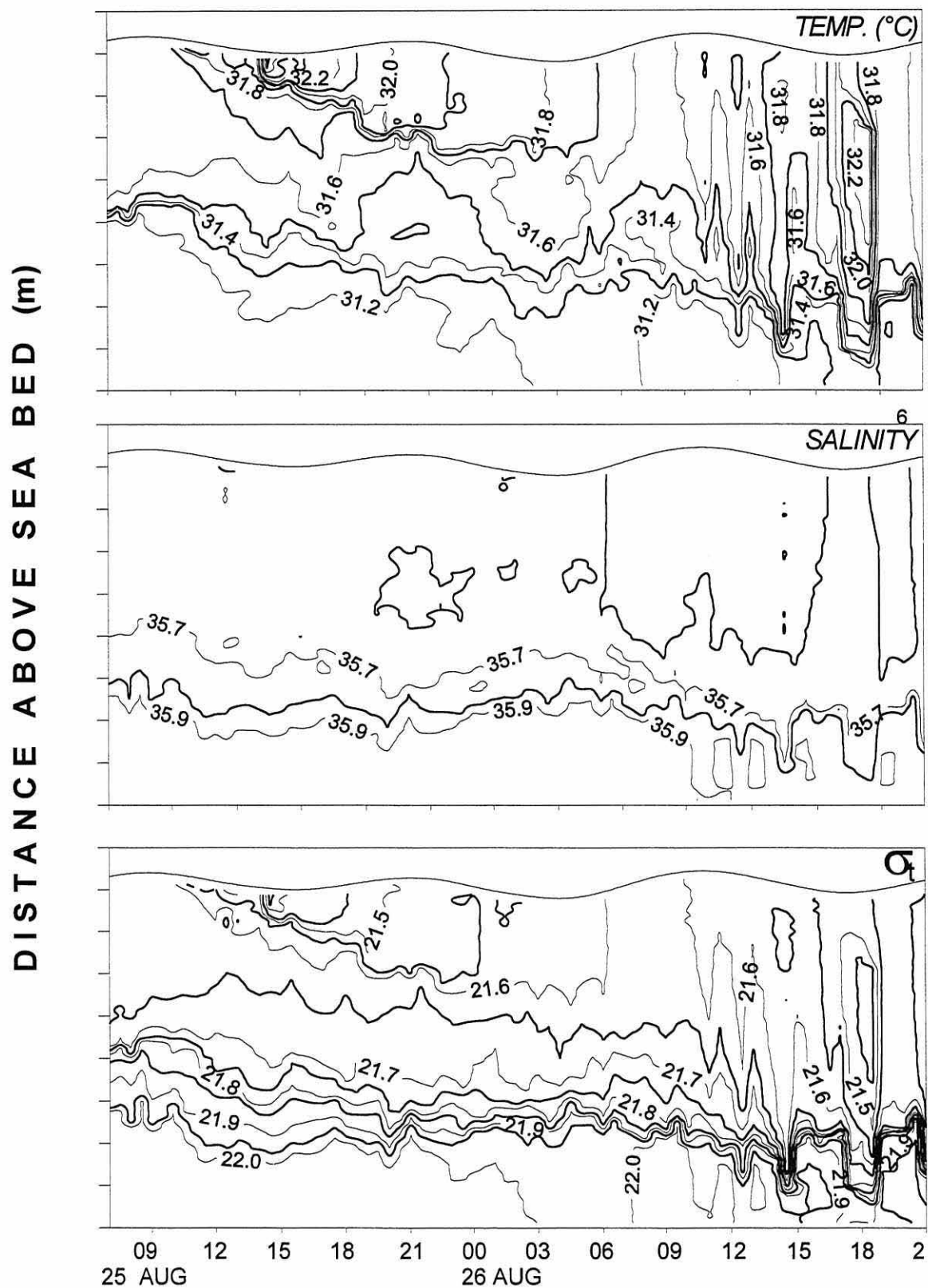


Figure 4.18. Neap-tide time series of temperature, salinity and density (σ_t) observed at site E1 in August, 1997 when vertical stratification developed.

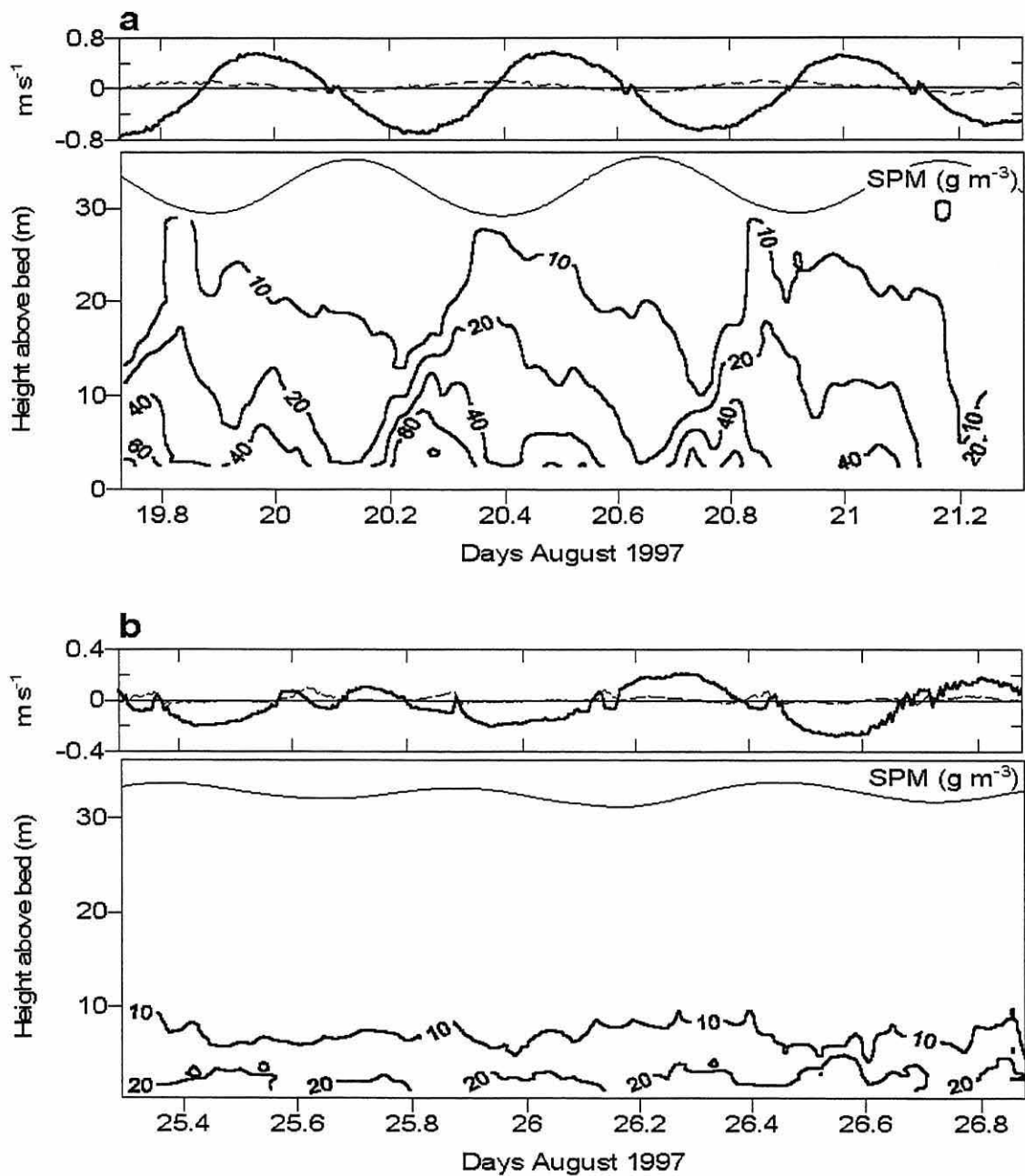


Figure 4.19. Time series of SPM concentration and current velocity 4.2 m above sea bed observed at site E1 in August 1997, under: a) spring tides and b) neap tides. The solid line is along-gulf velocity (positive for flood) and the dashed line is across-gulf velocity.

5. Velocity profiles and boundary layer parameters.

5.1. Introduction.

Bottom friction in oceanic water flows generates a turbulent boundary layer in which the time-mean horizontal velocity decreases gradually as the solid bed is approached. Tidal boundary layers in the ocean may extend several meters above the bottom or fill the entire water column in shallow waters. Within this layer, in a smooth turbulent flow a viscous sub-layer a few millimetres thick is in direct contact with the bottom. Above it a universal form of the velocity profile defines the logarithmic layer (or log layer) which extends to a height of a few meters. Further up an outer layer may extend some tens of meters and merge with the free-stream flow in which the flow is vertically uniform.

The well-known formulation of the log layer for steady, unstratified, rough turbulent flow is:

$$U(z) = (u_* / \kappa) \ln (z/z_0) \quad (5.1)$$

U is the time mean velocity, z is the height above the seabed, u_* is the friction velocity, κ is von Karman's constant (≈ 0.4), and z_0 is a bed roughness scale. In a rough turbulent flow the velocity distribution does not depend on the fluid viscosity ν . This regime exists when the size of the bed roughness is large compared with the thickness of the viscous sub-layer. This condition implies that the bed boundary Reynolds number $u_* D/\nu$ is larger than about 70 (Yalin, 1977; Dyer, 1986). D is the size of the bed roughness element and ν is the kinematic viscosity. For a small friction velocity of 10^{-2} m s^{-1} , a bed element size of 10^{-2} m and $\nu = 10^{-6} \text{ m}^2 \text{ s}^{-1}$, the Reynolds number is 10^2 . This implies that in the Upper Gulf of California a rough turbulent regime is likely to occur over most of the tidal cycle. However, if the bed elements are silt grains ($D = 0.5 \times 10^{-4}$

m) the Reynolds number is 0.5, i.e. a smooth turbulent flow condition cannot be excluded.

In the analysis of velocity profiles based on (5.1) a two-parameter linear fit of $U(z)$ vs. $\ln(z)$ yields the slope (κ/u_*) and the intercept (z_0). This procedure (the “profile method”) has been widely used to obtain the drag coefficient C_D , the bed stress τ_0 , the bed roughness z_0 , and the eddy diffusivity K_z for a large class of oceanic, estuarine and river flows. However, since deviations from this profile have been observed when the assumptions about the flow are violated, careful evaluation of stratification conditions, sea bed topography and flow uniformity must be made before the model can be applied to quasi-stationary flows. Mean velocity has been defined as the average over typically 10 to 30 minutes for tidal flows. This averaging avoids non-stationarity problems associated with tidal forcing, provided that energetic motions with period similar to the averaging interval are absent (Gross and Nowell, 1983; Soulsby, 1983; Trowbridge *et al.*, 1998).

Limited knowledge of the hydrodynamics of the benthic boundary layer has been a major deficiency in the study of bottom mixing and sediment transport generated near the bed. The recent development of acoustic Doppler current profilers (ADCP, ADP) have improved our understanding of the bottom boundary layer in the shallow coastal ocean by allowing long term observations of the vertical structure of current velocity. Applications and advantages of the acoustic profiling method have been described in, for instance, Lueck and Lu (1997), Cheng *et al.* (1998), Cheng *et al.* (1999).

Bottom-mounted current profilers have allowed better evaluation of the fundamental hydrodynamic parameters near the bed, the relevant region for sediment transport calculations. The bed shear stress (or friction velocity), which is induced by the large velocity gradient near the boundary, is the main control on erosion, resuspension and settling of the fine sea bed material. Bottom features like sediment distribution, bed forms and bed roughness depend on the distribution of the bed stress. However, since the profile method relies upon single location current observations, the boundary layer parameters so derived are site specific. In this section, acoustically measured velocity

profiles and simultaneous current meter observations are described. The profile method was used first to investigate the existence of a logarithmic layer at a shallow site in the Upper Gulf of California. Where this was found to be present the analysis was extended to obtain the hydrodynamic parameters of the tidal benthic boundary layer. These calculations used velocity data from ADP measurements made at site W3 (Fig 3.1). As described in Chapter 3, this site is located inside a ~12-km wide along-gulf channel, in 25 m water depth, on the western side of the Upper Gulf of California.

5.2. Analysis of velocity profiles.

The ADP velocity records were validated by comparing data from the first bin with velocity measurements at the same level (1.2 m above the sea bed) made with the Aanderaa 651. This current meter was moored 3.9 km northwest of the ADP, within the same along-gulf channel. The correlation between the two series was 0.98 for the u (at 0 time lag) and v (at one step time lag) components. The one-step (5 min.) delay of the current meter v with respect to that of the ADP reflects progress of the tide toward the northwest. Figure 5.1 shows the comparison between the velocity measured at both sites. The velocity measured by the current meter was ~5% higher than that recorded by the ADP at the same level. This difference is consistent with the difference in water depth between the two sites. Thus it can be assumed that the ADP measurements are valid, based on the good correlation between the two series.

The ADP recorded velocity profiles every 5 minutes, at 0.5 m depth intervals, from 1.2 m (centre of depth cell) to 16.2 m above the sea bed. The North (v) and East (u) velocity components at each level were projected along the principal axes: the axis of maximum variance and its perpendicular. A new U -component was defined as positive along the main flow direction, towards 323° . This direction varied only 2° from 1.2 to 16.2 m in the vertical, was parallel with the channel and local depth contours, and represents the along-gulf axis.

Consecutive sets of six profiles were time-averaged and the standard deviation computed for each bin. For an average of more than six profiles the standard deviation

increased markedly, perhaps due to tidal phase effects. A least-squares logarithmic fit was applied to the new series of velocity profiles at 30-minute intervals. Following Lueck and Lu (1997), the orthogonal form of (5.1) is:

$$U_i = \frac{u_*}{\kappa} [(\ln z_i - \overline{\ln z_i}) + (\overline{\ln z_i} - \ln z_0)] \quad (5.2)$$

The fitted model is of the form $Y = \theta_1 + \theta_2 X$:

$$U_i = \frac{u_*}{\kappa} (\overline{\ln z_i} - \ln z_0) + \frac{u_*}{\kappa} (\ln z_i - \overline{\ln z_i}),$$

in which

$$\theta_1 = \frac{u_*}{\kappa} (\overline{\ln z_i} - \ln z_0), \quad \theta_2 = \frac{u_*}{\kappa}$$

Here U_i is the along-gulf velocity component, i indicates the velocity bin included in the least square fit, and the over-bar indicates an average over the i bins involved in the fitting. This expression is equivalent to equation 5.1 but yields independent confidence intervals for the regression parameters (Lueck and Lu, 1997). Confidence intervals for u_* and z_0 are given in terms of the correlation coefficient R as follows:

$$\frac{\delta u_*}{u_*} = \pm \left[\frac{2}{N-2} f_{2,N-2}(1-\alpha) \right]^{1/2} \left(\frac{1}{R^2} - 1 \right)^{1/2} \quad (5.3)$$

$$\frac{\delta z_0}{z_0} = \frac{\delta u_*}{u_*} \left[\frac{1}{N} \sum_1^N (\ln z_i - \overline{\ln z_i})^2 + \frac{\kappa \overline{U_i}}{u_*} \right]$$

where $f_{2,N-2}$ is the F distribution with 2 and N-2 degrees of freedom, N is the number of velocity bins in the regression and α is the level of significance.

An iterative least-squares regression analysis was started by taking the first three velocity bins closest to the sea bed. The number of velocity bins was incremented upwards, one at a time, while the regression residuals remained less than or equal to 0.012 m s^{-1} . If this condition was violated, then the previous velocity bin was chosen as the upper limit of the logarithmic profile fit. The limiting value of the regression residuals corresponds to the average standard deviation of the 30-minute average velocity in the first bin (1.2 m above the sea bed). It was also the minimum in the observed water column. At 15 m from the bottom the standard deviation increased to 0.03 m s^{-1} on average, due presumably to larger eddy sizes away from the solid boundary. By taking the minimum standard deviation, more weight was given to the near-bottom velocity values while the regression residuals were kept low.

One condition for determining whether or not a log-profile exists relies upon the value of R, the correlation coefficient of the least squares fit. As the number of levels increases a lower value of R can be accepted. Based on velocity measurements at 3 levels Lesht (1979) adopted $R \geq 0.95$. A lower value ($R=0.894$) was accepted by Cheng *et al.* (1998) in the analysis of ADCP data using 30 levels. For the present work, the higher value was adopted. Thus, the logarithmic profile was assumed to exist if two conditions were fulfilled: the regression residuals were smaller than 0.012 m s^{-1} , and the correlation $R \geq 0.95$. These two conditions may not be sufficient for a log profile to exist in very shallow tidal flows over intertidal flats. In this case additional requirements should be met, as suggested by Collins *et al.* (1998) who proposed an internal consistency analysis.

The friction velocity u_* was obtained directly from the intercept and the slope of the fitted lines, and the roughness parameter $z_0 = \exp(\overline{\ln z_i} - \theta_1 / \theta_2)$. The bed stress parallel to the along-gulf principal axis was calculated as $\tau_0 = \rho u_*^2$, with τ_0 given the sign of the friction velocity. The bottom drag coefficient C_D was derived by linear regression from

$u_*^2 = C_{Dh} U_h^2$, where U_h is the along-gulf velocity at the reference level h above the sea bed. To account for changes in C_{Dh} due to changes in distance from the bed, the selected levels above sea bed were set at 1.2 m for the near-bed velocity, 4.2 m, and 12.2 m for the mid-depth velocity.

Setting the velocity average at the mid-point of the 0.5m bin introduces an error due to the logarithmic profile, as suggested by Murray (1992). It has been estimated that the error in velocity is only 1%, and the effect on the bed roughness scale z_0 is an increase of ~15% (A. Davies, pers. comm.). In the present study this deviation was assumed to be within the uncertainty of z_0 due to the least squares fit. Errors due to tilting or settling of the ADP bed mounting plate were not considered, since the ADP tilt (pitch and roll) and heading angles remained constant, within the error of the sensors. It was assumed that the 0.81 m² plate was stable through the measurement period, and that no vertical settling or instrument burial had occurred.

5.3. Results.

The observed currents in the Upper Gulf were mainly tidal and nearly unidirectional throughout the measured water column as shown by the velocity scatter and progressive vector plots at 5 and 15 m above the bed (Figure 5.2). The log layer thickness varied from 4.2 to 15 meters (8 to 30 bins), as defined by 526 profiles having log fits with $R \geq 0.95$. These profiles represent 70% of the 15-day series. As shown in Figure 5.3a, the variation of log profile heights over the fortnightly cycle reveals that the log layer was thinner during neap tides, at the beginning and at the end of the series. The thickness increased by a factor of ~2 during most of the remaining series, around spring tides. Figure 5.3b shows that values of the correlation R are generally larger around spring tides, and lower and more variable during neap tides. The logarithmic layer height was very thin or absent at near zero velocity during both spring and neap tides. A poor logarithmic structure was revealed by the correlation R decreasing to less than 0.95 and near zero at times around slack water. Figure 5.4 shows along-gulf velocity profiles

during selected semidiurnal cycles on spring and neap tides. The profiles show that the reversing tidal current nearly vanished close to the bed during neap tides, a feature observed at the beginning and again at the end of the fortnight cycle. The outcome was net outflow from the Upper Gulf (negative velocity) within a layer 7 to 8 m thick, next to the sea bed. The net outflow is also shown in the progressive vector diagrams of the current at 5.2 m above the bed (Figure 5.2). This contrasting flow condition is ascribed to a gravity current flow with the core centered 4-5 m above the bottom. The speed at the core varied between near zero and -0.3 m s^{-1} over 4-6 semidiurnal cycles. Valid log profile fits were obtained below the core of the gravity current. The time series of z_0 , u^* and τ_0 are shown in Figures 5.5, 5.6 and 5.7 in which the parameters are plotted as the 95% confidence interval. The gaps in the series correspond to times when the parameters were not computed due to log fits yielding $R < 0.95$ during low velocity.

5.3.1. Bed roughness length scale z_0

The sea bed roughness parameter z_0 was smaller than 0.05 m over most of the 15.7 days (Figure 5.5). However, the mean z_0 was 0.22 m (std. dev.=0.82 m) due to 4% of the values being higher than 1 m. If these are removed the mean z_0 is 0.09 m (std. dev.=0.12 m). The spring tide mean z_0 is 0.06 m (std. dev.=0.11) and the neap tide mean is 0.16 (std. dev.=0.14). The modal value (0.02 to 0.03 m) is a better statistic due to the marked asymmetry in the distribution, as shown in Figure 5.8. Figure 5.5 shows that the largest values of z_0 with broader confidence intervals were obtained under neap tide conditions. A sharp periodic peak to values near 1 m appeared around slack water time, especially during spring tides.

5.3.2. Friction velocity u^* and bed stress τ_0 .

The friction velocity u^* displayed a semidiurnal oscillation during spring tides with maximum values of $\pm 0.05 \text{ m s}^{-1}$. The corresponding maximum bed stress τ_0 was near $\pm 2.5 \text{ Pa}$. Neap tide maximum u^* and τ_0 were smaller by a factor of 2–3. Neap tide bed stress was in general less than $\pm 1.0 \text{ Pa}$ and mostly negative. The bed stress oscillation

was diurnal during neaps, in contrast with the semidiurnal frequency that dominated over most of the fortnightly cycle. The 14.7-day mean yielded a residual along-channel bed stress of -0.14 Pa toward the southeast, i.e. outward from the Upper Gulf.

5.3.3. Bottom drag coefficient C_D .

The bottom drag C_D was first obtained from $u_*^2 = C_{D1.2} U_{1.2}^2$ where $U_{1.2}$ is the along-gulf velocity from the first bin, 1.2 m above the sea bed. Different C_D values were obtained depending on how u_*^2 and U^2 were specified in the linear regression: a) as the full data set, b) separate ebb and flood tide data, and c) separate spring and neap tides data.

By taking the full data set the bottom drag coefficient and its 95% confidence interval were $(13.6 \pm 0.5) \times 10^{-3}$ when computed as the slope of $u_* \mid u_* \mid = C_{D1.2} U_{1.2} \mid U_{1.2} \mid$, i.e. keeping the sign of u_* and U (Figure 5.9). Regression of separate ebb and flood data yielded $C_{D1.2}$ as $(10.3 \pm 0.7) \times 10^{-3}$ and $(9.9 \pm 1.0) \times 10^{-3}$ respectively (Figure 5.10). Data around spring tides (7.3 days) yielded $C_{D1.2} = (13.2 \pm 0.5) \times 10^{-3}$, while data around neap tides (7.3 days) yielded a higher drag coefficient $C_{D1.2} = (21.3 \pm 3.6) \times 10^{-3}$, as shown in Figures 5.11 and 5.12. These three methods yielded a non-zero ordinate intercept, the last method producing the smallest intercept. By fitting $u_*^2 = C_{D1.2} U_{1.2}^2$ to the whole data set, regardless of sign, the slope was $(11.4 \pm 0.4) \times 10^{-3}$ but a y-intercept of 2.2×10^{-3} still remained. As the height of the reference velocity was increased C_D decreased to $(6.2 \pm 0.3) \times 10^{-3}$ for U_h at 4.2 m and to $(4.3 \pm 0.2) \times 10^{-3}$ for U_h at mid-water, 12.2 m above the sea bed. Since the profiles did not extend over the whole water column, the vertically averaged reference velocity was not available. These results are summarized in Table 5.1.

Table 5.1. Drag coefficient C_D with the 95% confidence interval obtained by least-squares fit.

Data used in the regression	Reference velocity level above sea bed	$C_D \pm 95\% \text{ c.i.} \times 10^3$	Intercept $\pm 95\% \text{ c. i.}$	Correlation R
All	1.2 m	13.6 \pm 0.5	2.2 \pm 0.3	0.87
Ebb	1.2 m	10.3 \pm 0.7	- 4.3 \pm 0.5	0.87
Flood	1.2 m	9.9 \pm 1.0	3.5 \pm 1.0	0.83
Springs 7.3 days	1.2 m	13.2 \pm 0.5	-1.1 \pm 1.1	0.96
Neaps 7.3 days	1.2 m	21.3 \pm 1.0	-0.23 \pm 0.7	0.76
All	4.2 m	6.2 \pm 0.3	3.6 \pm 0.4	0.78
All	12.2 m	4.3 \pm 0.2	2.0 \pm 0.2	0.92

5.4. Summary.

Currents were mainly tidal, along gulf, with velocity amplitudes $0.50\text{--}0.90 \text{ m}\cdot\text{s}^{-1}$ in spring tides and less than $0.30 \text{ m}\cdot\text{s}^{-1}$ in neaps. The principal axes were oriented 323.8° on the western side and 303.5° on the eastern side, parallel to the along-gulf channels and ridges. The change of current direction with depth was less than 3° over most of the water column.

An oscillatory logarithmic boundary layer was shown to develop under quasi-steady tidal flow in the lower half of the water column. This condition occurred mainly during the fast current stages of spring tides. The log layer did not develop near slack water times and it was thinner during neap tides, reaching less than 5 m from the bed.

The bed shear stress τ_0 derived from the log layer analysis displayed a semidiurnal variation oriented along gulf with amplitude reaching $\pm 2.5 \text{ Pa}$ in spring tides. The neap tide bed stress decreased by a factor 2–3, and displayed a semidiurnal variation.

The friction drag coefficient C_D based on the quadratic law and near bed reference velocity yielded large values $O(10^{-2})$. Consistent with the large drag coefficient the bed

roughness length z_0 was also large with mean 0.05 m during spring tides and increasing during neaps.

Gravity current events developed close to the bed during neap tides, flowing along gulf toward deeper waters. The core of this current had a velocity maximum at 4–5 m above the bed where it reached $0.30 \text{ m}\cdot\text{s}^{-1}$ during ebb flow, enhanced by the tidal current. The tidal boundary layer was disrupted during these events which persisted over ~ 3 days.

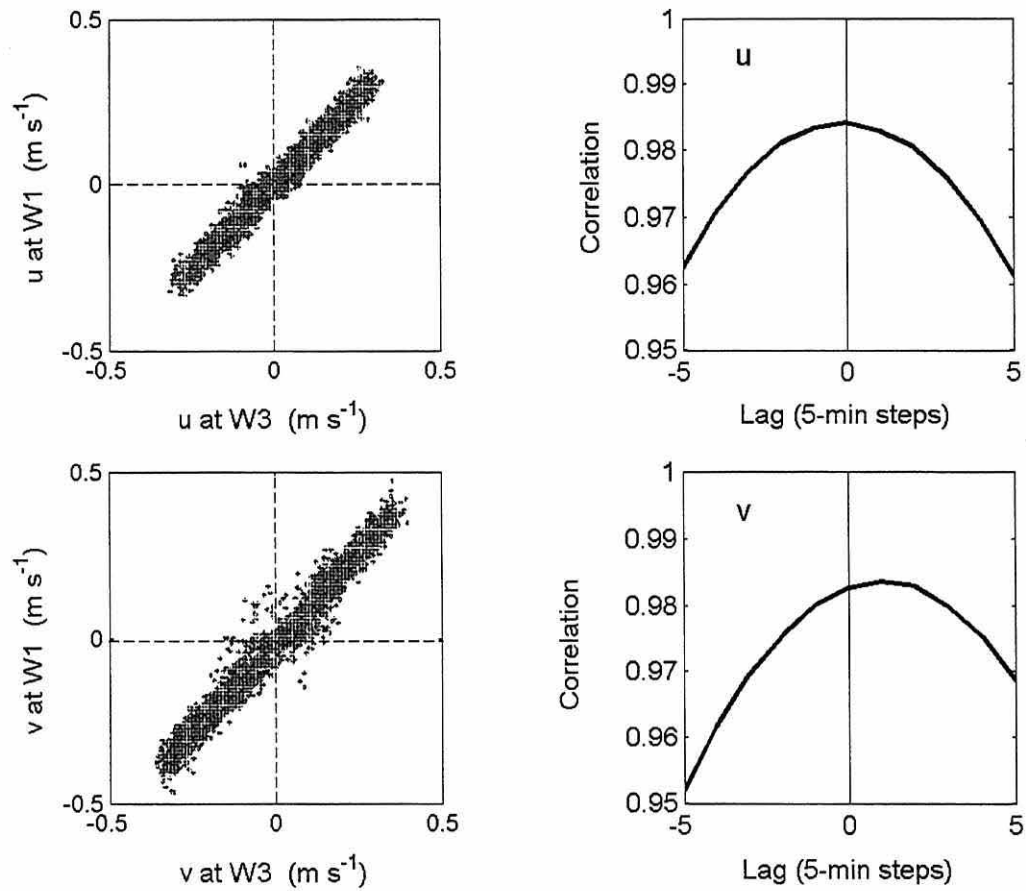


Figure 5.1. Comparison between velocity components 1.2 m above the bed from the current meter at site W1 and the ADP at site W3 (left frames). Cross-correlation of velocity components from both sites (right frames).

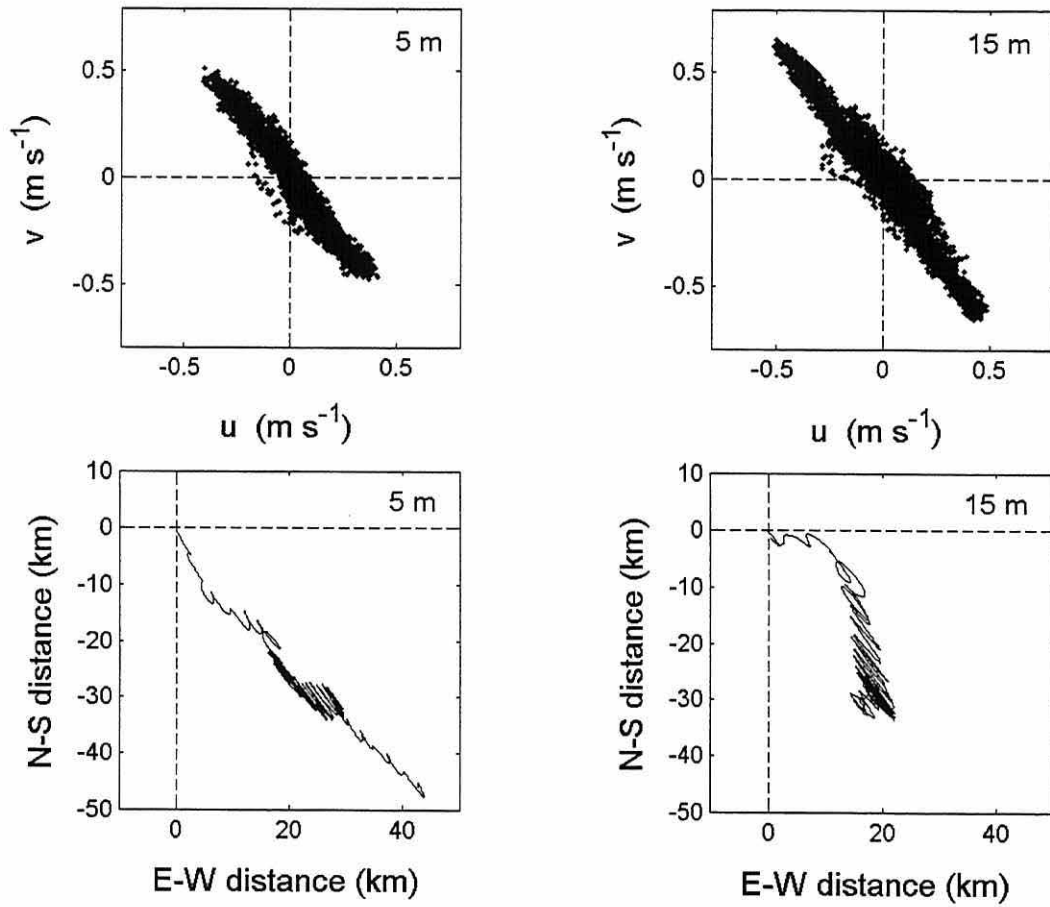


Figure 5.2. Velocity components u, v at site W3 at 5 m and 15 m above the sea bed (upper frames). Progressive vector plots at the same levels during the fortnightly cycle (lower frames). Neap tides are at the start and at the end of the distance plots.

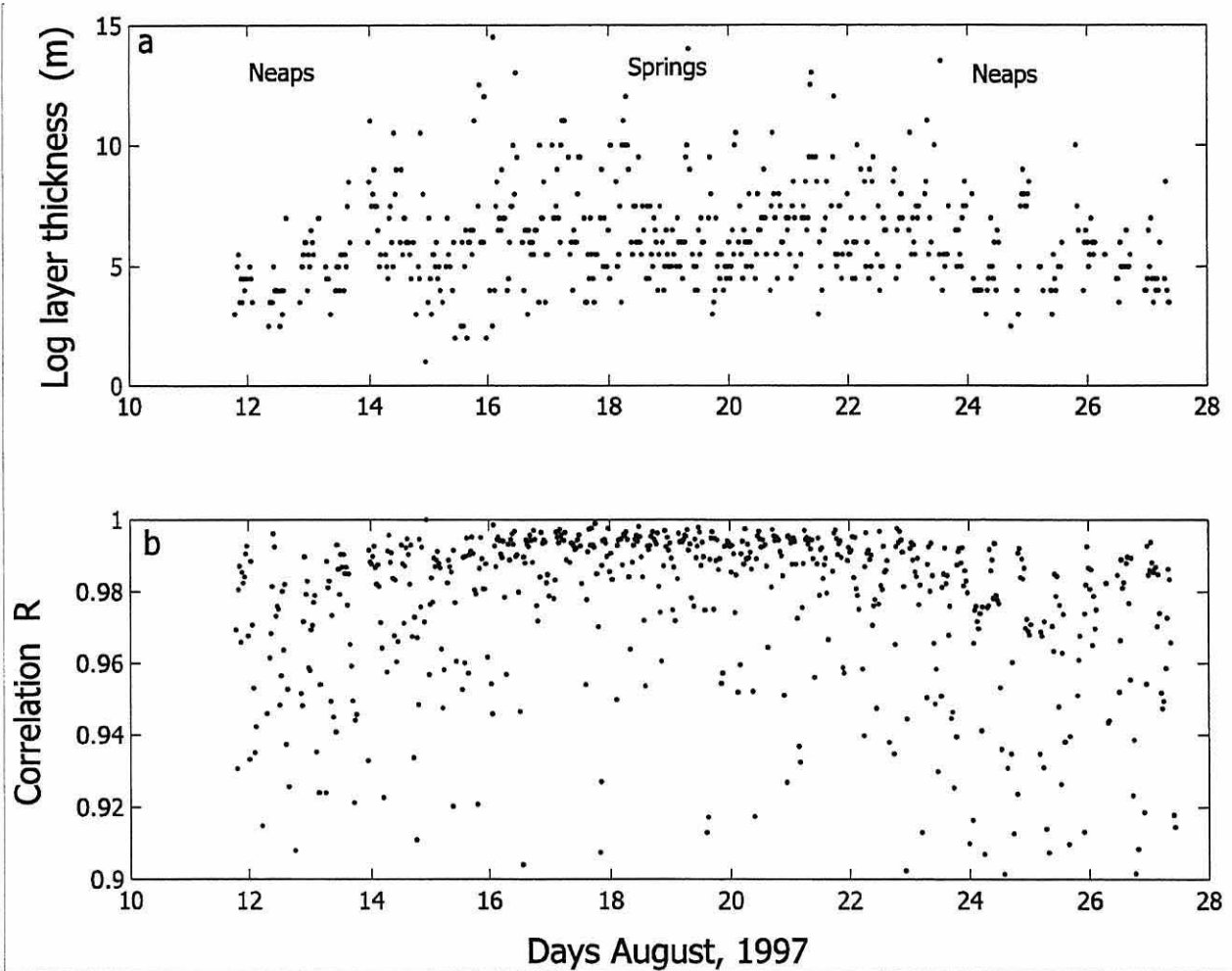


Figure 5.3. Logarithmic layer thickness above 1.2 m (a), and correlation coefficient R (b) of the log-layer fits during the fortnightly cycle. $R < 0.9$ is not shown.

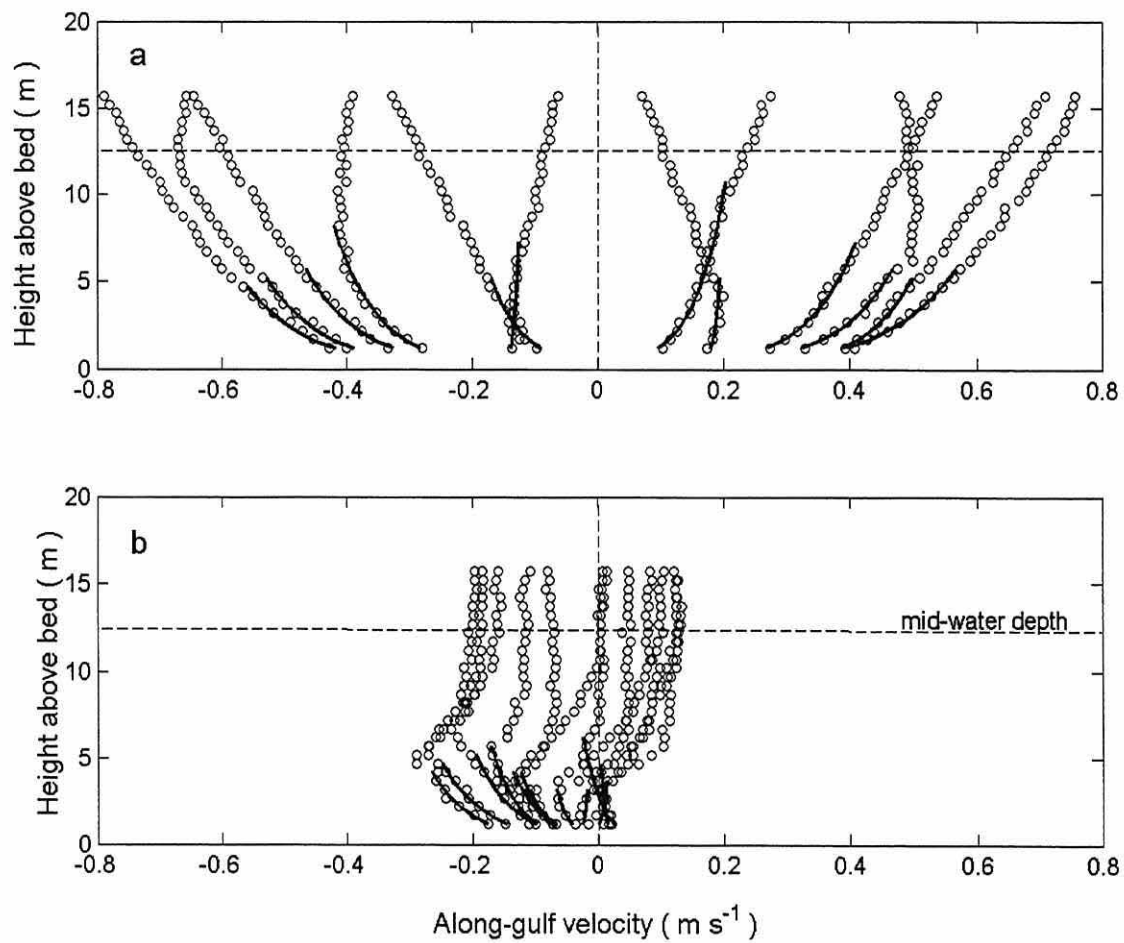


Figure 5.4. Selected along-gulf velocity profiles measured by the ADP at site W3 over one semidiurnal cycle (circles). The fitted log-layer profiles are indicated by the solid lines. (a) spring tides; (b) neap tides.

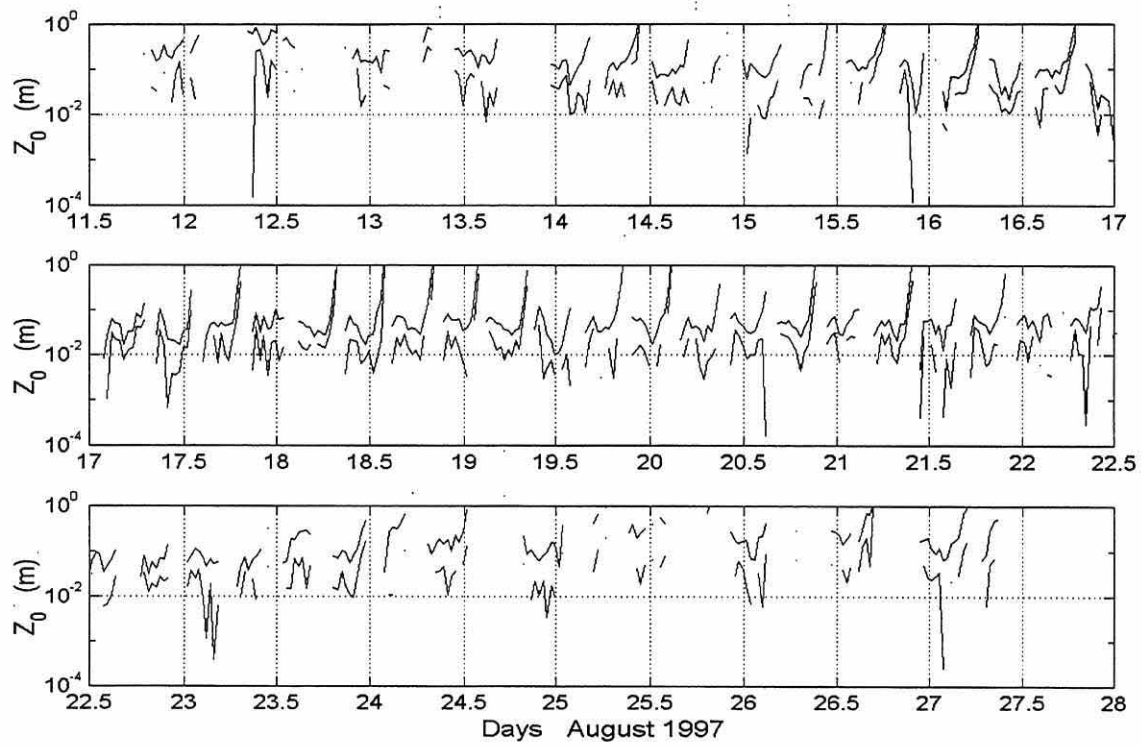


Figure 5.5. Bed roughness length z_0 obtained by log-layer analysis, plotted as the 95% confidence interval during the fortnightly cycle.

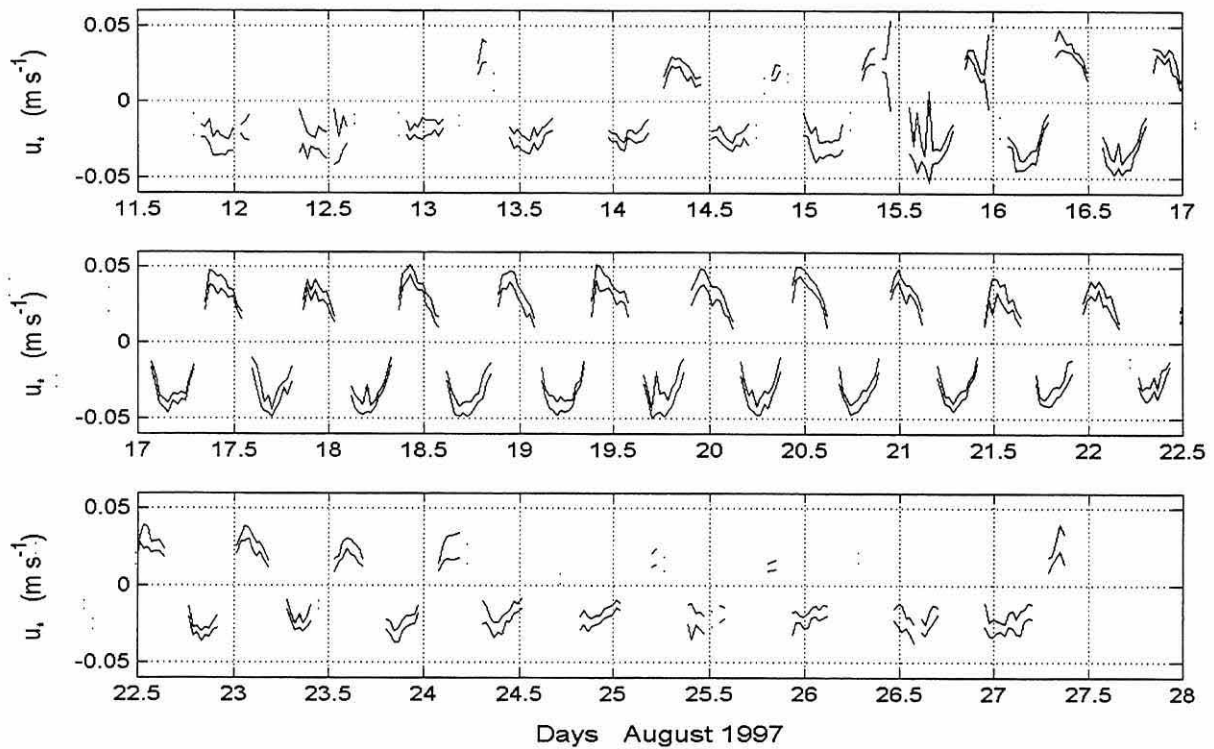


Figure 5.6. Friction velocity u_* obtained by log-layer analysis, plotted as the 95 % confidence interval during the fortnightly cycle.

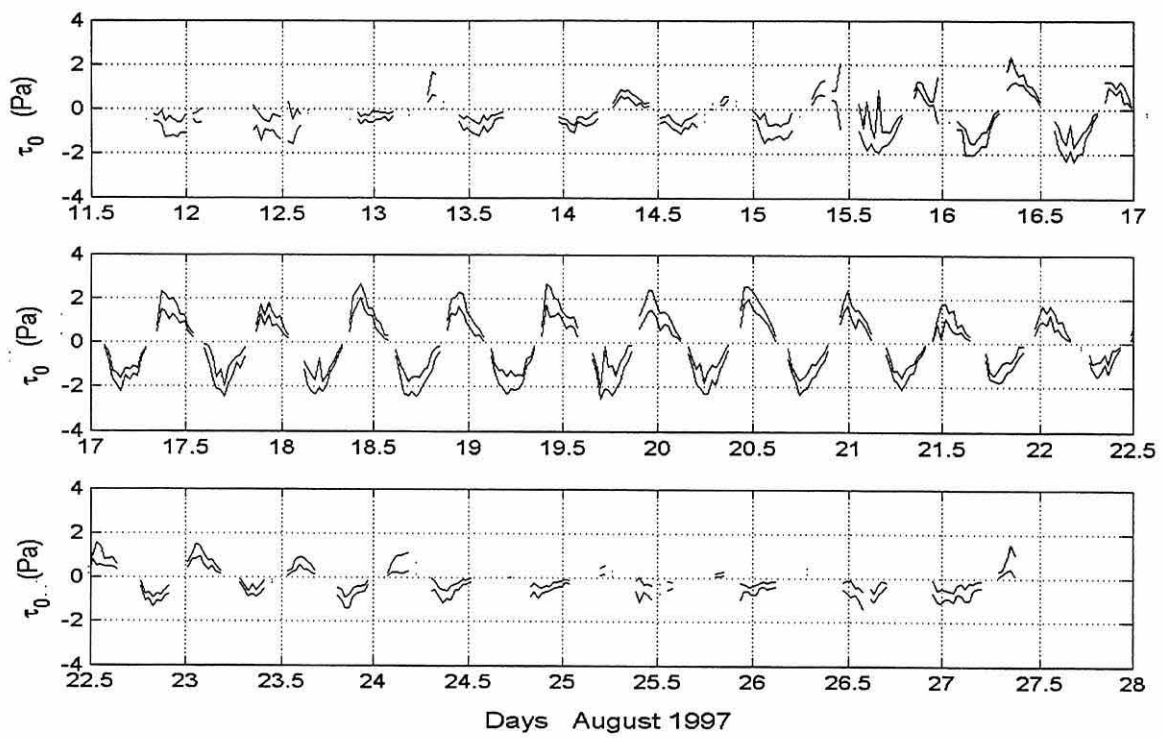


Figure 5.7. Bed shear stress τ_0 obtained by log-layer analysis, plotted as the 95% confidence interval during the fortnightly cycle.

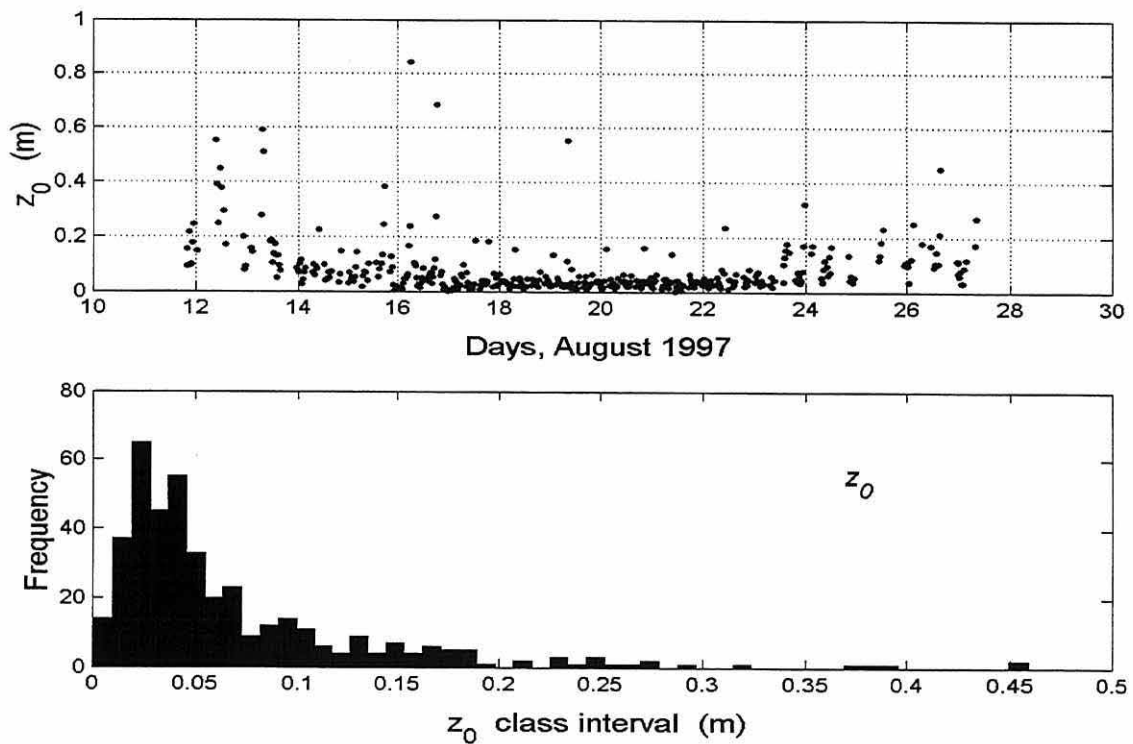


Figure 5.8. Distribution of the bed roughness z_0 during the fortnightly cycle (top) and histogram of z_0 (bottom). Values larger than 0.5 m were not plotted.

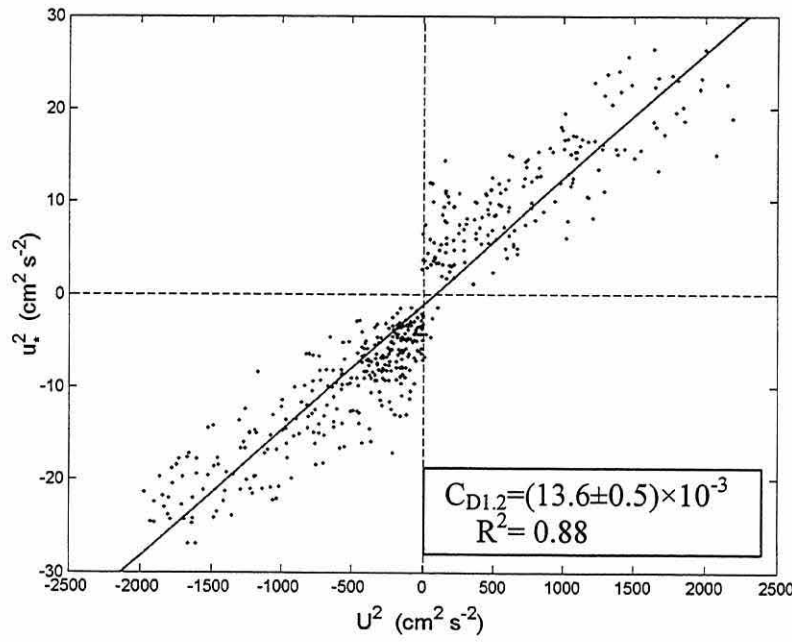


Figure 5.9. Drag coefficient C_D based on the reference velocity $U_{1.2}$ observed at site W3, at 1.2 m above the sea bed. The 95% confidence interval is indicated. The friction velocity u_* was obtained from the log-layer analysis.

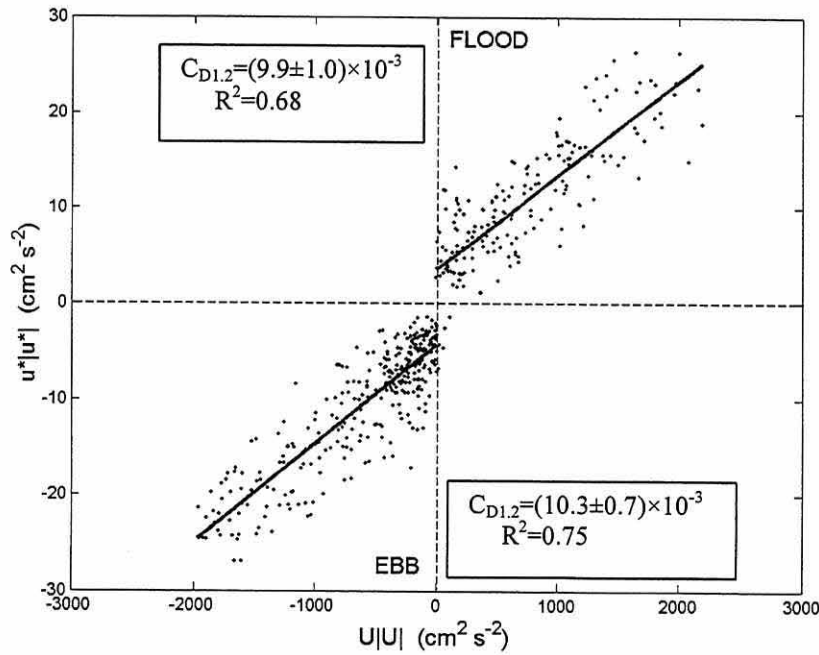


Figure 5.10. Drag coefficient C_D under ebb and flood based on the reference velocity $U_{1.2}$ observed at site W3, at 1.2 m above the sea bed. The 95% confidence interval is indicated. The friction velocity u_* was obtained from the log-layer analysis.

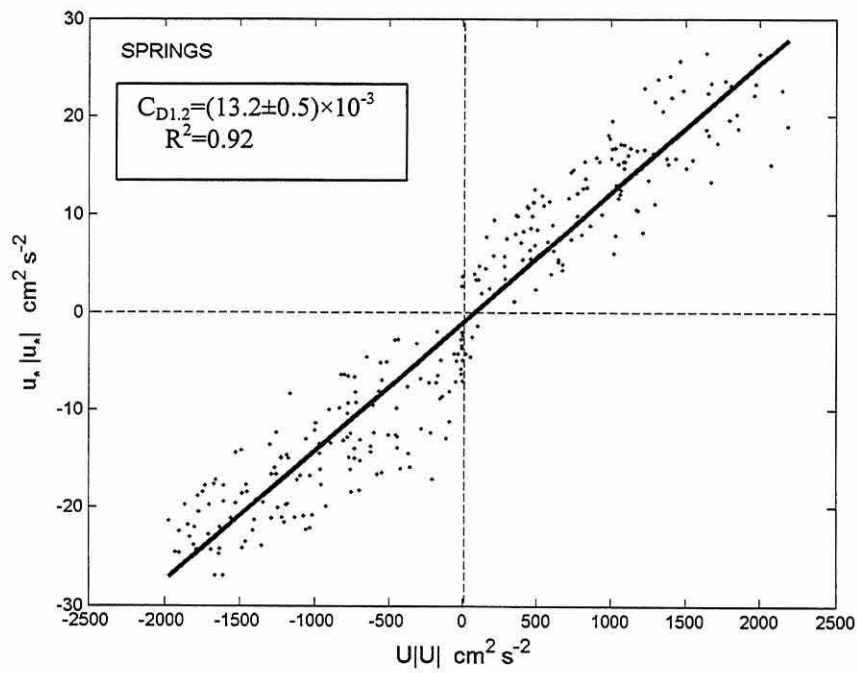


Figure 5.11. Drag coefficient C_D under spring tides based on the reference velocity $U_{1.2}$ observed at site W3 at 1.2 m above the sea bed. The 95% confidence interval is indicated. The friction velocity u_* was obtained from the log-layer analysis.

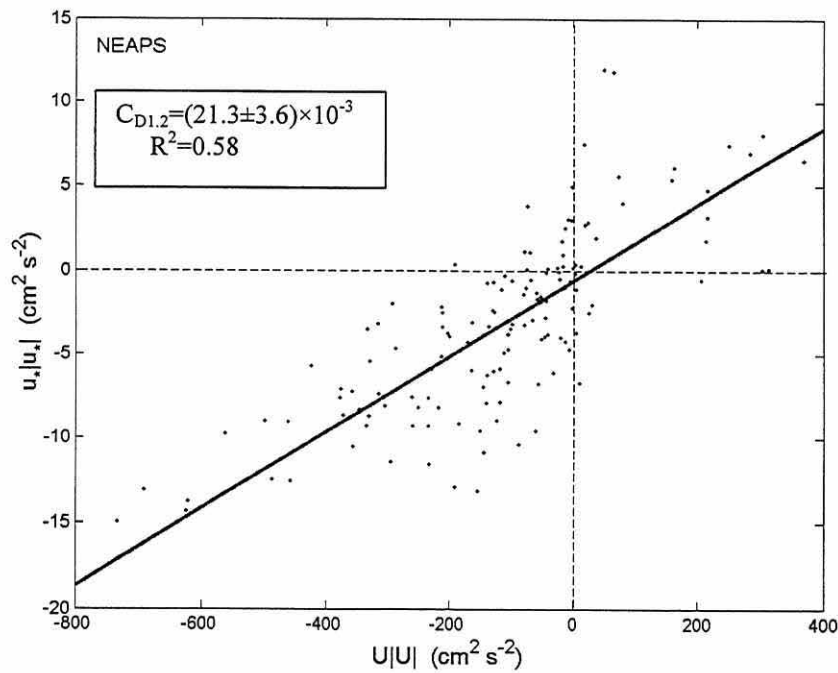


Figure 5.12. Drag coefficient C_D under neap tides based on the reference velocity $U_{1.2}$ observed at site W3 at 1.2 m above the sea bed. The 95% confidence interval is indicated. The friction velocity u_* was obtained from the log-layer analysis.

6. The sediment resuspension process.

6.1. Introduction.

Bed sediments are brought into suspension by the shear stress acting on the particles. Once lift forces overcome the immersed weight of sediment grains these leave the bed and diffuse up into the water column, under the effect of turbulent motions of the fluid. Once in suspension, particles are transported by currents which generate significant horizontal fluxes of sediment in the form of suspended load.

Before the 1960s researchers in general relied upon a critical velocity in formulating conditions for the initial motion of bed particles. Formulae for initial motion were developed using a near-bed velocity u_b or a depth-averaged velocity \bar{u} . However, according to Graf (1971), the near-bed velocity could not be properly defined. Furthermore, a proper relationship between depth-averaged and near-bottom velocity was not available. More recent developments in fluid mechanics suggested the friction velocity u_* as a better measure of the turbulent flow conditions. This quantity, as well as the bed shear stress $\tau_0 = \rho u_*^2$, were adopted in the Shields diagram for describing the erosion of non-cohesive particles over a flat bed.

Bed particles begin to move when τ_0 exceeds some critical value τ_{0e} . In the case of fine cohesive sediments, a relationship between the critical erosion shear stress and mud sediment properties has been difficult to establish. The threshold for sediment movement has been estimated by visual methods in the laboratory. New devices have made *in situ* threshold measurements possible, by observing natural sea bed deposits (Black and Paterson, 1997; Tolhurst *et al.*, 1999). Portable benthic flumes have been used for *in situ* observations of the erosion threshold and the erosion rate of cohesive bed deposits. The most common are straight flow-through devices, recirculating annular flumes (circular or race-way shaped), and alternative devices such as those using water jets fired vertically over the sediment bed (Amos *et al.*, 1992; Maa *et al.*, 1993; Widdows *et al.*, 1998; Ravens and Gschwend, 1999; Hawley, 1991; Tolhurst *et*

al., 2000; Aberle *et al.*, 2003). Deposition properties have also been studied in annular flumes by, for instance, Haralampides *et al.* (2003). Other methods rely upon field measurements of the increase in concentration of suspended sediment in the water caused by an increase in the current velocity (Dyer 1986). This procedure involves choosing the resuspension events by the worker, then introducing a subjective criterion, according to Tolhurst *et al.* (2000). Furthermore, resuspension episodes may be affected by other natural processes such as lateral advection, which may influence the data (Hawley, 1991). A procedure described by Clarke (1995) and Clarke and Elliott (1998) depends on the time change of the vertically averaged SPM content in the water column and the variation of the friction velocity during the acceleration period. The critical bed stress, erodibility constant and erosion rate can be derived by least squares analysis for different acceleration-erosion events. A key assumption of this method is that only erosion and deposition determine the total SPM content of the water column at a point, and that no horizontal transport processes are involved.

6.2. Erosion-deposition process.

As an initial step towards understanding how SPM concentration and current velocity are interrelated in the Upper Gulf of California, it can be assumed that the concentration depends only on erosion and deposition of bed sediments. This oversimplified model seemed feasible in the present case, since concentration and current velocity nearly co-varied over most of the fortnightly cycle. In resuspension dominated regimes the instantaneous SPM concentration can be specified by the vertical flux of particles due to the erosion rate E_r and the deposition rate D_p . The time change of sediment mass M per unit area, per unit time is:

$$dM/dt = E_r - D_p, \quad (6.1)$$

Lavelle, *et al.* (1984) and Teisson (1991) have expressed the erosion rate as:

$$E = \alpha \left(\frac{\tau_0}{\tau_{0e}} - 1 \right), \quad \text{for } \frac{\tau_0}{\tau_{0e}} > 1$$

(6.2)

$$E=0, \quad \text{for } \frac{\tau_0}{\tau_{0e}} < 1,$$

also known as the Ariathurai-Partheniades equation (McAnally and Mehta, 2001).

Here τ_0 is the bed stress, τ_{0e} is the critical bed stress for erosion, α is an erosion rate constant (mass per unit area per unit time) or erodibility, which is specific for a given mud type.

The deposition rate is:

$$D = w_s C_b \left(1 - \frac{\tau_0}{\tau_{0d}} \right), \quad \text{for } \frac{\tau_0}{\tau_{0d}} < 1$$

(6.3)

$$D=0, \quad \text{for } \frac{\tau_0}{\tau_{0e}} > 1$$

in which τ_{0d} is the critical shear stress for deposition, w_s is the settling velocity of a single particle, and C_b is the near-bed mass concentration of suspended particles.

Evaluation of the parameters required for this simple point model is described next.

The bed stress τ_0 was determined from the velocity profiles, as described in Chapter 5. However, the analysis of the sediment resuspension process was based on a synthetic bed stress series calculated at 5-minute intervals from the quadratic law:

$$\tau_0 = \rho C_{D1.2} U_{1.2} |U_{1.2}|$$

where $\rho = 1,022 \text{ kg m}^{-3}$ is the density of sea water for the Upper Gulf, $C_{D1.2} = 13.2 \times 10^{-3}$ is the drag coefficient obtained from the spring tides current speed $U_{1.2}$ measured 1.2 m above the sea bed, as described in Chapter 5. This procedure was adopted since:

- 1) the values of bed stress calculated by this method are in phase with the velocity measured closer to the sea-bed where resuspension takes place,
- 2) it allows the gaps around slack water in τ_0 fitted by the log profile method to be filled,
- 3) it avoids the uncertainty in stress values during neap tide.

6.3. Erosion parameters extraction method.

The erosion parameters τ_{0e} and α were obtained from two different sets of SPM data:

- 1) vertically integrated SPM concentration from the surface to 1–2 m above the sea bed;
 - 2) near-bed, single level measurements of SPM concentration.
- Calculations with the latter set were made because vertically integrated SPM concentration were available only during 1-4 semidiurnal cycles in neap and spring tides, while continuous measurements at 1 m above the bed spanned the full fortnightly cycle. The extraction method was that described by Clarke and Elliott (1998), henceforth referred to as the “least squares” method. In this procedure the critical stress for erosion τ_{0e} is defined as the bed stress at the time when M , the SPM content in the water begins to increase. In a plot of (dM/dt) vs. τ_0 , the critical stress for erosion is defined when dM/dt becomes positive. A least squares linear fit yields the τ_0 axis intercept ($=\tau_{0e}$), and the line slope m defines the erodibility $\alpha=m\tau_{0e}$. In addition, an alternate method (the “centroid method”) relied upon reading the critical bed shear stress directly from

the plots of dM/dt vs. τ_0 . The variation of dM/dt was approximated by a line joining the point $\tau_0 = \tau_{0e}$ with the centroid of the cluster of subsequent points (positive dM/dt) during the erosion stage. Then the erodibility α was obtained from the slope of this line. The least squares and centroid methods are graphically shown in Figures 6.1 and 6.2.

6.3.1. Erosion parameters from vertically integrated SPM concentration.

Simultaneous measurements of current velocity (and the computed bed stress) and SPM profiles extended over 1 to 4 semidiurnal cycles at site J in June 1996 and at sites W3 and E1 in August 1997. The vertically integrated SPM content M in the water column was computed as:

$$M(t) = \sum_1^{n(t)} C_i(t) \Delta z,$$

where $\Delta z = 0.5$ m and C_i is the concentration at each of the n depth cells, between ~ 2 m above the sea bed, and the water surface. The number of cells n varied with the tide.

In general, the time series of vertically integrated SPM lagged behind the current speed (or the bed shear stress) series. It was assumed that this lag resulted from an erosion threshold, i.e. a critical stress below which no scour of sea bed sediment takes place.

6.3.1.1. Critical bed stress for erosion τ_{0e} .

Least squares method.

The results based on vertically integrated SPM concentration from sites J, W3 and E1 are shown in Table 6.1. τ_{0e} was reasonably consistent during spring tides, with mean

0.30 Pa, 0.66 Pa and 0.62 Pa, respectively. Mean τ_{0e} values were estimated from fewer values during neap tides because low SPM concentration and noise in the series (a high frequency variation superimposed on the concentration time series) made estimation of the erosion threshold difficult. For this reason the critical bed stress for site E1 was estimated directly from the plots of dM/dt vs τ_0 as the point where dM/dt went positive and has been included in Table 6.1 for comparison.

At sites W3 and E1 the threshold values were scattered but notably smaller during neap tides than those obtained during spring tides. The neap tide mean was less than 0.1 Pa at sites W3 and E1. Notably larger, and similar to spring tide values, with mean 0.26 Pa were the values obtained at site J. The critical bed stress values for the three sites are plotted in Figures 6.4 and 6.5.

Table 6.1. Critical erosion bed stress τ_{0e} based on depth integrated SPM time series from sites J, W3 and E1 using the least squares method with 2 hours of data . n is the number of averaged values.

Tide conditions	Site J Jun. 1996			Site W3 Aug. 1997			Site E1 Aug. 1997		
	n	τ_{0e} (Pa)	s.d.	n	τ_{0e} (Pa)	s.d.	n	τ_{0e} (Pa)	s.d.
SPRINGS	3	0.30	0.08	7	0.66	0.24	5	0.62	0.37
NEAPS	3	0.26	0.01	1	0.06		2	0.03	0.02

Centroid method.

The critical bed stress for erosion obtained from the plots of dM/dt vs. τ_0 is given in Table 6.2. The values at sites J and W3 were slightly larger than those estimated by the least squares method and at site E1 the critical bed stress was slightly lower. Despite the spread of data around each mean, τ_{0e} was similar for the three sites under spring tide conditions. Neap tide values were one order of magnitude lower than spring tide values except that at site J which was 50% lower.

Table 6.2. Mean critical erosion bed stress τ_{0e} based on depth integrated SPM time series from sites J, W3 and E1 using the centroid method. τ_{0e} was read directly from the dM/dt vs τ_0 plot. n is the number of averaged values.

Tide condition	Site J Jun. 1996			Site W3 Aug. 1997			Site E1 Aug. 1997		
	n	τ_{0e} (Pa)	s.d.	n	τ_{0e} (Pa)	s.d.	n	τ_{0e} (Pa)	s.d.
SPRINGS	8	0.44	0.30	8	0.77	0.26	5	0.55	0.26
NEAPS	2	0.20	-	1	0.05		2	0.03	0.02

6.3.1.2. Erodibility α .

Least squares method.

The erodibility constant α [$\text{kg}\cdot\text{m}^{-2}\cdot\text{s}^{-1}$] was obtained as $\alpha = m\tau_{0e}$, where m is the slope of the regression line dM/dt vs. τ_0 . The values obtained from vertically integrated concentration are given in Table 6.3. During spring tides the mean erodibility at site J was $0.05 \times 10^{-4} \text{ kg}\cdot\text{m}^{-2}\cdot\text{s}^{-1}$. Larger values were obtained at W3 and E1 where the mean erodibility was $0.37 \times 10^{-4} \text{ kg}\cdot\text{m}^{-2}\cdot\text{s}^{-1}$ and $0.23 \times 10^{-4} \text{ kg}\cdot\text{m}^{-2}\cdot\text{s}^{-1}$, respectively. For neap tides the erodibility at sites J and W3 was derived from three and one regression values, yielding 0.11×10^{-4} and $0.15 \times 10^{-4} \text{ kg}\cdot\text{m}^{-2}\cdot\text{s}^{-1}$, respectively. Erodibility could not be calculated for site E1 during neap tides.

Table 6.3. Mean erodibility α based on vertically integrated SPM time series from sites J (June, 1996), W3 and E1 (August 1997) using the least squares method with 2 hours of data. n is the number of averaged values.

Tide conditions	Site J			Site W3			Site E1		
	n	<u>mean α</u>	<u>s.d.</u>	n	<u>mean α</u>	<u>s.d.</u>	n	<u>mean α</u>	<u>s.d.</u>
		($\text{kg}\cdot\text{m}^{-2}\cdot\text{s}^{-1} \times 10^4$)			($\text{kg}\cdot\text{m}^{-2}\cdot\text{s}^{-1} \times 10^4$)			($\text{kg}\cdot\text{m}^{-2}\cdot\text{s}^{-1} \times 10^4$)	
SPRINGS	3	.05	0.01	7	0.37	0.20	5	0.23	0.20
NEAPS	3	0.11	0.14	1	0.15	-		-	-

Centroid method.

Table 6.4 shows the erodibility constant obtained by the centroid method. Under spring tides the values for sites J and W3 were similar to the ones extracted by least squares. However, at E1 erodibility was nearly half that obtained by least squares. Neap tide values were lower than those under spring tides, except at site J, at which higher erodibility was obtained by both methods.

Table 6.4. Mean erodibility α based on vertically integrated SPM time series from sites J (June, 1996), W3 and E1 (August 1997) using the centroid method with 2 hours of data. n is the number of averaged values.

Tide conditions	Site J			Site W3			Site E1		
		<u>mean α</u>	<u>s.d.</u>		<u>mean α</u>	<u>s.d.</u>		<u>mean α</u>	<u>s.d.</u>
	n	(kg·m ⁻² ·s ⁻¹ ×10 ⁴)		n	(kg·m ⁻² ·s ⁻¹ ×10 ⁴)		n	(kg·m ⁻² ·s ⁻¹ ×10 ⁴)	
SPRINGS	8	0.06	0.05	8	0.27	0.14	5	0.10	0.08
NEAPS	2	0.2	0.14	1	0.14	-	2	0.01	-

6.3.2. Erosion parameters from single level SPM concentration.

Supplementary estimates of the critical bed stress for erosion were obtained from the single level SPM concentration series recorded at 1 m above the sea bed at sites W1 E1 and W3. The fortnightly time series yielded between 26 and 46 values of the erosion parameters. They were grouped around maximum springs and minimum neap tides and the mean values under both tide conditions were calculated. It was expected that the single level threshold estimates extracted from the full fortnightly cycle would compare with those derived from vertically integrated SPM and perhaps reveal a spring-neap variation. Extracting erosion parameters from single level measurements was performed by the centroid method only. It must be kept in mind that single level

concentrations were used here instead of the total SPM content in the water column as is required by the method by Clarke and Elliott (1998). This approach therefore assumes that the concentration at this level co-varies with the depth averaged concentration.

6.3.2.1. Critical bed stress for erosion.

The erosion threshold values obtained from the single-level measurements at sites W1, W3 and E1 are given in Table 6.5. The mean τ_{0e} was less than 0.1 Pa during neaps and increased to ~ 0.4 Pa during springs (Figures 6.4 and 6.5). The values at W3 and E1 were in general 0.2–0.3 Pa smaller than those based on vertically integrated SPM concentrations.

Table 6.5. Critical erosion bed stress τ_{0e} based on single level SPM time series from sites W1, W3 and E1 (August 1997) using the centroid method with 2 hours of data. n is the number of averaged values.

Tide conditions	Site W1			Site W3			Site E1		
	N	τ_{0e} (Pa)	s.d.	n	τ_{0e} (Pa)	s.d.	n	τ_{0e} (Pa)	s.d.
SP (cen 2h)	27	0.37	0.21	15	0.33	0.17	23	0.20	0.17
NP (cen 2h)	7	0.17	0.12	11	0.12	0.10	22	0.10	0.10

Despite the large spread of the threshold values, a significant increase from neap to spring tides is evident at sites W1 and W3 (Figure 6.4) and a less marked one can be inferred at site E1 (Figure 6.5). The trend also suggests a decrease towards the following neap tides. The critical stress for erosion was more consistent during springs than during neap tides due to a weaker resuspension signal in neaps. The high SPM concentration events observed at site W3 during neap tides (Figs. 4.6 and 6.3), apparently unrelated to local resuspension, made the analysis difficult and allowed extraction of only two to three values of the erosion threshold. The variation of the erosion threshold with time suggested a dependence on the spring-neap tidal cycle.

Therefore, a 14.76 days harmonic, which corresponds to the Msf tidal frequency, was fitted to the single-level threshold values. The least squares fit to the critical erosion bed stress from the two western sites W1 and W3, and the eastern site E1 yielded:

For W3:

$$\tau_{0e}(t) = 0.216 + 0.161 \cos[(2\pi/14.76)t - (-171.30^\circ)], \quad (6.4)$$

For W1:

$$\tau_{0e}(t) = 0.184 + 0.152 \cos[(2\pi/14.76)t - (-163.82^\circ)] \quad (6.5)$$

For E1:

$$\tau_{0e}(t) = 0.150 + 0.070 \cos[(2\pi/14.76)t - (116.08^\circ)] \quad (6.6)$$

Figures 6.4 and 6.5 show plots of the harmonic fits to the critical bed stress from the single level SPM observations.

An apparent asymmetry was evident in the series of extracted erosion threshold values from sites W1 and W3 within the fortnightly cycle: before the spring tides the erosion threshold increased at a lower rate and decreased at a faster rate afterwards. The maximum occurred 2–3 days after the maximum spring tide range as shown in Figure 6.4. Therefore, an asymmetric periodic representation of the erosion threshold was approximated by a two harmonic least squares fit to the data. The harmonic fits using the Msf and 2·Msf frequencies for both sites are:

For W3:

$$\begin{aligned} \tau_{0e}(t) = & 0.198 + 0.176 \cos[(2\pi/14.76)t - (122.32^\circ)] \\ & + 0.034 \cos[(4\pi/14.76)t - (-62.28^\circ)] \end{aligned} \quad (6.7)$$

For W1:

$$\begin{aligned}\tau_{0e}(t) = & 0.162 + 0.170 \cos[(2\pi/14.76)t - (157.10^\circ)] \\ & + 0.035 \cos[(4\pi/14.76)t - (304.00^\circ)]\end{aligned}\quad (6.8)$$

These harmonic fits and the erosion threshold data are shown in Figure 6.6.

A two-harmonic fit was not calculated for the erosion threshold data from site E1 because no asymmetry trend was discernible.

6.3.2.2. Determination of the rate of change of concentration α_{sl} .

The erodibility constant α [$\text{kg}\cdot\text{m}^{-2}\cdot\text{s}^{-1}$] parameterises the rate of sediment mass transfer from the bed to the water column, per unit bed area, i.e. it determines the increase of SPM in the water in a depth-integrated sense. If the time series of SPM concentration is available only at a single level, the erodibility constant can not be obtained. Instead, a rate of change of concentration α_{sl} [$\text{kg}\cdot\text{m}^{-3}\cdot\text{s}^{-1}$] was defined, which represents the rate of increase of SPM concentration at the measurement depth.

Analysis of single level measurements at 1m above the bed yielded 26 to 46 values for α_{sl} [$\text{kg}\cdot\text{m}^{-3}\cdot\text{s}^{-1}$]. These were averaged after grouping them around maximum spring and minimum neap tides. Table 6.6 shows the results from series measured at sites W1, W3 and E1, under each tide condition. At W3 and E1 α_{sl} was $O(10^{-5})$ $\text{kg}\cdot\text{m}^{-3}\cdot\text{s}^{-1}$ with large dispersion, as indicated by the large standard deviation. At W1 the values were about one order of magnitude smaller.

Table 6.6. Concentration rate of change α_{sl} ($\text{kg}\cdot\text{m}^{-3}\cdot\text{s}^{-1}$) based on single level time series from sites W1, W3 and E1 (August, 1997) using the centroid method with 2 hours of data. Spring tides (SP), neap tides (NP). n is the number of averaged values and s.d. is the standard deviation.

Tide conditions (extraction method)	Site W1			Site W3			Site E1		
	n	$\underline{\text{mean } \alpha_{sl}}$ ($\text{kg}\cdot\text{m}^{-3}\cdot\text{s}^{-1}\times 10^4$)	$\underline{\text{s.d.}}$	n	$\underline{\text{mean } \alpha_{sl}}$ ($\text{kg}\cdot\text{m}^{-3}\cdot\text{s}^{-1}\times 10^4$)	$\underline{\text{s.d.}}$	n	$\underline{\text{mean } \alpha_{sl}}$ ($\text{kg}\cdot\text{m}^{-3}\cdot\text{s}^{-1}\times 10^4$)	$\underline{\text{s.d.}}$
SP (cen 2h)	27	0.015	0.009	15	0.08	0.03	23	0.087	0.096
NP (cen 2h)	7	0.009	0.014	11	0.14	0.14	23	0.036	0.039

6.4. Deposition parameters.

Fine cohesive sediments in suspension start to settle once the bed stress falls below a critical value τ_{0d} . In general the threshold for deposition is lower than the erosion threshold because cohesive forces within the bed deposit have to be overcome before erosion takes place. The near-bed time series of SPM concentration and velocity indicated that, while concentration increased almost in phase with current speed after slack water, implying a low erosion threshold τ_{0e} , they also reduced only shortly after maximum current speed, implying a rather higher deposition threshold τ_{0d} . Therefore, the estimated critical bed stress for deposition was larger than that for erosion. This behaviour was observed also in the vertically integrated SPM concentration, as can be inferred from Figure 6.3a. This suggests that the deposition regime was not behaving as expected for cohesive sediments, but rather like fine non-cohesive sediments. Since no deposition threshold was evident no further calculations were made on deposition parameters and it was assumed that a continuous deposition regime existed.

6.5 A simple point model.

The point model based on equations 6.1, 6.2 and 6.3 was used to calculate the erosion-deposition balance and simulate the time series of vertically integrated SPM

concentration at sites J, W3 and E1. The simulations were restricted to 1-2 days during spring tide conditions because vertical distribution of SPM was available only during short periods. This simple approach was intended to test the significance of the parameters previously derived and to test whether the vertical exchange process was the main source of variability through a sediment resuspension-deposition cycle.

The rate of change of the vertically integrated mass concentration M is given in terms of the erosion rate E and deposition rate D as:

$$\frac{dM}{dt} = [E(t) - D(t)]$$

which was approximated numerically using the trapezoidal rule:

$$\Delta M_t \cong \frac{\Delta t}{2} [(E_t - D_t) + (E_{t+1} - D_{t+1})],$$

in which ΔM_t is the change in vertically integrated SPM concentration at time t . The time step Δt was 5 minutes at W3 and E1, and 30 minutes at site J. The rates of erosion E and deposition D are given by equations 6.2 and 6.3 on page 88. Then,

at time t :

$$(E_t - D_t) = \frac{\Delta t}{2} \left[\alpha \left(\frac{\tau_{0t}}{\tau_{0et}} - 1 \right) - w_s C_{bt} \left(1 - \frac{\tau_{0t}}{\tau_{0dt}} \right) \right], \quad (6.9)$$

and at time $t+1$:

$$(E_{t+1} - D_{t+1}) = \frac{\Delta t}{2} \left[\alpha \left(\frac{\tau_{0t+1}}{\tau_{0et+1}} - 1 \right) - w_s C_{bt+1} \left(1 - \frac{\tau_{0t+1}}{\tau_{0dt+1}} \right) \right] \quad (6.10)$$

The values for erodibility α , bed shear stress τ_0 , and the critical bed stress for erosion τ_{0e} were obtained from field data at sites J, W3 and E1, as described previously in this chapter. C_b was defined as the SPM concentration measured 1 m above the sea bed, since no data were collected closer to the bed. The settling velocity was the median w_s obtained from settling tube data collected during the August 1997 cruise at site W3, reported by Fisher (1998), and at site E1, reported by Probert (1998). A deposition threshold was not evident in the data so a continuous deposition regime was assumed. This condition was prescribed in equation 6.3 by defining:

$$\left(1 - \frac{\tau_0}{\tau_{0d}}\right) = 1$$

A summary of the input parameters and variables is shown in Table 6.7.

Table 6.7. Erosion and deposition parameters used in the point modelling of vertically integrated SPM concentration at sites J, W3 and E1 under spring tide conditions. The settling velocity w_s was measured with settling tubes, and the near bed concentration C_b was measured 1 m above the sea bed.

Site	Extraction	τ_{0e} Pa	α kg·m ⁻² ·s ⁻¹	w_s m·s ⁻¹	C_b kg·m ⁻³
J	least sq.	0.30	0.000005	0.00010	variable
	centroid	0.44	0.000006		
W3	least sq.	0.66	0.000037	0.00010	variable
	centroid	0.77	0.000027		
E1	least sq.	0.62	0.000026	0.00023	variable
	centroid	0.55	0.000010		

6.5.1. Vertically integrated SPM concentration.

Figures 6.7 to 6.9 show the time series of the erosion and deposition rates and the observed and calculated SPM content in the water column at the three sites. Despite the continuous deposition assumption, remarkably low deposition rates were obtained

at J and W3, i.e. small values of the product $w_s \cdot Cb$. The critical erosion bed stress at E1 was 0.55 Pa, a value between 0.44 Pa and 0.77 Pa obtained at J and W3, respectively. The erodibility constant at E1 was also between the values at J and W3.

The erosion-deposition balance based on least squares-derived parameters yielded an excess of erosion over deposition for the three sites J, W3 and E1. As shown in Figures 6.7b to 6.9b the simulated SPM integrated concentration yielded an increasing trend due to relatively low deposition rates. The calculations based on parameters derived by the centroid method better simulated the observed vertically integrated SPM time series only at site E1 for which the calculated SPM concentration exceeded the observed concentration by 53%, on average. For the other sites the simulated series exceeded the observed series by 240%–500% on average. The main difference was that at site E1 the settling velocity was higher by a factor of ~ 2 compared with that at J and W3.

6.5.2. Single level near bed SPM simulation at site W3.

It has been shown that the near-bed concentration of suspended sand C can be reasonably well represented in terms of the bed shear stress. For instance Dyer (1980) reported that the concentration at a height of 0.1 m was $C \propto u_*^5$. Based on this concept, the erosion parameters extracted from the single-level SPM concentration measured at W3 were used to calculate erosion rates and concentration at 1 m above the sea bed. Instead of using a power law based on the friction velocity, the concentration was assumed to vary with the normalized excess bed shear stress according to:

$$C = a_{sl} \left(\frac{\tau_0}{\tau_{0e}} - 1 \right) \Delta t = E \Delta t ,$$

in which a_{sl} is a concentration rate of change and the time interval Δt is 5 minutes. The other variables were extracted from the field data as described in Section 6.3.2.

The value for a_{sl} was estimated as the average over the fortnightly cycle, and assumed constant ($=0.000011 \text{ kg}\cdot\text{m}^{-3}\cdot\text{s}^{-1}$). Three formulations were used for τ_{0e} : (a) constant ($=0.26 \text{ Pa}$), averaged over the fortnightly cycle; (b) variable, given by a single Msf period harmonic (Equation 6.4), symmetric around a maximum of 0.40 Pa , as shown in Figure 6.4; (c) variable, given by a two harmonic series (Equation 6.7), asymmetric around the peak value of 0.4 Pa , as shown in Figure 6.6. A semi-permanent slow-varying background concentration observed in the data was added to the calculations as a constant value of $0.014 \text{ kg}\cdot\text{m}^{-3}$.

Figure 6.10 shows the calculated and observed SPM concentration over the fortnightly cycle for the three erosion threshold conditions. A constant τ_{0e} yielded good qualitative agreement during spring tides (Fig. 6.10a) but failed to reproduce the high concentration events during neap tides at both ends of the series. A variable τ_{0e} underestimated the spring tide concentrations while high concentrations were obtained in neap tides, when the erosion threshold was low (Fig. 6.10b). However, the peak magnitudes were in general underestimated and out of phase with respect to the observed concentration peaks. This phase difference caused a poor correlation between the observed and calculated series during neap tides while during springs the correlation improved significantly. Under spring tides the observed and calculated SPM concentration peaks were nearly in phase, with a small shift due to the twin-peak structure of the observed series. The two-harmonic asymmetric τ_{0e} series was a better representation of the threshold data during the fortnightly cycle and improved the simulated series only slightly, as shown in Figure 6.8c. However, the main features of the fortnightly cycle were preserved, i.e., the quarter diurnal resuspension signal, the fortnightly modulation of this signal, and the high concentration events in neap tides although not all in phase with the observed concentration peaks.

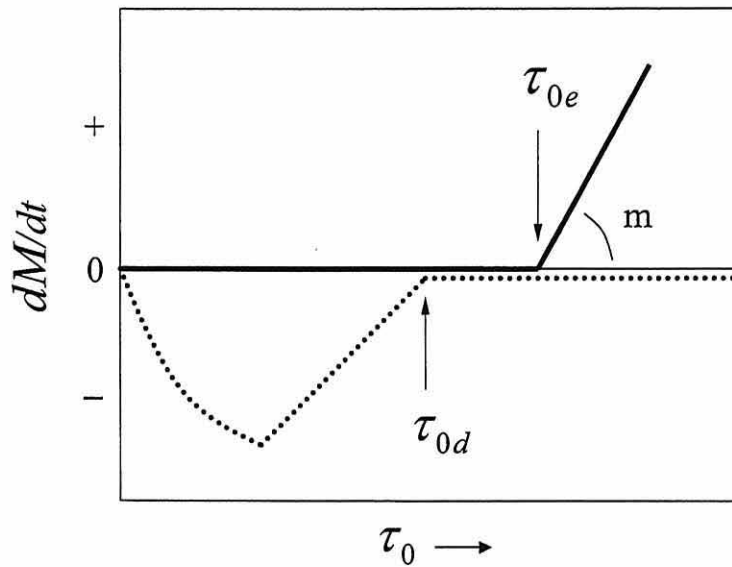


Figure 6.1. Conceptual diagram of the critical bed stress for erosion (τ_{0e}) and for deposition (τ_{0d}) in the sediment resuspension-settling cycle. M is the SPM content in the water column and τ_0 is the bed stress (after Clarke and Elliott, 1998).

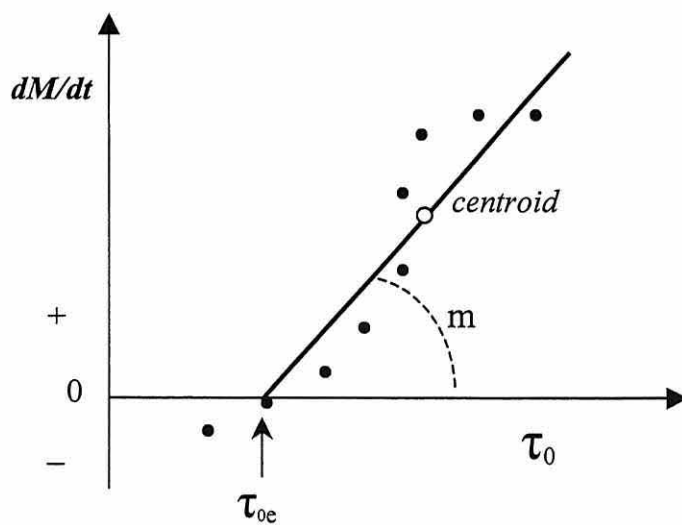
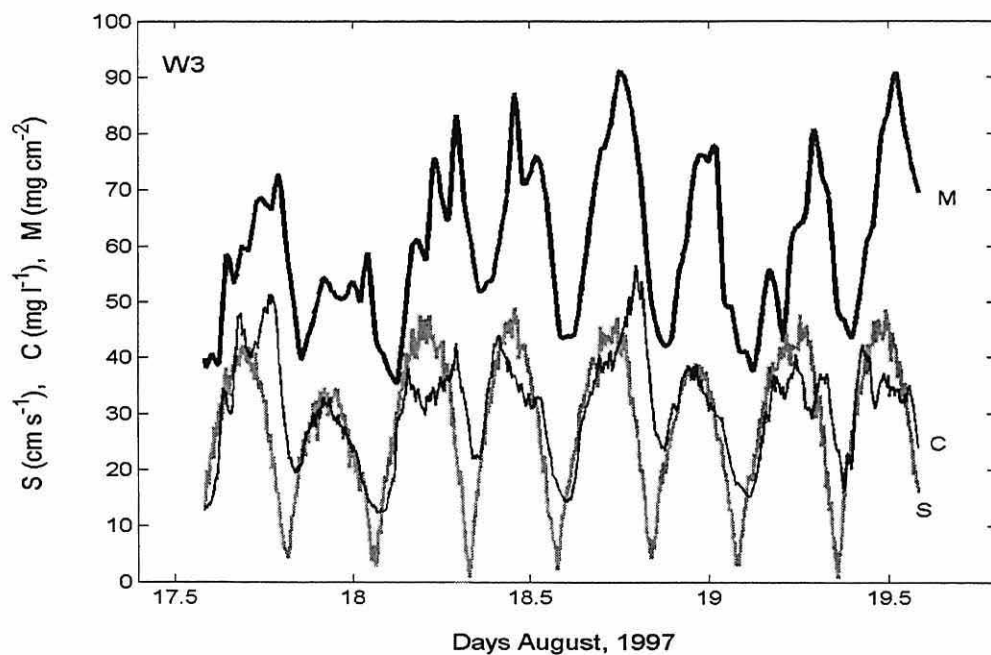


Figure 6.2. Conceptual diagram of the centroid method showing the critical bed shear stress for erosion τ_{0e} , the centroid, and the slope angle of the line through the points.

a



b

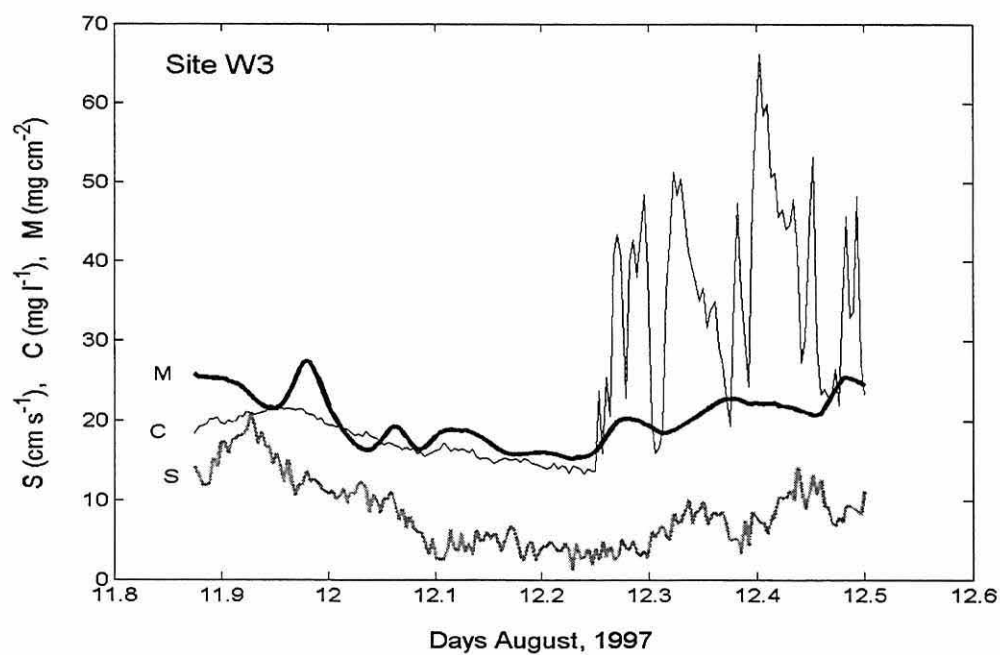


Figure 6.3. Time series current speed 1.2 m above the bed (S), SPM concentration at 1 m above the sea bed (C) and SPM concentration vertically integrated (M) during the tidal cycle stations at site W3 under spring (a) and neap tides (b).

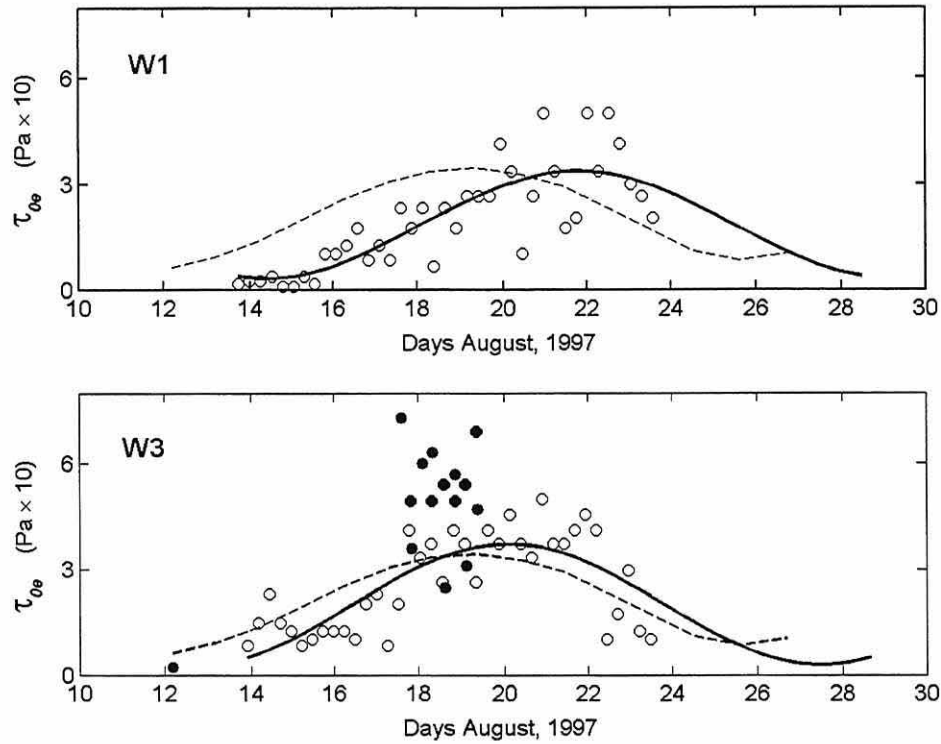


Figure 6.4. Critical bed stress for erosion at sites W1 and W3 during the fortnightly cycle, estimated by least squares fits. The black circles are the values obtained from the vertically integrated SPM concentration during tidal cycle stations under spring and neap tides. Open circles are values extracted from single-level SPM concentration time series. The solid line is the fortnightly frequency fit and the dashed line is the tidal amplitude (m). Site W1 is 3.4 km northwest of site W3, on the west side of the Upper Gulf.

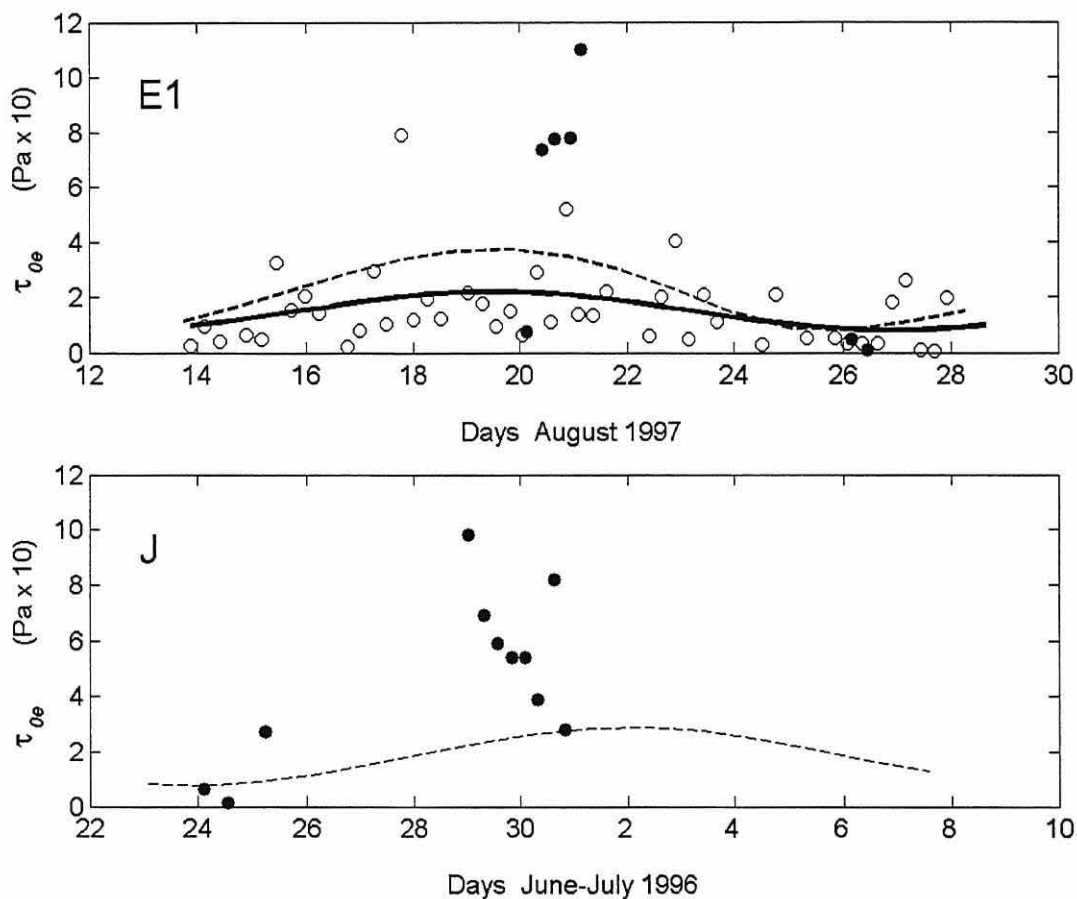


Figure 6.5. Critical bed stress for erosion at sites E1 and J (black circles). The values were obtained by least squares fits from the vertically integrated SPM concentration during the tidal cycle stations under spring and neap tides. Open circles are the values extracted from single-level SPM concentration time series. The solid line is the fortnightly frequency fit and the dashed line is the tidal amplitude (m). Site E1 is on the east side and site J is on the west side of the Upper Gulf.

7. Horizontal SPM fluxes.

7.1. Introduction.

Rivers discharge fresh water and sediments to the coastal ocean. The resulting estuarine environments become the pathways through which finer sediments may reach the open sea. Within an estuary the fine sediment particles are dispersed along paths determined by water motion. Tidal energy continually erodes, transports and deposits bed sediments. Thus, within the classic estuary the suspended particulate matter (SPM) concentration is generally high even with little new sediment input (Dyer, 1995). These low salinity water bodies respond to seasonal fluctuations of fresh-water discharge. Extensive research in shelf seas has been oriented to determine the fate of the high river runoff that occurs during the wet season. In contrast, dry season estuarine dynamics has only received attention in recent years. The tropical estuaries of northern Australia, for instance, are influenced by large seasonal fluctuations in fresh-water discharge (Wolanski, 1988). In arid regions where little precipitation and runoff combine with a high evaporation rate, hypersaline water bodies develop called negative estuaries or inverse estuaries. Large-scale examples of this are the Persian Gulf, the Red Sea, the Arabian Sea, the South Australian gulfs and the Gulf of California (Bowers, 1989; Nunes Vaz *et al.*, 1990).

In contrast with the classic estuary model, the inverse estuary in arid regions requires a net flow of oceanic water toward its head to compensate for the fresh water loss due to evaporation. The tendency for salt accumulation inside the inverse estuary requires an opposing mechanism that removes the high salinity water. One process involves the sinking of saltier (denser) water in the shallower areas and its flow toward the open ocean boundary as a near-bed gravity current (Nunes Vaz *et al.*, 1990). Among the smaller-scale examples, coastal lagoons in arid regions can also exhibit inverse-estuarine behaviour when high evaporation causes a net loss of water. In these so-called anti-estuarine lagoons, the seaward flowing circulation near the bottom can

carry SPM from the lagoon out to the ocean (Groen, 1967; Postma, 1967). Enhancement of the seaward flux of SPM can be expected since both gravity currents and high SPM concentration may develop close to the sea bed concurrently. Sediment transport under these conditions has not been widely documented, perhaps as a consequence of the relatively little attention given to inverse estuaries in the past.

The proposed circulation of the Upper Gulf and the reported inverse estuarine features may account for the fine sediment dispersal pattern found in previous studies of bed samples. Indirect evidence suggests that a cyclonic residual circulation is generated in the Upper Gulf (Hendrickson, 1973; Hernández-Ayón *et al.*, 1993). A similar pattern was reported by Marinone (1997), through numerical modelling of the tidal residual currents, and also by Carriquiry and Sánchez (1999), based on calculated sediment transport pathways. The patterns of suspended sediment plumes observed in satellite images have been attributed to the effect of this residual circulation. Carbajal *et al.* (1997) have speculated that the transport of sediments to deeper basins takes place through the mechanism of residual currents.

Hydrographic surveys and current measurements reported by Lavín *et al.* (1998) have revealed that the Upper Gulf normally behaves like an inverse estuary, in which salinity and density increase toward the head throughout the year, despite reversal of the temperature gradient from summer to winter. As in other inverse estuaries, the horizontal density gradients in the shallow coastal areas of the Upper Gulf are sustained by intense vertical mixing during spring tides. During neap tides the decrease in mixing allows, given the horizontal contrast of density, the onset of gravity currents: the warmer but saltier and denser water ($\Delta\sigma_t=0.2$) in the shallow, well-mixed regions flows underneath the colder, fresher and lighter offshore water with a down-slope component and just near the bed. The same authors reported that currents flowing out of the Upper Gulf were similar to geostrophically adjusted speeds of gravity currents observed by Nunes and Lennon (1987) in Australian Gulfs.

In this chapter currents and SPM concentrations at two opposite sites in the Upper Gulf are used to calculate horizontal fluxes. The aim was to investigate the processes

influencing sediment fluxes using intensive observations made for the first time in this shallow macro-tidal region with inverse estuarine features.

7.2. Observations.

The measurement sites and station plan dealt with in this Chapter is shown in Figure 7.1. The SPM flux calculations that follow are based on results described in Chapters 4 and 5:

West side:

- Velocity profiles measured at site W3 with the bottom-mounted ADP during 15 days, in water 25 m deep, as described in Chapter 3, Sections 3.1 and 3.2.
The velocity record consists of consecutive 5-minute averages from 0.5 m depth ‘bins’. The site is located on the western side of the Upper Gulf, 20 km off the coast of Baja California, and 25 km northwest of San Felipe, as shown in Figure 3.1. The mooring was set inside a 10-km wide trough with the shallow coastal shelf on the west and a narrow ridge rising 8–10 m on the east. This long, gently sloping channel reaches Wagner Basin 40 km to the southeast of the measurement site.
- Current measurements made at site J, 1 and 6 m above the bed in June 1996.
- CTD-OBS casts made at sites J and W3 in June 1996 and August 1997 respectively, during tidal cycle stations under spring and neap tides.
- Time series of SPM measured with a calibrated OBS sensor at 1 m above the sea bed in August 1997.

East side.

- Short time series (~1.5 days) of velocity concurrently measured at site E1 at 1.2 and 4.2 m above the sea bed. The current meters were moored inside a 6-8 km wide

channel, 32 m deep at the mooring site. This 60-km long channel borders the east coast and also reaches Wagner Basin as shown in Figures 3.1, 4.1 and 7.1.

—CTD-OBS casts made at site E1 during tidal cycle stations under spring and neap tides.

7.3. Data analysis.

7.3.1. Acoustic signal strength and SPM concentration.

Besides velocity data the ADP stored the 5-minute mean backscattered acoustic signal strength at each one of the 0.5 m bins. The signal can be converted into SPM concentration through calibration. Water samples from CTD-mounted bottles were used to measure SPM concentration by filtering a known volume of the water sample and by differential weighing of the dried filters. 42 samples were collected less than 0.9 km from the ADP site, and the directly measured SPM concentration range appeared to encompass most of the spring to neap tide variation observed in this area.

For each one of the three beams the ADP stored ‘counts’ of the raw acoustic signal strength backscattered from particulate matter in the water. Counts were converted to decibels (dB) using the relation $\text{dB} = 0.43 \times (\text{counts})$. The signal strength was corrected for decay D due to water sound absorption and geometric spreading of the acoustic beams according to (SonTek Technical Notes, 1997):

$$D = -20 \log_{10}(R_{\text{beam}}) - 2\alpha(R_{\text{beam}})$$

where

D = decay in signal strength (dB) as function of range,

R_{beam} = along-beam range in meters,

α = sound absorption = 0.68 dB/m for 1.5 MHz frequency and salinity of 35.

The corrected signal strength from the three beams was averaged and normalized by subtracting the minimum value from the whole data set. Corrected signal strength values from selected range cells between 3 m and 15 m above the transducers were extracted at suitable times. These values were compared to SPM concentrations measured from water samples collected at corresponding times and depths. A linear regression procedure yielded the calibration curve:

$$\log_{10} C = 1.186 \pm 0.070 + (0.0245 \pm 0.0040) A ,$$

where: C is the concentration of SPM in $\text{kg}\cdot\text{m}^{-3}$ and A is the corrected return signal strength in decibels. The regression parameters are given with the 95% confidence intervals. Figure 7.2 shows the SPM concentration values and the regression line, which accounted for 80% of the variance in the data.

Close to the transducers, within the so-called near-field range, a complex acoustic beam pattern develops. It deviates from the spherical spreading of the far-field, in which the acoustic signal strength is inversely proportional to the range (r) from the transducers. The boundary between the near-field and the far-field backscatter regions is at a distance $r = \pi\alpha^2/\lambda$ (SonTek Technical Notes, 1998), where α is the transducer radius and λ is the acoustic wavelength. For the ADP used, r is 1.25 m. Thorne *et al.* (1996) have applied a factor of 2 that in our case yielded the first three bins within the near-field. Since the suspended sediment samples for calibration were collected in the far-field region, only signal strength values measured 2.7 m from the sea bed and above were used for estimating SPM concentrations and fluxes.

7.3.2. Horizontal SPM fluxes.

Instantaneous horizontal fluxes between 2.7 and 10.7 m above the sea bed were obtained as the product of velocity times SPM concentration at 0.5 m increments. Vertically integrated instantaneous fluxes were calculated by numerically integrating

$$\int_{z1}^{z2} UCdz \quad \text{and} \quad \int_{z1}^{z2} VCdz$$

where U is the along-gulf velocity, V is the across-gulf velocity, $z1 = 2.7$ m and $z2 = 10.7$ m above the sea bed, with 0.5 m increments. Further calculations yielded instantaneous and time averages of along-gulf (principal axis) and across-gulf fluxes during spring tides, neap tides, and over the full fortnightly cycle.

7.3.3. Near-bed velocity profiles.

Additional analysis was performed to calculate velocity at 0.5 m depth intervals at sites in which measurements were made at two levels only. The data analysed were from site J (June 1996) at 1 and 6 m and from site E1 (August 1997) at 1.2 and 4.2 m. Velocity was assumed to conform to the logarithmic profile law and profiles between the two depths were fit by least squares. Since only two data points were available for each fit the regression residuals and the correlation R were not suitable criteria for rejecting invalid log profiles. Therefore only velocity profile fits yielding bed roughness scale $z_0 \leq 0.2$ m were considered valid. Profiles yielding larger z_0 occurred when velocity was low, around slack water, and were rejected. In this case velocity was linearly interpolated between the two depths. Along-gulf velocity data and profiles during spring and neap tides are shown in Figure 7.3. Only 30-50% of the profiles from J and E1 complied with the condition $z_0 \leq 0.2$ m during neap tides, whereas during springs the proportion increased to 75% or more.

7.3.4. Near-bed horizontal SPM fluxes.

The aim was to compare horizontal SPM fluxes within similar levels at three sites in the Upper Gulf using the spring and neap tide series of velocity and concentration lasting 1-4 semidiurnal cycles. Near bed fluxes were based on SPM concentration from OBS profiles and single-level time series at selected depths. The fluxes were calculated at 0.5m depth intervals as well as vertically integrated within a 4 m-thick layer between 1.2 and 5.2 m from the bed. At site E1 saturation of the OBS sensor

prevented SPM concentration measurements close to the bed at the time when velocity was recorded. Thus, SPM flux was estimated only at a single level, at 4.2 m above the bed. At site W3 the ADP velocity profiles between 1.2 and 5.2 m from the bed were extracted for flux calculations.

7.4. Results.

7.4.1 Hydrographic setting. Along-gulf transects.

Figure 7.1 shows the location of three CTD along-gulf transects made in this area, 1 to 2 days after the neap tides. Transect A was made along the channel in which the time series were obtained. Transect B was made along an adjacent channel to the East of A to depths of about 100 m, at the edge of Wagner Basin. Transect C was made on the east side along the narrow channel adjacent to the coast of Sonora. Salinity, sigma-t and SPM distributions are given in Figures 7.4 and 7.5. Although these transects were made at different stages of the tide, they revealed consistently higher values of salinity, sigma-t and SPM toward the shallow depths in the head of the Upper Gulf. Denser, more saline and turbid water was found close to the sea bed. In transect B this water left the bottom at a depth of ~50 m and intruded into the ambient fluid with a sigma-t value near 22.4, as shown in Figure 7.4(b). The high salinity and turbid water that became detached from the sea bed could be traced as a subsurface maximum to at least 10 km away from the point of detachment.

7.4.2. SPM fluxes. Fortnightly cycle.

At levels between 2.7 and 10.7 m above the sea bed, instantaneous along-gulf SPM fluxes based on the ADP backscattered signal reached $\sim \pm 30 \text{ g} \cdot \text{m}^{-2} \cdot \text{s}^{-1}$ during spring tides and $\sim -6 \text{ g} \cdot \text{m}^{-2} \cdot \text{s}^{-1}$ during neap tides (negative fluxes are out from the Upper Gulf). The time series of instantaneous SPM fluxes revealed a marked spring-neap modulation at all the measurement levels. This modulation can be seen in the time series of instantaneous fluxes measured 5.2 m above the sea bed, at the level of the

maximum gravity current flow (Figure 7.6). Spring tide fluxes were nearly symmetric about zero, unlike those during neap tides, in which fluxes were predominantly out of the Upper Gulf. Vertically integrated instantaneous fluxes yielded maximum transport per unit width near $-40 \text{ g}\cdot\text{m}^{-1}\cdot\text{s}^{-1}$ during neap tides, $\pm 290 \text{ g}\cdot\text{m}^{-1}\cdot\text{s}^{-1}$ during spring tides, and an average of $-12 \text{ g}\cdot\text{m}^{-1}\cdot\text{s}^{-1}$ over the full fortnightly cycle.

In addition to the ADP time series, calibrated OBS profiles from site W3 have provided independent SPM concentrations and instantaneous flux calculations for two short periods during spring and neap tides. Fluxes estimated from both ADP and OBS measurements were in good agreement as shown in Figure 7.7, in which both time series of fluxes at 5.2 m above the bed are plotted. Along-gulf fluxes during the 15-hour neap-tide series show maximum near $-6 \text{ g}\cdot\text{m}^{-2}\cdot\text{s}^{-1}$. These figures are also similar to the neap-tide maximum flux ($-5 \text{ g}\cdot\text{m}^{-2}\cdot\text{s}^{-1}$) measured 6 m above the sea bed at site J during the two-day preliminary survey in June 1996.

Figure 7.8 shows the time-average of instantaneous flux profiles. The average over a spring–neap cycle (14.7 days) yielded a residual flux out of the Upper Gulf, as shown in Figure 7.8b. This residual flux is one order of magnitude smaller than the maximum instantaneous fluxes. The remarkable contrast between spring- and neap-tide fluxes is better shown by averaging the fluxes under each tide condition. Since the neap-tide outflow events lasted around three days, the average over six semidiurnal cycles was obtained for each tide condition. It was found that near-zero residual SPM fluxes prevailed during spring tides, as shown in Figure 7.8c, while during neap tides they reached $-2.5 \text{ g}\cdot\text{m}^{-2}\cdot\text{s}^{-1}$ (Fig. 7.8a). The average fluxes during spring tides show only a very weak vertical structure. In contrast, the average fluxes during neap tides display a significant maximum at 4 m above the sea bed, which is the same level as the maximum velocity of the gravity current.

7.4.3. SPM fluxes. Near-bed series.

The velocity data and fitted profiles used in the flux calculations are shown in Figure 7.3. SPM fluxes at sites J, W3 and E1 under neap and spring tides are given in Table

7.1. The maximum spring tide flux was $147 \text{ g} \cdot \text{m}^{-1} \cdot \text{s}^{-1}$ at site W3, and $71 \text{ g} \cdot \text{m}^{-1} \cdot \text{s}^{-1}$ at site J. Smaller, notably asymmetric fluxes were obtained in neap tides: maximum ebb fluxes (–) were one order of magnitude larger than maximum flood fluxes (+). The uncertainty in fluxes larger than $30 \text{ g} \cdot \text{m}^{-1} \cdot \text{s}^{-1}$ was <10%. Small fluxes less than $1.5 \text{ g} \cdot \text{m}^{-1} \cdot \text{s}^{-1}$ had uncertainty >30%. The average over one semidiurnal cycle yielded a net transport of suspended matter outward from the Upper Gulf on the western side at sites J and W3. At site E1 on the eastern side, single-level fluxes at 4.2 m above the bed did not reveal an ebb-flood asymmetry as observed on the western side during neap tides, so no significant net flux was obtained. The flux asymmetry can be inferred from the velocity profiles on the west side under neap tides (Fig. 7.3).

Table 7.1. Horizontal along-gulf SPM fluxes during spring (Sp) and neap (Np) tides. Fluxes at sites J and W3 were integrated over the indicated depths. Fluxes at site E1 were estimated at 4.2 m above the bed. The numbers in parenthesis indicate the full semidiurnal cycles used in the calculations.

Site/ Layer thickness	J 1m to 5m ($\text{g} \cdot \text{m}^{-1} \cdot \text{s}^{-1}$)		W3 1.2m to 5.2m ($\text{g} \cdot \text{m}^{-1} \cdot \text{s}^{-1}$)		E1 at 4.2m ($\text{g} \cdot \text{m}^{-2} \cdot \text{s}^{-1}$)	
Tide conditions	Sp (4)	Np (4)	Sp (3)	Np (1)	Sp (3)	Np (3)
Max. flood flux	71.4	2	145.6	1.5	31.9	4.2
Max. ebb flux	-53.5	-21.5	-147.3	-24.9	-56.6	-6.4
Mean flux	1.3 ± 2.7	-6.7 ± 1.25	-4.8 ± 2.9	-8.6 ± 1.1	-5.7 ± 2.4	-0.6 ± 0.8
Standard deviation	28.9	6.5	78.3	8.4	23.4	2.3

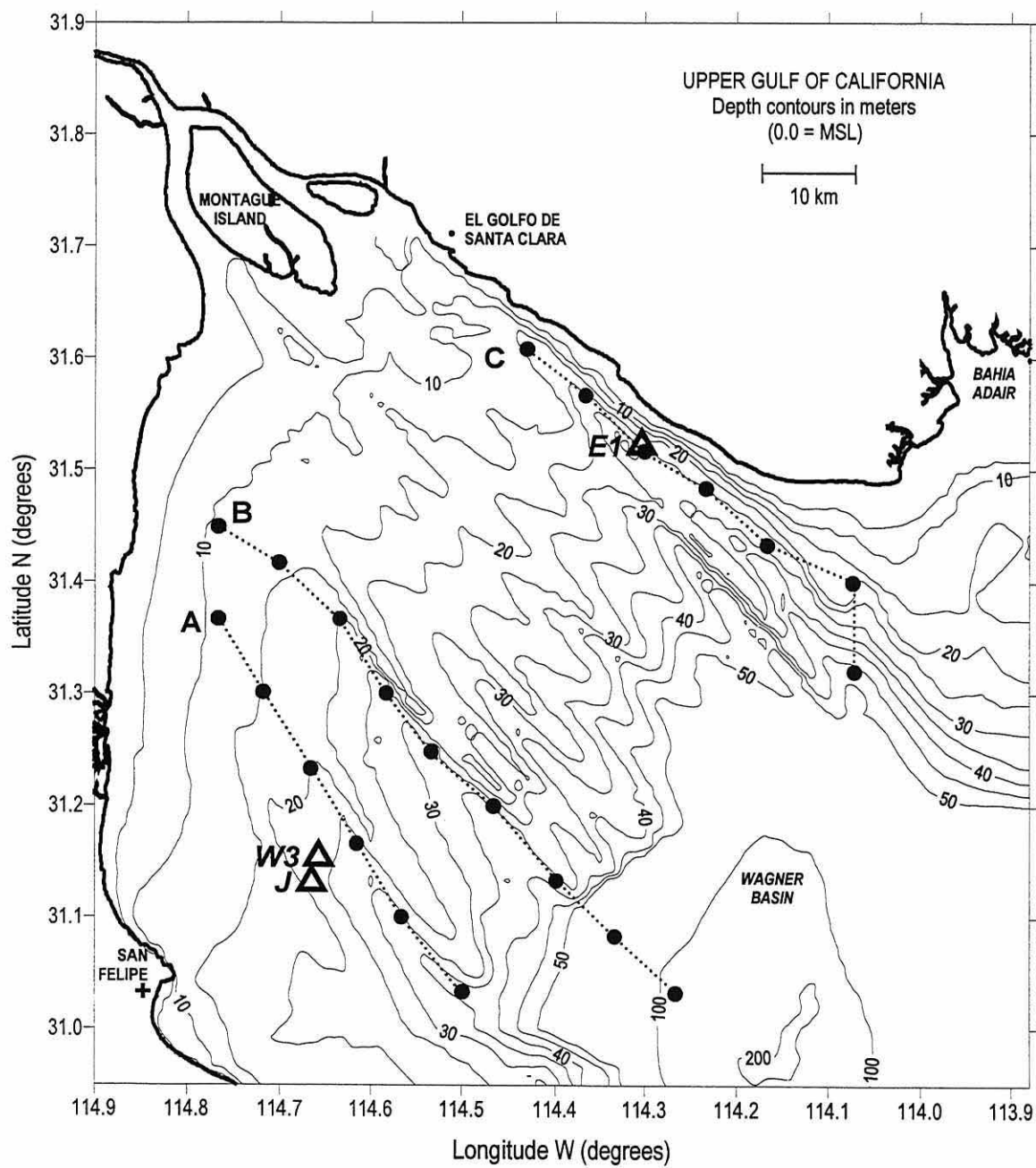


Figure 7.1. Instrument mooring sites J, W3 and E1, and three along-gulf transects (A, B, C) of hydrographic stations made in the Upper Gulf in August 1997.

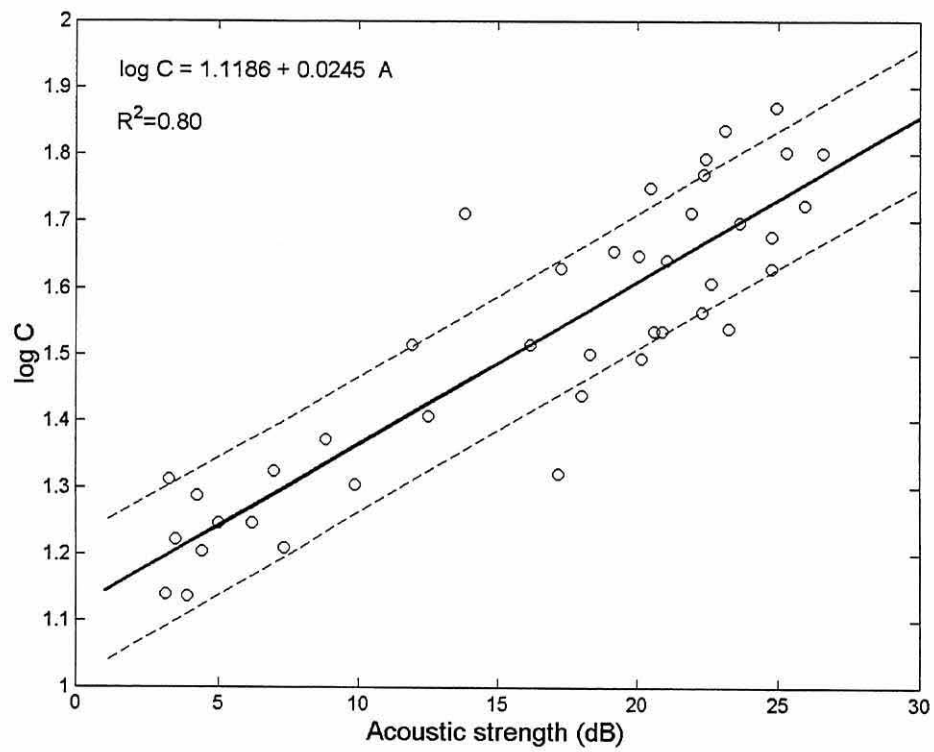


Figure 7.2. Observed SPM concentration vs ADP acoustic signal strength (circles). The regression line (solid line) is shown with the 68% confidence interval (dashed lines).

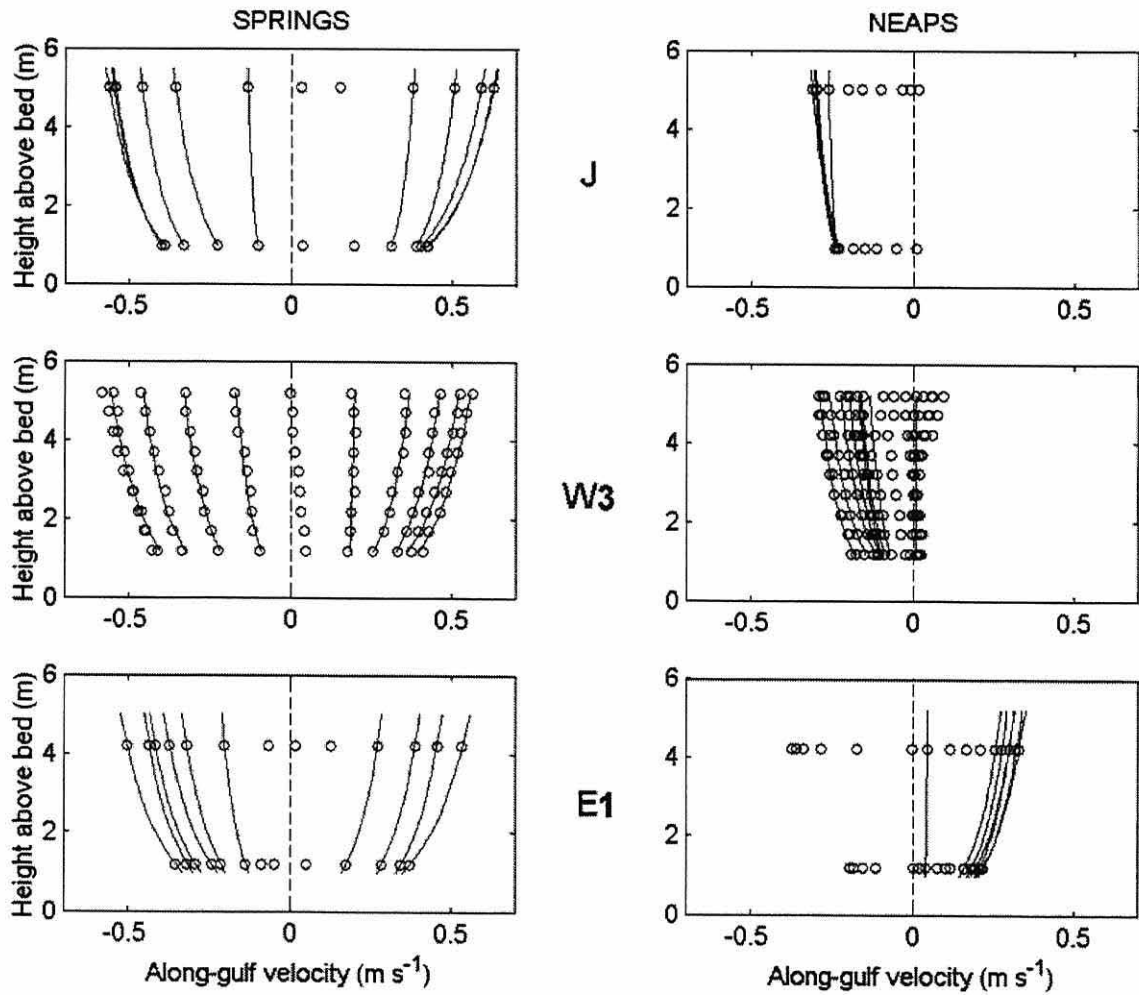


Figure 7.3. Along-gulf velocity profiles during one semidiurnal cycle, under spring and neap tides at sites J (June, 1996), W3 and E1 (August 1997). Circles represent the observations and the solid lines represent the logarithmic fits for which the roughness length was less than 0.2 m.

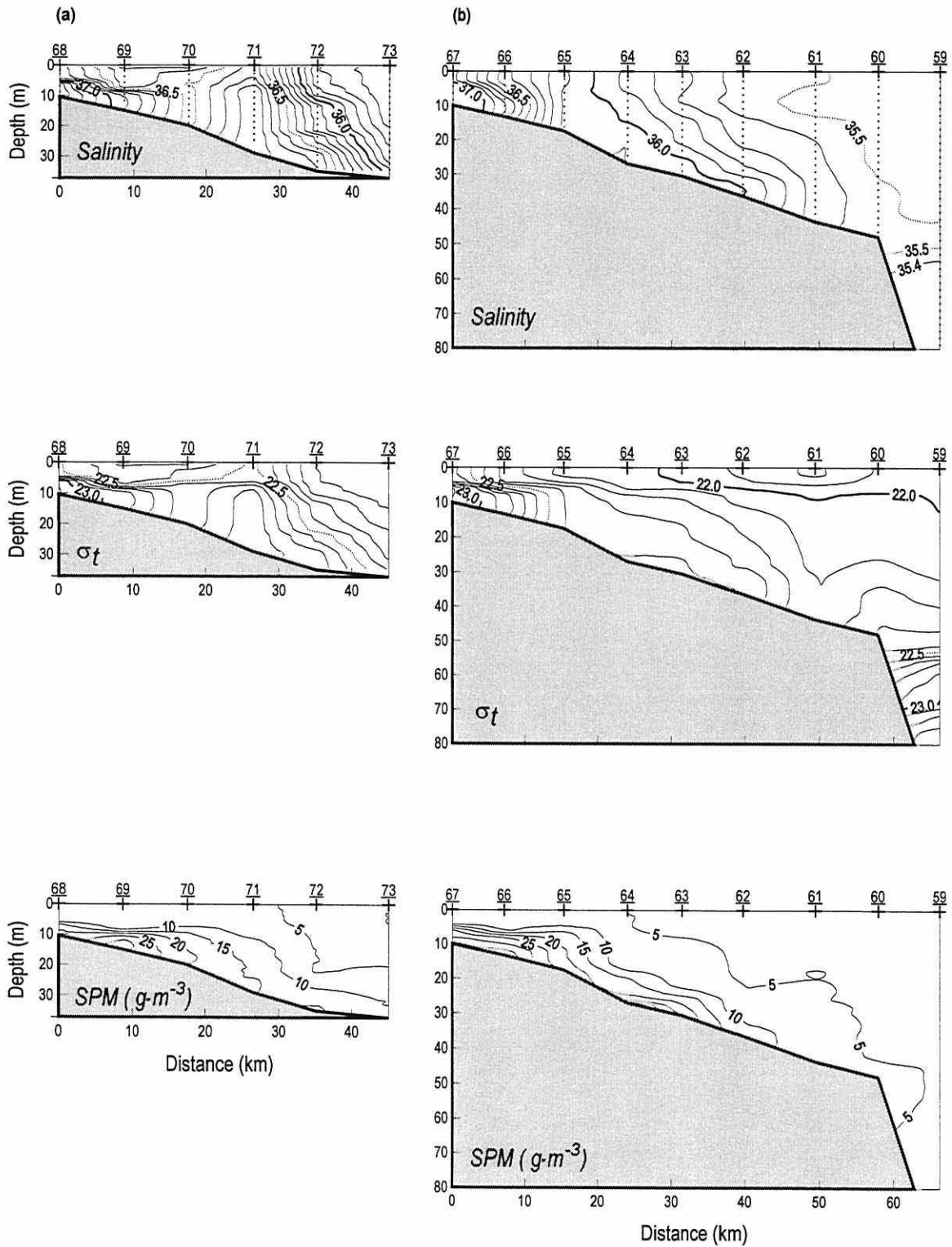


Figure 7.4. Vertical distributions of salinity, sigma-t and SPM concentration observed on 14 August 1997. (a) transect A and (b) transect B shown in Figure 7.1. Station numbers are shown above each transect. The ADP was moored near station 71 in transect A.

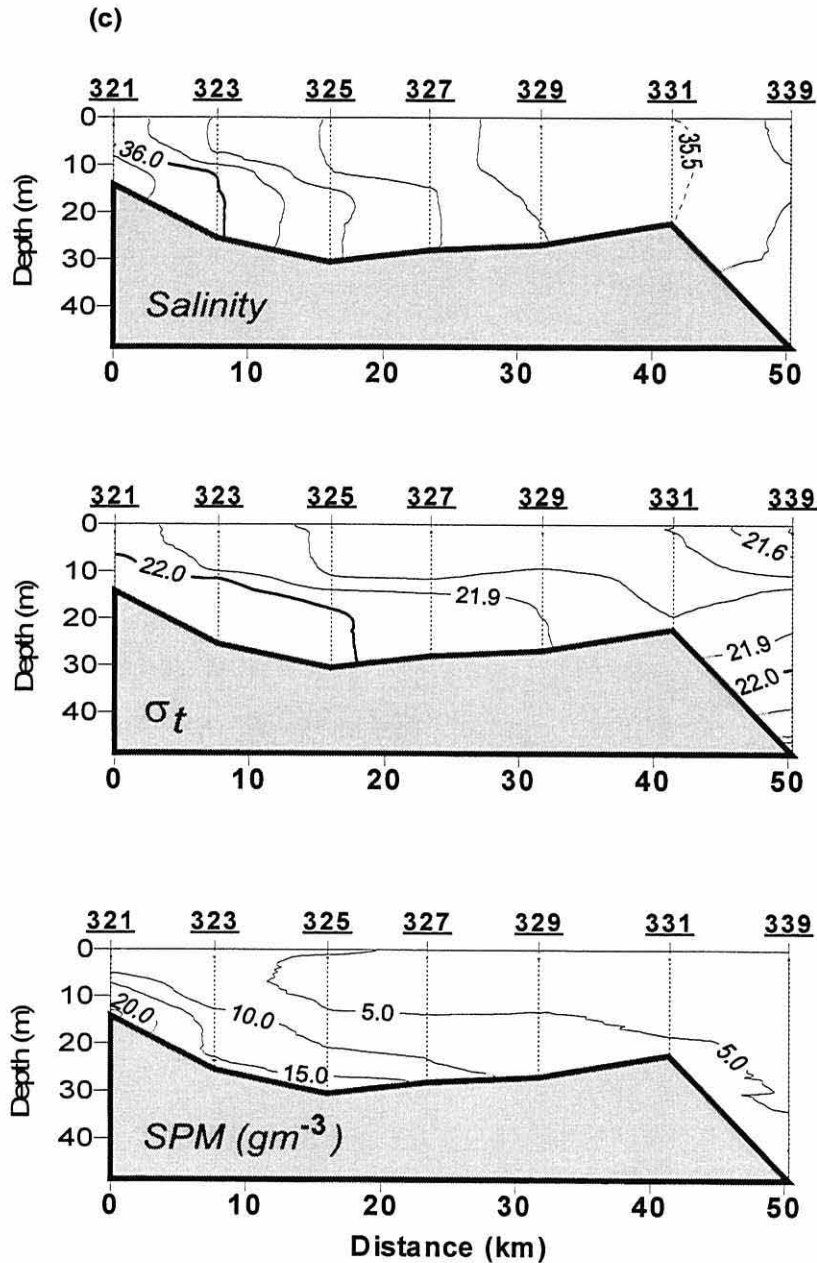


Figure 7.5. Vertical distributions of salinity, sigma-t and SPM concentration observed on 23 August 1997, along transect C shown in Figure 7.1. Station numbers are shown above each transect. The mooring site E1 was located near station 325.

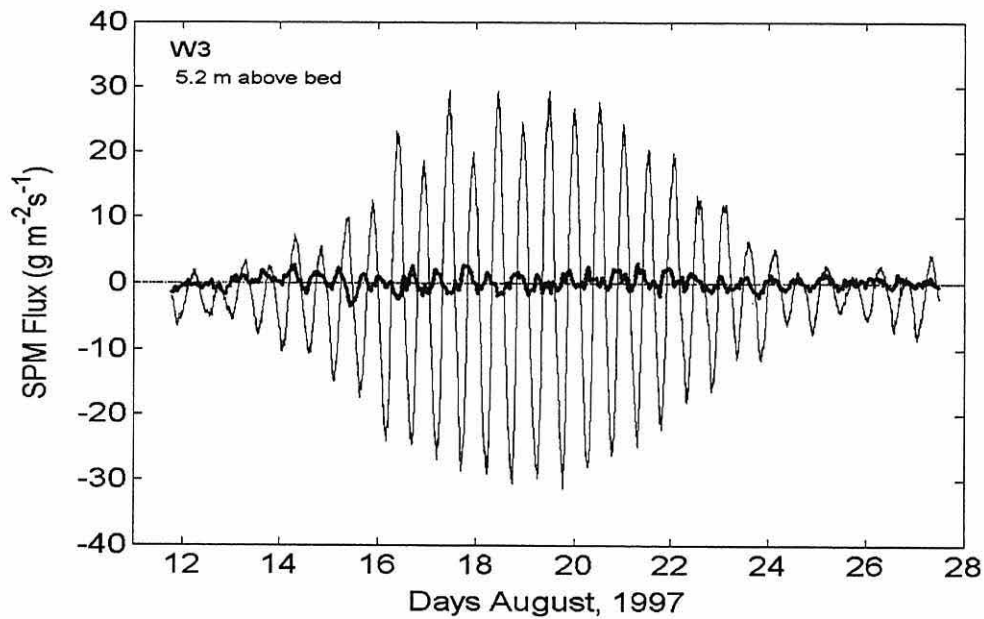


Figure 7.6. Horizontal SPM fluxes derived from ADP data at the level of the gravity current core (5.2 m above the bed), at site W3. Fluxes along- (thin line) and across-gulf (heavy line) are 5-minute averages.

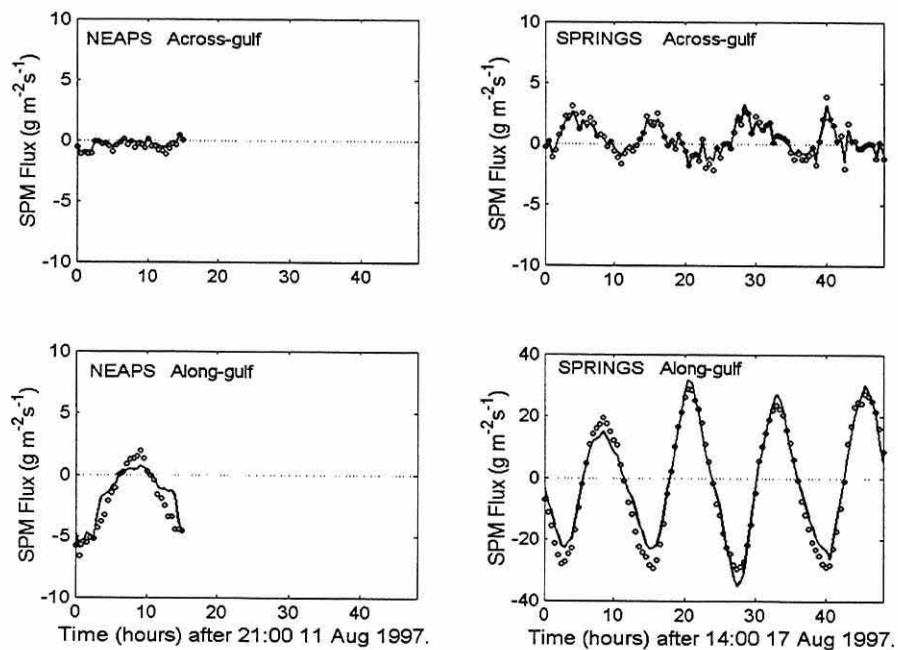


Figure 7.7. Comparison between horizontal SPM fluxes at 5.2 m above the bed at site W3, obtained from OBS (circles) and ADP backscatter (solid line), under spring and neap tides. The flux scale in the lower right frame is a factor four larger.

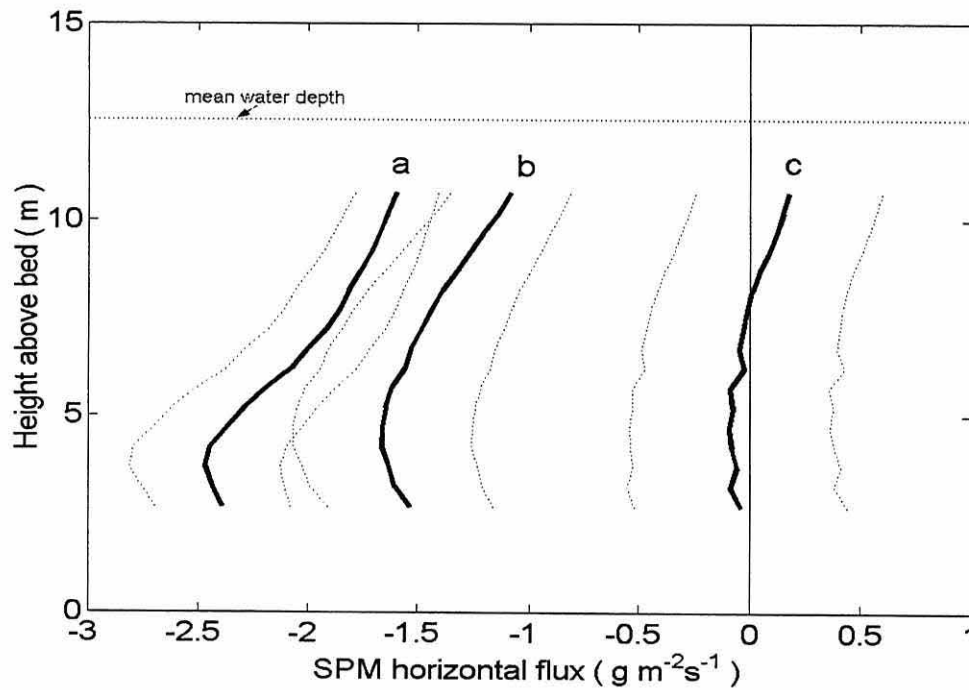


Figure 7.8. Profiles of time-averaged along-gulf SPM fluxes at site W3 in August 1997: (a) averaged over six semidiurnal cycles in neap tides, (b) averaged over 14.7 days, and (c) averaged over six semidiurnal cycles in spring tides. Negative fluxes are outward the Upper Gulf. The dotted lines indicate the 68% confidence interval for each profile.

8. Discussion.

A quantitative study of SPM concentration and factors influencing its distribution has been made for the first time in the Upper Gulf of California. Detailed investigation of vertical and tidal variation of SPM concentration at selected sites has been combined with a larger scale study of spatial variation in the region. This has allowed a detailed analysis of processes of sediment resuspension and flux which will have wider application in coastal sediment research. It has also allowed specific investigation of the impact of inverse estuarine circulation on the transport of SPM, a mechanism which to date has received little attention. The results will benefit future ecological research in the region by contributing to understanding of organism-sediment interactions and fluxes of particle-bound pollutants, nutrients and particulate organic matter. They will also be useful for the planning and operation of man-made structures which may be affected by transport and deposition of suspended sediment, e.g. harbour basins, fish-farming ponds, artificial reefs and dredging works.

8.1. Currents and boundary layer parameters.

Bed roughness and drag coefficients.

The present study was the first of its kind in the Upper Gulf dealing with near-bed current profiles, thus, boundary layer parameters based on the log-profile method are reported for the first time. These parameters will be further discussed in relation to suspended sediment dynamics and fluxes.

Small bed roughness length z_0 is expected where sediments are mostly silt and clay, like those at the measurement sites in the Upper Gulf. Typical bed roughness in mud-sand bed sediments ranges from 0.0002 m to 0.0007 m according to Soulsby (1983). In the present study the profile method has yielded larger bed roughness (modal value 0.02-0.03 m) at site W3 during the fast current stages in spring tides. During slower currents in neap tides and near slack water the mean roughness length increased to abnormally high values one and two orders of magnitude larger than the mode (out of scale, in Figure 5.4). Although

some of these values were statistically significant there is no direct evidence of large sea bed roughness developing at low current speeds. According to Wilkinson (1984), the most significant cause of apparent variation in the roughness length is unsteadiness of the currents.

Since the bed roughness and the drag coefficient are interrelated a proper analysis must yield compatible values for these two parameters. To verify this an internal consistency test was made following Collins *et al.* (1998): The drag coefficient derived from the quadratic friction law $C_{D1.2} = u_*^2 / U_{1.2}^2$ should be equal to that derived from the log profile:

$$C_{D1.2} = \frac{\kappa^2}{\left(\ln \frac{1.2}{z_0} \right)^2}$$

Computations using both formulae were made using data from the whole fortnightly cycle. The results revealed that both values of the drag coefficient were indeed similar, as shown in Figure 8.1, although there is a tendency to deviate from a 1:1 relationship at higher values.

A mean rather than an “instantaneous” bed roughness has been proposed to better represent the bed surface adjustment to the flow conditions. This concept was applied by Cheng *et al.* (1999) in a study of tidal estuarine flows in San Francisco Bay. Mean z_0 values were computed assuming that z_0 should remain nearly constant over some time, typically a few hours. This time span has to have a physical meaning according to the current regime (ebb or flood, tidal period, a day, etc.). For comparison with Cheng’s results, the full fortnightly series of the Upper Gulf was divided into subsets of one semidiurnal cycle and the average of z_0 was obtained for each. The conventional average value z_{0ca} was computed as:

$$z_{0ca} = \langle z_0 \rangle$$

The brackets $\langle \rangle$ indicate averaging over one semidiurnal period. According to Cheng *et al.* a better estimate of the mean roughness length results by first averaging the exponent in the expression for computing z_0 by the profile method. This new mean roughness z_{0ea} , consistent with the least square formulation used in this study, is:

$$z_{0ea} = \exp\left(\overline{\ln(z)} - \frac{\theta_1}{\theta_2}\right)$$

The mean roughness length based on both expressions is shown in Figure 8.2. The series of mean roughness z_{0ca} based on the conventional averaging shows larger and more dispersed values, especially during neap tides. The second method yielded smaller less noisy means z_{0ea} , showing a consistent decrease to values near 0.04 m around spring tides. Cheng *et al.* also obtained a decreasing trend toward spring tides, however their values were smaller: 0.004–0.01 m for spring tides and 0.01–0.04 m for neaps. The same authors found that the bed roughness length of muddy sediments in San Francisco Bay was independent of ebb or flood.

The results of this analysis revealed unusually large bed roughness that exceeds typical values of muddy beds. In rough turbulent boundary layer flow the roughness element size is $D=30z_0$ or 0.3–0.9 m for the modal value of z_0 . Since the bed sediment texture in this site of the Upper Gulf is a mud-sand mixture, the roughness elements should not develop to this size by sediment-flow interaction only. Thus, the roughness scale remains to be investigated further, preferably by direct sea bed observations. The unusually high values of z_0 obtained within the semidiurnal cycle, near slack water are unrealistic and almost certainly due to the absence of a well-developed logarithmic layer under slow currents, especially during neap tides. Under these conditions the log-profile method would be unreliable for estimating z_0 and these values will not be considered further.

The bed stress values in this study compare well with ADCP profile-derived stresses reported by Lueck and Lu (1997), for similar flow conditions in a tidal channel. The marked semidiurnal cycles of the bed stress τ_0 (and u_*) showing quarter-diurnal peaks during spring tides reflect the strong tidal influence in the Upper Gulf. By contrast, during

neap tides the regular quarter-diurnal peaks became semi-diurnal, and broader confidence intervals prevailed. The switching to semi-diurnal peaks with generally prevailing negative stresses was attributed to the onset of the gravity current flows near the bed. These events dominated during the two neap-tide periods observed and caused a mean bed stress directed out of the Upper Gulf. Closer inspection of the observed neap tide conditions follows at the end of this section.

The values of the drag coefficient $C_{D1.2}$ in the present study were obtained from velocity measurements in the upper part of the logarithmic layer (more than ~ 1 m from the sea bed). This implies that the drag coefficient estimates may have included a bed form drag effect besides that of skin friction (Smith and McLean, 1977; Dyer, 1986). A large dispersion and time change in $C_{D1.0}$ ($h=1$ m) has been attributed in other studies to an increase in bed roughness due to bed form growth in mobile beds in response to changes in bed stress. These bed forms develop mainly as ripples in sandy deposits, but not in beds containing significant portions of silt and clay like the bed deposits the Upper Gulf.

It has been accepted that the drag coefficient is depth-dependent, and that higher values would be expected as the reference velocity moves closer to the sea bed (Soulsby, 1983). The results of this study are consistent with this concept since, as shown in Table 5.1, C_D decreased to 6.2×10^{-3} and 4.3×10^{-3} as the reference velocity was set at 4.2 and 12.2 m above the sea bed, respectively.

It is instructive to compare these results with values obtained in other studies, in particular with those derived from similar hydrodynamic conditions and measurement methods. The computed C_D based on $U_{1.2}$ exceeded by a factor of 3–4 the usual values based on the vertically averaged velocity. It is slightly larger than that reported by Lueck and Lu (1997) from ADCP velocity profiles measured in water 30 m deep and for similar tide conditions. Based on velocity measured 1 m above the sea bed they reported $C_{D1.0} = 9 \times 10^{-3}$, which compares well with $\sim 10^{-2}$ obtained in this study. Large $C_{D1.0}$ values are not uncommon in earlier studies of tidal flow regimes: Sternberg (1968) has reported a large spread in $C_{D1.0}$ estimates based on log-profile analysis, ranging from 10^{-3} to 10^{-2} . Ludwick (1975) reported a mean value of 13×10^{-3} for the entrance to Chesapeake Bay, but two thirds of the values obtained were between 3.5×10^{-3} and 5.4×10^{-2} . Chriss and Caldwell

(1982) estimated drag coefficients from 3.2×10^{-3} to 8.8×10^{-3} under hydrodynamically rough flow conditions. Green and McCave (1995) found that although a mean $C_{D,0}$ for the Irish Sea was close to the typical value of 2.5×10^{-3} , the variation included values from 0.8×10^{-3} to 10×10^{-3} . Values of C_D exceeding the typical value have been reported associated with large values of z_0 , as shown by Gross and Nowell (1983), Whitehouse (1995), Green and McCave (1995), Collins *et al.* (1998), Lueck and Lu (1997) and Cheng *et al.* (1999). The last two studies were based on ADCP measurements under conditions similar to those of the present work. Lueck and Lu reported $C_{D,0}$ of 8.6×10^{-3} to 12.5×10^{-3} with only 70% of $z_0 < 0.05$ m and 30% smaller than 0.01 m. Cheng *et al.* obtained $C_{D,1.56}$ of 5×10^{-3} to 6×10^{-3} and corresponding z_0 between 0.03 and 0.04 m. Green and McCave attributed the large variation in z_0 to the lack of neutrally stratified conditions in which high concentration of suspended sediment created stable stratification near the bed. Near-bed stratification may have affected the observations made in the Upper Gulf however, no SPM observations were made closer than ~ 1 m from the bed.

A non-zero y-intercept in the u_*^2 vs. U^2 regression shown in Figure 5.9 and Table 5.5 was unexpected. It would imply that a bed stress is exerted in quiescent conditions, which is a physically unsound result. The non-zero y-intercept was attributed to a phase difference between the calculated friction velocity and the current velocity at different reference heights above the sea bed. Phase differences may occur in the presence of large vertical gradients of velocity near the bed, at times close to current reversals. Earlier reports have stated that bed stress (or u_*^2) is not quite in phase with the reference velocity (Soulsby, 1983). A phase lag arises because the upward transfer of the bed frictional effects is not instantaneous in the water column. The following calculations illustrate this effect: The correlation between u_* and U at different heights indicates that the friction velocity lagged 1 time step (0.5 h) behind the current velocity at 1.2 m above sea bed. By contrast, at 16 m above the bed, the friction velocity was ahead by 1 time step. At some intermediate level both would be in phase. In order to resolve better the time lag, the log-layer fit was performed on a sequence of velocity profiles averaged over 10 min (the mean of two consecutive profiles) instead of the 30-minute averages. The new results were similar: the friction velocity was 2 time steps (20 min) behind the current velocity at 1.2 m, and 1 time step (10 min) ahead of the current velocity at 16 m above the sea bed. Both current velocity and friction velocity were in phase at 8–10 m above the bed.

Two shortcomings in the log profile method were identified in the present analysis:

- a) The phase difference between the friction velocity (or bed stress) and the current velocity at various levels. This could result from acceleration effects and the adjustment time of the current profile. The extreme effect of this phase difference was to link non-zero bed stress with zero velocity. This in turn leads into the following:
- b) The non-zero intercept in the linear regression to estimate the drag coefficient C_D .

In Figures 5.8 and 5.9 there are clusters of points of relatively large u_*^2 for small U^2 which seem to lie out of the linear trend. It was found that log profile fits having $R \geq 0.95$ were more frequent during decelerating flows than during the accelerating current (Figure 8.3). Based on the adopted validity conditions, logarithmic fits under the slow currents of the early acceleration stage were rejected. By contrast, during the deceleration stage the logarithmic fits were valid under slow currents having the same magnitude.

Neap tide conditions.

Neap-tide currents in the lower half of the water column at site W3 were not typical of a shallow, well-mixed tidal sea. During spring tides, velocity decreased toward the sea bed, as expected in tidal boundary layers regardless of ebb or flood conditions. Neap tide profiles, by contrast, revealed a significant increase in velocity reaching a maximum 5–6 m above the sea bed, then a decrease toward the bottom (Figure 5.3b). Individual profiles display a 0.3 m s^{-1} maximum within the flow core, while above it the velocity remained at about 0.2 m s^{-1} . Since the near-bed current opposed the tidal flow reversal, a net southeast flow developed toward the deeper waters outside the Upper Gulf. The effect on the residual displacement can be seen in Figure 4.6b, at both ends of the progressive vector diagrams at 5 m above the sea bed. The two near-bed residual flow events observed were due to the onset of gravity current episodes as tidal mixing decreased during neap tides. The temperature, salinity and σ_t time series shown in Figures 4.12, 4.15, as well as the

down slope, near bed flow shown in Figures 5.2, 8.7 and 8.8 correspond to the hydrography and circulation of an inverse estuarine regime.

Despite the modification of the tidal boundary layer observed in the present study, some logarithmic profile fits were obtained below the current core maximum velocity, as shown in Figure 5.4b. The computed bed stress under this condition was mostly negative and displayed weak semi-diurnal peaks instead of the strong quarter-diurnal peaks of the remaining part of the series. Despite the vertical stratification and current unsteadiness during these gravity current events, the adopted R values of the least squares fits revealed a logarithmic flow structure below the current core, within ~5–6 m from the sea bed. Earlier laboratory experiments have shown that the velocity distribution below the level of maximum velocity in gravity flows is logarithmic and determined by the roughness of the bed (Middleton and Southard, 1984). However, the bed stress calculated in the neap tides is rather high, as is the drag coefficient based on the regression of u_*^2 vs. U^2 . The slope $C_{D1.2}$ so derived was 21.3×10^{-3} . There is no explanation for these results and research is needed to further understanding of the frictional regime in neap tides, under the effects of the gravity current flow. An increase in drag can result from larger bed roughness due to an increase in bed form size, however development of bed forms is not feasible under these slow neap tide currents. Since this is the first study of its kind in the Upper Gulf, the $C_{D1.2}$ values derived under neap tides remain as a first approximation until additional data and an alternative method is available for comparison. It is evident that during neap tides the velocity profile above mid-water depth was uncoupled from that below this depth due to the intrusion of out-flowing water near the bed. Thus, computing the bed stress by the quadratic law may lead to errors if the reference velocity is measured above mid-water levels under neap-tide conditions. A better estimate of τ_0 via the quadratic law should be based on near-bed measurements, say, within 3 m from the bottom. This is critical in sediment resuspension studies for which proper evaluation of the bed stress is essential.

8.2. SPM concentration and tidal effects.

The general trend of increasing SPM concentration with depth revealed that the main source of suspended matter was the bed sediment deposit. The resuspension and settling cycles of the bed sediments revealed also the dominant influence of the semidiurnal tide during most of the fortnightly cycle, since SPM concentration and current velocity (or the bed shear stress) were well correlated, mainly near the bed. The strong quarter-diurnal SPM signal was forced by the tidally dominated flow at the M_2 frequency especially around spring tides. The twin-peak structure in the series of SPM concentration has been widely recognised as the superposition of a quarter-diurnal resuspension signal and a semidiurnal advection signal due to the displacement of a background concentration gradient (Weeks and Simpson, 1991; Jago *et al.*, 1993; Jones *et al.*, 1994). Another proposed mechanism is the asymmetry in ebb-flood velocity cycles resulting in uneven SPM maxima, as suggested by Jago and Jones (1998), Hill (1999) and Hill *et al.* (2003). A combination of these two processes seems a plausible explanation for the twin-peak structure present in the spring tide series, especially at site E1 shown in Figure 4.19. The lower SPM concentration observed in neap tides reflects the decrease in current velocity and bed shear stress. The quarter-diurnal signal persisted throughout the fortnightly cycle in the series from site E1 where the flow was dominated by the semidiurnal tide. In contrast, at the western sites J and W3 during the neap-tide part of the cycle, an ebb-flood asymmetry revealed the influence of a near-bed gravity current flowing out from the Upper Gulf, as discussed in Section 8.4. Under this neap-tide flow, the resuspension signal in the SPM series was semidiurnal instead of quarter-diurnal, as shown in Figures 4.13b and 4.16b. This was a direct consequence of the inverse estuarine conditions observed in June 1996 at site J, and in August 1997 at site W3, when the decrease in vertical mixing during neap tides allowed the down-slope flow of denser water close to the bed. Similar gravity current flows are known to occur in other inverse estuaries like those in southern Australia (Nunes and Lennon, 1986; Nunes and Lennon, 1987; Bowers, 1989; Nunes Vaz *et al.*, 1990). However, the present study is the first account of the observed effect of a gravity current on the resuspension of bed sediments. The widely accepted model relating the quarter- and semi-diurnal frequencies in SPM concentration with M_2 tidal resuspension and advection does not fully apply to the Upper Gulf of California. Here the gravity current episodes, typical of inverse estuaries, were observed

to enhance the neap-tide ebb current and bed stress, and generate a semidiurnal signal in SPM concentration which was due not to pure advection, but mainly to resuspension. As shown in Figures 4.13b, 4.16b and 4.19b, the semi-diurnal peaks in near bed SPM concentration were nearly in phase with the velocity peaks at this frequency during neap tides.

It is unlikely that the short-crested waves observed during the survey contributed significantly to the resuspension and transport of sea bed sediments at depths 25-30 m where observations were made. Linear theory predicts that the maximum orbital velocity due to 1.5 m waves at 5 s intervals is less than 0.02 m s^{-1} at this depth. According to Gayman (1969), the prevailing sea breeze waves probably do not stir up sea bed sediments in water depths more than $\frac{1}{4}$ wavelength. The wave action of a 4 s wave is limited to a depth of 6 m. Waves of longer periods are rare.

8.3. Suspended sediment dynamics.

Concurrent time series of SPM and bottom stress $|\tau_0|$ indicate that the maximum values of both series were nearly simultaneous. A slight phase difference can be associated with the “twin-peak” effect: the first peak in SPM concentration appears delayed relative to the bottom stress, while the second SPM peak is advanced. In contrast, the minimum values in SPM concentration were consistently delayed with respect to the minimum bed shear stress. This delay was interpreted as a threshold for erosion of the sediment deposit. The bottom stress had to increase up to a critical value τ_{0e} before the bed sediments were lifted from the bed.

Fine slow-settling sediments having a clay fraction as low as 5% to 10% behave as cohesive (Dyer, 1986). This can be expected for the bed sediments in the Upper Gulf, based on the textural composition reported by Thompson (1968) and Carriquiry and Sánchez (1999). However, the bed shear stress and SPM concentration were nearly in phase, i.e. the SPM concentration started to decrease when, or shortly after the bed shear stress did. This was observed in the concentration time series of both integrated and single level SPM time series at $\sim 1\text{m}$ above the bed. Many studies on cohesive sediment

transport have assumed mutually exclusive erosion and deposition, as shown by Sanford and Halka (1993) and references therein: Erosion of the bed sediments only begins after the bed stress exceeds a critical value τ_{0e} (the erosion threshold), and deposition to the bed takes place when the bottom stress decrease below τ_{0d} (the deposition threshold). Since $\tau_{0e} \geq \tau_{0d}$ there is a range of stress values for which no erosion or deposition takes place. By contrast, in non-cohesive sediment transport models a deposition threshold is not included so continuous deposition is possible. The conceptual difference between these two models is shown in Figure 8.4 in which the relative phases of SPM and bed shear stress can be compared. The SPM time series of the Upper Gulf (for instance, those shown in Figure 6.3a) reveal that the erosion-deposition cycle corresponds better to the model for non-cohesive sediments. The total SPM concentration started to decrease at nearly the same time as the bottom stress did, so the increase in total SPM beyond time of the maximum stress was not observed. Net deposition occurred as soon as the bed stress started to decrease, in disagreement with the idealised model of mutually exclusive erosion and deposition of cohesive sediments. Sanford and Halka (1993) and Sanford and Chang (1997) reported better agreement between observed and modelled concentration when a continuous exchange of suspended sediments with the bed was assumed, independent of any critical stress for deposition. In order to simulate this process, modelling techniques have assumed that bed sediments consist of a number of particle size classes each associated with a critical erosion and deposition stress. In this case the last class eroded starts to settle very soon after the bottom stress begins to decrease. The multi-class approach seems suitable for the sediments in the Upper Gulf, since the reported mixture of poorly sorted fine sediments could be represented as a set of eroding/settling classes according to size. At the time of maximum stress, the sediment remaining at the bed would be the coarser fractions. A careful evaluation of this process would require frequent sampling of the bed sediments at a site over at least a full semidiurnal cycle.

An interesting finding was that the critical bed stress for erosion increased from neap to spring tides reaching maximum values 1-3 days after maximum spring tides. This fortnightly modulation was obtained from analysis of independent observations made at the two western sites W1 and W3, as shown in Figures 6.4 and 6.6. It was also evident that τ_{0e} decreased at a faster rate back to low values in the following neap tide. The

asymmetric erosion threshold cycle suggested by these findings was better described throughout the fortnightly cycle by periodic two-harmonic functions. Interestingly, a similar evolution of τ_{0e} with time was not observed at the eastern site E1, where the spring-neap modulation of the erosion threshold was weak, as shown in Figure 6.5.

The variable erosion threshold cannot be explained solely in terms of the observed currents and SPM. It may result from the consolidation process and grading of the bed deposit that consists of different grain-size classes ranging from fine sand to clays. The variable erosion threshold obtained by Clarke and Elliott (1998) during the spring-neap cycle was attributed to an increase in consolidation of the settled sediments during quiescent conditions. As the slack water times became longer toward neap tides, the bed sediments consolidated more, so that the highest erosion threshold occurred soon after neap tides. In contrast, the Upper Gulf data show that the maximum erosion threshold occurred during, or shortly after the maximum spring tides, i.e. when tidal currents were high. In this case the sediment consolidation process does not explain clearly the variation of the erosion threshold in the Upper Gulf. The effect of a graded bed with grain-size increasing downwards from the bed surface might explain the observed change in τ_{0e} . The active layer in the erosion-deposition process could be only a few centimetres thick. As the maximum bed stress decreases after peak spring tides, the coarser fractions settle and remain at the bed. The sediments that settle later are gradually finer until neap tide bed stresses allow the smallest fraction to deposit at the bed surface. When the maximum bed stress increases right after neap tides, the fine fraction at the bed surface is readily eroded and resuspended at lower τ_{0e} . It has been found that the bed surface may comprise two layers at slack water: a thin loose fluffy layer overlying a more rigid bed deposit. The upper layer has a threshold shear stress of 0.06 Pa to 0.1 Pa and is fairly easy to erode as the tidal current begins to increase. Erosion of this layer is often quite sufficient to explain the concentration observed throughout the water column at maximum current according to Dyer (1995).

Since the sediment fractions underneath are coarser, a larger bed stress is needed to bring them into suspension, until the maximum critical stresses required by the coarsest sediment particles are attained around spring tides. Figure 8.5 shows the photograph of a sediment core of the top 15 cm collected under fast currents during the June 1996. A bed

surface layer of coarser sediment roughly 3 cm thick overlies a lower layer of finer sediment consisting mainly of mud. This texture change was interpreted as evidence of the high erosion threshold required to lift the coarser sediment remaining at the bed while the finer fractions were in suspension. The concept of a graded sediment bed has been adopted in explaining observed SPM concentrations as well as in numerical simulations in which different textural sediment classes can be specified. This resource has allowed a closer representation of measurements in the water column (Campbell, 1996; Jones *et al.*, 1996).

8.3.1. Point models of SPM dynamics.

8.3.1.1. Vertically integrated SPM concentration.

The large discrepancies between observed and simulated SPM concentrations were due to unrealistic deposition rates. Since no deposition threshold was prescribed the deposition rate was given in terms of near bed concentration and settling velocity. Assigning proper values to these variables has been a difficult task. Compared with erosion, deposition processes have received less attention and are often not even discussed (Sanford and Chang, 1997). The erosion rates estimated for the Upper Gulf are assumed to be realistic because the mean values of the erosion parameters (like the critical values of τ_{0e} or u_*) did not change significantly from one site to another or by using a different extraction method. According to Kineke and Sternberg (1989), our ability to estimate u_* is significantly better than our ability to estimate settling velocity. In contrast, the deposition rate was a function of two variables that are difficult to measure in the field: the particle settling velocity w_s and the near bed concentration C_b .

The reported median w_s measured at site W3 was $0.1 \times 10^{-3} \text{ m}\cdot\text{s}^{-1}$, one order of magnitude smaller than data from other studies made in similar environments and sediment particle sizes. Inferred settling velocities of flocs summarized by Hill (1998) in different environments range from $\sim 0.7 \times 10^{-3}$ to $2.1 \times 10^{-3} \text{ m}\cdot\text{s}^{-1}$. In a tidal inlet and a macrotidal estuary the mean floc settling velocity was approximately $2 \times 10^{-3} \text{ m}\cdot\text{s}^{-1}$. These values compare well with settling velocities observed in estuaries, which range from 0.56×10^{-3} to

$3 \times 10^{-3} \text{ m}\cdot\text{s}^{-1}$. Simulations of SPM distribution in bottom boundary layers often require settling velocities of about $1 \times 10^{-3} \text{ m}\cdot\text{s}^{-1}$ in order to fit the data. The reported median settling velocity at site E1 ($0.23 \times 10^{-3} \text{ m}\cdot\text{s}^{-1}$) was about twice as large as that at site W3 and the discrepancy between observed and calculated SPM concentration was smaller.

The near bed concentration C_b was observed at a height of $\sim 1\text{m}$ above the bed and therefore is probably an underestimate of the concentrations closer to the sea bed. The low values contributed to the low deposition rates obtained at the western side sites J and W3. Instead of using an arbitrary height, Sanford and Halka (1993) support using an outer boundary layer bursting time scale for obtaining the height z_{oc} at which C_b can be specified:

$$z_{oc} = 6 \cdot w_s \cdot \delta_{bl} / U_{max}$$

w_s is the median settling velocity, δ_{bl} is the thickness of the boundary layer, here taken as the water depth, and U_{max} is the maximum free stream velocity during the tidal cycle. For $\delta_{bl} = 25 \text{ m}$, $U_{max} = 0.8 \text{ m}\cdot\text{s}^{-1}$, and $w_s = 0.1 \times 10^{-3} \text{ m}\cdot\text{s}^{-1}$, z_{oc} is $\sim 0.02 \text{ m}$. Assuming that the vertical distribution of SPM concentration is given by the Rouse profile during spring tide peak flow ($u_* = 0.04 \text{ m}\cdot\text{s}^{-1}$), at the height of 0.02 m C is expected to be $1.02 \cdot C_a$, where C_a is the reference concentration 1 m above the sea bed. Even if u_* is as low as $0.01 \text{ m}\cdot\text{s}^{-1}$ the increase in concentration would be only 10%. These results support the conclusion that the single value of w_s derived from settling tube observations was too low for obtaining a realistic deposition rate based on equation 6.3. The implicit assumption was that a single particle size represented the natural range of grain size and settling velocity.

One more test was made by assuming that the observed SPM concentration profiles conform to the Rouse equation and that settling velocity w_s can be estimated from concentrations at two adjacent levels close to the bed. At site W3 the available concentrations were measured at 2 m and 3 m above the bed, since casts did not reach lower levels. From the Rouse equation:

$$\frac{w_s}{\beta \kappa u_*} = \frac{\ln C_z - \ln C_a}{\ln \left(\frac{h-z}{z} \cdot \frac{a}{h-a} \right)}$$

where: $z=3$ m and $a=2$ m are the two adjacent near bed levels, $h=25$ m is the water depth, $\kappa=0.4$ is the von Karman constant, and $\beta=1$ is the ratio between the diffusion coefficients of sediment and fluid momentum. The friction velocity u^* at corresponding times was selected from previously estimated values. Tidal station time series under spring and neap tides yielded a large spread in w_s , as shown in Table 8.1. As expected, spring tide settling velocity is larger due to larger particles in suspension. Under both spring and neap tides the estimated values of w_s are larger than those obtained from settling tubes.

Table 8.1. Statistics of settling velocity obtained at site W3 from observed SPM at 2 m and 3 m above the bed, and from the Rouse profile assumption. N is the number of samples. Units are $\text{m}\cdot\text{s}^{-1}$.

	N	Median	Mean	Std. Dev.	Maximum.
Neaps	11	0.0006	0.0015	0.0016	0.0044
Springs	52	0.0022	0.0036	0.0043	0.0235

There is still considerable uncertainty regarding the measurement of settling velocity in the field. Increasing use of *in situ* video technology has consistently resulted in estimates of settling velocity many times higher than the gravimetric method based on settling tubes. The accuracy of measurements made with the Owen tube technique has been questioned due to circulations within the settling water column produced by the sampling technique. The use of median velocity may also be an over-simplification of the problem – if there is a range of settling velocities present then concentration time series may not be adequately described by behaviour of the median value. . This may be exacerbated further if the median settling velocity is changing over the tidal cycle due to flocculation/disaggregation processes. The variable settling velocity reported by Fisher (1998) at site W3, and the results of calculations based on the Rouse profile (Table 8.1) support the notion of a wide range of settling velocity values within the tidal cycle. The variability in w_s may result from aggregation and break-up of flocs due to changes in concentration and bed shear stress, as suggested by laboratory experiments (Krone, 1993; Lick and Huang, 1993). Theoretical work by Lavelle (1993) indicated that at least two settling velocity classes (micro and macro aggregates) should be included in suspended particle transport

models. Deposition rates are likely to improve by using more elaborate models that account for changes in settling velocity.

8.3.1.2. Single level SPM concentration.

Single level SPM concentration at 1 m above the sea bed followed the bed shear stress variation during most of the fortnightly cycle, especially around spring tides, when the calculated and observed quarter-diurnal resuspension peaks were similar. This is because the settling lag is likely to be smaller close to the bed than at upper levels, according to Dyer (1986). The difference between observed and calculated concentrations has provided important clues for understanding the processes occurring near the bed. The high concentration episodes observed in neap tides were not reproduced when a constant erosion threshold was prescribed. In contrast, these events were simulated when a variable threshold was prescribed having lower values in neap tides. The predicted high concentration events in neap tides were not completely in phase with the observed peaks, as if these were not due to local resuspension. This phase difference may result from advection of high SPM concentration clouds resuspended elsewhere along the stream path. Gravity current events observed during the two neap tide periods are likely to have developed resuspension-advection processes close to the sea bed bringing high concentration to the observation site. The near-bed nature of the high concentration events can be observed in Figure 6.3b in which the vertically integrated SPM concentration at site W3 reflects only slightly the remarkable increase in concentration at a single level 1m above the bed. Furthermore, these events have occurred under neap tides, when the bed stress was small but sufficient for resuspending fine particles, provided that the erosion threshold was low, as was shown to occur at site W3. Dyer (1986) summarised results from various authors showing that the thin surface layer of loosely held flocs seems to erode at a shear stress of ~ 0.1 Pa. Once this layer has been suspended, the underlying deposits generally has a critical erosion shear stress of ~ 1 Pa. In the Upper Gulf the estimated erosion threshold in neap tides was 0.01 to 0.26 Pa. Thus, the resuspension of a fine fluffy layer is likely to have caused the high concentration events in neap tides, restricted to the lower levels ~ 1 m from the bed. The high SPM concentration events were recorded by the OBS sensors at the western sites W2 and W3 but not by the transmissometers at the western site W1 (3.9 km from W3) and at the

eastern site E1. This may indicate that the high concentration events did not occur at these sites, or that the optical response of the instruments to sediments in suspension was different. Beam attenuation and SPM concentration are linearly well-correlated if the effects of particle shape, size and refraction index are negligible or mutually compensating. The most influential variable is particle size. The size effect is shown by the fact that very fine silt (particle size 8.5 μm) attenuates 660 nm light 15 times more efficiently than medium to coarse silt (particle size 48 μm) (Gordon *et al.*, 1980; Baker and Lavelle, 1984). The transmissometer is more sensitive to fine particles than to coarse particles (being relatively insensitive to particles coarser than 80 μm – this is because larger particles forward scatter light into the sensor of the transmissometer (which has a beam acceptance angle of 1 degree), thereby reducing the beam attenuation and hence the measured concentration. Furthermore, laboratory experiments have shown that the beam transmissometer is more sensitive to clay-sized particle than is the OBS (Benms and Pilgrim, 1994). Thus, the high concentration events during neap tides could have been flocculated particles resuspended from the low threshold “fluff layer” developed during neap tides.

8.4. SPM fluxes.

8.4.1. SPM and the acoustic backscatter signal.

There has been considerable interest recently in converting acoustic signal strength measured by acoustic Doppler current profilers to SPM concentration (Jones *et al.*, 1994; Thorne *et al.*, 1996; Holdaway *et al.*, 1999). The calibration methods adopted have ranged from obtaining simple height dependent calibration coefficients to full consideration of particle size dependence and attenuation of the signal received from a given layer by SPM in the intervening layers. Most studies have concluded that the technique is sensitive to variations in particle size, and it has been shown that SPM attenuation can act to increase apparent concentrations by up to 26% in high concentration environments (Holdaway *et al.*, 1999). This study considers spreading and attenuation by water but not by SPM; nevertheless, a convincing calibration has been found using samples from a range of heights above the bed.

At short ranges (~ 1.5 m) and low concentrations ($< 1000 \text{ g}\cdot\text{m}^{-3}$), the attenuation of the acoustic signal by suspended fine sand is only slight. This effect can be neglected in estuarine sediment suspensions if concentrations are less than $100 \text{ g}\cdot\text{m}^{-3}$ (Thorne *et al.*, 1993). In our measurements, the range was longer and the concentrations were lower: maximum spring tide concentrations 1 m above the sea bed reached $85 \text{ g}\cdot\text{m}^{-3}$ only during short time intervals. Further up, near the top of the water column analysed, concentrations were $\sim 50\%$ lower. Hence, attenuation by suspended particles was assumed to be small. However, uncertainties introduced by changes in the particle size may be important in natural environments. Since bed sediments of the Upper Gulf are poorly sorted, changes in the bed stress due to the oscillatory tidal current are likely to change the size distribution of suspended sediments. Moreover, the presence of fine silts and clays is expected to cause flocculation and therefore increase the effective particle size. Our measurements were not sufficient for a detailed evaluation of these effects; however, a comparison with earlier studies has provided bounds for the expected uncertainties in concentration. Thorne *et al.* (1991) have accounted for the effect of variable particle size by introducing a constant k_o that incorporates the scattering properties of the particles in suspension. In their study, the particle size varied from 55 to 210 μm and the detection range was up to 1 m using a 3 MHz system. A change in particle size by a factor of four produced $\sim 20\%$ change in k_o . It was also estimated that a 10% uncertainty in k_o translated into a 20% uncertainty in concentration values. During our observations the median particle size near the bed varied within a factor of four (40 to 180 μm) throughout the spring-neap cycle (Jones, *et al.*, in preparation). Therefore we can expect that uncertainties in the acoustically estimated concentration were less than 50% in the lower levels of the concentration profiles, and it can be assumed that the effects of variable particle size and attenuation by suspended sediment have introduced uncertainties having magnitude similar to the error of the regression equation. Conversion of ADP signal strength to SPM concentration has therefore allowed the estimation of instantaneous and time-averaged horizontal fluxes of SPM between 2.7 and 10.7 m above the bed under contrasting flow and SPM concentration conditions during a fortnightly cycle. A more detailed calibration may be needed before finer details of the temporal and vertical variation of flux profiles can be relied upon.

The near-bed region could not be calibrated using the method described as no concentration samples were collected in this near-field region of the transducers. This region may contribute significantly to depth-integrated fluxes as measured concentration profiles often indicate sharp increases toward the bed. However, currents decrease rapidly in this region and the flux profiles during periods of high flux indicate a maximum at 4 m above the bed, well above the limit of measurement. Therefore, it is likely that the main features of near-bed flux have been measured in this study.

8.4.2. Horizontal SPM flux.

Two key factors influencing SPM flux have been identified within the 15-day intensive sampling period: the spring neap modulation, and the near bed gravity current associated with inverse estuarine conditions. The roles of the along-gulf bathymetric features and contrasting dynamic conditions across-gulf were less evident but it has been possible to speculate about their potential influence. The large range of the barotropic tide in the Upper Gulf generates fast currents and large horizontal tidal excursions up to 10 km near the surface, during spring tides. However, tidal residual flows are $\sim 0.01 \text{ m}\cdot\text{s}^{-1}$ according to numerical models. (Carbajal, 1993; Marinone, 1997; Argote *et al.*, 1998;). Therefore, residual displacement of a particle due to tides is less than 0.5 km in one semidiurnal period and SPM flux produced by this mechanism is approximately $0.3 \text{ g}\cdot\text{m}^{-2}\cdot\text{s}^{-1}$. This residual flux is smaller than that associated with the baroclinic near bed current.

8.4.2.1. Gravity current effects.

Gravity currents, first observed in this region by Lavín *et al.* (1998), are shown here to produce near-bed fluxes that, despite their short duration, are one order of magnitude larger than those induced by tidal residual currents, at least during summer. Therefore, the gravity current can be expected to be the main cause of SPM flux during each neap tide, and hence to contribute significantly to net fluxes during summer. Furthermore, the salinity observed in Wagner Basin has been explained in terms of water mass formation occurring throughout the year, in the shallow areas. The dense, high salinity water mass flows down-slope toward the basin as sporadic gravity current pulses (Lavín *et al.*, 1998). Thus, sediment fluxes induced by the near-bottom gravity current may occur not only

during summer, but also through the year. The present study has revealed that a net transport of fine sediments is occurring out of the Upper Gulf. However, contrary to what has been speculated, the barotropic tidal residual is not the main cause. The baroclinic gravity current was found here to be the dominant mechanism for near-bed SPM flux toward deeper waters. The contrast between the hydrography, SPM and currents during spring tides and those in neaps on the west side of the Upper Gulf is summarised graphically in Figures 8.6 to 8.8.

The near-bed fluxes based on OBS measured SPM concentration are in general agreement with those derived from the acoustic signal strength. The net sediment flux during neap tides was dominated by the gravity current outflow on the west side of the Upper Gulf in June 1996 and in August 1997 as shown in Table 7.1. The asymmetry in the along-gulf velocity during neap tides shows a prevailing outflow that was not observed during spring tides. In contrast, at site E1 off the east coast, ebb and flood currents were nearly symmetric during neap tides at the time when marked asymmetry was observed at site W3 on the west side, as shown in Figure 7.6. In support of this, the progressive vector plots in Figure 7.9, based on simultaneous velocity measurements at sites E1 and W1 also revealed different net displacements at 4.2 m above the bed, in a time scale of ~ 1 day.

Constraints imposed by the coast and earth rotation seem to restrict the gravity currents to the western side of the Upper Gulf. This is a plausible explanation for the absence of net outflow during neap tide observations at site E1, in contrast with observations made on the west side. Furthermore, this difference agrees with the notion of a cyclonic circulation in the Upper Gulf with southward flow occurring along Baja California, enhanced by gravity current episodes. The mean fluxes during neap tides revealed a significant near-bed export of SPM on the west side, but not on the east side. This may indicate that SPM flux induced by gravity currents did not occur on the east side of the Upper Gulf.

8.4.2.2. Topographic effects.

As shown in Chapter 4, the gravity current core was observed within 6-7 m from the bed. Therefore, the bathymetry may have significant effect on this type of flow. The bottom relief shows several narrow along-gulf submarine ridges up to 40 km long and 15 m high.

The ridges off Baja California form channels 8-10 km wide having an asymmetric cross section with gentler slopes on the west side (Fig. 3.1). By joining the head of the Upper Gulf with the Wagner Basin, these channels must play an important role in along- and across-gulf exchange processes, especially in those that take place near the bed. As suggested in Figure 7.4(b), sediments in suspension seem to be conveyed through the channels to the deeper waters of Wagner Basin. Transect B made along the second channel off Baja California revealed a down-channel decrease of SPM concentration, in support of this idea. The horizontal intrusion of turbid water at 50 m depth indicates that part of the suspended sediment load reached the edge of the Wagner Basin, while another fraction seems to have settled along the current path. If sediments were settling mainly on the western side of the channel, an asymmetric cross-section would develop in the long term. This process might explain also the seaward growth of the shallow western shelf, in agreement with the suggestion by Carriquiry and Sánchez (1999) that this shelf is a slowly prograding feature.

One can speculate on an asymmetric sediment deposition based on rotation effects. The earth's rotation constrains a gravity current to flow along the western boundary of a channel (in the Northern Hemisphere) if time and space scales are sufficiently large. A crude estimate can be made to test whether the conditions in the Upper Gulf would allow for this adjustment: The shallow head and western side of the Upper Gulf are the sources of heavier water which is ~ 0.2 sigma-t units denser than the water found further offshore (Lavín *et al.*, 1998). By taking a 10 m water depth, the internal Rossby radius of deformation gives a cross-flow scale of less than 4 km, which is about half the width of the channels and about one tenth their length. Since the time scale for geostrophic adjustment is ~ 1 day ($2\pi/f$) and the gravity current event lasts at least 3 days, then this current could evolve into a flow along the western boundary of the channels. This type of buoyancy driven flow along a boundary has been observed in laboratory rotating tanks by Wadhams *et al.* (1979) and Griffiths and Hopfinger (1983), among others. Thus, a plausible explanation for the eastward progradation of the western boundary of the channels involves the settling of suspended load that the gravity current transports mainly along the western side of the wide along-gulf depressions. More observations at adequate scales are needed before a precise evaluation of this concept can be made.

8.5. Concluding remarks.

A tidal logarithmic bottom boundary layer was observed during most of the fortnightly cycle when the water column was vertically mixed, except during times near slack water and during neap tides.

The SPM load in the Upper Gulf varied in general from 10^{-2} to $10^{-1} \text{ kg}\cdot\text{m}^{-3}$. The highest concentrations occurred near the sea bed, which was identified as the main source of suspended matter.

SPM concentration was controlled by resuspension induced by the prevailing semidiurnal tide currents, as shown by the quarter-diurnal, fortnightly modulated peaks in the SPM time series. An exception to this occurred during neap tides, when interaction between the slow tidal current and near-bed gravity current events induced weak resuspension peaks at the semidiurnal frequency.

The bed shear stress–SPM concentration behaviour fits the continuous deposition model better than the mutually exclusive erosion-deposition model.

A simple erosion-deposition point model overestimated the observed SPM concentration due to an excess of erosion over deposition. This was ascribed to an underestimation of the prescribed particle settling velocity.

The erosion threshold varied during the fortnightly cycle, with lower values during neap tides. This result is in agreement with the concept of different particle size classes and associated threshold values.

SPM fluxes were mainly along-gulf. A net flux out of the Upper Gulf was induced by near-bed gravity current events during neap tides. This flux was one order of magnitude larger than that induced by the tidal residual current.

8.6. Ways forward.

The role of gravity currents in relation to suspended sediment fluxes in the long term, i.e. seasonal and yearly time scales, should be studied. It has been suggested that optimum conditions for the development of gravity currents may occur in late fall or winter, though no data is presently available.

It has been hypothesised that the gravity current is affected by rotation and constrained to flow along the western side of the along-gulf channels. Observations of the flow structure along sections normal to the channel axis using ADP/ADCP would provide evidence of any flow asymmetry during the gravity current events. Concurrent SPM concentration measurements would reveal whether along-gulf fluxes of suspended sediment do have asymmetries along sections normal to the channels. Studies on the deposition pattern along the gravity current flow and ridge morphology could also be undertaken.

The available data are insufficient to reveal where the high density, high turbidity water is stored at the time when the gravity current events are triggered. Is there only one source at the head of the estuary, or are there other sources along the western side of the Upper Gulf? Is there a temperature-salinity-SPM concentration relationship that is typical of the gravity current water? More detailed spatial surveys of the hydrography, SPM and currents are needed concurrently with remote sensing imagery. Suitable interpretation of satellite data can also be a valuable tool for assessing the synoptic gulf-wide spatial distribution of suspended matter near the sea surface. This can hardly be achieved by ship-borne observations alone.

The nature of the sea bed is known only in an “averaged” sense. A more dynamical and direct knowledge of the textural properties of the bed deposits is needed: variation of grain size during the tidal erosion-deposition cycles, development of bed forms, the presence and nature of a fluff layer during periods of low bed shear stress are key issues for future studies.

Another challenging problem is posed by the need for observations in the water column. Current velocity and SPM concentration data were missing within 1 m from the sea bed

in the present study. Measurements of velocity and SPM concentration should be made closer to the bed. Better estimation of boundary layer parameters such as the bed roughness scale and the critical bed shear stress for erosion/deposition can then be made. Turbulence measurements by high-speed sampling sensors could provide independent estimates of the critical shear stress and the drag coefficient.

Future modelling should include point models that account for the effect of near bed density stratification on the eddy viscosity and SPM concentration profiles. The influence of near surface vertical mixing due to waves could also be addressed. The settling velocity prescribed for modelling the erosion-deposition balance in this study was an obvious oversimplification. Point models should include at least fast- and slow-settling particles or, preferably, a settling velocity spectrum. The variable erosion threshold proposed in this study should be analysed further through observations and modelling. The development of point models is a logical step towards fully three-dimensional models.

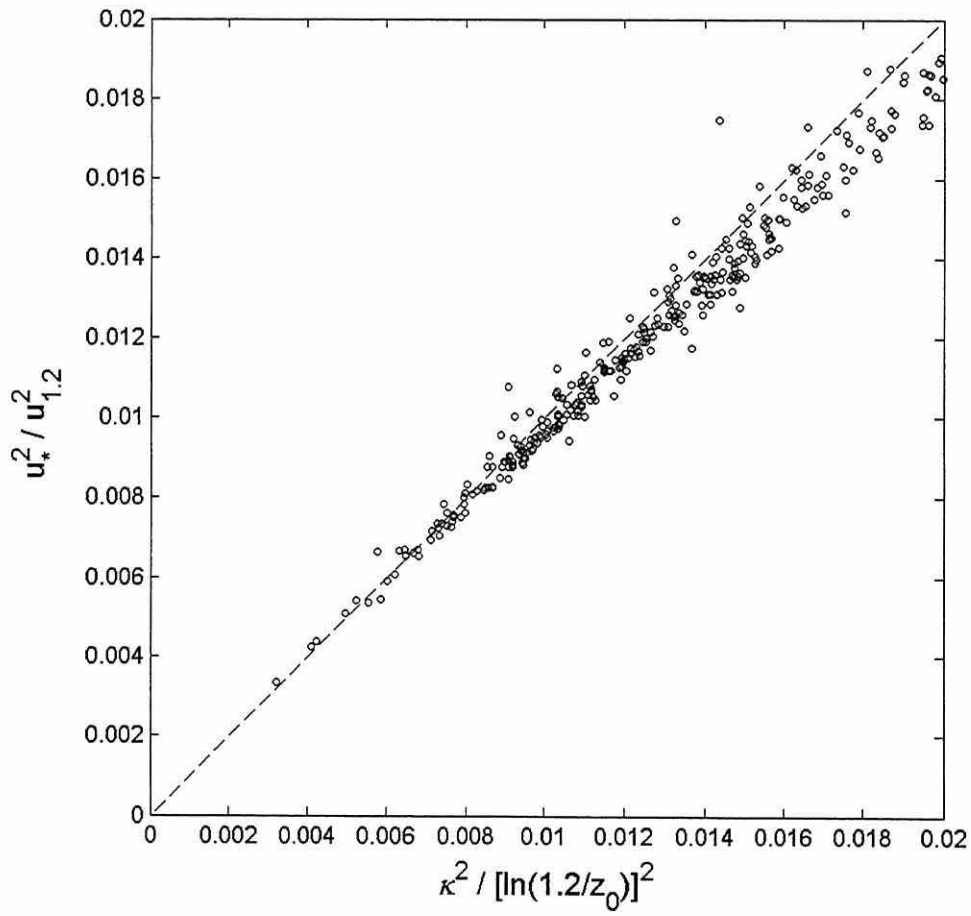


Figure 8.1. Relationship between $C_{D1.2}$ from the quadratic law (y-axis) and that from the logarithmic profile law (x-axis), as an internal consistency test following Collins *et al.* (1998). The dashed line has slope 1 as reference.

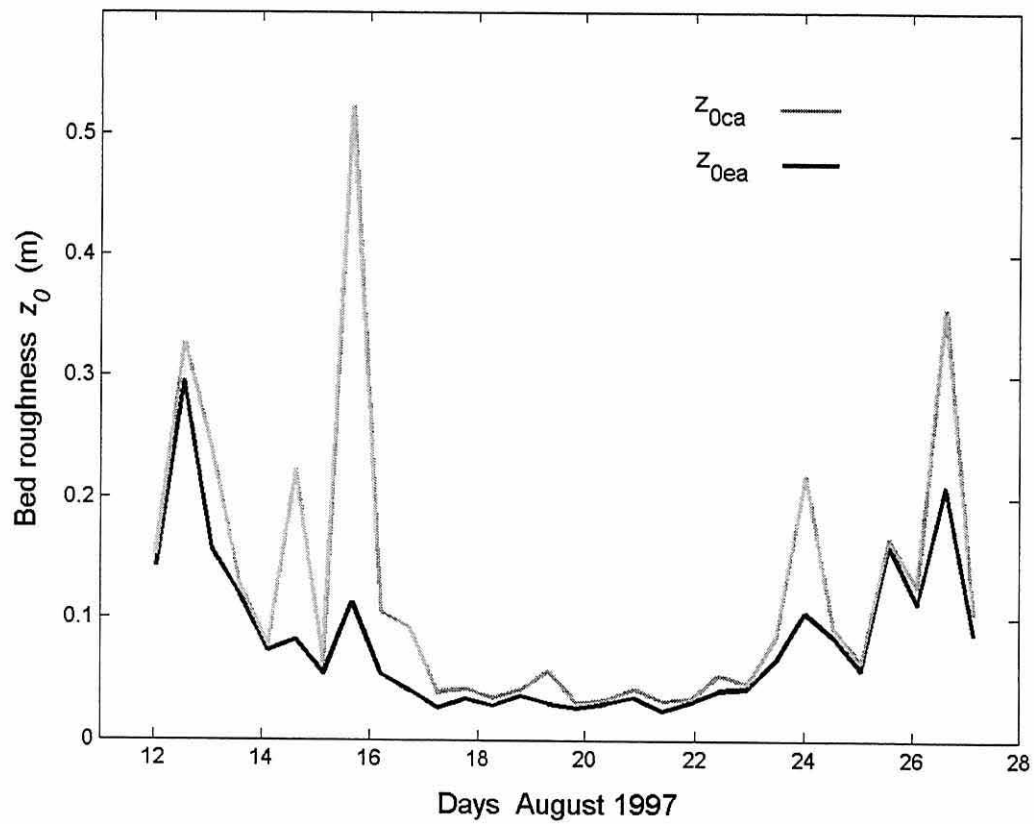


Figure 8.2. Fortnightly variation of the bed roughness z_0 averaged over consecutive semidiurnal cycles. Conventional average (z_{0ca}) and exponent average (z_{0ea}), after Cheng, *et al.* (1999).

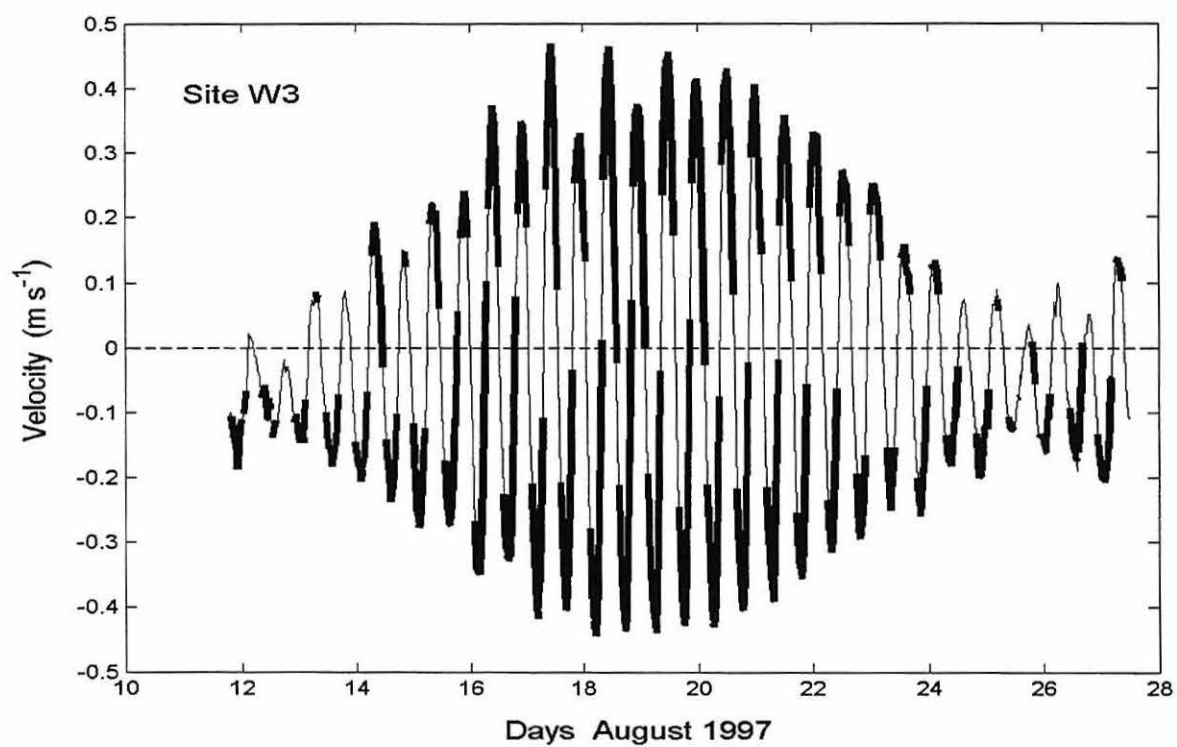


Figure 8.3. Along-gulf velocity 1.2 m above the sea bed at site W3 (thin line). The superimposed heavy line corresponds to time intervals during which the logarithmic profiles were valid ($R \geq 0.95$).

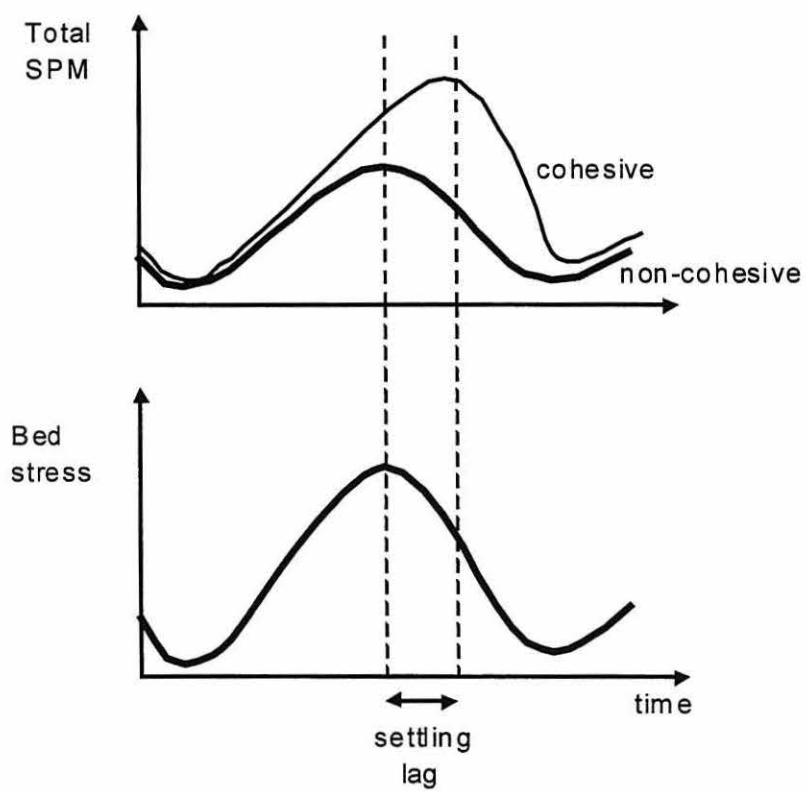


Figure 8.4. Hypothetical behaviour of SPM concentration and bed shear stress as described by two conceptual models: the continuous deposition model (non-cohesive sediments), and the mutually exclusive erosion and deposition model (cohesive sediments), after Sanford and Halka (1993).

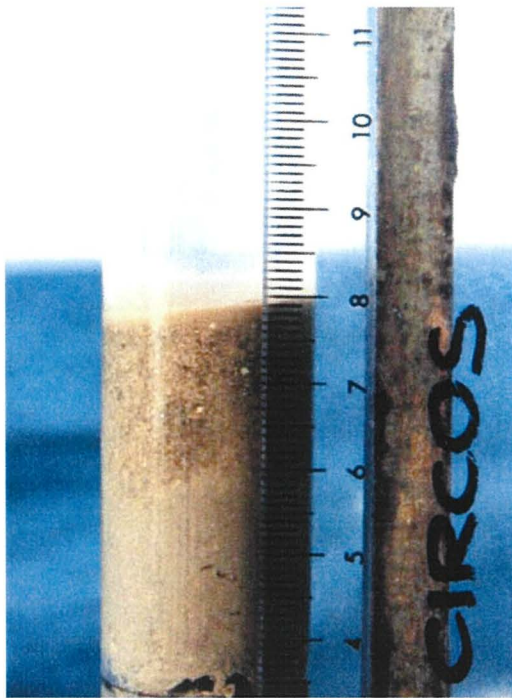


Figure 8.5. Segment of a core showing the upper 5 cm of the sea bed sediments in the central Upper Gulf. The core was obtained during spring tides when current speed was $\sim 0.7 \text{ m s}^{-1}$. The top 2 cm show coarser texture overlying muddy sediments. The thin surface film was a fluff layer that settled from the water column trapped inside the core.

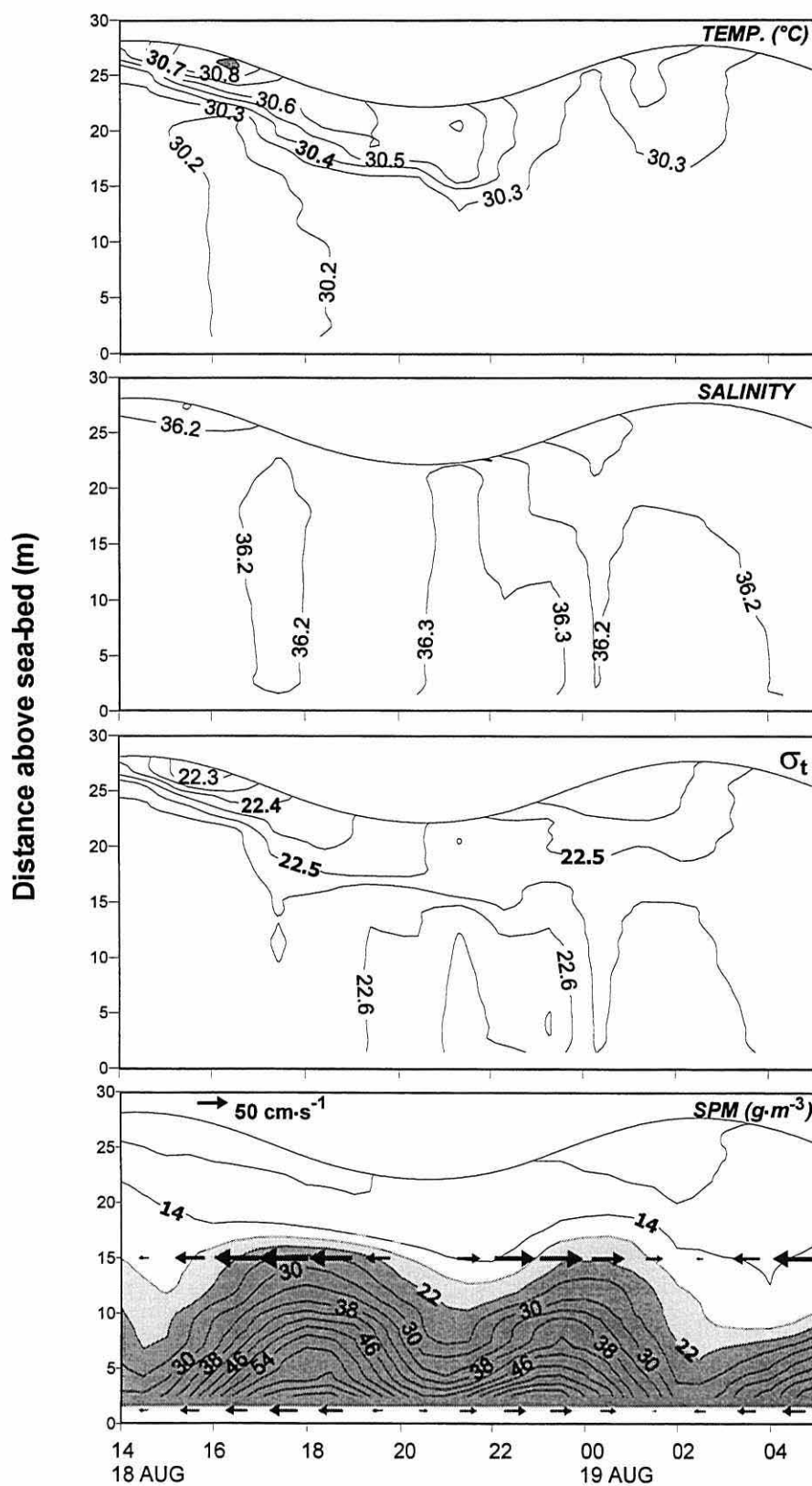


Figure 8.6. Spring tide temperature, salinity, sigma-t and SPM concentration from casts made every half-hour at site W3, in August 1997. Along-gulf velocity vectors drawn in the lower frame are at 1.2 m and 15.0 m above the sea bed. Arrows pointing to the left indicate outflow from the Upper Gulf.

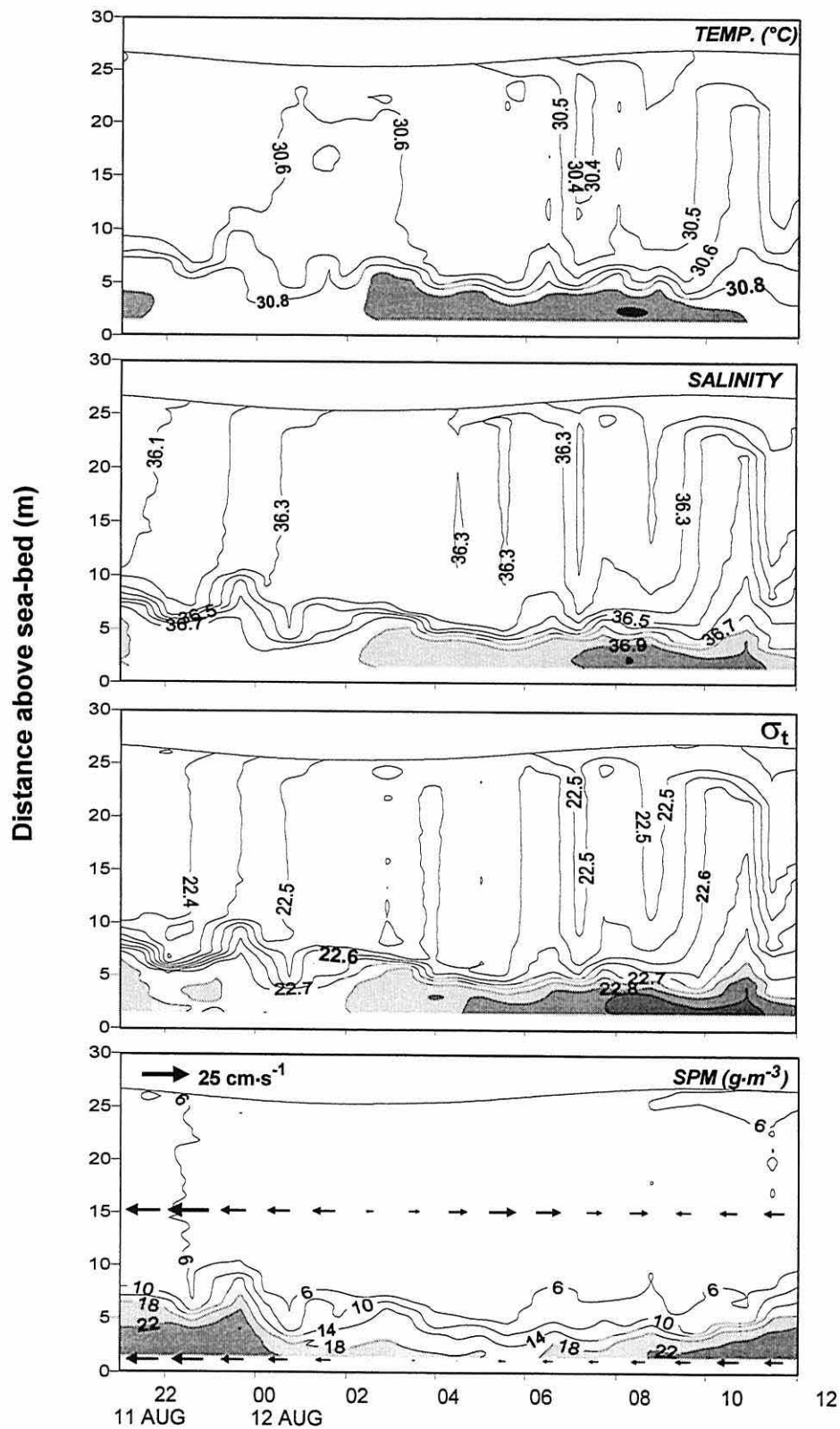


Figure 8.7. Neap tide temperature, salinity, sigma-t and SPM concentration from casts made every half-hour at site W3, in August 1997. Along-gulf velocity vectors drawn in the lower frame are at 1.2 m and 15.0 m above the sea bed. Arrows pointing to the left indicate outflow from the Upper Gulf.

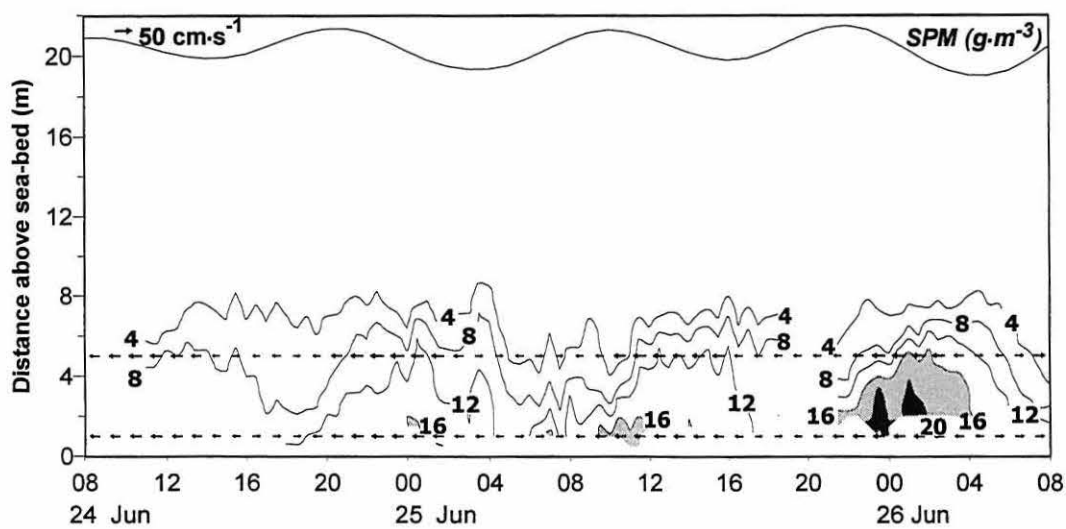


Figure 8.8. Neap tide SPM concentration from casts made every half-hour at site J, in June 1996. Along-gulf velocity vectors are drawn at 1 m and 5 m above the sea bed. Arrows pointing to the left indicate outflow from the Upper Gulf.

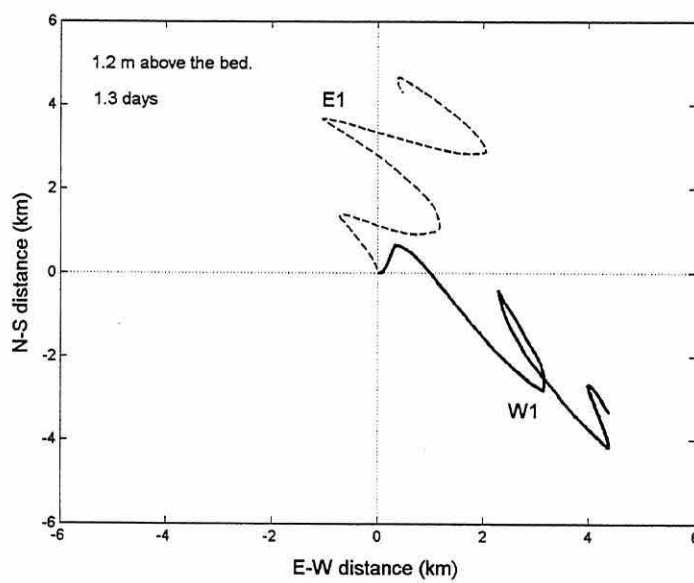


Figure 8.9. Progressive vectors plot using simultaneous velocity data from opposite sides of the Upper Gulf during neap tides, at 1.2 m from the bed: W1 (west side) and E1 (east side). The plot represents 1.3 days.

References.

Aberle, J., Nikora, V., McLean, S., Doscher, C., McEwan, I., Green, M., Goring, D. and Walsh, J. 2003. Straight benthic flow-through flume for in situ measurement of cohesive sediment dynamics. *Journal of Hydraulic Engineering*, 129, 1, 63-67.

Alvarez-Borrego, S., Flores-Baez, B.P. and Galindo-Bect, L.A. 1975. Hidrología del Alto Golfo de California II. Condiciones durante invierno, primavera y verano. *Ciencias Marinas* 1, 46-64.

Amos, C.L., Daborn, G.R., Christian, H.A., Atkinson, A. and Robertson, A. 1992. In situ erosion measurements on fine-grained sediments from the Bay of Fundy. *Marine Geology*, 108, 175-196.

Argote, M.L., Amador, A., Lavín, M.F. and Hunter, J.R. 1995. Tidal dissipation and stratification in the Gulf of California. *Jour. Geophys. Res.* 100, 16103-16118.

Argote, M.L., Lavín, M.F. and Amador, A. 1998. Barotropic residual circulation in the Gulf of California due to the M_2 tide and wind stress. *Atmósfera* 11, 173-197.

Austin, R.W. 1972. Surface truth measurements of optical properties of the waters in the northern Gulf of California. In: Fourth Annual Earth Resources Program Review. Vol. 4. NASA Manned Spacecraft Center. Houston, Texas.

Baba, J., Peterson, C.D. and Shrader, H.J. 1991. Fine-grained terrigenous sediment supply and dispersal in the Gulf of California during the last century. In: Simoneit B. and Dauphin P. (Eds.). *The Gulf and Peninsular Province of the Californias*. Amer. Assoc. Petroleum Geologists, Memoir 47, Tulsa Oklahoma.

Baker, E.T. and Lavelle, J.W. 1984. The effect of particle size on the light attenuation coefficient of natural suspensions. *Journal of Geophysical Research*, 89, C5, 8197-8203.

Benns, E.J. and Pilgrim, D.A. 1994. The effect of particle characteristics on the beam attenuation coefficient and output from an optical backscatter sensor. *Netherlands Journal of Aquatic Ecology*, 28, 245-248.

Black, K.S. and Paterson, D.M. 1997. Measurement of the erosion potential of cohesive, marine sediments: a review of current in situ technology. *Journal of Marine Environmental Engineering* 4, 43-84.

Bowers, D.G., 1989, Models of density current outflows from inverse estuaries: With application to Spencer Gulf, South Australia. In: Davis, A.M. (Ed.). *Focus on Modelling Marine Systems Vol. 2 CRC State-of-the-art series on Numerical Modelling of Marine Systems*, pp 1-24.

Bray, N. and Robles, J .1991.Physical oceanography of the Gulf of California. In Simoneit B. and Dauphin, P. (Eds.). *The Gulf and Peninsular Province of the Californias*. Amer. Assoc. Petroleum Geologists, Memoir 47, Tulsa, Oklahoma.

Campbell, A.R. 1996. Effects of turbulence on suspended sediment concentrations in a tidal flow. Ph.D. Thesis, Univesity of Wales, Bangor, 225 pp.

Carbajal, N. 1993. Modelling of the circulation in the Gulf of California. Ph D Thesis. University of Hamburg. Hamburg, Germany, 186 pp.

Carbajal, N., Souza, A. and Durazo, R. 1997 A numerical study of the exROFI of the Colorado River. *Journal of Marine Systems*, 12, 17-33.

Carriquiry, J.D. and Sánchez, A. 1999 Sedimentation in the Colorado River delta and Upper Gulf of California after nearly a century of discharge loss. *Marine Geology*, vol.158, 125-145.

Cheng, R.T., Gartner, J.W., Cacchione, D. and Tate, G.B. 1998. Flow and suspended particulate transport in a tidal bottom layer, South San Francisco Bay, California. In: Dronkers and Scheffers (Eds) *Physics of Estuaries and Coastal Seas*. Balkema, Rotterdam.

Cheng, R.T., Ling, C-H., Gartner, J.W. and Wang, P.F.1999. Estimates of bottom roughness length and bottom shear stress in South San Francisco Bay, California. Jour. Geophys. Res. 104, C4, 7715-7728.

Chriss, T.M. and Caldwell, D.R. 1982. Evidence for the influence of form drag on bottom boundary layer flow. Jour. Geo. Res., 87, C6, 4148-4154

Clarke, S. 1995. Advective/diffusive processes in the Firth of Forth. UCES Report U95-13. University of Wales, Bangor, 262 pp.

✈ Clarke, S. and Elliott, A. 1998. Modelling suspended sediment concentrations in the Firth of Forth. Estuarine, Coastal and Shelf Science 47, 235-250.

Collins, M.B., Ke, X. & Gao, S. 1998 Tidally-induced flow structure over intertidal flats. Estuarine, Coastal and Shelf Science, 46, 233-250.

Cupul-Magaña, A. 1994. Flujos de sedimento en suspensión y de nutrientes en la cuenca estuarina del Río Colorado. M. Sc. Thesis. Univ. Aut. de Baja California, Ensenada, B. C., nov 1994. 177 pp.

Daesslé, L.W., Ramos, S.E., Carriquiry, J.D. and Camacho-Ibar, V.F. 2002. Clay dispersal and the geochemistry of manganese in the Northern Gulf of California. Continental Shelf Research, vol. 22, issue 9, 1311-1323.

Delgado-Gonzalez, O.E., Ocampo-Torres, F.J. y Larios-Castillo, S. 1994. Las brisas durante algunos meses de primavera y verano en el noroeste del Golfo de California. Ciencias Marinas, 20 (3), 421-440.

Durazo-Arvizu, R.1989. Frentes térmicos de verano en el Alto Golfo de California. MSc. Thesis. CICESE, Ensenada, B.C., México.

Dyer, K.R. 1980. Velocity profiles over a rippled bed and the threshold of movement of sand. Estuarine and Coastal Marine Science, 10, 181-199.

Dyer, K.R. 1986. Coastal and Estuarine Sediment Dynamics. John Wiley & Sons, New York, 342 pp.

Dyer, K.R. 1995. Sediment transport processes in estuaries. In: Perillo, G.M.E. (Ed.) Geomorphology and Sedimentology of Estuaries. Developments in Sedimentology 53, 423-449.

Filloux, J.H. 1973. Tidal patterns and energy balance in the Gulf of California. *Nature*, 243, 217-221.

Fisher, N. 1998. Tidal variations in the characteristics of suspended particulate matter at a site in the Gulf of California. Unpublished BSc. 3rd year project. University of Wales, Bangor. 32 pp.

García de Ballesteros, M. G. y Larroque, M. 1974. Elementos sobre la turbidez en el Alto Golfo de California. *Ciencias Marinas* 1 (2), 1-30.

García-Hernández, J., King, K.A., Velasco, A.L., Shumilin, E., Mora, M.A., and Glenn, E.P. 2001. Selenium, selected inorganic elements, and organochlorine pesticides in bottom material and biota from the Colorado River delta. *Journal of Arid Environments*, 49, 65-89.

Gayman, W. 1969. Turbidity in the extreme northern Gulf of California. In: Thomson, D.A., Mead, A.R. and Schreiber, J.R. (Eds.). The northern Gulf of California: A synopsis based on available information. Environmental Impact of Brine Effluents on Gulf of California. U.S. Dept. of the Interior, Research and Development Progress Rep. No. 387. March 1969.

Gordon, H.R., Smith, R.C. and Zaneveld, J.R.V. 1980. Introduction to ocean optics. *SPIE Ocean Optics* VI, 208, 14-55.

Gorsline, D.S. 1967. Sedimentologic studies of the Colorado Delta. University of Southern California, Dept. of Geology, Los Angeles, California. unpub. man. 89 pp.

- Graf, W. H. 1971. *Hydraulics of Sediment Transport*. Mc Graw-Hill Book Co.
- Green, M.O. and McCave, I.N. 1995. Seabed drag coefficient under tidal currents in the eastern Irish Sea. *Journal of Geophysical Research* 100, C8, 16,057-16,069.
- Griffiths, R.W. and Hopfinger, E. 1983. Gravity currents moving along a lateral boundary on a rotating fluid. *Journal of Fluid Mechanics* 134, 357-399.
- Groen, P., 1967, Physical hydrology of coastal lagoons. In: Ayala-Castañares, A., and Phleger, F.B., (Eds). *Coastal Lagoons, a Symposium. Memoir of the International Symposium on Coastal Lagoons*. UNAM-UNESCO, México, D.F., 275-280.
- Gross, F.T. and Nowell, A.R.M. 1983. Mean flow and turbulence scaling in a tidal boundary layer. *Continental Shelf Res.* vol. 2, no 2/3, 09-126.
- Haralampides, K., McCorquodale, J.A. and Krishnappan, B.G. 2003. Deposition properties of fine sediment. *Journal of Hydraulic Engineering*, 129, 3, 230-234.
- Hawley, N. 1991. Preliminary observations of sediment erosion from a bottom resting flume. *Jour. of Great Lakes Research*, 17, 3, 361-367.
- Hendershott, M. and Speranza, A. 1971. Co-oscillating tides in long narrow bays; the Taylor problem revisited. *Deep-sea Res.* 18 (10) , 959-980.
- Hendrickson, J. R. 1973. Study of the marine environment of the northern Gulf of California. University of Arizona, Biological Sciences. Dept. Final Report. October, 1973. 106 pp.
- Hernández Ayón, J. M., Galindo-Bect, M. S., Flores-Baez, B. P. and Alvarez-Borrego, S. 1993. Nutrient concentrations are high in the turbid waters of the Colorado River Delta. *Estuarine, Coastal and Shelf Science*, 37, 593-602.
- Hill, D.C. 1999. A methodology for numerical estimation of physical sediment parameters in coastal waters. PhD Thesis, University of Wales, Bangor, 119 pp.

Hill, D.C., Jones, S.E. and Prandle, D. 2003. Derivation of sediment resuspension rates from acoustic backscatter time-series in tidal waters. *Continental Shelf Research* 23, 19-40.

Hill, P. S. 1998. Controls on floc size in the sea. *Oceanography* 11, 2, 13-18.

Holdaway, G.P., Thorne, P.D., Flatt, D., Jones, S.E., Prandle, D. 1999 Comparison between ADCP and transmissometer measurements of suspended sediment concentration. *Continental Shelf Research* 19, 421-441.

Jago C F, A J Bale, M O Green, M J Howarth, S E Jones, I N McCave, G E Millward, A W Morris, A A Rowden and J J Williams. 1993. Resuspension processes and seston dynamics, southern North Sea. *Phil. Trans. R. Soc. London. A* 343, 475-491

Jago, C.F. and Jones, S.E. 1998. Observation and modelling of the dynamics of benthic fluff resuspended from a sandy bed in the southern North Sea. *Continental Shelf Research* 18, 1255-1282.

Jones S.E., Alvarez, L.G., Fisher, N. and Probert, D. (In preparation) Physical characteristics of suspended particles in the Upper Gulf of California.

Jones, S. E., Jago, C. F. Prandle, D. and Flatt, D.. 1994. Suspended Sediment Dynamics: Measurement and modelling in the Dover Strait. In: *Mixing and Transport in the Environment*. Chapter 10. Ed. by K J Beven, P C Chatwin and J H Millbank. John Wiley and Sons Ltd.

Julien, P.Y. 1995. *Erosion and Sedimentation*. Cambridge University Press, 280 pp.

Kineke, G.C. and Sternberg, R.W. 1989. The effect of particle settling velocity on computed suspended sediment concentration profiles. *Marine Geology*, 90, 159-174.

Krone, R.B. 1993. Sedimentation Revisited. In: Mehta, A.J. (Ed.) Nearshore and estuarine cohesive sediment transport. Coastal and Estuarine Studies 42. American Geophysical Union, Washington, D.C.

Lavín, M F and Organista, S. 1988. Surface heat flux in the northern Gulf of California. Journal of Geophysical Research, 93, 14033-14038.

Lavín M F, Gaxiola-Castro, G., Robles, J. M. and Richter, K. 1995. Winter water masses and nutrients in the northern Gulf of California. Journal of Geophysical Research 100, 8587-8605.

Lavín, M.F., Godínez V.M. and Alvarez, L.G. 1998. Inverse-estuarine features of the Upper Gulf of California. Estuarine, Coastal and Shelf Science, 47, 769-795.

Lavín, M.F. and Sánchez, S. 1999. On how the Colorado river affected the hydrography of the Upper Gulf of California. Continental Shelf Research 19, 1545-1560.

Lavelle, J.W. 1993. A model of estuarine sedimentation involving marine snow. In: Mehta, A.J. (Ed.) Nearshore and estuarine cohesive sediment transport. Coastal and Estuarine Studies 42. American Geophysical Union, Washington, D.C. 148-168.

Lavelle J. W., Mofjeld, H. O. and Baker, E .T. 1984. An in-situ erosion rate for a fine-grained marine sediment. Journal of Geophysical Research 89, 6543-6552.

Lesht, B.M. 1979. Relationship between sediment resuspension and the statistical frequency distribution of bottom shear stress. Marine Geology 32, M19-M27.

Lick, W. and Huang H. 1993. Flocculation and the physical properties of flocs. In: Mehta, A.J. (Ed.) Nearshore and estuarine cohesive sediment transport. Coastal and Estuarine Studies 42. American Geophysical Union, Washington, D.C.

López, M. 1997. A numerical simulation of water mass formation in the northern Gulf of California during winter. Continental Shelf Research 17, 1581-1607.

Ludwick, J.C. 1975. Variations in the boundary-drag coefficient in the tidal entrance to Chesapeake Bay, Virginia. *Marine Geology* 19, 19-28.

Lueck R.G. and Lu Y. 1997. The logarithmic layer in a tidal channel. *Continental Shelf Research* 17, 14, 1785-1801.

Maa, J.P.-Y., Wright, L.D., Lee, C.-H. and Shannon, T.W. 1993. VIMS Sea Carousel: A field instrument for studying sediment transport. *Marine Geology*, 115, 271-287.

McAnally, W.H. and Mehta, A.J. 2001. Preface. In: McAnally W.H. and Mehta, A.J. (Eds) *Coastal and Estuarine Fine Sediment Processes. Proceedings in Marine Science* 3, v-vii. Elsevier.

Marinone, S.G. 1997. Tidal residual currents in the Gulf of California: Is the M_2 tidal constituent sufficient to induce them? *Journal of Geophysical Research* 102, 8611-8623.

Marinone, S. G. y Lavín, M. F. 1997. Mareas y corrientes residuales en el Golfo de California. In: . MF Lavín (ed) *Contribuciones a la Oceanografía Física en México*, Monografía No. 3, Unión Geofísica Mexicana, pp 117-144.

Martinez-Rojas-Reynoso, M. K. 1990. Distribución espacial y registros circadianos de temperatura, salinidad y oxígeno disuelto en el Delta del Río Colorado. B Sc Thesis. Universidad Autónoma de Baja California, Ensenada, México. 90 pp.

Mathews, J. B. 1969. Tides in the Gulf of California. In: D A Thomson, A R Mead and J R Schreiber (Eds) *The northern Gulf of California: A synopsis based on available information. Environmental Impact of Brine Effluents on Gulf of California*. US Dept. of the Interior, Research and Development Progress Rep. No. 387. March 1969.

Merrifield, M. A. and Winant, C. D. 1989. Shelf circulation in the Gulf of California: A description of the variability. *Jour. Geophys. Research*, 94 18, 133-18, 160.

Middleton, G.V. and Southard, J.B. 1984, *Mechanics of sediment movement*, 2nd Edition. Society of Economic Paleontologists and Mineralogists. Short Course No. 3, 401 pp.

Miranda-Reyes, F., Reyes-Coca, S. y García López, J. 1990. Climatología de la región noroeste de México, Parte I: Precipitación. Rep. Téc. EBA no 3. CICESE, Ensenada, B.C. 160 pp.

Morales-Perez, R. y Gutierrez de Velasco, G. 1989. Mareas en el Golfo de California. *Geofisica Internacional*, 28, 25-46.

Murray, P.B. 1992. Sediment pick-up in combined wave-current flow. PhD Thesis. University College of North Wales, Menai Bridge, 189 pp.

Nunes, R.A. and Lennon, G.W. 1986. Physical property distributions and seasonal trends in Spencer Gulf, South Australia: an inverse estuary. *Australian Journal of Marine and Freshwater Research* 37, 39-59.

Nunes, R.A. and Lennon, G.W. 1987. Episodic stratification and gravity currents in a marine environment of modulated turbulence. *Journal of Geophysical Research* 92, C5, 5465-5480.

Nunes Vaz, R.A., Lennon, G.W. and Bowers, D.G. 1990 Physical behaviour of a large, negative or inverse estuary. *Continental Shelf Research*, 10, (3), 277-304.

Postma, H. 1967 Chemistry of coastal lagoons. In: Ayala-Castañares, A., and Phleger, F.B., (Eds.) *Coastal Lagoons, a Symposium. Memoir of the International Symposium on Coastal Lagoons*. UNAM-UNESCO, México, D.F., 421-429.

Pritchard, D.W., 1967. What is an estuary: Physical Viewpoint. In: Lauff, G.H. (Ed) *Estuaries*. AAAS Publication No. 83 pp 3-5.

Probert, D.M. 1998. Resuspension and transportation of sediments in the Gulf of California. Unpublished BSc. 3rd year project. University of Wales, Bangor. 54 pp.

Quirós, G. A., Badan-Dangon, A. and Ripa, P. 1992. M_2 currents and residual flow in the Gulf of California. *Netherlands Journal of Sea Research* 28, 251-259.

Ravens, T.M. and Gschwend, P.M. 1999. Flume measurements of sediment erodibility in Boston Harbor. *Journal of Hydraulic Engineering*, 125, 10, 998-1005.

Reyes, A. C. and Lavín, M. F. 1997. Effects of the autumn-winter meteorology upon the surface heat loss in the Northern Gulf of California. *Atmósfera*, 10, 101-123.

Sanford, L.P. and Halka, J.P. 1993. Assessing the paradigm of mutually exclusive erosion and deposition of mud, with examples from upper Chesapeake Bay. *Marine Geology* 114, 37-57.

Sanford, L.P. and Chang, M.L. 1997. The bottom boundary condition for suspended sediment deposition. *Journal of Coastal Research*, SI no. 25, 3-17.

Schreiber, J.F. Jr. 1969. The northern Gulf of California: A synopsis based on available information. Geographical and Geological Features. In: Thomson, D.A., Mead, A.R. and Schreiber, J. R. (Eds.). *Environmental Impact of Brine Effluents on Gulf of California*. US Dept. of the Interior. Research and Development Progress Rep. No. 387. March 1969.

Smith, J.D. and McLean, S.R. 1977. Spatially averaged flow over a wavy surface. *Journal of Geophysical Research*, 82, 12, 1735-1746.

SonTek Technical Notes, 1997 Acoustic Doppler profiler (ADP) principles of operation. SonTek, Inc., San Diego, CA, USA, 12 pp.

SonTek Technical Notes, 1998 Acoustic Doppler profiler: Signal strength correction. SonTek, Inc., San Diego, CA, USA, 12 pp.

Soulsby, R.L. 1983. The bottom boundary layer of shelf seas. In: B. Johns (Ed.) *Physical Oceanography of Coastal and Shelf Seas*, chapter 5, Elsevier Pub. Co. Amsterdam, 189-266.

Sternberg, R.W. 1968. Friction factors in tidal channels with differing bed roughness. *Marine Geology*, 6, 3, 243-260.

Teisson, C. 1991. Cohesive suspended sediment transport: feasibility and limitations of numerical modelling. *Journal of Hydraulic Research* 29, 755-769.

Thompson, R.W. 1968. Tidal flat sedimentation on the Colorado River delta, Northwestern Gulf of California. *The Geological Society of America, Memoir* 107, 129 pp.

Thompson, R. W. 1969. The northern Gulf of California: A synopsis based on available information. *Bathymetry and Sedimentation*. In: Thomson, D.A., Mead, A.R. and Schreiber, J. R. (Eds.). *Environmental Impact of Brine Effluents on Gulf of California*. US Dep. of the Interior. Research and Development Progress Report 387. March, 1969.

Thorne, P.D., Vincent, C.E., Hardcastle, P.J., Rehman, S., and Pearson, N. 1991. Measuring suspended sediment concentrations using acoustic backscatter devices. *Marine Geology*, 98, pp 7-16.

Thorne, P.D., Hardcastle, P.J. and Soulsby, R.L. 1993 Analysis of acoustic measurements of suspended sediments. *Journal of Geophysical Research*, 98,C1, 899-910.

Thorne, P.D., Hogg, A., Hardcastle, P.J. and Grubb, M. 1996 Application of multi-frequency acoustic backscattering to the measurement of sediment eddy diffusivity, 3rd European Conference in Underwater Acoustics, Heraklion, Greece.

Tolhurst, T.J., Black, K.S., Shayler, S.A., Mather, S., Black, I., Baker, K. and Paterson, D.M. 1999. Measuring the *in situ* erosion shear stress of intertidal sediments with the cohesive strength meter (CSM). *Estuarine, Coastal and Shelf Science* 49, 281-294.

Tolhurst, T.J., Black, K.S., Paterson, D.M., Mitchener, H.J., Termaat, G.R. and Shayler, S.A. 2000. A comparison and measurement standardisation of four *in situ* devices for determining the erosion shear stress of intertidal sediments. *Continental Shelf Research*, 20, 1397-1418.

Trowbridge, J. H., Chapman, D. C. and Candela, J. 1998. Topographic effects, straits and the bottom boundary layer. In: Brink, K.H. and Robinson, A.R. (Eds), *The Sea*, Vol 10. John Wiley & Sons, Inc.

Wadhams, P., Gill, A.E. and Linden, P.F. 1979 transects by submarine of the East Greenland polar front. *Deep-Sea Research* 26A pp 1311-1327.

Weeks, A. R. and Simpson, J. H. 1991. The measurement of suspended particulate concentrations from remotely-sensed data. *International Journal of Remote Sensing*, 12, 725-737.

Whitehouse, R. 1995. Observations of the boundary layer characteristics and the suspension of sand at a tidal site. *Continental Shelf Research*, 15, 13, 1540-1567.

Widdows, J., Brinsley, M.D., Bowley, N. and Barret, C. 1998. A benthic annular flume for in situ measurement of suspension feeding/biodeposition rates and erosion potential of intertidal cohesive sediments. *Estuarine, Coastal and Shelf Science*, 46, 27-38.

Wilkinson, R.H. 1984. A method for evaluating statistical errors associated with logarithmic velocity profiles. *Geo-Marine Letters*, 3, 49-52

Wolanski, E. 1988 Circulation anomalies in tropical Australian estuaries. *Dynamics of Estuaries*, vol. II, 53-59.

Yalin, M.S. 1977. *Mechanics of sediment transport*. Pergamon Press, Oxford, 290 pp.

Zamora-Casas, C. 1993. Comportamiento del seston en la desembocadura del Río Colorado, Sonora-Baja California. BSc thesis. Universidad Autónoma de Baja California, Junio 1993. 73 pp.

Appendix

Sample calculation of the critical bed shear stress for erosion (τ_c) and erodibility based on the centroid method, using vertically integrated SPM concentration. Data shown in Table A.1 are for site W3, on the western side of the Upper Gulf, during spring tides. The average values and standard deviations are shown in Tables 6.2 and 6.4.

Table A-1. Sample calculation of the critical bed shear stress for erosion and erodibility.

DATA COLUMNS INFO: (N=8)

Time index	τ_c	slope	erodibility
11.00	1.05204535907	0.00003663666	0.00003854343
80.00	0.74969279515	0.00003467534	0.00002599585
155.00	1.14524456650	0.00003081110	0.00003528624
225.00	0.78117853550	0.00002887893	0.00002255960
292.00	0.28670779069	0.00004007213	0.00001148899
374.00	0.68742487986	0.00005527189	0.00003799527
444.00	0.60043315944	0.00000926974	0.00000556586
522.00	0.89078567093	0.00004040307	0.00003599048
MEANS:	0.77418909464	0.00003450236	0.00002667821
STANDARD DEVIATION:	0.26845779800	0.00001300403	0.00001266913

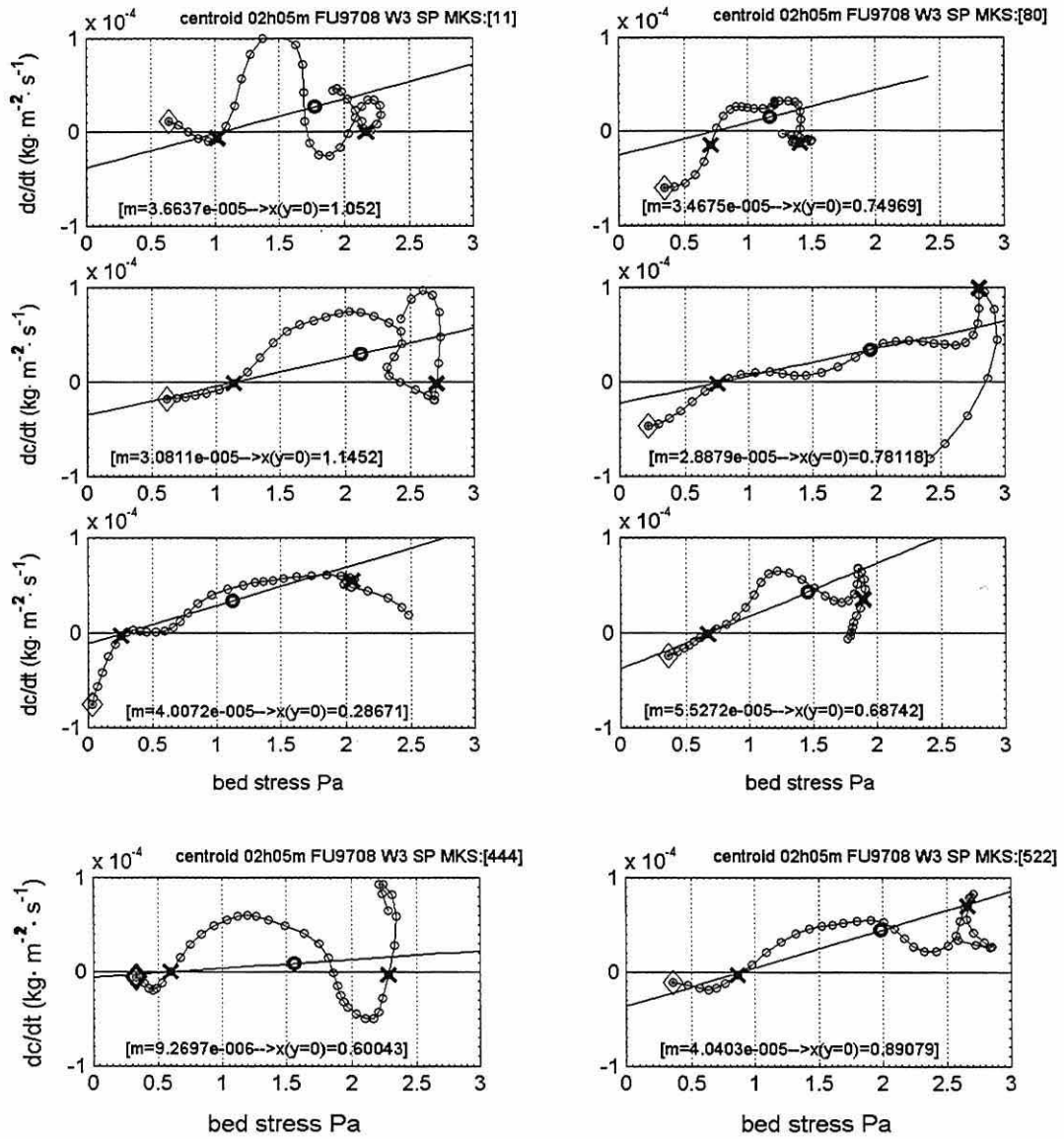


Figure A.1. Sample plots of the centroid method calculations for the critical bed shear stress for erosion and the erodibility constant. The 2-hour interval is marked by \times and the centroid by the bold circle. The slope of the line and the x-axis crossing are given as m and $x(y=0)$, respectively.